Design, Fabrication and Characterisation of Cross Compound Parabolic Concentrators for Solar Power Generation

A thesis submitted to Cardiff University in the candidature for the degree of

Doctor of Philosophy

By

Mazin Amur Ali Al-Shidhani

School of Engineering

Cardiff University

March 2020

Acknowledgements

All praises are due to Allah the most merciful, the most gracious and magnificent who gave me the strength, courage and health to complete this research project.

I would like to thank my supervisor Prof. Gao Min for his support and guidance throughout the project. I am really grateful for all the efforts made by him, which enabled me to complete this thesis.

My sincere thanks to my second supervisor Dr. Victoria for her kindness, patience and support during my study. Deepest appreciation also goes to the Mechanical and Electrical workshop for their technical support; in particular, special thanks to Mr. Andrew Rankmore, Mr. Craig, Mr. Steve, Mr. Malcolm, Mr. Clave and Mr. Denley.

I would like to thank my beloved wife Tamadher Al-Rawahi for her patience, motivation and constant support. Despite the challenges of undertaking this study, she has stood beside me, and ensured that this dream has turned to reality. I owe her extreme thanks. Gratitude is also due to my children Reema and Azzan- thank you for always cheering me up.

I would not have overcome the challenges and difficulties of this level of study without the continuous encouragement and prayers of my parents Amur Al-Shidhani and Zainab Al-Mamari. I would like to thank my brothers and sisters for their support throughout the progression of my research – their questions and interest have been much appreciated.

I would like to thank the Ministry of Higher Education (MOHE) in Oman for granting me the scholarship needed to carry out my postgraduate study and the Petroleum Development Oman (PDO) who supported me financially and also granted me sabbatical leave to allow me to complete this work.

I am grateful to all my friends at Cardiff University, particularly Mohammed Al-Najdeen, with whom I shared my thoughts and ideas throughout the project. The time we have spent brainstorming, and in discussion of specific matters of science and technology has been invaluable. Many thanks to Abdullah Al-Tuwairgi for the time spent in discussion

and debate throughout the project period. Many thanks also go to Guillermo, Martin, Alex and all the new researchers who joined our group.

Lastly, I would like to offer my highest gratitude to all those who have supported me in any aspect during my research and who I have been in continuous contact with during my stay in Cardiff.

Abstract

Concentrating Photovoltaics (CPV) have the potential to increase the power output and reduce the cost of photovoltaic (PV) systems by replacing expensive PV materials with cheaper optical materials that concentrate the sunlight onto a smaller PV area. This thesis describes a detailed investigation into the design, fabrication and characterisation of Crossed Compound Parabolic Concentrators (CCPC) for photovoltaic application. A set of high-performance CCPCs, which have concentration ratios of 2.9x, 4.0x, 6.0x, 8.3x and 9.0x, respectively, were fabricated using state-of-the-art 3D printing and highly reflective thin-film mirrors. Excellent optical efficiencies from 82.0% to 84.5% were obtained using these concentrators.

The angular response of the fabricated concentrators was carried out to provide robust experimental data for the design and optimisation of non-stationary CCPC solar power systems. The experimental results show that the half acceptance angle decreases as the concentration ratio increases, which agrees well with computer simulation using TracePro. The results from a novel rectangular CCPC show that the angular response of the CCPC can be significantly improved with appropriate use of the second reflection, which demonstrates the important role of multiple reflections in the design for high-performance concentrators. The uniformity of light distribution across a PV cell has a significant effect on the power output and stability of the PV cell. It is therefore crucial to ensure the uniformity on the exit aperture of the concentrator. Hence, a systematic study was carried out to determine the appropriate position of the PV cell with reference to the exit aperture of the concentrator. The results show that an optimal position exists for a given concentration ratio, although it varies for different concentration ratios. The optimal value for the concentrators that are investigated in this work ranges from 1.5 mm to 3.0 mm below the exit aperture of the concentrators.

A tracking system can be employed to maximise the daily power generation in response to changing positions of the sun during the day. A calculation procedure was developed to determine the minimum tracking movements while obtaining the maximum daily energy production of a CCPC solar power system. The optimal tracking movements for the concentrators investigated in this project were determined using this procedure. The results indicate that a simple and low-cost tracking system is sufficient. Finally, a cost analysis and the potential economic benefit of the developed concentrators are discussed.

Dedication

I dedicate this thesis to his majesty Sultan Qaboos bin Said

The former sultan of the sultanate of Oman

Who granted me the scholarship to carry on my higher studies

May Allah rest his soul in "Firdaws" heavens

Contents

List of Figures

List of Tables

List of Abbreviations

2D	Two dimensional
3D	Three dimensional
ACPC	Asymmetric Compound Parabolic Concentrator
AM	Air Mass
AOI	Angle of Incidence
a-Si	Amorphous Silicon
BICPV	Building Integrated Concentrating Photovoltaic
CAD	Computer Aided Design
CC	Capital Cost
CCPC	Cross Compound Parabolic Concentrator
CdTe	Cadmium Telluride
CIGS	Copper Indium Gallium (di) Selenide
CIS	Copper Indium Diselenide
CMM	Coordinate Measuring Machine
CNC	Computer Numerical Control
CPC	Compound Parabolic Concentrator
CPV	Concentrated Photovoltaic
CR	Concentration Ratio
c-Si	Crystalline Silicon
CUF	Concentrator Uniformity Factor
CZ	Czocharlski
DC	Direct Current
DCB	Direct Copper Bonded
DiACPC	Dielectric Asymmetric Compound Parabolic Concentrator
DNI	Direct Normal Irradiance
E-W	East West plane direction
EDC	Equation Driven Curve
EXP	Experimental
FF	Fill Factor
FL	Fresnel lens
GaAs	Gallium Arsenide
HCPV	High Concentrating Photovoltaic
hp	Horsepower

IEA	International Energy Agency
I-V	Current – Voltage
InP	Indium Phosphide
IPA	Isopropyl Alcohol
LCPV	Low Cost Photovoltaic
LGBC	Laser Grooved Buried Contact
LST	Local Solar Time
LT	Local Time
MCPV	Medium Concentrating Photovoltaic
MPP	Maximum Power Point
Mono-Si	Monocrystalline Silicon
MJ	Multijunction
N-S	North South plane direction
n	Number of days
NIDC	Non-imaging Dish Concentrator
NIR	Near Infrared
NREL	National Renewable Energy Laboratory
OM	Optical Mixer
POE	Praimary Optical Element
PMMA	Polymethyle Methacrylate
PV	Photovoltaic
PV/T	Photovoltaic/ Thermal system
RACPC	Rotational Asymmetric Compound Parabolic Concentrator
RCCPC	Rectangular Cross Compound Parabolic Concentrator
RPM	Revolution Per Minute
SEH	Square Elliptical Hyperboloid
SIM	Simulation
SLA	Stereolithographic
SOE	Secondary Optical Element
STC	Standard Test Condition
TF	Thin Film
TIR	Total Internal Reflection
UV	Ultra-Violet
UV-VIS	Ultra-Violet –Visible light
Xe	Xenon lamp

List of Symbols

Symbol	Definition	Unit
A_{Entry}	Entry area	m^2
A_{Exit}	Exit area	m^2
A_r	Reciever area	m^2
α_s	Solar altitude angle	Degree
α'	Absorber width	m
α	Short-circuit current temperature coefficient	/°C
β	Open circuit voltage temperature coefficient	/°C
C_{geo}	Geometric concentration ratio	-
C_{exp}	Experiment concentration ratio	-
Dev	Deviation	%
d_1	Input diameter	m
d_2	Output diameter	m
E_{gap}	Band gap of the semiconductor	e.V
ε	Temperature coefficient of maximum power	/°C
f	Focal point of concentrator	m
GD	Direct solar radiations	W/m^2
h	Full height of concentrator	m
h_T	Truncated height	m
I	Electrical current	Amp
I_a	Insolation incident	W/m^2
I_{max}	Current at maximum power	Amp
I_0	Diode saturation current	Amp
I_r	Average flux	W/m^2
I_{sc}	Short-circuit current	Amp
I_{ph}	Photocurrent	Amp
k	Boltzmann constant	$m^2kgs^{-2}K^{-1}$
n	Ideality factor of the diode	-
η_{pv}	Electrical conversion efficiency	%
$\eta_{optical}$	Optical efficiency	%
$\eta_{Exp,optical}$	Experimental optical efficiency	%

P	Power	Watt
ρ	Reflectivity	%
q	Charge of an electron	coulomb
R	Distance of earth from the sun	m
R_s	Series resistance	Ohm
R_{sh}	Shunt resistance	Ohm
P_{max}	Maximum power output	Watt
T_{ref}	Temperature at reference	°C
V_{max}	Voltage at maximum power	Volt
V_{OC}	Open-circuit voltage	Volt
δ	Declination	Degree
γ	Surface azimuth angle	Degree
ω	Hour angle	Degree
Θ	Full acceptance angle	Degree
Θ_c	Half acceptance angle	Degree
Θ_e	Effective acceptance angle	Degree
Θ_i	Angle of incidence	Degree
Ø entry	Flux at the entry aperture	-
Ø exit	Flux at the exit aperture	-
Θ_m	Maximum acceptance angle	Degree
Θ_z	Zenith angle	Degree
ω_r	Sun rising time	hour
ω_s	Sunset time	hour
γ_s	Solar azimuth angle	Degree

Chapter One: Introduction

1.1 Background and Motivation

One of the biggest challenges that the world faces is to eliminate the dependence on fossil fuels. Renewable energy resources are a promising solution to overcome this challenge. It has been reported by the International Energy Agency (IEA) that by 2040, nearly 60% of the power generated in the world is projected to come from renewable energy [1]. Solar energy is one of the most abundant sources of renewable energy on earth which produces clean energy. The sunlight is a limitless source of energy and the amount of solar energy received in one hour by the earth is sufficient to power the entire world for one year, if fully utilised [2]. However, harvesting this energy efficiently and cost-effectively is a big challenging [2, 3].

Renewable energy is expected to grow by 50% between 2019 and 2024 based on a recent projection by International Energy Agency (IEA). Solar photovoltaic energy alone represents approximately 60% of the anticipated growth. The IEA reports that 2.6% of global power output in 2018 was from photovoltaics [4]. Regardless of current regulatory changes and uncertainty, the competitiveness of solar photovoltaics has continued to improve in China, India and the United States. Solar PV continues to grow to the expected levels of sustainable development scenario, with an annual average increase of 16% from 2018 to 2030 [5].

Solar radiation can be collected and concentrated using mirrors to produce high-temperature heat for electricity generation by using steam turbines or heating the buildings directly. The solar radiation can also be harnessed using photovoltaic (PV) devices that converts the sunlight directly into electricity. In order to realise the vision of replacing the fossil fuel based systems with clean energy systems, it is necessary to reduce the cost of renewable energy systems. Replacing high-cost PV materials with low-cost solar concentrators has potential to reduce the total system cost and make this technology economically viable. The design of high performance and low-cost solar concentrators plays an important role in enhancing PV system economic competitiveness.

There have been various types of solar concentrators developed over the past decades, including Fresnel Lenses, quantum dot concentrator, parabolic trough concentrator, parabolic dish concentrator and compound parabolic concentrator (CPC). The CPC is the stationary concentrator that has been studied by many researcher and is said to be an optimal concentrator because it has the best performance for all radiation within the acceptance angle [6]. Among different types of CPC concentrators, the most popular one is the Cross Compound Parabolic Concentrator (CCPC). This type of concentrator is the main focus of this project as it has the advantages of: 1) better optical efficiency and 2) relatively larger acceptance angle. However, the CCPC also has limitations for example, its acceptance angle decreases with an increase in the concentration ratio. As a result, the tracking system may be needed for the concentrators with higher concentration ratios. Another limitation is the non-uniformity of the light distribution across the receiver surface. This project addresses these limitations in attempt to improve the performance of this type of concentrators.

1.2 Aim and Objectives

This project is aimed at investigating low concentration photovoltaic systems for rooftop applications, particularly in the regions where direct solar irradiance is dominant such as Oman. The project will focus on studying the characteristics and responses of concentrators to the angular change of solar irradiation. It is anticipated that the results obtained from systematic experimental investigations (with support of simulation) will provide insights and knowledge toward the development of efficient rooftop PV systems. The key objectives of the project include:

1) Identify suitable solar concentrators that have potential for developing low-cost and efficient rooftop PV systems.
2) Develop design, simulation and fabrication procedures/techniques for construction of the solar concentrators with improved performances.
3) Investigate the main characteristics of the fabricated concentrators, including the optical efficiency, angular response and light uniformity of the concentrators.
4) Develop a theoretical framework for the calculation of optimal movement of tracking to maximise the solar energy collection at minimum cost.
5) Perform cost analysis of low concentration solar power systems for evaluation of economic viability of the concentrated solar power systems.

1.3 Thesis Outline

This thesis describes a detailed experimental investigation and simulation of compound parabolic concentrators for developing high-performance and low-cost solar power systems. It comprises of seven chapters. The purposes and main focuses of each chapter are summarised as follows;

Chapter One - The chapter gives an introduction to the background and motivation of this research project and presents the aim and key objectives of the research activities described in this thesis.

Chapter Two - This chapter presents an extensive literature review on solar energy harvesting based on photovoltaic (PV) devices. The basics and principles of PV cells and their applications are summarised. Progress on concentrated photovoltaic (CPV) systems, their classification and applications are reviewed with a focus on the Cross Compound Parabolic Concentrators (CCPCs) because they are main concentrators employed in this research. In addition, literature review related to the uniformity of light distribution across a PV cell under concentration, and the advantages and disadvantages of concentrated PV is also carried out. Finally, the literatures about the sunlight tracking systems and their types and applications are included.

Chapter Three - This chapter presents the experimental techniques that were employed and developed for fabrication and characterisation of the concentrators constructed in this project. Detailed information are given regarding the correct use of the key instruments, appropriate setup of the testing equipment and careful calibration of the measurement systems in order to ensure correct functionality of the equipment and the reliability experimental results. A detailed description and know-hows are also provided on the procedures and techniques developed in this project, which include the fabrication procedures/methods for making high-performance concentrators and the rotary stage for investigating the angular response.

Chapter Four - This chapter provides detailed description on design, simulation and fabrication of low-cost and high-performance CCPCs. The design was carried out using SolidWorks based on an established theoretical framework of compound parabolic concentrators. Prior to fabrication, the performance of the designed concentrators was simulated using a ray-tracing software (TracePro®). The fabrication process of the concentrators using 3D printing is explained in detail. The highlight of this chapter is

successful fabrication of a CCPC that has the highest optical efficiency reported to date. The reasons for the high optical efficiency are discussed.

Chapter Five - The chapter describes systematic investigations of angular response and light uniformity of the fabricated CCPCs. The methodologies used to study the angular response and light distribution are explained. The angular response of the fabricated CCPCs are characterised and the optimal position to achieve the high uniformity are determined. The work has led to development of new concentrators, which show significant improvement in angular response and light uniformity. To my knowledge, these results are new, which will make original contribution to knowledge.

Chapter Six - This chapter describes the development of a theoretical framework for calculating the optimal movements of tracking required for a concentrator in order to maximise the solar energy collection at minimum cost. The results of the required tracking movements were calculated using the available solar irradiation data and the angular response data obtained in Chapter Five. The chapter also presents the results of cost analysis of CCPC solar power systems and evaluation of their economic viability in comparison with a commercial flat PV panel.

Chapter Seven - This chapter provides a summary of the main findings and conclusions of this research, together with the recommendations for future work to explore and investigate the interesting problems and challenges that were encountered in this research.

1.4 List of publications

Published

1. **Al-Shidhani**, M., et al. *Design and testing of 3D printed cross compound parabolic concentrators for LCPV system*. in *AIP Conference Proceedings*. 2018. AIP Publishing.
2. Al-Najideen, M., **M. Al-Shidhani**, and G. Min. *Optimum design of V-trough solar concentrator for photovoltaic applications*. in *AIP Conference Proceedings*. 2019. AIP Publishing.

To be published

1. *Angular Response and Uniformity Study for 4.0x Symmetrical and Rectangular Compound Parabolic Concentrators for LCPV Application.*
2. *Theoretical Study Calculation for Obtaining Optimal Tracking Movement for Low Cross Compound Parabolic Concentrators.*

Presentations

1. *Gregynog 2017 conference, Cardiff School of Engineering 9th ENGIN Postgraduate Conference – Gregynog, 3-5 July 2017.*
2. *Speaking of Science 2018 Conference, Cardiff, 2nd of May 2018.*
3. *CPV-14 Conference in Spain, 16-18 April 2018.*

Chapter Two: Literature Review

2.1 Introduction

This chapter will give an overview of solar energy and the associated technologies that are used to harvest solar energy and convert it into electricity. The literature review starts with the basic principle of the PV cell, the types of solar cells, and the solar collector classifications and applications. The main attention is on Low Concentration Photovoltaic (LCPV) systems, with particular focus on 3D Crossed Compound Parabolic Concentrator (CCPC). As a result of sunlight concentration, the concentrator receiver is affected by non-uniformity light distribution. Thus, the effect of non-uniformity distribution on system performance is discussed broadly. Maximising the energy production per day is needed and may be achieved by using a tracking system, which is another of the areas covered in this chapter. The last part of this chapter summarises the findings and determines the research gaps that will be studied and explored in this thesis.

2.2 Renewable Energy: An Overview

Energy is necessary for human society, and it has played an essential role in development and maintenance. Although the demand for energy continues to increase, energy crises and global warming have become a serious threat. The main causes of global warming are CO_2 emissions from fossil fuels [7, 8], which is expected to increase to more than 104 million barrels/day by the year 2030 [9]. The first step to control the percentage of these emissions and to reduce the risk of global warming was taken by the Paris Agreement [10], which moved towards a united energy policy [11].

Renewable energy can play an important role in reducing pollution and can be the best replacement of fossil fuels [12]. Basically, this energy is gathered by renewable sources that are naturally available, such as sunlight, tidal, wind, wave, geothermal heat, and rain. Renewable energy may change the direction of global energy consumption. Figure 2.1 shows the share of recent global renewable capacity statistics for 2019. It is clear that hydropower takes a major preference with 50% capacity, compared to other renewable energy sources, accounting for the largest share of 1,172GW from 2,351GW of the total global capacity [13].

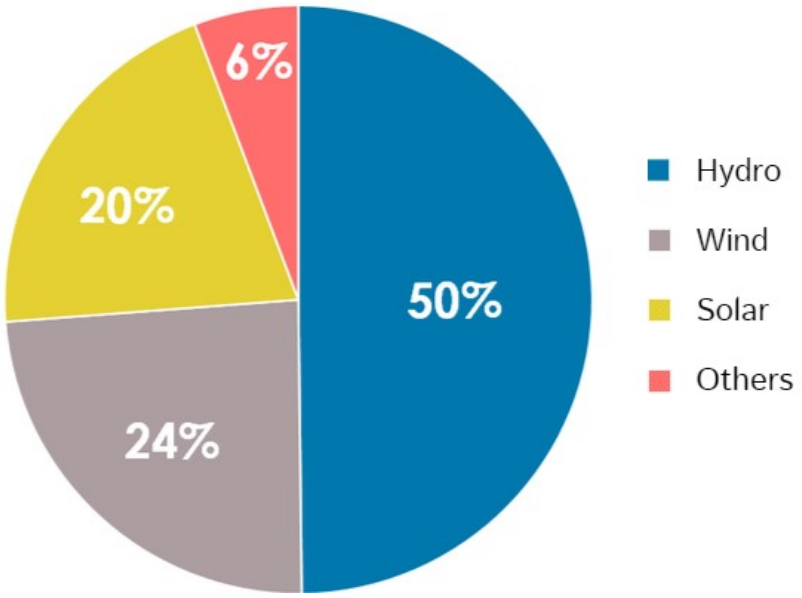

Figure 2.1: Renewable generation capacity by energy source (IRENA 2019)[13].

Although solar energy contributes only 20% of the global renewable sources capacity, it is the most abundant, clean and safe energy source [14]. Solar energy is freely available and is a promising source of energy that can solve an issue of energy crisis [15]. It has been estimated that the sun delivers 120 petajoules of energy per second to the earth [2]. Chen [16] calculated that the sun produces 5.46×10^6 exajoule/year over the earth surface, which is 10,000 times more than the annual average needed by the world in 2005–2010. The main advantage of solar energy as compared with other energy sources is that it is clean and does not produce any environmental pollution [17].

Mirrors are used to concentrate the solar radiation to provide a high temperature that can be used to generate electricity by using turbines [18]. Another way to use solar energy is by converting the sunlight directly to electricity by using Photovoltaic (PV) modules [19]. There is also an indirect way used to utilise solar radiation because most of the sunlight is absorbed by the oceans, which are warmed and add water vapour to the air, which condensates as rain which feeds the rivers. The water cycle can be utilised by making dams and turbines to extract the energy from the water [20].

2.3 Photovoltaic Technology

PV devices convert sunlight to electrical power, depending on the semiconductor material used. The principle of the solar cell is to absorb the photons from the sun and to generate power after the separation process of electron and holes. Meanwhile, the main function of PV devices is to convert the energy from solar radiation to electricity by the voltage difference that produces once the light falls on the cell. This is called the PV effect,

which was discovered by Edmond Becquerel in 1839 [21, 22]. The first solar cell was built in 1883 by Charles Fritts, whose efficiency was 1%. Then modern solar cell was patented to Russel Ohl in 1946 [23-25]. The name 'photovoltaic' is derived by the combination of two different words: 'photo', the Greek word for light; and 'Volt', from Count Alessandro Volta, the inventor of the battery [18]. There are many types of solar cell that can do the same operation but with a different capability of harvesting the amount of light due to the spectrum used.

2.3.1 Operating Principles of a Solar Cell

A solar cell is an essential element in any solar PV system and many works of literature have discussed the basic operation of a solar cell [18, 26-29]. The photovoltaic cell (PV cell) is a specialised semiconductor diode that converts the visible light into direct current (DC). The PV cells generally consist of two thin regions, one above the other—N-type and P-type. Since there is an internal electrical field, these pairs are separated and create the p-n junction in the middle. The collection of light-generated carriers by the p-n junction causes a movement of the electrons to the n-type side and holes to the p-type side of the junction, as illustrated in Figure 2.2.

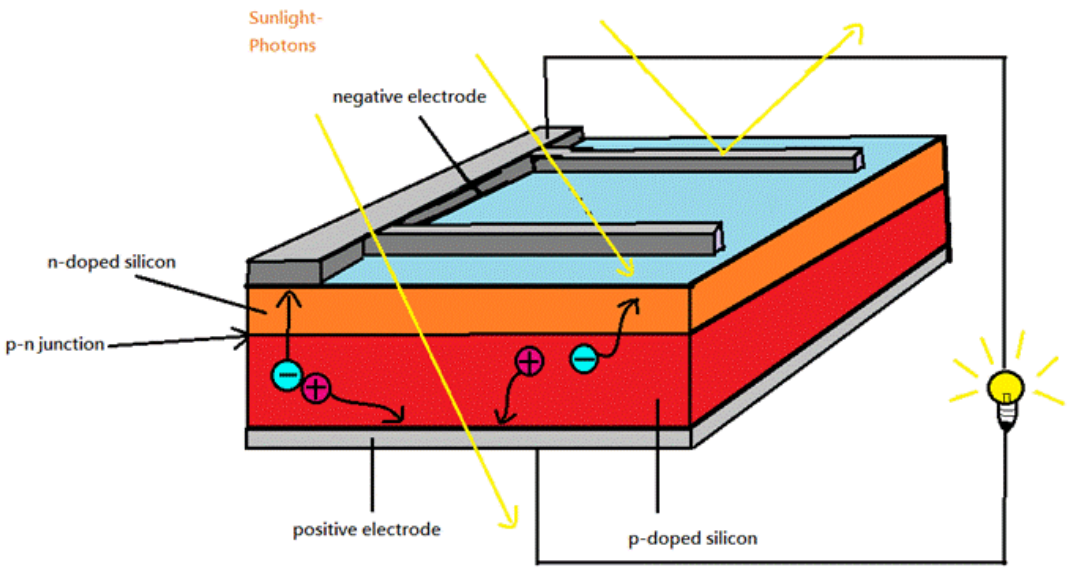

Figure 2.2: Basic operation of a solar cell [30].

The negative layer (n-type) is usually made by doping the silicon with phosphorus to provide an extra electron. Through the excitation of the electrons to the higher energy level, the electrons become free to move through the material if the energy of a falling

photon is higher than the semiconductor bandgap. The positive layer (p-type) is usually made by doping the silicon with boron to create extra holes.

A closed-circuit is formed by using a conducting wire, which connects the negative electrode, the load and the positive electrode in series, causing the current to pass throughout the terminals [31]. A solar panel or module is formed by connecting many individual solar cells, either in series or in parallel. The output voltage can be connected to a grid or it can act as a standalone system, as illustrated in Figure 2.3.

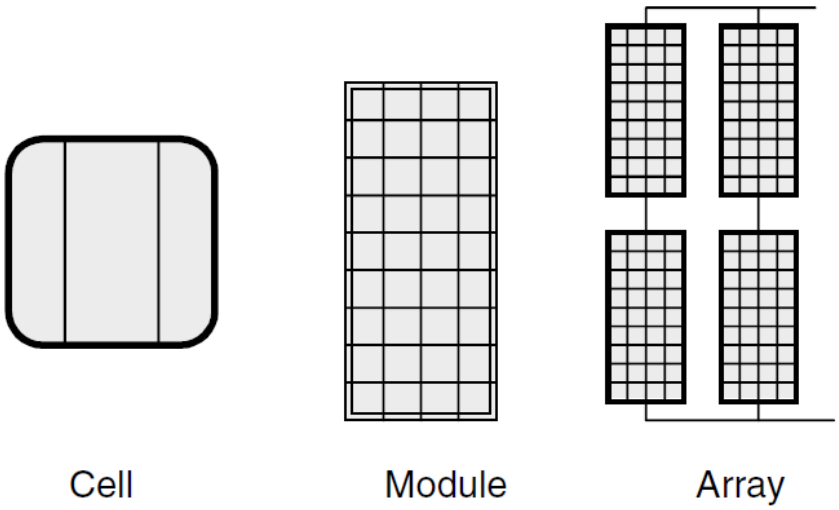

Figure 2.3: PV cells, modules and arrays [32].

2.3.1.1 Equivalent Circuit of a Solar Cell

The properties of a solar cell are similar to a diode; hence, the diode circuit can be described as an equivalent circuit of a solar cell (as shown in Figure 2.4).

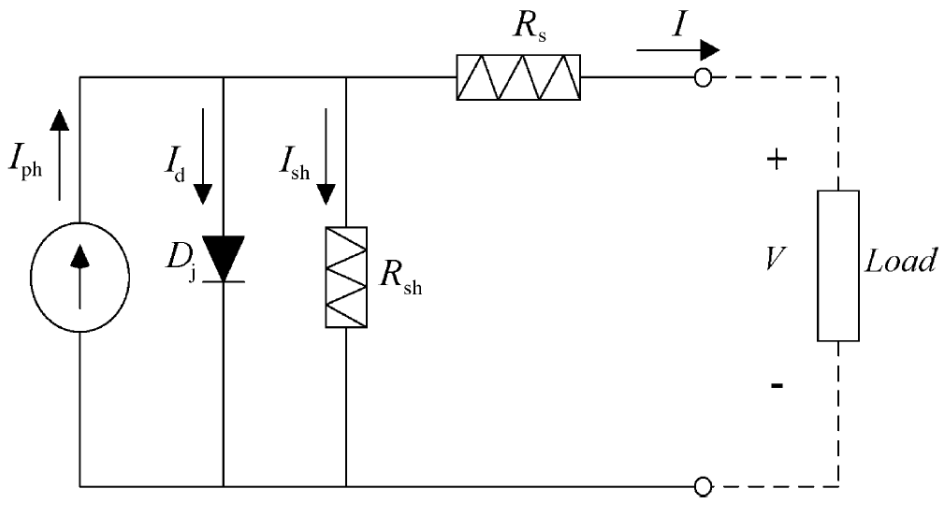

Figure 2.4: Electrical equivalent circuit model of PV cell [33].

The operation of an ideal cell is described by the Shockley solar cell operation [26, 32]

$$I = I_{ph} - I_0 \left[e^{\frac{qV}{kT}} - 1\right] \quad (2.1)$$

where I_{ph} is the photocurrent (Amps) that increases with the irradiance increase, I_0 is the diode saturation current (Amps), q is the electron charge (1.6×10^{-19} C), V is the voltage across the terminals of the cell, k is the Boltzmann Constant (8.617×10^{-5} eV/K) and T is the Temperature in Kelvin.

The equivalent solar cell circuit can be extended to include a series resistor and shunt resistor to represent the losses throughout the PV cell. The series resistor R_S represents the sum of the front and back contact resistance surface (external resistance), connection strip and soldered joint. Whereas, the R_{Sh} represents the leakage of current across the p-n junction (internal resistance) [34].

The output current of the solar cell for the single diode including the effect of resistance losses is given in Equation 2.2:

$$I = I_{ph} - I_0 \left[e^{\frac{q(V+R_S \cdot I)}{n.k.T}} - 1\right] - \frac{V+R_S \cdot I}{R_{sh}} \quad (2.2)$$

where n is the ideality factor of the diode.

The two important parameters in photovoltaics are the short-circuit current (I_{sc}) and the open-circuit voltage (V_{OC}). The former is obtained when the leads are shorted together, which lead to zero voltage and no current flows across the diode. The latter is obtained when the leads are not connected, and thus the current is zero. Both I_{SC} and V_{OC} can be obtained from the I-V curve shown in Figure 2.5.

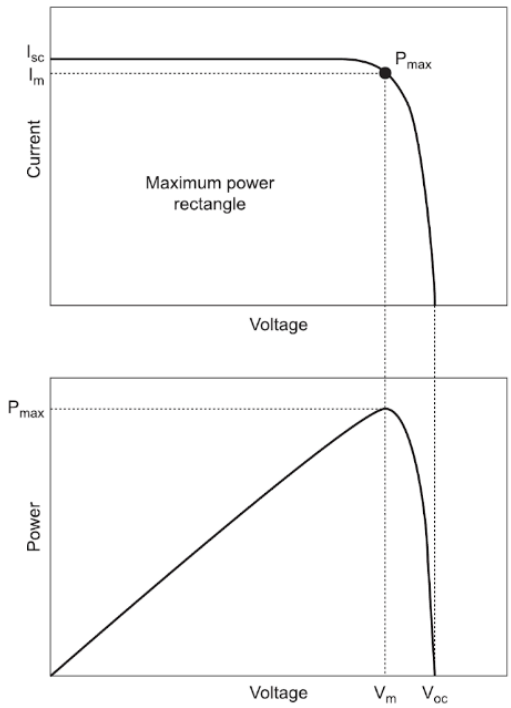

Figure 2.5: The I-V characteristics of an ideal solar cell: (a) and power produced by the cell (b) [26].

The Maximum Power Point (MPP) or (P_{max}) in the I-V curve is determined as the product of the current at the maximum power point (I_{mp}) and the voltage at the maximum power point (V_{mp}). The conversion efficiency (η_{pv}) of the solar cell is calculated by using Equation 2.3 [35]:

$$\eta_{pv} = \frac{P_{max}}{I \cdot A} \tag{2.3}$$

where P_{max} is the maximum output power of the cell, I is the solar radiation intensity (W/m^2) and A is the area of the entrance aperture. Consequently, the fill factor (FF) of the cell is an important parameter to determine the quality of the cell [36]. This compares between the theoretical power of the cell and the maximum power obtained: the quality of the solar cell is better when the fill factor is higher, which can be calculated by using Equation 2.4 [32, 37]:

$$\mathrm{FF} = \frac{P_{max}}{V_{OC} \cdot I_{SC}} \tag{2.4}$$

where the V_{OC} and I_{SC} are the open-circuit voltage and short-circuit current, respectively. There are many types of PV cells on the market, such as crystalline silicon cells, thin-film cells, multi-junction cells and organic cells. These types can be categorised under different generations, as shown in Figure 2.6. The details will be discussed in the next sections.

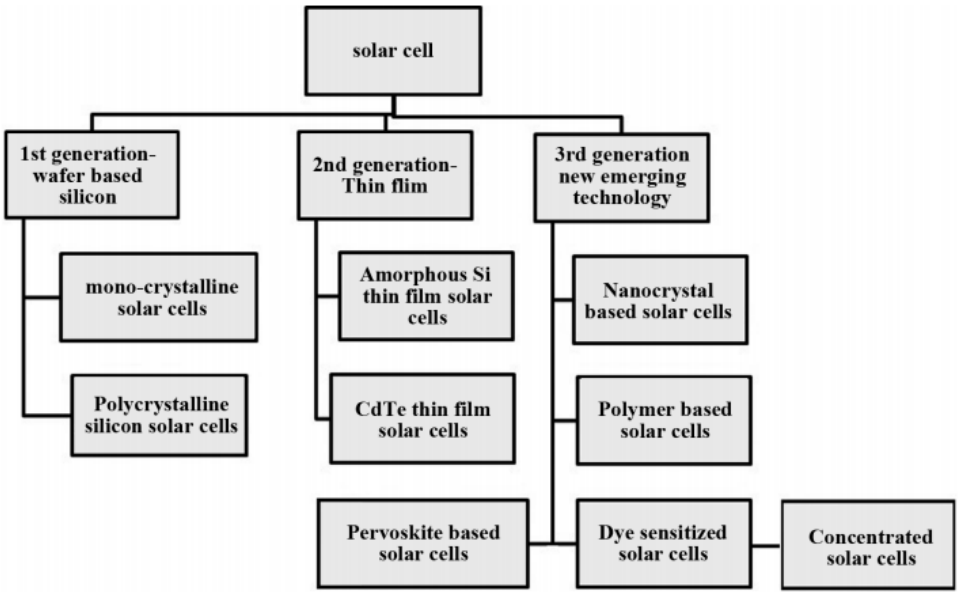

Figure 2.6: Various types of solar cell technologies [38].

2.3.2 First Generation Solar Cells

The first generation of the solar cell was built by using silicon wafers. It has been reported that around 90% of installed PV capacity around the world is made from silicon wafers [39-41]. The crystalline family are subdivided into the two most popular types, which are monocrystalline (single) and polycrystalline (multi). The difference between these two types can be seen in Figure 2.7, and both types are produced by screen printing the device structure.

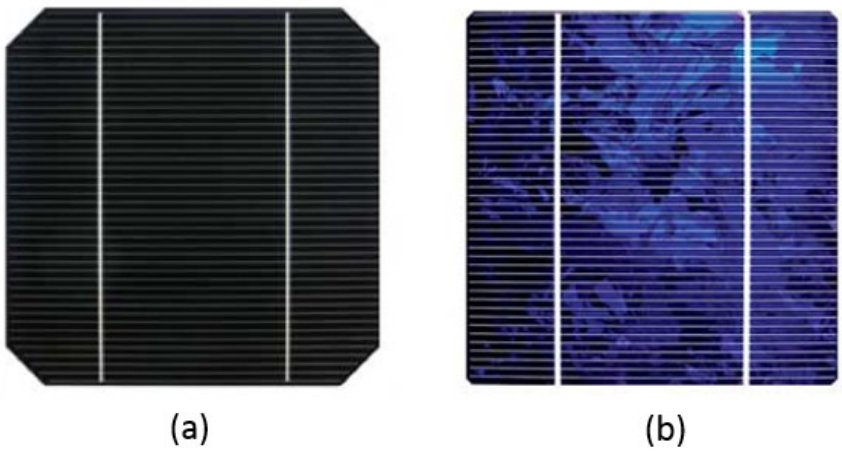

Figure 2.7: Crystalline silicon cell: (a) monocrystalline and (b) polycrystalline [42].

The highest electrical conversion efficiencies reported by National Renewable Energy Lab (NREL) for crystalline cells (c-Si) are between 21.2–27.6% [43]. Conventional crystalline silicon (c-Si) has a layer thickness of 200–500μm. The monocrystalline cell is

made of silicon ingots, which have a cylindrical shape. For better performance and cost reduction, the four sides of the monocrystalline module are cut out of the cylindrical ingots to make silicon wafers. Most monocrystalline cells are grown by using Czocharlski (CZ) process, which uses a high grade of silicon. One of the most common types of monocrystalline cells that used in the literature is Laser Grooved Buried Contact (LGBC), which has the advantage of minimising the shading losses of the cell by using the laser to form the grooves [44]. The main advantages of the monocrystalline cell are: the silicon abundance, high-efficiency value, silicon non-toxicity, it is well established in commercial markets and it is proven to have high stability under outdoor conditions [45]. However, the major drawback lies in the complicated manufacturing process, which results in a slightly higher cost than other cell technologies, such as polycrystalline [46].

In contrast, the polycrystalline solar cell does not use the CZ process and it is based on melting the raw silicon and then pouring it into a square mould, which is then cooled and cut into square wafers. The main advantage of polycrystalline silicon is the simpler process to produce this type of cell, which makes it less expensive compared to monocrystalline cells, while its disadvantage is its lower cell efficiency.

2.3.3 Second Generation Solar Cells

The second generation of solar cells are thin-film PV cells that have a layer thickness of only 1–10 μm of PV material. The amount of silicon is less than the crystalline silicon and the manufacturing process is also different. Thus, thin-film PV cells normally cost less than the conventional silicon cell because they require less material. The semiconductor material used in these cells is deposited on a glass substrate, which is a relatively low-cost material [47]. An example of a thin-film solar cell can be seen in Figure 2.8.

Figure 2.8: Thin-film solar cell [48].

The name of the thin-film solar cell is derived from the cell's thin layer, which causes fewer photons to be absorbed by the cell and results in less energy conversion efficiency compared with c-Si cells. The reported efficiencies of these cells by NREL varies from 13–23.3% [43]. Most of the thin-film modules are made from amorphous silicon (a-Si), but also different compounds are used such as; Cadmium Telluride (CdTe), Gallium Arsenide (GaAs), Copper Indium Gallium Diselenide (CIGS) and Copper Indium Diselenide (CIS). The major advantages of these cells are: lower cost, simple production process and attractive shape that suits house façades. The drawbacks are their low delivered efficiencies and fast degradation of the cells.

2.3.4 Third Generation Solar Cells

Research in PV systems has focused on increasing the total efficiency of the cells at different generation levels. The main type of the third generation solar cell is a multijunction solar cell (MJ) that is made of III-V compound semiconductors, which aims to increase the cell's efficiency by having two or more layers/junctions stacked on top of each other and which uses various band gaps (E_{gap}) to utilise more of the solar spectrum [49]. The higher electrical conversion efficiency for the MJ cells can be produced by adding substances such as Gallium Arsenide (GaAs) and Indium Phosphide (InP). The solar spectrum can be split to be absorbed by each of the junctions and thus minimise the thermal losses due to different bandgap energies at each junction [50]. Figure 2.9 shows a comparison between the silicon cell solar spectrum (a) and the multi-junction cells (b), with respect to the AM1.5D solar spectrum.

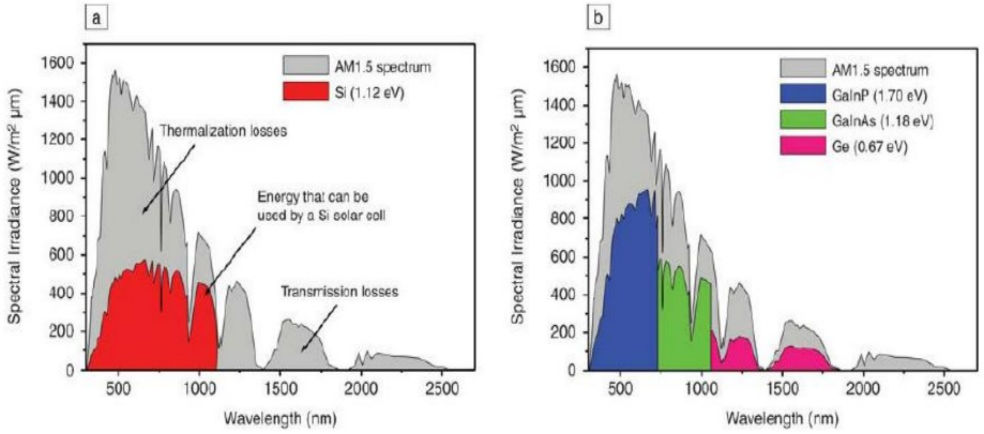

Figure 2.9: The AM1.5D solar spectrum: (a) for Si solar cells and (b) GaInP/GaInAs/Ge solar cells [49].

A schematic of the MJ cell with a different E_{gap} at each layer can be seen in Figure 2.10. The three cells are connected to absorb a wider part of the spectrum, starting with the

shorter wavelength that is normally placed on top of the stack and ending with the longer wavelength that is placed at the bottom of the stack. Hence, each junction produces lower photocurrent but as the sum of all junctions, the generated power is larger than the single junction. To date, the highest recorded efficiency by NREL for the MJ cell is 46%, which is more than double the efficiency of crystalline silicon cells.

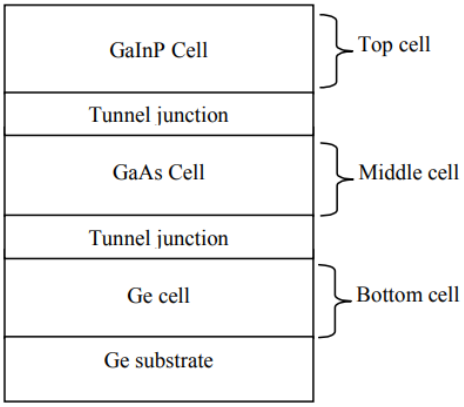

Figure 2.10: Schematic baseline of GaInP/GaAs/Ge MJ solar cell [51].

In addition, other types of cells have shown great potential but require further development to replace the conventional solar cells, such as dye sensitised solar cells, perovskite cells and organic cells. The highest reported dye sensitised cell efficiency was 11.9%, whereas 24.2% and 15.6% were reported for perovskite single junction cell and organic cells, respectively. A high conversion efficiency of 35.5% can be achieved by the perovskite-Si triple junction cell [52]. The advantages of the perovskite cell include less requirement for high temperature in the manufacturing process and it is considered as environmentally friendly, whereas the drawbacks mainly fall on the expensive compounds that it uses and its high volatility [53]. Figure 2.11 shows the best research cell efficiencies at laboratories by the National Renewable Energy Laboratory (NREL), since 1975.

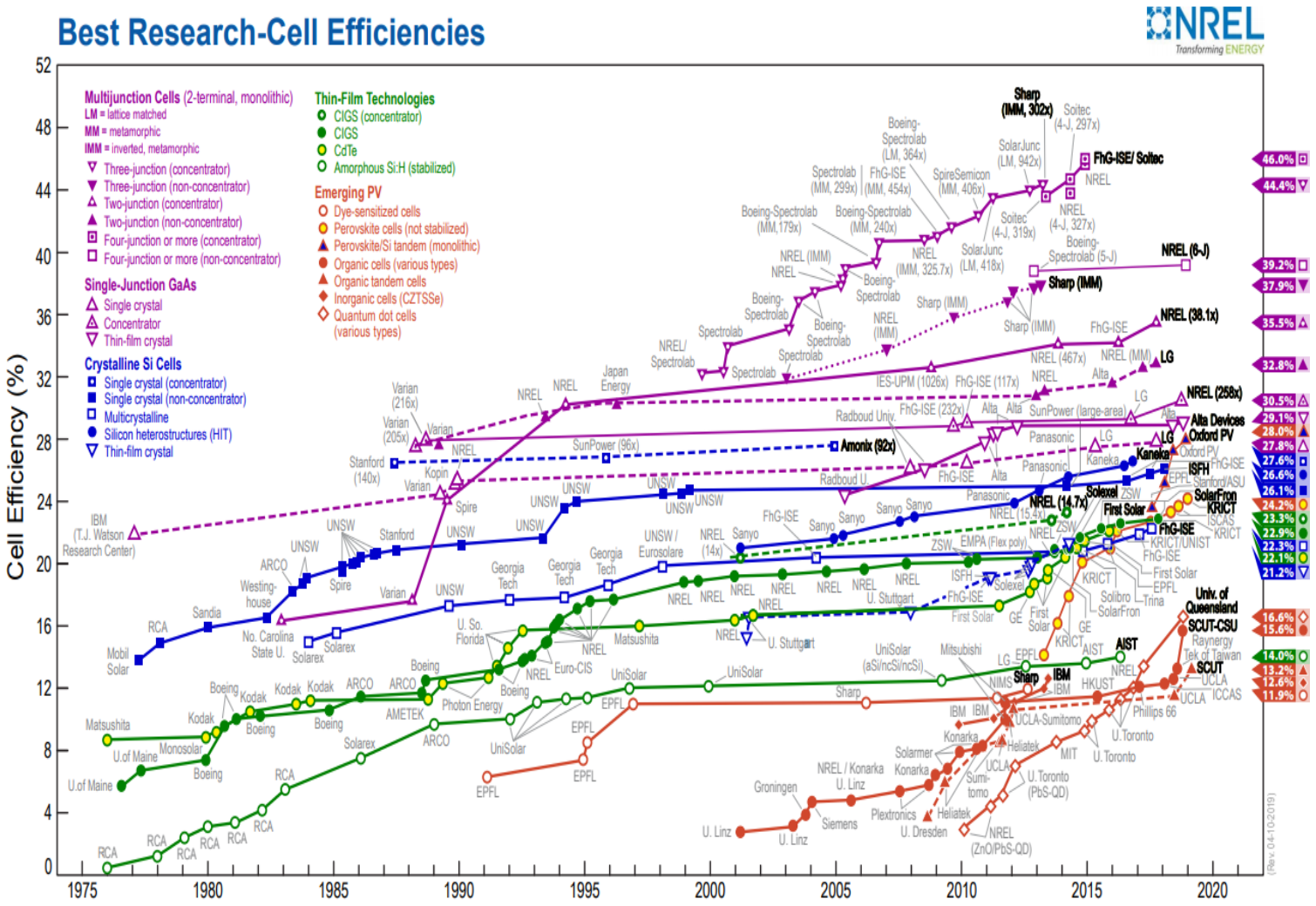

Figure 2.11: Best research cell efficiency chart [43].

2.4 Concentrated Photovoltaics (CPV)

The concentrated photovoltaic (CPV) system is a promising solution for cost reduction and to increase the power generation of the solar cell compared with a typical PV system [54, 55]. The first solar concentrator was reportedly developed in the fourth century in Greece, where a mirror reflected sunlight at a specific focal length to light a fire for religious ceremonies [56]. The cost of the material of a PV cell contributes 50% of the cost of the total PV system [57]. CPV has shown to be a great improvement in terms of component material recycle, space use, and less amount of toxic materials used in the production process [58]. Concentrated photovoltaics use two methods to overcome the limitation of higher photocell cost: the first method uses Building Integrated Photovoltaic (BIPV) based on available space on the building roof or façade, and the second method uses a CPV [59]. CPVs are based on using optics, such as lenses or mirrors, to concentrate the sunlight onto a small area of the solar cell to generate electricity [19, 60]. Generally, the concentrator system consists of three main parts: entry aperture, reflector or refractor, and exit aperture. The entry aperture collects the incoming sunlight, and the reflector is used to concentrate and direct the sunlight to the exit aperture, where the third concentrator element takes place and the PV cell is attached. The concentrator material can be made of glass, mirrors or acrylic plastics, which are a comparatively inexpensive optical element that can reduce the cost of PV material in general [61]. An example of a PV concentration principle is shown in Figure 2.12 using a Fresnel lens (FL) as a concentrator optic.

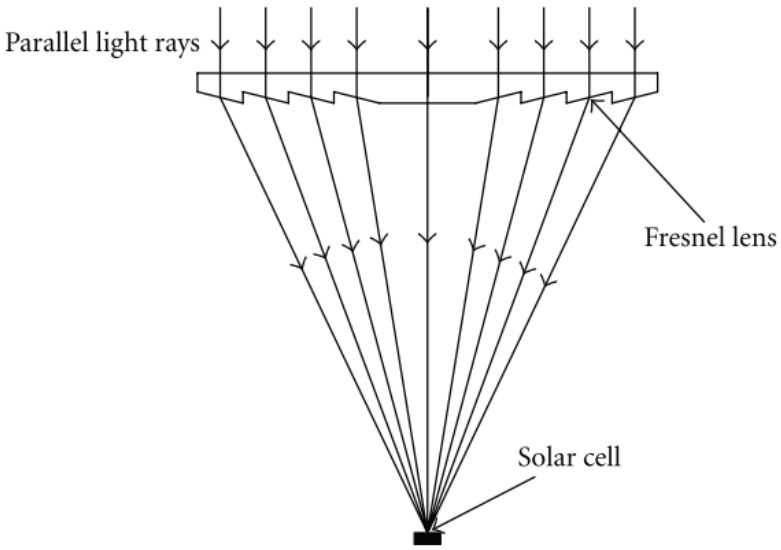

Figure 2.12: Schematic illustration of PV concentrator using a Fresnel lens[62].

Authors such as Rabl and Winston have investigated the basics and fundamental concepts of concentrators [63, 64]. Prior to exploring more about the classifications of the concentrator, their categories and types, it is essential to explain some basic terms and concepts of concentration ratio (CR) and the concentrator limit, as follows:

1- Geometrical concentration ratio,
2- Optical concentration ratio,
3- Acceptance angle of the concentrator.

2.4.1 Geometrical Concentration Ratio

The geometrical concentration ratio (C_{geo}) is the most commonly used term in solar concentrators, where it is the main definition to determine the ability of the concentrator to concentrate light rays. It is defined as the ratio between the entrance aperture area (A_{entry}) and the exit aperture area (A_{exit}) of the concentrator [64]:

$$C_{geo} = \frac{A_{entry}}{A_{exit}} \tag{2.5}$$

The concentration ratio is also referred to as 'suns' [65] and has a unit of 'x', which simply explains the number of the concentration that the concentrator has delivered; for example, a (4x) or (4 suns) concentrator can concentrate four times compared to a flat panel. Meanwhile, for the normal PV panel the C_{geo}=1 and if it is integrated with a concentrator the C_{geo}> 1 [66, 67].

2.4.2 Optical Concentration Ratio

The optical concentration ratio is another term that is used to calculate the concentration ratio. It is defined as the average flux or intensity (I_r) that comes out from the concentrator exit multiplied with receiver area (A_r) to the insolation incident (I_a), which goes in the concentrator entry aperture and is given by [68]:

$$CR_{optical} = \frac{\frac{1}{A_r}\int I_r dA_r}{I_a} \tag{2.6}$$

2.4.3 Acceptance Angle of the Concentrator

The acceptance angle defines the limit to which the incidence light can still be collected by the concentrator and delivers the rays from the aperture plane to the absorber plane [68]. A schematic diagram of the sun and a concentrator is illustrated in Figure 2.13, where R is the distance from the sun to the concentrator aperture, r is the radius of the sun, (Θ_m) is half of the angle subtended by the sun, and Aa and Ar are the aperture area and receiver area of the concentrator.

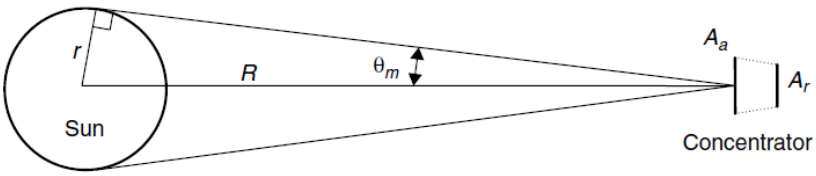

Figure 2.13: Schematic of the sun and a concentrator [67].

The half acceptance angle is also can be described by the symbol (θ_c). The maximum concentration ratio that can be obtained from 2D and 3D concentrators are a function of (Θ_c), and can be described as follows:

$$C_{\max(2D)} = \frac{1}{\sin(\Theta_c)} \ , \ C_{\max(3D)} = \frac{1}{\sin^2(\Theta_c)} \tag{2.7}$$

While solar concentrators increase the power output of the cell, they also increase the temperature and non-uniformity of light distribution (as will be discussed later in this chapter).

2.5 Solar Concentrators: Classifications and Types

There are several ways to collect and concentrate the sunlight in PV technology. The conventional PV cells or modules are normally a standalone system, which is not attached with a concentrator and which is called non-concentrated PV. Meanwhile, a PV system that is attached to a concentrator is called CPV system and generally can be split into three main categories: solar PV, solar thermal or solar PV/Thermal. Furthermore, the light that is concentrated and which exits the concentrator to be focused on the solar cell can be divided into three categories based on illumination intensity and known as CR [2, 58, 69, 70]. These three categories are as follows:

- **Low Concentration Photovoltaic (LCPV)**

The concentration ratio under the LCPV is under 10x (CR < 10x), and no essential need for tracking mechanism due to the high acceptance angle [71]. The Si-based solar cell is normally used under this category and MCPV [72].

- **Medium Concentration Photovoltaic (MCPV)**

The concentration ratio for the MCPV varies between 10 and 100x (10x < CR<100x), where a single-axis tracking system is required to convert the maximum of the incident sunlight [73].

- **High Concentration Photovoltaic (HCPV)**

The concentration ratio for the HCPV is greater than 100x (CR >100x), a high precision tracking system with two axes is required [74] and the cell based on III-V materials is best suited under this category [65].

The two most common methods used to concentrate the sunlight are reflectors (mirrors) or refractors (lenses) [75]. In case of using reflectors, the light is reflected once it hits the reflector material applied in the concentrator, where it is concentrated and focused at the receiver. Whereas using lenses, the light is refracted through the material and is concentrated and focused at the receiver. Both designs can be used for PV application, as well as thermal applications. The two major classes of solar concentrator (i.e. imaging and non-imaging concentrators) [76] will be discussed in the next section. To compare between the two types Figure 2.14 gives a schematic illustration.

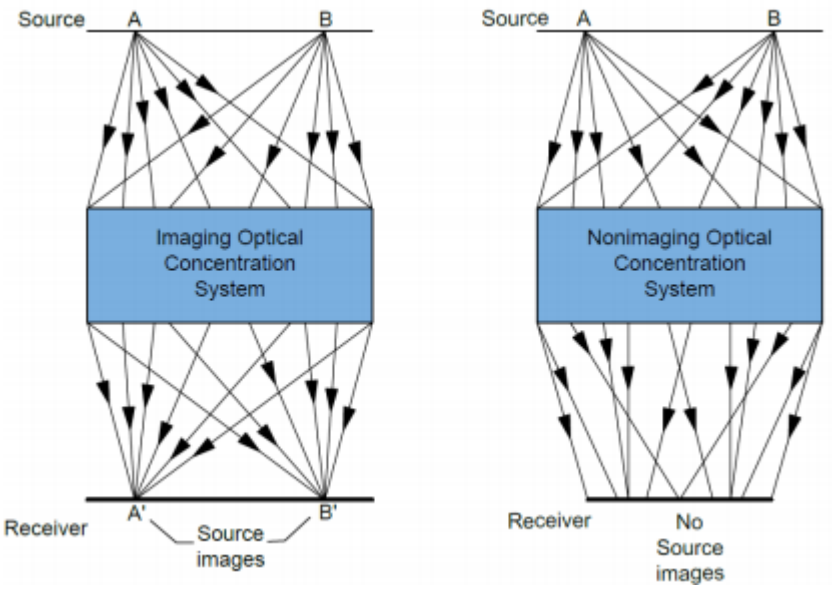

Figure 2.14: Difference between imaging and non-imaging concentrator [77].

2.5.1 Imaging Concentrators

Imaging concentrators are called imaging because they produce an optical image of the sun on the receiver side [78]. Many authors discussed the point focused CPV type where this system combines the optical element and the solar cell to increase the amount of irradiation reached to the receiver side and thereby increase the efficiency and solar concentration [79]. Normally the MCPV and HCPV fit this category and the most common two types of the imaging concentrators for generating power in the power plant or domestic are as follows [80]:

- **Reflective Dish Concentrator**

The reflective dish concentrator is based on point focus technology and mainly consists of three parts: a reflector mirror, MJ solar cell that is placed at the focal point and a sun tracking system, as shown in Figure 2.15.

Figure 2.15: 1.5 MW concentrated PV solar dish concentrator in Mildura, Australia [81].

Each dish concentrator consists of more than 100 curved mirrors that reflect the sunlight and concentrate it up to 500 times and then directed these rays to the high-efficient solar cell that can convert energy at efficiency reached up to 46% compared to the average PV panel efficiency of 15%. This CPV system generates enough power to light 500 homes [82]. Another type of reflective point focus CPV system called Cassegrain Mirror Optics (CMO). Max et al. [83] studied this design which composes of two concentrators: a primary parabolic reflector and a hyperbolical secondary optic. A schematic diagram of this type of system is shown in Figure 2.16.

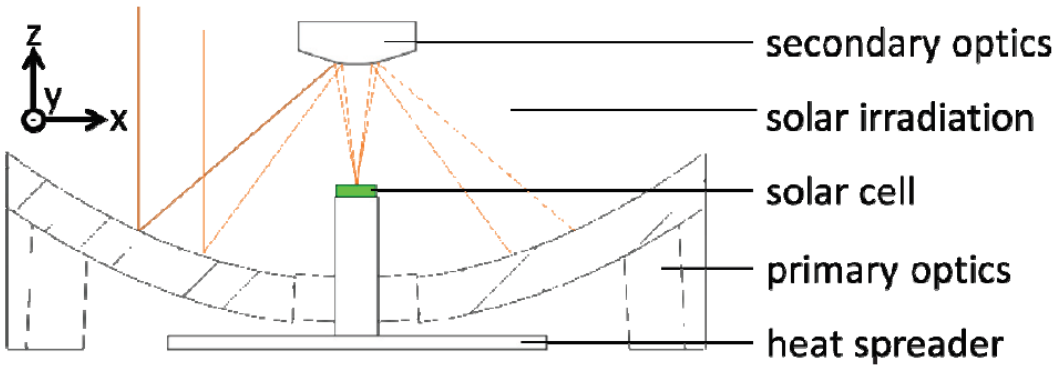

Figure 2.16: Schematic structure of the Cassegrain mirror [83].

The authors developed a high concentrating passive cooled CPV module with a Cassegrain mirror that has a geometrical concentration ratio of 1037x.

- **Refractive Fresnel Lens**

Fresnel lens is widely used in CPV application as a primary optical element to refract the incoming rays to a focal point. A schematic diagram of this CPV system is shown in Figure 2.12 (section 2.4). A conventional CPV system uses only one optical element such as Fresnel lens as a primary optic to concentrate solar radiation on the solar cell that can cause a non-uniform illumination distribution on the solar cell. Irfan [84] proposed an efficient approach to deliver a uniform distribution across the solar cell as the non-uniform illumination is a well-known problem in the CPV system [85]. The author used the Fresnel lens as a Primary Optical Element (POE) and an element made of cylindrical and spherical parts as a Secondary Optical Element (SOE). Figure 2.17 shows a layout of the proposed CPV system under ray-tracing simulation.

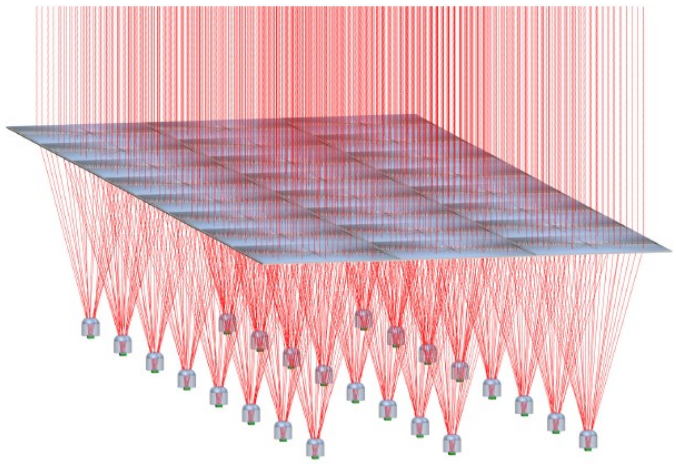

Figure 2.17: Array level layout of eight-fold Fresnel-based CPV system [84].

A similar approach has been proposed by Tien and Shin [86] to improve the irradiation uniformity across the solar cell but with the use of a plano-concave lens as SOE.

2.5.2 Non-imaging Concentrators

Unlike the imaging concentrators, the non-imaging concentrators do not attempt to form an image of source at the receiver end [87]. The most well-known type of non-imaging concentrator is the Compound Parabolic Concentrator (CPC), which was first used by Winston and Hinterberger in 1974 [88] and considered as an ideal concentrator working for a given acceptable angle. The typical CPC parameters with two symmetric parabolas at each side are shown in Figure 2.18.

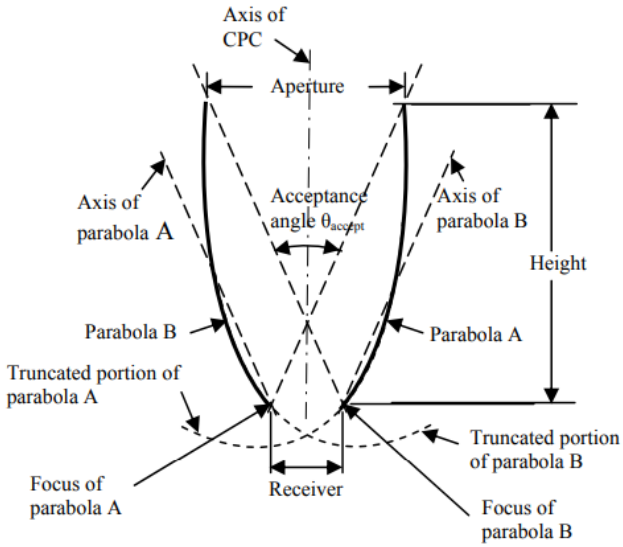

Figure 2.18: Cross-section of a CPC [89].

The geometrical characteristics of CPC include: aperture area, receiver area, acceptance angle and height of the CPC [88]. The main advantage of the CPC concentrator is the ability to concentrate the light within the designed acceptance angle[90], in addition to its wide acceptance angle [91, 92]. To maximise the power production of CPC for LCPV system, a tracking system is often needed to harvest more illumination to get maximum efficiency [93]. CPC concentrators can be classified into two categories: 2D and 3D. The subdivisions of the two types are shown in Figure 2.19. The 2D system will be explored under this section of literature, whereas the 3D system will be discussed in detail in the following section.

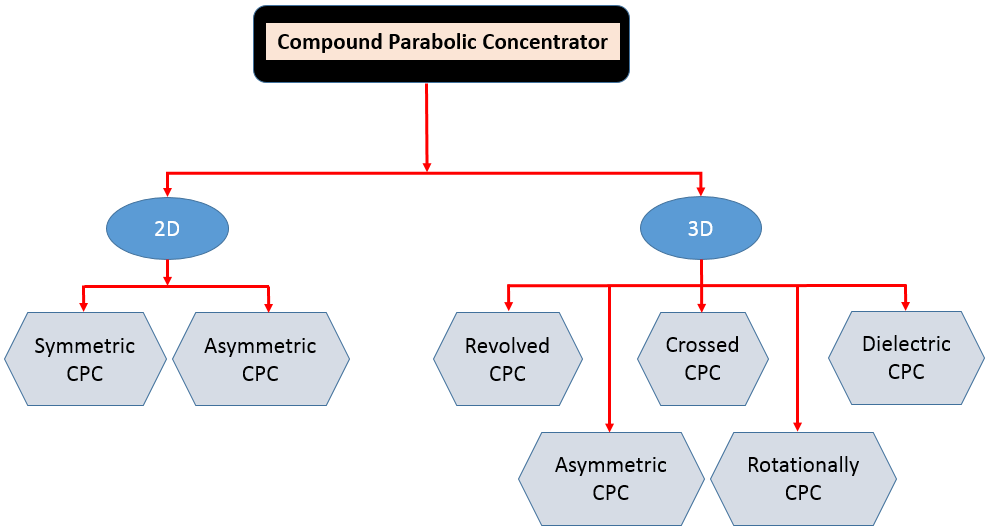

Figure 2.19: Classification of CPC concentrators.

Hatwaambo et al. [94] experimentally evaluated the performance of a 2D CPC concentrator with different specular reflectors (e.g. rolled aluminium foil, anodized aluminium and mirror reflectors). The symmetric CPC is used for the outdoor experiment that can be seen in Figure 2.20.

Figure 2.20: Symmetric CPC reflector with 10-cell module string [94].

The results show that a more uniform distribution was found with a rolled aluminium reflector than the other two types. However, this reflector delivered less power output of 30.5 W compared to mirror reflector, which reached 33.4 W and 32.9 W for the anodized aluminium.

A novel 2D asymmetric compound parabolic concentrator (ACPPVC) has been designed by Mallick et al. [95] to be used in a vertical façade in the UK. The main advantage of the presented design is its ability of collecting the diffuse solar radiation in addition to the

direct component. The prototype was tested outdoors and the concentrator reflector was removed from the PV to compare the results with non-concentrated PV. It was found that the power of ACPPVC is 1.62 times more than the power produced by the non-concentrated system. Moreover, the experimental results were different from the theoretical value calculated for power output, due to the series resistance tapping of wires between cells. Later on, Mallick et al. [96] presented a similar comparison between the non-concentrating system and asymmetric compound parabolic concentrator. Their results show that for the concentrating system, the solar to electrical conversion efficiency was 6.8% compared to 8.6% for the non-concentrating system and the average cell temperature was captured only 12 °C difference to the non-concentrating system. Both systems have the same cell type and size of (50 mm x 125 mm) connected in eight-string (five cells in a string) making a total number of 40 cell/system. The two systems were kept outside for 30 days and the results showed an increased in maximum power point by 62% after using the ACPPVC-50. Figure 2.21 shows the outdoor experiment setup for both systems.

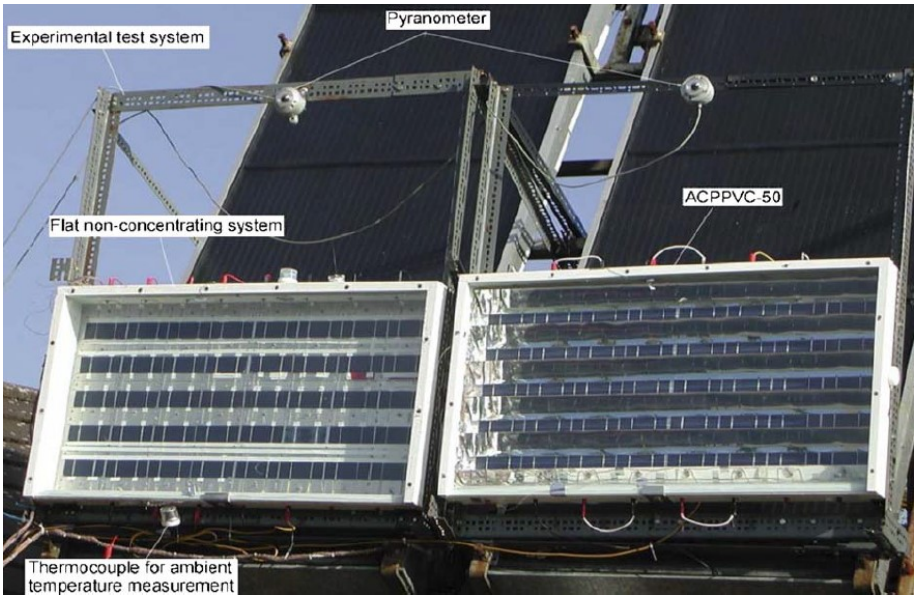

Figure 2.21: Non-concentrating and ACPPVC-50 outdoor experiment at the University of Ulster in Northern Ireland [96].

On the basis of 2D CPC, a uniquely designed lens-walled CPC was proposed by Guiqiang et al. [97-99], which is considered as a combination of lens CPC shape (dielectric) with a reflector CPC; as shown in Figure 2.22.

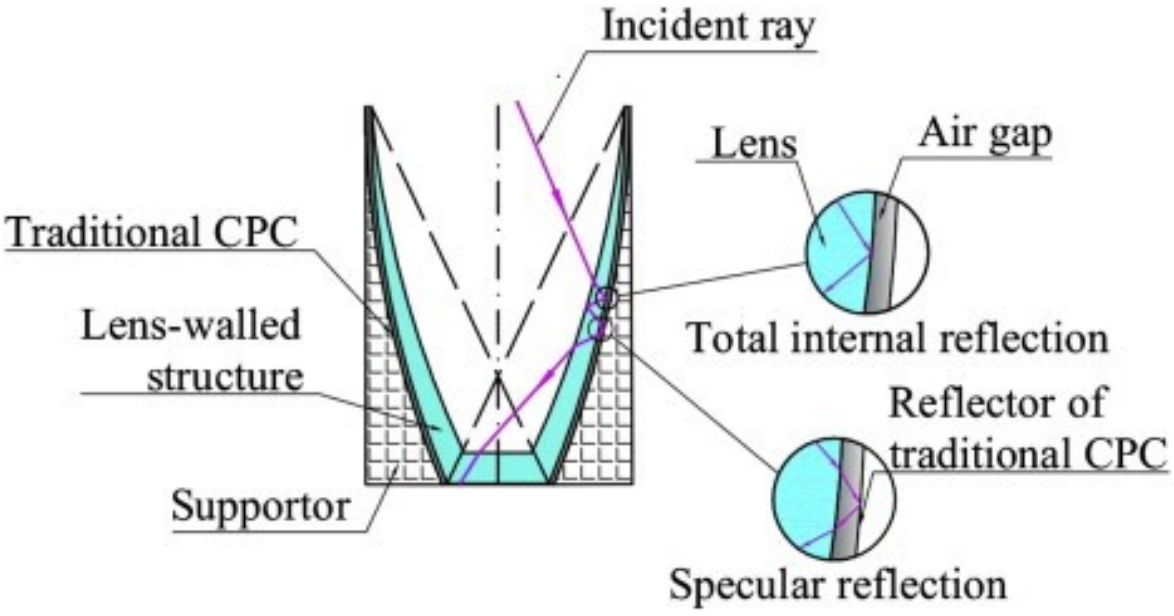

Figure 2.22: Cross-section view of lens-walled [99].

Their results illustrated a good agreement between the simulated and experimental results in terms of optical efficiency and the maximum difference reached 5%. Meanwhile, a comparative study between lens-walled CPC with the common mirror and dielectric CPC was carried out by Y Su et al. [100] in terms of annual solar energy collection. The CPC has a geometrical concentration ratio of 2.5 and a half acceptance angle of 23.5°. However, despite the higher acceptance angle for lens-walled CPC indicated by the simulation results, the lens-walled CPC proved to have less optical efficiency than other CPCs. The results showed that the lens-walled CPC can achieve about 80% of the dielectric CPC and 20–30% larger than the mirror CPC.

2.6 Cross Compound Parabolic Concentrator (CCPC)

This section of the literature review will focus closely on the CCPC designs, characteristics, optical efficiency and reflector types that have been used by several researchers to date. Optical efficiency is an essential element for success in any concentrator because it is the main indicator that measures the fraction of ray's transmission from the entry aperture to the exit aperture [101]. A concentrator with better optical efficiency will ensure the high overall performance of the system. The CCPC is generated based on the original 2D CPC, as stated by Winston [88]. It is within the non-imaging concentrator family, which basically does not reflect the image of the sun at the receiver side. The design of CCPC is obtained by rotating the 2D CPC parabolic curves across the axis of CPC, which results in a 3D CPC with a square entry and square exit area. Prior to designing the CCPC, several parameters need to be taken into consideration (as

discussed in detail in Chapter Four). In this section, a comprehensive literature review is given for this particular type of concentrator because it is considered to be the main content of this thesis. Many authors have considered CPC as the best stationary concentrators because it does not require a tracking mechanism [102], while it has a concentration ratio below 10x and a wide acceptance angle [63, 64]. The CCPC can be reflective or refractive, depending on the type of material that is used to direct the sunlight to the receiver end. The most common refractive CCPC type is made by a dielectric material, hence it is called a dielectric CCPC. It has been reported that the optical efficiency is reduced to 80% by using a FL or other refractive element [103]. The CCPC is normally symmetric parabola curve with the same size, which has a square shape at the entry aperture. Another type that has been discussed in the literature of CCPC is the Asymmetric Compound Parabolic Concentrator (ACPC). These three different CCPC types are discussed briefly in the following sections.

2.6.1 Reflective Cross Compound Parabolic Concentrator

The low-concentrator CCPC normally uses reflective material to provide a specular surface, such as aluminium foil, or by applying the coating in the inner surface of the CCPC to reflect the light towards the receiver end.

Mammo et al. [35] designed and experimentally tested a 3D cross-compound parabolic concentrator to build an integrated PV application with a half acceptance angle of 30˚. Their design consisted of 81 single 3D CCPCs, as shown in Figure 2.23 (b). The original geometrical concentration ratio was 4x and after truncation it becomes 3.61x. A simulated ray-tracing optical efficiency of 94.6% was reported compared with an experimentally optical efficiency of 75.2%, which gave a deviation of 19.4%. Despite the high reflectivity of the inner surface for the CCPC, which reached 96%, the maximum optical efficiency measured for this geometry is relatively low.

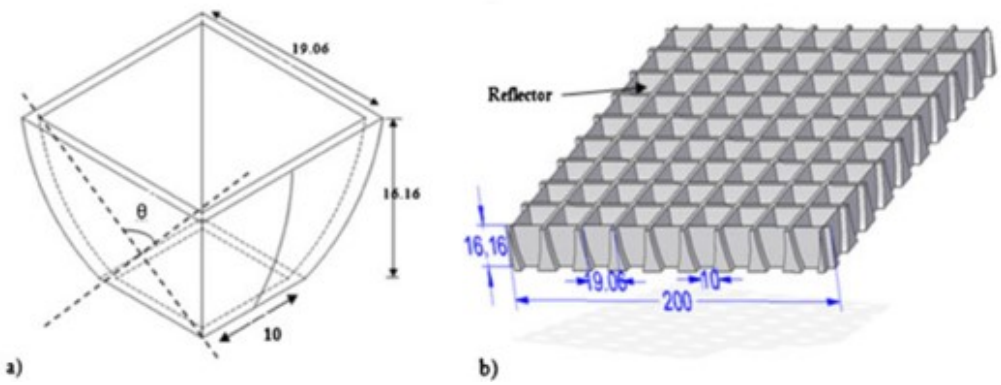

Figure 2.23: Schematic diagram of: (a) unit 3D CCPC profile and (b) 9x9 3D CCPC (dimension in mm) [35].

The LGBC concentrating solar cell was used and was found to have an electrical efficiency of 14%. These authors validated the electrical performance by developing MATLAB simulation code and obtained a maximum power of 4.25 W for the 3D CCPC PV. Compared with the non-concentrating PV panels, they achieved a maximum power of 1.45 W. The short-circuit current achieved with the 3D CCPC PV was 318 mA compared to 122 mA for non-concentrating PV. Moreover, the maximum electrical conversion efficiency for the design reached 14.2% at 1 sun. Thermal analysis shows that average module temperature reached to 50 °C after 3 hours of operation and the output power decreased by 0.014 /°C for each increasing temperature degree. Angular response of the 3D CCPC PV was taken for different angles from 0° to 45°.

On the basis of previous work, Sellami et al. [104] studied the optical, electrical performance and uniformity distribution of a crossed CPC; as shown in Figure 2.24. The geometrical concentration ratio of CCPC is 3.6 and it has a half acceptance angle of 30°. It was made by using a 3D printer. The simulated and experimental optical efficiency was 95% and ~80%, respectively.

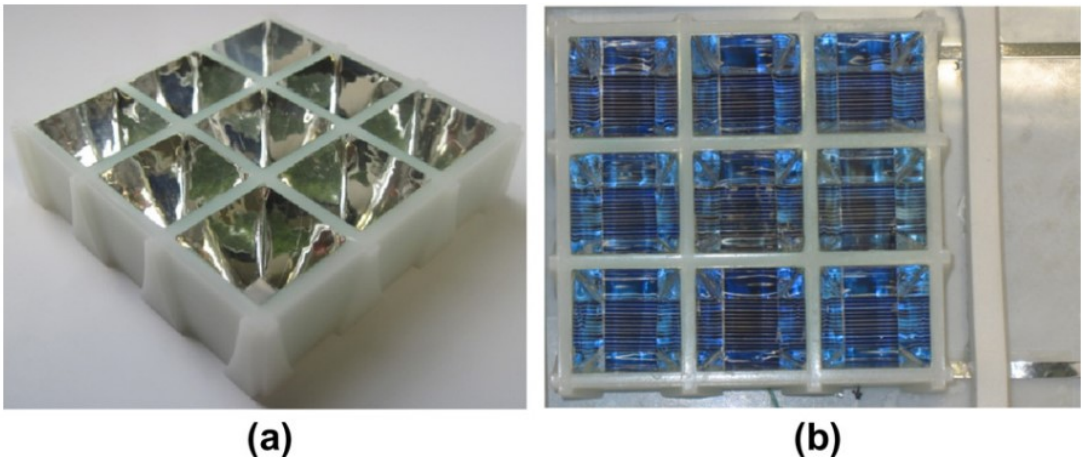

Figure 2.24: Array of nine experimental models of 3D CCPCs: (a) covered with reflective film; (b) concentrating cells assembly with CCPCs [104].

These authors found non-uniform distribution on the cell surface under concentration, which leads to a decrease in the efficiency of the solar cell. Meanwhile, the optical efficiency was recorded at different incident angles.

A similar design of 3D CCPC has been investigated in the indoor environment by Biag et al. [105]. The original geometrical concentration ratio was 4x but after truncation it becomes 3.6x and it has a half acceptance angle of 30°; as can be seen in Figure 2.25 (b).

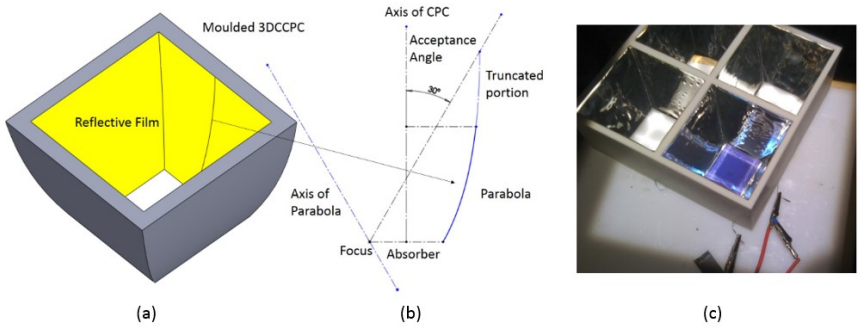

Figure 2.25: 3D crossed compound parabolic concentrator: (a) schematic for a unit reflective 3D CCPC, (b) design of CCPC and (c) the module of the CPV system [105].

Although the aluminium reflective material used in the system has a reflectivity of 94%, the maximum experimental optical efficiency only reached 77.2%, which represents a deviation of 16.8% from the simulated results. The output power of the cell was boosted after it was integrated with the CCPC and a power ratio of 2.82 was achieved compared to the non-concentrating PV system. The same system was studied further in an outdoor environment. In this case, the optical efficiency dropped by 4.2% from the indoor testing, which leads to an increase in the deviation from the simulation optical efficiency to 21%.

A further study of CCPC design integrated with the thermoelectric device was proposed by Sweet et al.[106]. A triple-junction solar cell with an active area of 5.5 mm x 5.5 mm was used in this study. The calculated cell efficiency and optical efficiency of the system after introducing the CCPC was 23.83% and 78.8%, respectively. A photograph of the CCPC optic can be seen in Figure 2.26.

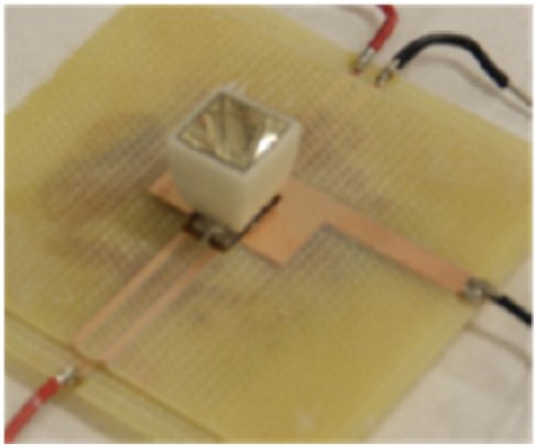

Figure 2.26: A photograph of CCPC optic that used in the system [106].

Baig et al.[107] introduced a novel 3D CCPC design, called a conjugate CCPC, which consists of refractive dielectric material and an enveloped reflective geometry of the

same shape to maintain an air gap between the two materials; as illustrated in Figure 2.27.

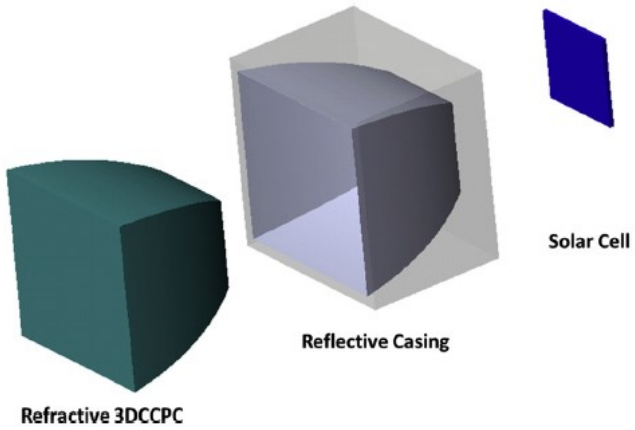

Figure 2.27: Components of the conjugate system [108].

The system was designed to have a geometrical concentration ratio of 3.6x. A reflective film was used at the edge of the CCPC to direct the skipped light to an LGBC solar cell. The maximum optical efficiency of the system reached 77% at the incidence angle of 10° and a power ratio of 2.76 was delivered.

A recently developed novel design by Baig et al. [108] has been investigated with five units of CCPCs connected with a heat extraction unit. The reflective concentrators were fabricated with a 3D printing technique and were coated with an average reflectance of 96%; as shown in Figure 2.28. The system was designed to have a geometric concentration ratio of 3.6x and an active LGBC cell area of $1cm^2$ placed at the exit aperture.

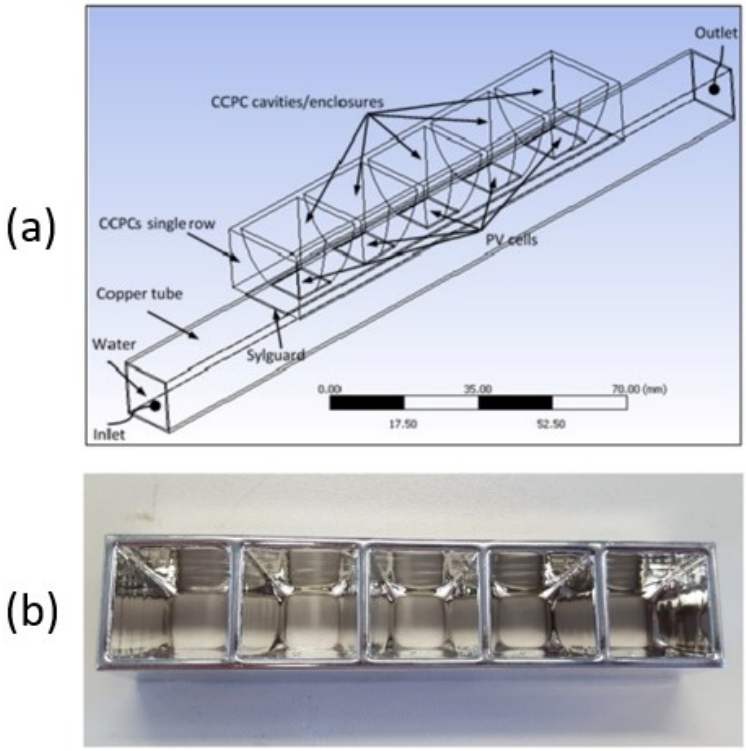

Figure 2.28: A 3D printing CCPCs: (a) computational domain of the system and (b) reflective coating of CCPC array [108].

Due to the roughness of the reflector's inner surface, the maximum optical efficiency was found to be under 67% under normal incidence and a maximum power ratio of 2.41 was achieved.

2.6.2 Dielectric Cross Compound Parabolic Concentrator

The refractive type of CCPC normally uses a dielectric-filled material that works on a principle of Total Internal Reflection (TIR) to direct the light towards the receiver end. The dielectric material offers better acceptance angle compared to reflective CCPC type, while the optical efficiency is lower than the reflective type [108].

This type of concentrator was first established and put forward by Winston[109]. Many researchers have subsequently analysed the performance of dielectric material for linear concentrating PV systems [109-112].

Baig et al. [113] introduced a refractive 3D CCPC that was used to build an integrated system. The design has a geometrical concentration ratio of 3.6x and it is made from a clear polyurethane material, as shown in Figure 2.29 (a), which worked on the concept of TIR to concentrate the light to the LGBC solar cell attached on the receiver aperture.

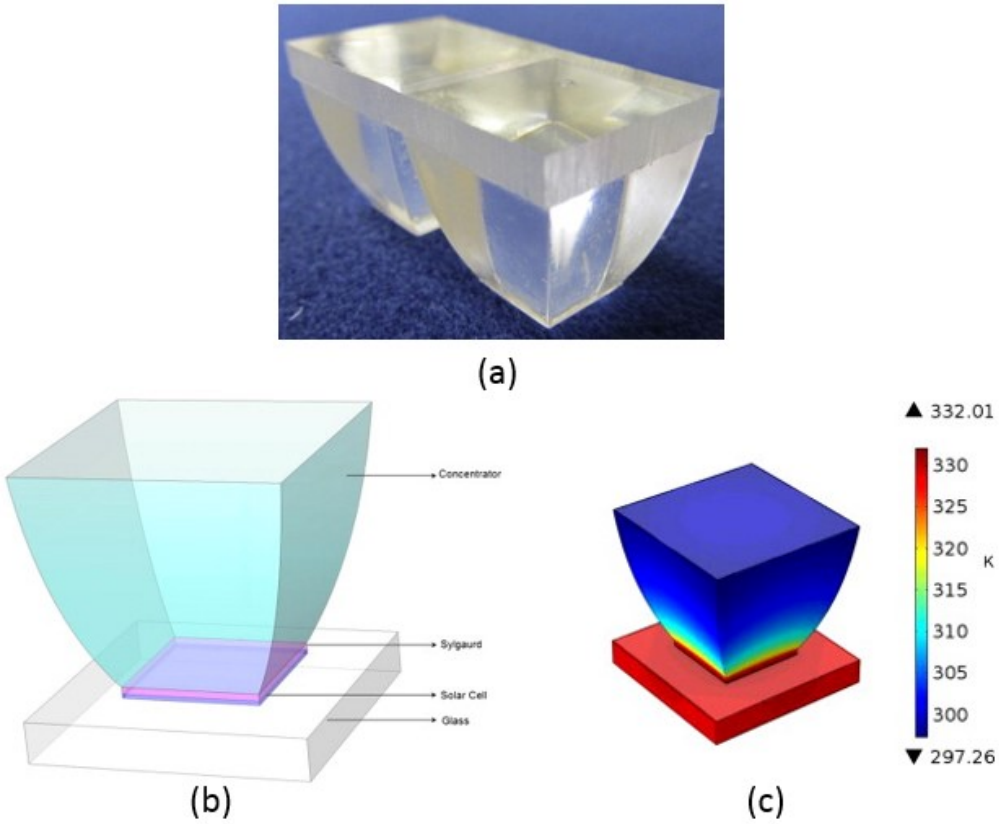

Figure 2.29: 3D CCPC: (a) made by polyurethane material, (b) geometry used for thermal analysis and (c) temperature distribution across the CCPC system [113].

These authors carried out theoretical and experimental studies, which include optical efficiency, power output and uniformity distribution on the cell surface. This system achieves maximum optical efficiency of 73.4% and a power ratio of 2.67. The authors discovered a drop of 2.2% in the I_{SC} due to non-uniformity distribution of light. The highest temperature value of 332K recorded at 0° incident angle and dropped to 299K at 60° incidence. To improve the system, the authors extended their research on a dielectric 3D CCPC and added reflectors on the edges of the optical element to collect the escaped light; as shown in Figure 2.30 (a) [114].

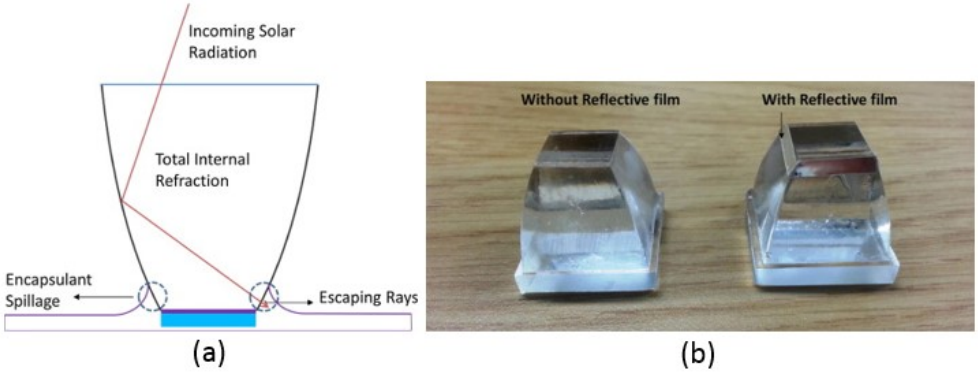

Figure 2.30: Dielectric 3D CCPC: (a) schematic diagram and (b) prototype without and with a reflective film [114].

Their results show an improvement in the power ratio from 2.67 to 2.73. However, this model shows less effect on the optical efficiency when using the reflector film at the edges. The authors also found that the maximum short-circuit current and optical efficiency for reflective film concentrator observed at an incident angle of ±10° was 96.4 mA and 73%, respectively.

To improve the flux intensity and uniformity under dielectric 3D CCPC, Chong et al. [115] proposed a design based on Non-imaging Dish Concentrator (NIDC) as POE and a dielectric CCPC as a SOE. The primary concentrator (NIDC) consists of mirrors that reflect the light to the dielectric 3D CCPC, which have a wide acceptance angle and work to further concentrate the sunlight to the CPV module. Their results show an improvement in the electrical performance after integrating the two concentrator systems.

Other dielectric 3D symmetric concentrators were proposed by Mallick et al. [116], who introduced a novel design introduced called Symmetric Elliptical Hyperboloid (SEH). This design has a geometrical concentration ratio of 6x and the concentrator is made from polyurethane material. The dimensions of the SEH prototype are given in Figure 2.31 (a). This design consists of elliptical entry shape, square exit aperture and hyperboloid profile.

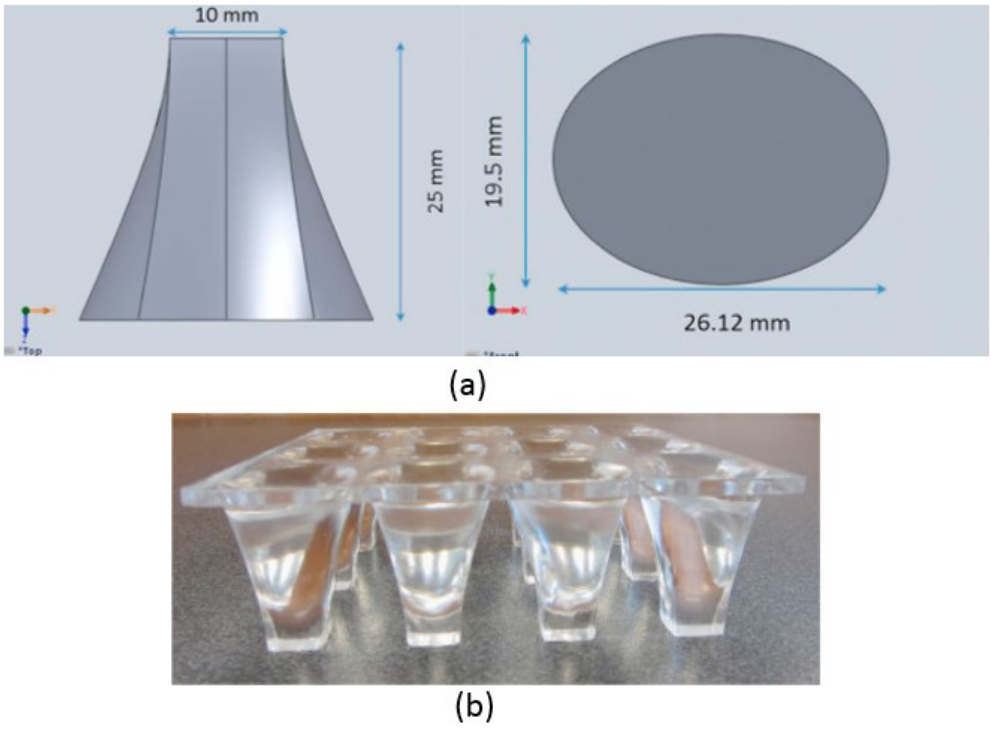

Figure 2.31: SEH prototype: (a) dimensions of the design and (b) concentrator array made of polyurethane [116].

These authors optically simulated and experimentally evaluated the concentrator. Their results show that the concentrators maximum optical was 61.6% and the power ratio was 3.7. Their thermal study showed that the maximum solar cell temperature was 319 K under normal irradiance. However, some losses were observed, due to manufacturing defects, which reduce the efficiency of the concentrator. Consequently, different shaped 3D CPCs have been developed, which will be described in the next section.

2.6.3 Asymmetric Compound Parabolic Concentrator

The LCPV design has less requirement for tracking and a wide acceptance angle. Consequently, a Three-dimensional Asymmetric Compound Parabolic Concentrator (3D ACPC) has been proposed. The parabola in the asymmetric concentrator has two different lengths, which lead to a wider acceptance angle as a result of the asymmetric shape. The 3D ACPC has been found to be more suitable to be used in building façades compared to the symmetric CCPC [96] and it can be also used for highly seasonally-dependent locations [117].

Schuetz et al. [118] designed and experimentally tested a 7x 3D ACPC using an aluminized acrylic mirror on the inner surface of the concentrator. These authors coupled 120 LGBC solar cells with concentrators, forming an array of (10 x 12) to be used for single-tracking; as shown in Figure 2.32.

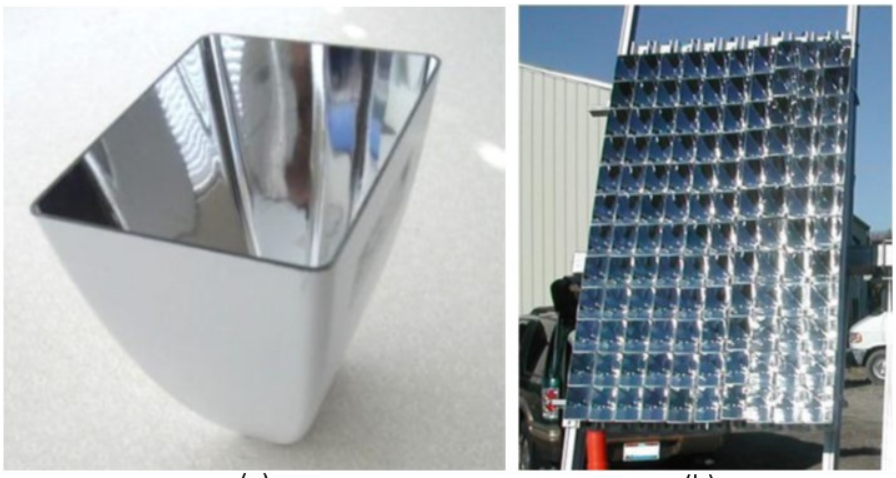

Figure 2.32: 3D ACPC: (a) unit prototype and (b) array of 10x12 ACPC [118].

Their results show that the I_{sc} increased from 0.45 A to 2.53 A, while the V_{OC} increased from 566 mV to 626 mV under concentration. The maximum optical efficiency delivered per unit concentrator is ~55%, which is due to low specular reflectance of the ACPC.

Abu-Baker et al. [92] designed a Rotationally Asymmetric Compound Parabolic Concentrator (RACPC), which is a novel type of solar concentrator that can be used to build an integrated application with a geometrical concentration ratio ranging from 1.73 to 6.59x. A simulation study has been undertaken and the maximum optical efficiency was 98%.

Later, Abu-Baker et al. [119] evaluated the performance of the RACPC system and carried out indoor testing. Their design has a geometrical concentration ratio of 3.6675x and a 1cm^2 monocrystalline LGBC solar cell has been coupled with the RACPC system; as shown in Figure 2.33 (b).

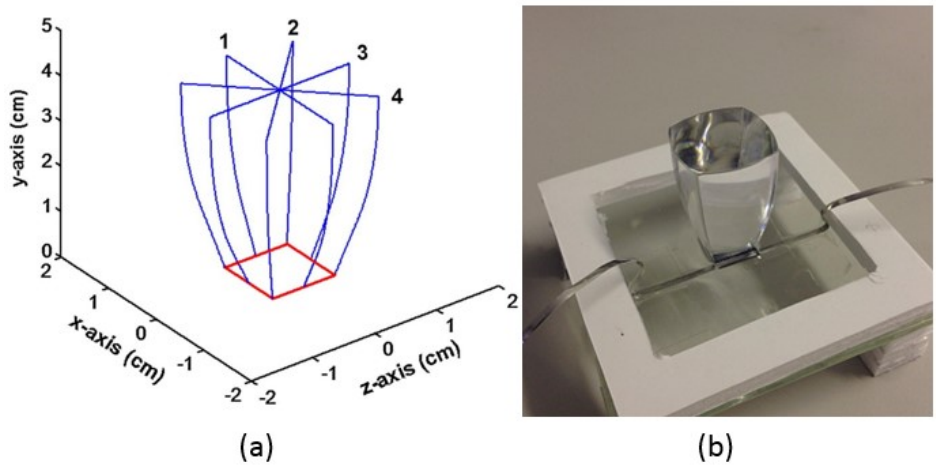

Figure 2.33: (a) Demonstration of the angular rotation of 2-D, (b) prototype of RACPC-PV system [119].

Their results show that there was a boost in short-circuit current from 35.5 mA to 107.0 mA for the bare cell and with RACPC prototype, respectively, while the optical efficiency of the concentrator was 82%. The maximum prototype temperature was 57 °C after 2.75h of exposure under solar simulator and the maximum power coefficient was 0.2188 mW/°C.

Table 2.1 provides a summary of the literature of the different types of CPC and it also gives the maximum recorded optical efficiencies of the concentrator.

Table 2.1: Summary of different types of 3D CCPC in the literature.

Sr. No	Authors	Year	Type of 3D CPC	Geometrical Concentration Ratio	Optical Efficiency (η_{opt})	Research Test Category	Findings
1	Kara et al. [120]	2011	Asymmetric Reflective	10.3x	60%	Indoor	Optical losses
2	Schuetz et al. [118]	2012	Asymmetric Reflective	10.3x	55%	Outdoor	Optical losses
3	Mammo et al. [35]	2012	Symmetric Reflective	3.61x	75.2%	Indoor	-Manufacturing errors -Miss-match -Series resistance losses -Thermal losses
4	Sellami et al. [59]	2012	(SEH) Refractive	4x	70%	Indoor	- Non-uniform distribution for different dimensions
5	Sellami et al. [104]	2013	Symmetric Reflective	3.6x	80%	Indoor	Non-uniform flux distribution
6	Baig et al. [113]	2014	Symmetric Refractive	3.6x	73.4%	Indoor	-Non-uniform distribution -Misalignment issues
7	Baig et al. [116]	2015	(SEH) Refractive	6x	-	Indoor	-Manufacturing losses of the concentrator
8	Chong et al. [115]	2015	Symmetric Reflective	5.998x	-	Outdoor	-Transmissivity of dielectric material is 87.5%
9	Abu-Baker et al. [119]	2015	Rotationally Reflective	3.6x	82%	Indoor	The maximum temperature reached is 57 °C and the power coefficient is 0.2188mW/°C
10	Mallick et al. [114]	2015	Symmetric Refractive	3.6x	73%	Indoor	Drop-in V_{OC} after adding the reflective film

11	Baig et al. [105]	2016	Symmetric Reflective	3.6x	78%	Indoor	Thermal issues
12	Tracy et al. [106]	2016	Symmetric Reflective	4.0x	78.8%	Indoor	Temperature coefficient for maximum power output is -0.162%/K
13	Paul et al. [121]	2016	Symmetric Reflective	3.6x	66.7%	Indoor	Different parameters affect the performance of the system (i.e. circuit current, reverse saturation current etc.)
14	Baig et al. [122]	2017	Symmetric Reflective	3.6x	73%	Outdoor	Thermal issues
15	Chong et al. [123]	2017	Symmetric Refractive	5.998x	67.9%	Outdoor	-Fresnel reflection losses in the primary optical element. -Absorption losses from the dialectic CCPC
16	Baig et al. [107]	2018	Symmetric Reflective	3.6x	77%	Indoor	Increasing the air gap between the conjugate system reduces the optical efficiency
17	Ferrer-Rodriguez et al. [124]	2018	Symmetric Refractive	5.998x	73.4%	Indoor	Surface roughness imperfections
18	Baig et al. [108]	2018	Symmetric Reflective	3.6x	67%	Indoor	-Reflective coating depends on the surface finish of the substrate

2.7 Effect of Non-uniformity Illumination on PV Output

The non-uniform illumination and performance of solar cells have been investigated by several researchers, who have found a strong link between non-uniform illumination and the overall PV performance [79, 125, 126]. The uniform distribution of light in optical systems, such as a CPV system, is one of the most important parameters and requires more attention to reduce non-uniformity because it can reduce the efficiency of the system due to the effect of series resistance [127]. For example, Hasan et al [79] discussed the effects of non-uniformity in the PV system and summarised them in three main effects; such as hotspots, which reduce the overall efficiency of the system and create a current mismatch. The authors also mention that the effects may either be electrical or thermal. Meng et al. [128] carried out a study of flux distribution on CCPC combined of absorber and reflector absorber, called AR-CCPC. Figure 2.34 (b) shows hotspots at four focal points of the CCPC at the solar cell surface.

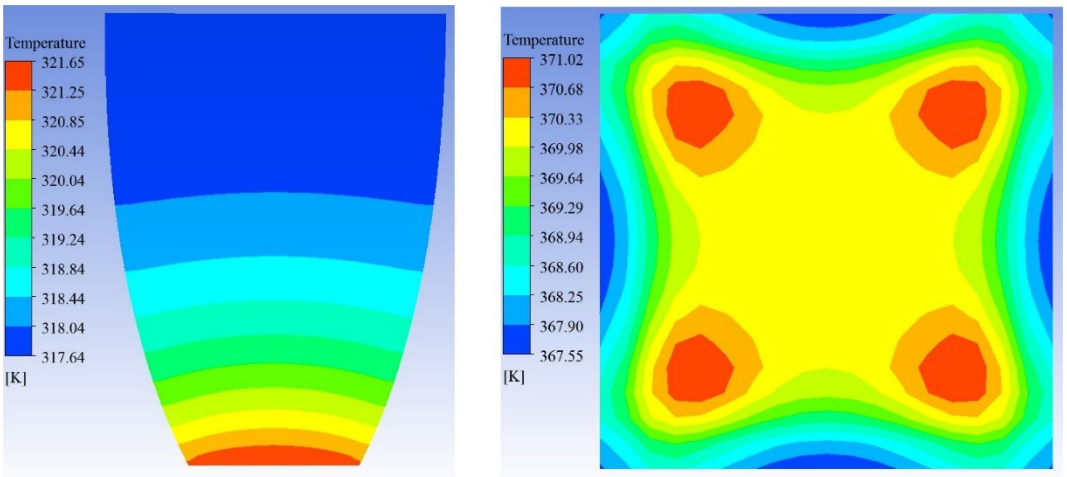

(a) AR-CCPC wall (b) Assembled solar cell

Figure 2.34: Heat flux distribution: (a) AR-CCPC wall and (b) solar cell at the bottom of the AR-CCPC [128].

Cuevas and Lopez [129] stated that the internal current still flows in a non-uniform cell, even in open-circuit conditions, and this current is directly proportional to the degree of uniformity. This causes a voltage drop. It also causes the open-circuit voltage (V_{OC}) to reduce due to non-uniform illumination. Luque et al. [130] explain that the electrical impact of non-uniformity arises because it produces ohmic drops that are higher than expected when the cell is normally operating in higher irradiance. The major electrical parameters that are affected by non-uniformity are short-circuit current, open-circuit voltage, electrical efficiency, fill factor and solar cell power. The optical system concentrates the sunlight on the solar cell, which illuminates some parts of the cell while other portions are not exposed to the sunlight, which leads to non-uniform illumination

of the cell. The non-illuminated part of the cell will produce low current, while the illuminated part of the cell will produce a high current. Consequently, the least illuminated part carries the high current due to series connection and this causes the PV to become reverse bias and drop some power [131].

Non-uniformity in the PV cell can be directly or indirectly caused by improper design of the concentrator, an imperfection in the mirror's geometry, a structure misalignment, or optical properties [132]. Franklin et al. [133] experimentally evaluated the cell under uniform and non-uniform illumination, and noticed a huge drop in open-circuit voltage and efficiency for the non-uniform case. These authors experienced a large reduction of these two factors with the increase of the illumination profile. The I-V curves for both situations were recorded and they revealed a significant reduction in V_{OC} and the efficiency of the solar cell.

Lu et al. [134] Investigated the impact of non-uniform illumination on a conventional polycrystalline solar cell and emphasised that the maximum power (P_{max}) and the fill factor (FF) decreases with the increase of the non-uniformity illumination distribution. These authors found that the power loss in a low concentrated PV system is not only due to non-uniformity illumination itself but is also due to the temperature rise due to the non-uniformity. Andreev et al. [135] investigated the effect of non-uniform light intensity on the I-V curve of GaAs single-junction solar cell. Their results show a significant deviation in the curve due to fill factor and voltage open-circuit drop.

Minimising non-uniform illumination can increase the power output and deliver better PV system performance. Chen et al. [136] aimed to reduce the uniformity effect in the concentrator with a tubular absorber by using the first-order differential equation for the reflector profile. The concentrator's length is optimised with the help of the ray-tracing process. Ricardo et al. [137] proposed a method to enhance the flux uniformity in the receiver side of a point focus solar concentrator integrated with 18 spherical mirrors. The author optimised the receiver distance and adjusted it to reduce the hot spot by using optical ray-tracing software. Another method proposed by [127] for the indoor procedure measured the losses of the non-uniformity of the cell using a camera that produces non-uniform Gaussian irradiance profile of the CPV cell. Furthermore, Diego and Ivan [138] used a diffuser segment to distribute the light illumination evenly across the PV panel. These diffusers can eliminate the high peaks caused by the CPC concentrator. Another method uses an Optical Mixer (OM) to provide uniform illumination of the PV surface integrated with a CPC concentrator [139], and for PV/TEG/STC [140]. A two-stage PV concentrator technique can enhance the uniformity illumination of light on the PV surface, while increasing the concentration ratio [141]. A

flux distribution simulation has been used by Cooper et al [142] for various polygonal CPCs at different half acceptance angles; as illustrated in Figure 2.35.

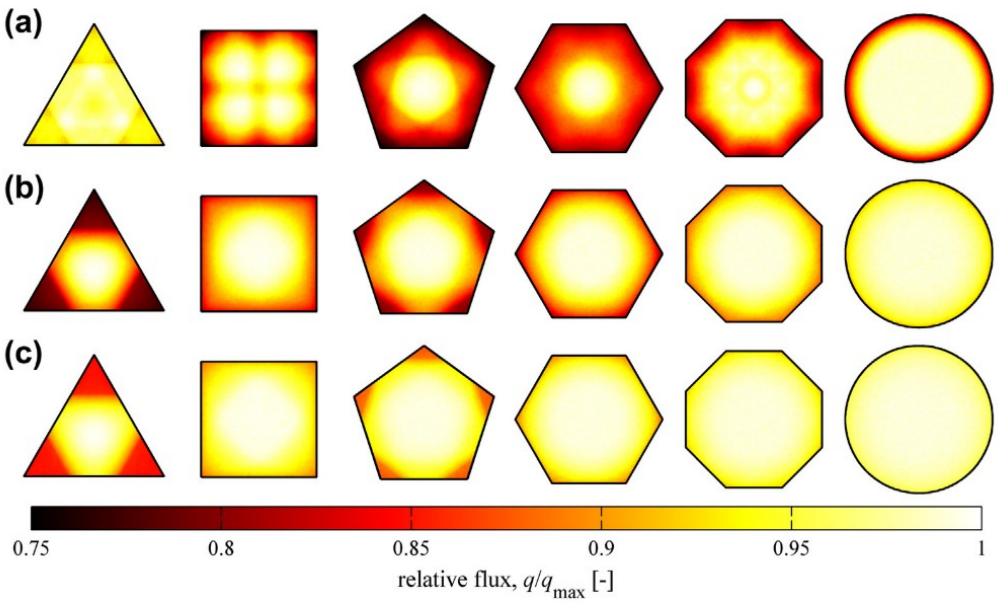

Figure 2.35: Flux distribution at the receiver for various polygonal CPCs with half acceptance angle: (a) Θc =5°, (b) Θc =30°, and (c) Θc =45° calculated by Monte Carlo ray-tracing with 10^9 rays [142].

Although a higher flux uniformity can be achieved for revolved CPC compared to other polygonal CPCs, it is not easy to find a circle cell in the market to attach at the outer aperture of the revolved CPC.

Non-uniformity not only affects the individual cell but it can also affect the whole string of a PV module that is connected in series [129]. For example, if the string of PV modules is not uniformly illuminated, then an internal current flows from a higher intensity region to a lower intensity region, which produces a voltage drop and affects the overall PV system.

2.8 Advantages and Disadvantages of Concentrated Photovoltaics (CPV)

CPVs offer many benefits in addition to electricity production and higher efficiencies compared to other types of PV technologies. However, like any other system, CPV faces some challenges and have some drawbacks. Many authors have discussed the advantages and disadvantages of solar concentrator, as summarised and listed in Table 2.2 [19, 143-147].

Table 2.2: Summary of the advantages and disadvantages of solar CPVs.

Sr.no	Advantages	Disadvantages
1	Increases the total efficiency of the cell	Concentrator system collects a fraction of diffuse radiation
2	Reduces the required solar cell area	Some of the concentrators required a tracking system
3	Reduces semiconductor material	May require periodic cleaning of the reflectors
4	Reduce the cost	Less reliable
5	Better performance under hot conditions	Required a rigid structure base (ground mount)
6	High –grade thermal energy	Risk of PV overheating

2.9 Sun-tracking Mechanism

A sun-tracking mechanism is probably required for medium and high solar concentrators (as discussed in Section 2.5). The main reason behind using a sun-tracking system is to move the concentrator or the module to follow the sun's path across the sky, placing the axis of concentrator perpendicular to the sun rays to capture the maximum Direct Normal Irradiance (DNI). A tracking system has the advantage of increasing the daily energy production over the non-tracking flat panels, as illustrated in Figure 2.36. This figure shows a typical illustration and comparison of fixed and two-single axis tracker for one day in a year, and hours may change per the season and the location of the installed tracker, but generally they will look the same. The tracking systems quickly reach a plateau of power for several hours, while the stationary systems only reach their maximum power around midday. The date and location in this figure are not given as it is a typical illustration. However, a more accurate tracking system is required when the concentration ratio is higher, which leads to a more costly tracking mechanism [148].

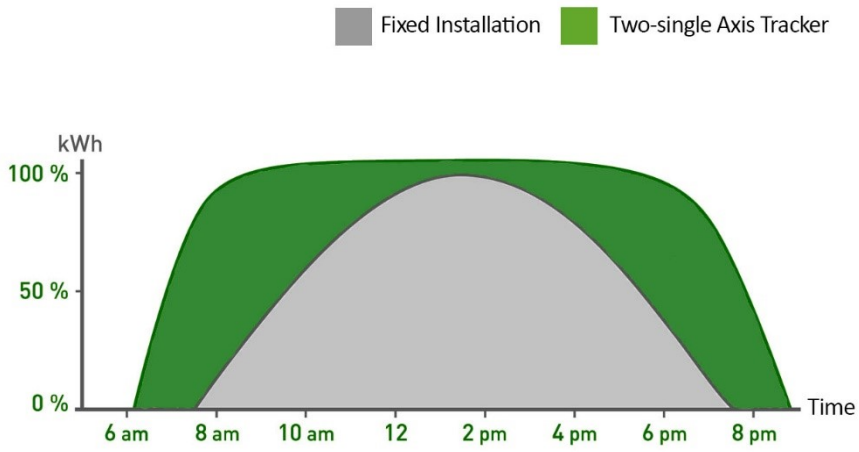

Figure 2.36: Typical daily power production comparison between fixed installation and two-single-axis tracker [149].

The tracking mechanism can be split into two types based on the concentration ratio: single-axis tracking (C_{geo} > 10x < 100x) and dual-axis tracking (C_{geo} > 100x).

Figure 2.37 illustrates the two-tracker types and the orientation directions for both types. Single-axis tracking is normally used for line focus concentrators, such as a linear Fresnel reflector [150] and a parabolic trough solar concentrator [151]. Meanwhile, dual-axis tracking is used for point focus concentrators, such as solar dish concentrator [152] and heliostat concentrator [153]. Alireza et al. [154] gave further details for the different types of sun trackers in terms of solar system output.

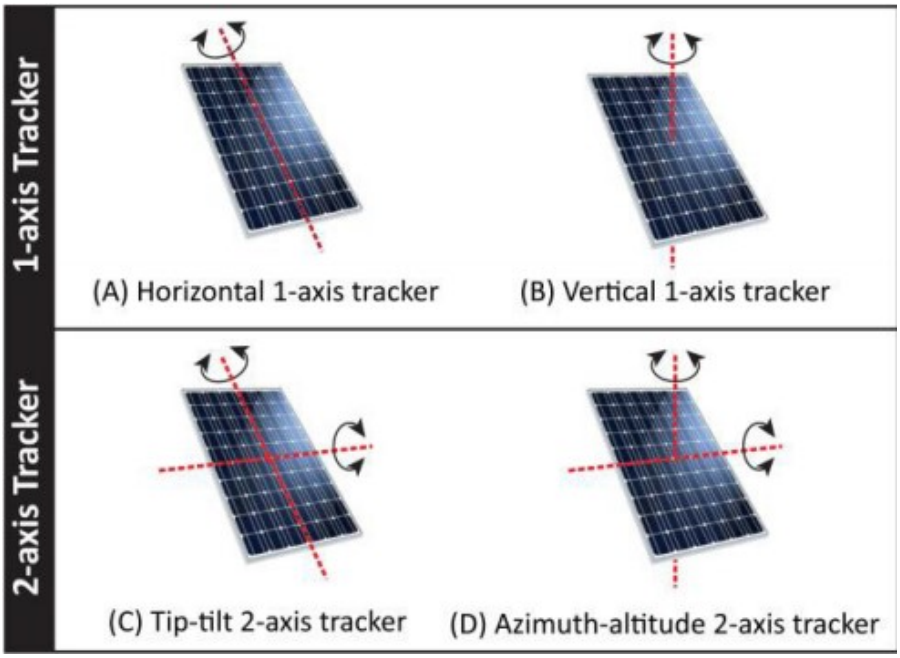

Figure 2.37: Tracker types and orientation direction [155].

The tracking angle mainly depends on the concentrator's latitude and the climate. Although the tracking system is not necessary for (C_{geo}< 10x), a simple tracking system can enhance the daily energy production of the LCPV system, with less accuracy tolerance. Generally, the tracking system is designed for power plant applications; however, some low-profile rooftop CPV panels are available; (as described in the next section).

2.10 CPVs for Rooftop Application

CPVs for a low concentration system can be installed on rooftops as a fixed system [148] or as a tracking system [156]. Normally, a high concentration architecture creates

challenges for CPV installations [157], which can differ from city to city because of the wide variety of architectural designs. For example, terraced houses in the UK do not have much roof space, as shown in Figure 2.38 (a), whereas the houses in Oman have a large and open flat space on the roof, as shown in Figure 2.38 (b), where a PV/CPV system with simple tracking can easily be installed.

Figure 2.38: Rooftop architecture for: (a) the UK, and (b) Oman.

2.11 Summary

This chapter has reviewed the literature of the topics that are covered within this PhD project. It began with an introduction to the history of the PV cell, the principle of the PV cell operation, cell types and different types of solar concentrator used to harvest solar energy. It then focused on solar PV collectors, with a special interest in LCPV concentrators—specifically under the 3D CPC category.

The CPC concentrator has been studied by many authors and it has been found to be the best static concentrator to be used for a low concentration system that offers a wide acceptance angle. It also has better advantages than the V-trough concentrator, which is not suitable for a concentration ratio more than 3x. The optical efficiency of any concentrator can play a major role and has a direct link to determine the performance of the CPV system. As a result of the literature review, the reflective CCPC is shown to have a maximum optical efficiency of 80%. Therefore, it is beneficial to design a properly crossed compound parabolic concentrator with a high specular reflector to increase the optical efficiency, which will increase the power output.

The non-uniformity distribution at the receiver end (PV cell) of CCPC concentrator has been found to be an inherent problem, which requires further investigation to improve

the uniformity and find an optimum CCPC design to reduce the non-uniformity to improve the performance of the CCPC system. A spectroradiometer will be used in the uniformity test to validate the ray-tracing simulation as a new approach.

Apart from the crossed CPC, no experimental study has examined a revolved CPC with circular entry aperture and square exit aperture. Consequently, this design will be explored, and will be fabricated to evaluate the design experimentally and compare it with the CCPC design in terms of power output and optical efficiency.

A comparative study of different geometrical CCPCs at different angular responses will be conducted in this thesis to give a comprehensive picture of the CCPC affects at different geometry heights.

Although the tracking system has been covered in the literature, a basic tracking system with less and optimised tracking movements for different CCPCs needs to be calculated and will contribute more knowledge about this kind of concentrator. It is beneficial to conduct a specific study by using the designed concentrators to provide a forecast of energy production at a specific region (i.e. Oman) and to calculate the real solar radiation to be received at a specific date and compare it with simulation fixed radiation of 1000 W/m^2.

Chapter Three: Experimental Techniques

3.1 Introduction

This chapter describes the key facilities and experimental techniques that have been employed in this research to develop a low concentrating photovoltaic system. A brief description of the purpose and function of each equipment used in this work is also provided. The I-V curves were obtained for two types of solar cells (silicon and GaAs cell) to ensure that the measurement system employed can produce accurate and repeatable result. The temperature coefficient of the silicon cell is determined and compared with the published data. A unique rotary stage is designed and constructed to test the angular response of the CPV system. The fabrication of low-concentration photovoltaics (LCPVs) using 3D printing is developed. Moreover, a spectroradiometer is used in this work to study the optical uniformity of the fabricated concentrators. TracePro software is used to visualise and analyse optical performance of the designed concentrators before fabrication. Finally, the soldering methods for mounting the solar cell on to a Direct Copper Bonded (DCB) ceramic base are discussed in detail.

3.2 Characterisation System

The solar characterisation system was established previously. In this work, it is employed to determine the performance of the solar cell and the characteristics of the solar concentrators. Figure 3.1 shows a photograph of the system with the main components labelled, which include a solar simulator as the light source, an Autolab to obtain the I-V curve, a thermocouple and Picologger for temperature measurement, and a pyranometer or solar survey to monitor the light intensity.

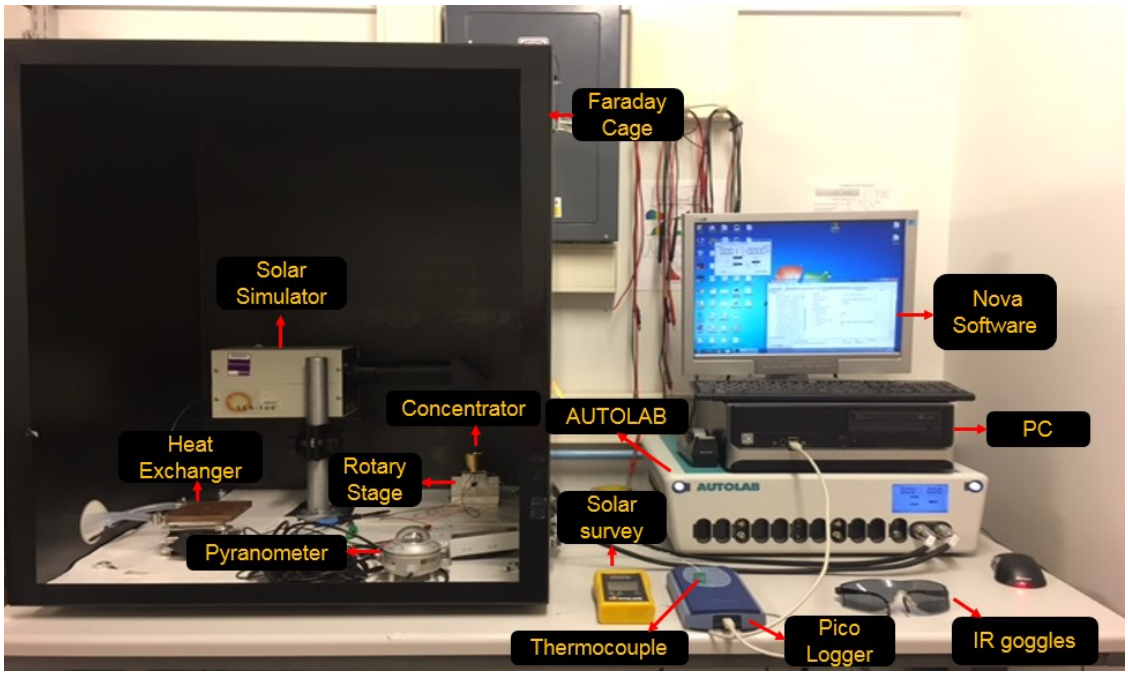

Figure 3.1: A photograph of the solar cell characterisation system employed for this study.

A solar simulator is used to provide illumination for testing, which has a similar spectrum to that of the sun. The solar simulator is an LCS-100 Class ABB system, which was purchased from Oriel Instruments Newport Corporation [158]. The quality and performance of the solar simulator is classified based on the ASTM, IEC and JIS standards. Table 3.1 lists the key specification of the three classes in terms of the spectral match, non-uniformity and temporal instability.

Table 3.1: Classification of small area simulator performance [159].

Class	A	B	C
Spectral match	0.75 – 1.25	0.6 – 1.4	0.4 – 2.0
Non-uniformity	≤±2%	≤±5%	≤±10%
Temporal instability	≤±2%	≤±5%	≤±10%

The solar simulator has an input power of 240 VAC, 50/60 Hz, and 130 W. The area of illumination is approximately 40 mm x 40 mm, it has a Xenon lamp (Xe) of 100 W and lifetime of 1000hrs. The device has a variable attenuator to allow a full or partial solar irradiance. The filter used in the device is a standard filter AM1.5G filter that reaches 1 sun (1000 W/m^2) for the working distance of 8.0inch (20.3) cm. This distance may vary depending on the age of the lamp. If aging occurs, then the illumination intensity can be maintained by reducing the distance of the simulator to the sample.

The solar simulator is kept inside a Faraday cage to shield it from the influence of external light and external electromagnetic fields if it is available nearby. Prior to carrying out any experiments, the simulator bulb needs to be warmed-up for approximately 20-30 minutes to avoid spectral or temporal anomalies. Moreover, the device has a beam divergence half-angle of < 6°.

The Autolab is a versatile measurement system that can be used to determine I-V curves, impedance spectroscopy and electrochemical characteristics, etc. The Metrohm Autolab (PGSTAT302N) that was used in this study is shown in Figure 3.1, and is available at the Cardiff Solar Laboratory [160]. The Autolab is connected to a PC for control and data acquisition using NOVA software. Table 3.2 lists some of the Autolab's specifications.

Table 3.2: Metrohm Autolab specification.

Specifications	
Potential range	± 10V
Compliance voltage	± 30V
Current ranges	1 A to 10 nA
Input impedance	>1 TOhm
Computer interface	USB
Control software	NOVA

Two devices are available to measure the light energy flux produced by the solar simulator: the solar survey and the pyranometer, as shown in Figure 3.1. The solar survey, which is also called the reference silicon cell, is simple to use and quick to display. The solar survey used in this work, was manufactured by SEAWARD [161] and has a measurement range from 100 W/m^2 to 1250 W/m^2, with a resolution of 1 W/m^2. The temperature range can vary from -30°C to +125°C. The device has a built-in compass and inclinometer to measure the roof orientation and pitch. The solar survey is a portable device powered by a lithium battery and no external power is required. After turning on the solar simulator, the solar survey was placed under light illumination and the intensity was immediately displayed on the screen in units of W/m^2. The distance between the light source and the solar survey was determined using a ruler, for a given

light intensity (usually 1 sun = 1000 W/m^2). During the experiments, the solar survey is replaced by a solar cell at the same height.

The second device that can be used to measure solar irradiance is the pyranometer. Although the pyranometer is usually used for outdoor testing, it can also be used for indoor testing. The pyranometer used in this work is manufactured by Kipp & Zonen [162]. It is designed to cover a spectrum range from 285 nm to 2800 nm, which is much wider than the solar survey. To ensure the correct operation of the pyranometer before using it, a sensitivity test was done by checking the output of the pyranometer using a multimeter. The sensitivity of the CMP11 pyranometer is 7 μV/ Wm^{-2}. When the solar irradiance is 1000 W/m^2, the pyranometer's output is 7 mV, which can be measured using a multimeter.

The Picologger is a data acquisition device, which can record, view and analyse the data of temperature measurement from thermocouples. The specific model used in this work is TC-08 purchased from Pico Technology [163], and it provides real-time data collection and display. In this work, this device was used to visualise and display temperature readings for the solar cell by logging thermocouples in one of the provided channels, as shown in Figure 3.1. The device can support all popular thermocouples types and has a fast sampling rate of up to 10 measurements per second. Table 3.3 provides the specifications of the device.

Table 3.3: Specification of data logger.

Specifications	
Number of channels	8
Temperature accuracy	Sum of ±0.2% of reading and ±0.5 °C
Voltage accuracy	Sum of ±0.2% of reading and ±10 μV
Thermocouple types supported	B, E, J, K, N, R, S, T
Measurement range	–270 °C to +1820 °C
Power requirements	USB port

A thermocouple is a sensor that is used to measure and monitor temperature. In this work, K-type thermocouples supplied from RS Components, (UK 363-0250) are used.

Matthew [164] have carried out a comprehensive survey of measurement uncertainties of the equipment used in Figure 3.1, which was used to evaluate the error contribution of each device. Table 3.4 illustrates the modified version of the uncertainties of the corresponding equipment.

Table 3.4: Measurement uncertainties for the experiment devices used in the lab, modified from [164].

Equipment	Range of reading	Uncertainty	Other
Autolab	I: ± 2A	Accuracy: ±0.2%	Potential resolution: 0.3µV
	V: ± 10V		
Pyranometer (Kipp & Zonen CMP11)	285-2800 nm	Temp. Change: <1%	Range: -40 >80°C
		Time Change: <5s	4000W/m² max
Silicon reference cell (Seaward Solar Survey 100)	100-1250 W/m²	±5% digits	1 °C ± 0.5°C (resolution angles)
Pico Logger (TC-08)	–270 °C to +1820 °C	Temperature: Sum of ±0.2% of reading and ±0.5 °C	Resolution: 20bits
		Voltage: Sum of ±0.2% of reading and ±10µV	
Thermocouples (Type K)	-75 °C – 250 °C	± 1.1 °C or 0.4%	Resolution: -250 °C to +1370 °C range

3.2.1 Determination of Light Intensity

Solar irradiance needs to be measured to ensure that the collected irradiance on the testing cell is set at a given level, usually at the Standard Test Condition (STC): irradiation 1000 W/m², air mass 1.5 G and a cell temperature of 25 °C. A Solar Survey is mostly used to measure the intensity of light source throughout the project. Throughout the project all the testing will be under STC.

3.2.2 Solar Simulator Light Distribution Evaluation

Before performing any test using the solar simulator, the light uniformity has to be evaluated to ensure that the simulator is sufficiently uniform in accordance with the standard (see Table 3.1).

The test was taken by using Solar Survey that has a rectangular silicon cell with a length of 20 mm and a width of 5 mm. The solar illumination area was segmented into nine areas with a width size of 13.3 mm for each area as shown in Figure 3.2. After reading the intensity of 1000 W/m^2 (one sun) by placing the Solar Survey in the middle (Area 5), the intensity reading was taken at each of the other eight areas. During each testing, the centre of the solar survey was made to coincide with the centre of each area.

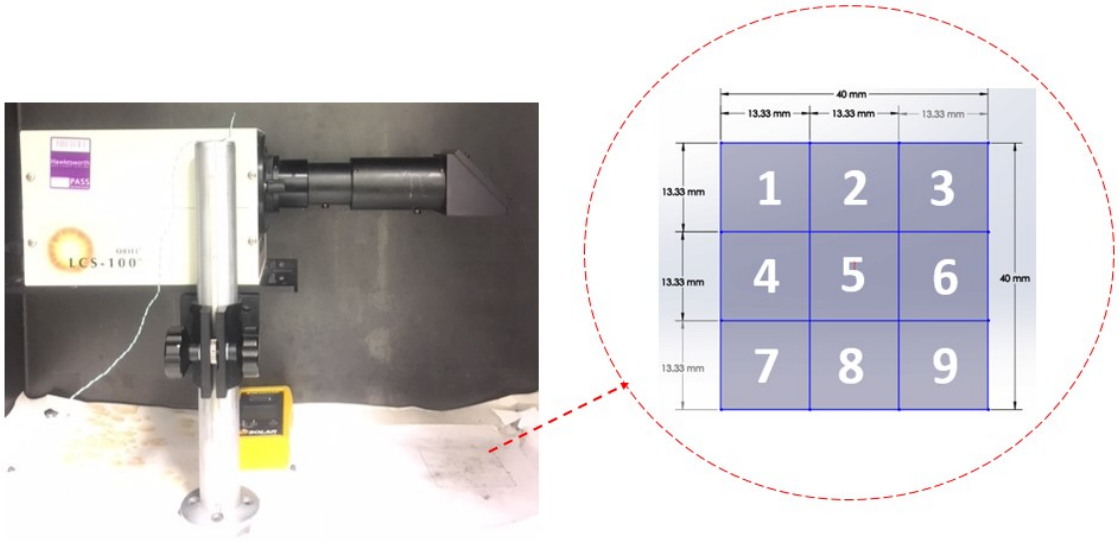

Figure 3.2: The solar simulator and the position.

To ensure that the Solar Survey is placed accurately in each area, a transparent sheet, on which nine areas were divided within 40 mm x 40 mm illumination area, was used and placed above the solar survey. During the tests, the solar survey was moved underneath the transparent sheet across the nine positions and the intensity at each position is recorded. The transparent sheet was removed after being used to indicate the area location and the intensity reading was taken. The test was repeated three times and the average result of the three tests for each position are shown in Figure 3.3.

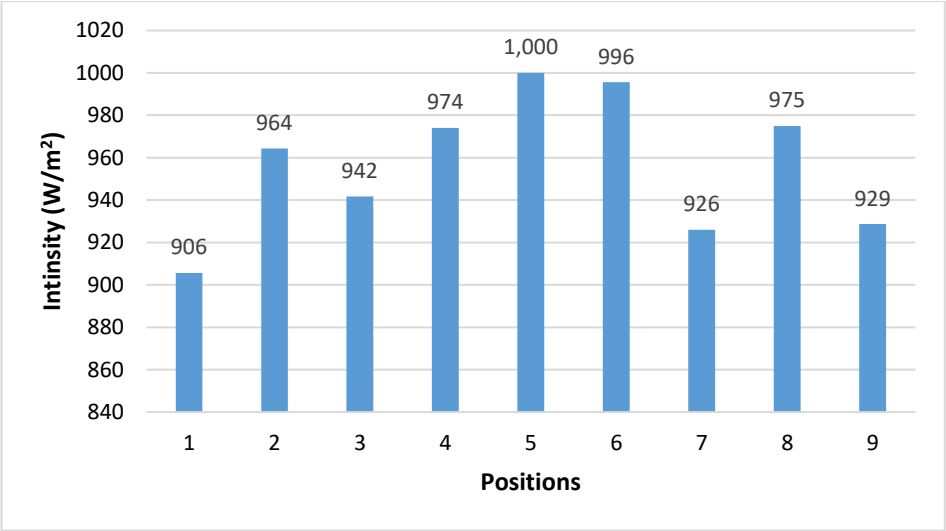

Figure 3.3: Light distribution at nine different positions at one sun illumination within an area of (40 mm x 40 mm).

According to the ASTM standard, the spatial non-uniformity of the Class B solar simulator should be within 5%. Using the spatial non-uniformity of the irradiance equation below [165]:

$$Non-uniformity\ (\%) = \frac{max\ irradiance - min\ irradiance}{max\ irradiance + min\ irradiance}\ \text{x}\ 100\% \qquad (3.1)$$

The non-uniformity calculated by using the results from this test was 4.95%, which indicates that this light source is just within the upper bound of the Class B simulator.

3.2.3 I-V Curve for the PV Cell

The I-V and P-V curves of solar cells are obtained using the Autolab instrument. The solar cell terminals are connected to the probes that is connected to the potentiostat of the Autolab. The solar simulator is switched on and the solar cell's voltage is displayed on the Autolab. The I-V scan procedure is imported to the NOVA software in order to obtain the I-V curves. The displayed voltage of the solar cell is inserted as an initial potential voltage and the I-V curve is obtained. Two types of solar cells have been tested to determine the performance of the devices, which are a monocrystalline silicon cell based on Laser Grooved Buried Contact (LGBC) and a GaAs cell. The I-V and P-V curves for the two solar cells are shown in Figure 3.4. It is obvious from Figure 3.4 (b) that the GaAs cell has the highest maximum power of 20.00 mW, when compared to 10.44 mW for silicon cell.

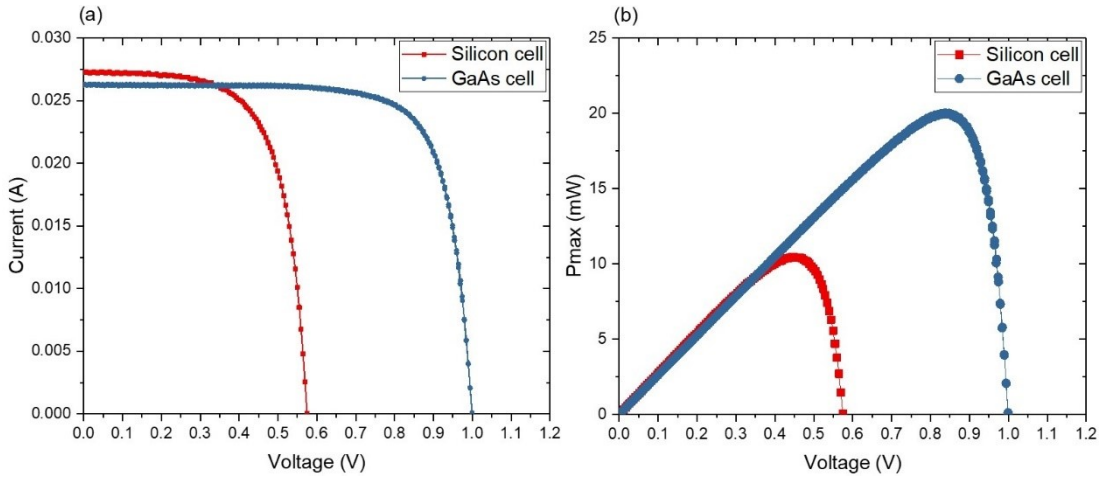

Figure 3.4: Comparison of Silicon and GaAs cell: (a) I-V curve and (b) power- voltage curve.

Another test was carried out to demonstrate the influence of the irradiance intensity level on the silicon cell parameters. Under the STC conditions, the I-V and P-V curves were plotted for the silicon solar cell with light intensity varies from 400 W/m^2 to 1000 W/m^2 as shown in Figure 3.5.

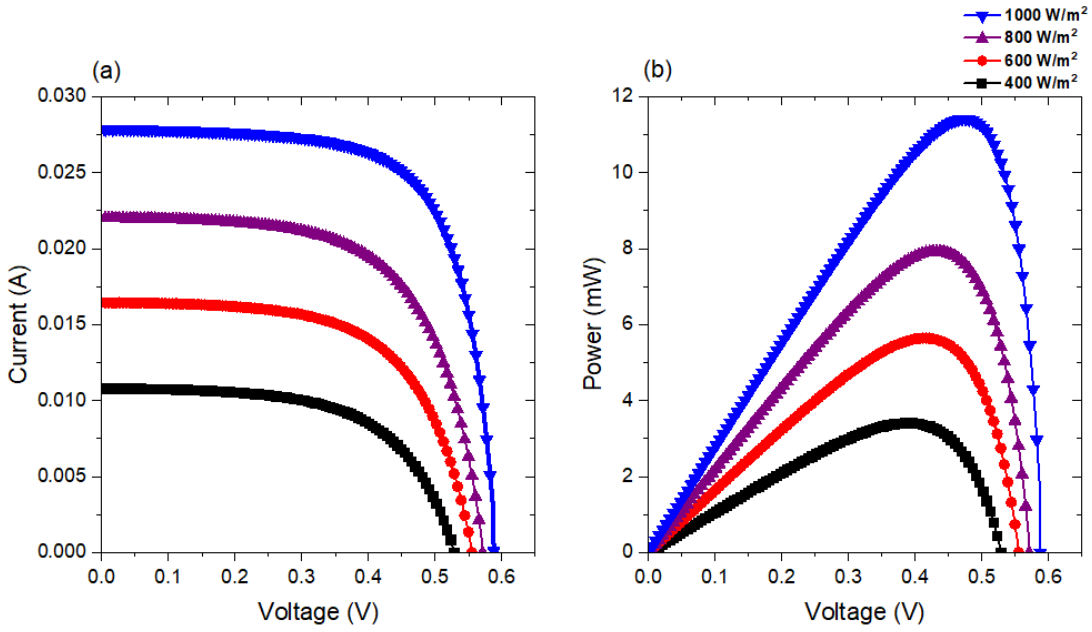

Figure 3.5: Testing solar cell at different light intensities: (a) I-V curve and (b) power-voltage curve.

It has been observed that the short-circuit current (I_{sc}) increases significantly with the increasing light intensity and a slight increase in the solar cell voltage. Figure 3.6 shows this positive linear trend for (a) short-circuit current, (b) open-circuit voltage and (c) power conversion efficiency as a function of light intensity. The increase in the power conversion efficiency offers another advantage for using concentration (in addition to reducing the cost).

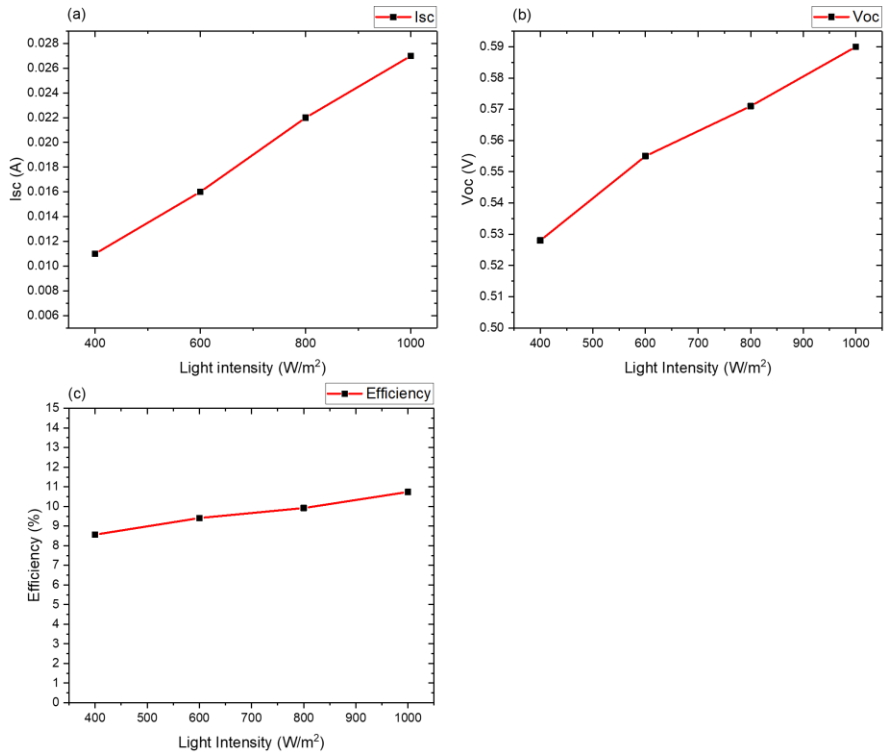

Figure 3.6: Solar cell parameters at various light intensities: (a) I_{sc}, (b) V_{OC} and (c) power cell efficiency.

Table 3.5 shows the experimental results of solar cell performance parameters obtained from two types of solar cells. The datasheet for the monocrystalline silicon cell was obtained under concentrated light (not under 1 sun) according to the manufacturer, whereas the data obtained from this study was taken under 1 sun, which are different from the datasheet. To check and ensure the measurement accuracy of our system, the solar cells are sent to the Centre for Renewable Energy Systems Technology (CREST) at Loughborough University to provide standard references. It can be seen from Table 3.5 that the I_{sc} and the V_{OC} of a silicon cell measured at Cardiff are 0.0269 A and 0.585 V, respectively, which are in good agreement with the results of 0.0262 A and 0.569 V provided by CREST (Appendix A1). In the case of the GaAs, the I_{sc} and V_{OC} obtained at Cardiff are 0.0263 A and 0.999 V, which shows a good agreement with the results (0.0279 A and 1.0 V) in the datasheet (Appendix A2). In addition, the measured efficiency of the silicon cell is 10.44%, which compares well with the CREST results of 10.30% (Appendix A1). In the case of GaAs, the measured efficiency is 20%, which can be compared to the datasheet measurement of 23.4%. The difference from the measured and the datasheet results could be a result of many factors, including but not limited to the soldering resistance, the exact distance of 1 sun, the instrument uncertainties, the cooling system used to cool the cell and the time period of the I-V curve measurement taken.

Table 3.5: Electrical characteristics of silicon and GaAs cells.

Solar Cell Type	I_{sc} (A)	V_{OC} (V)	Fill Factor (FF) (%)	ŋ (Cell Efficiency) (%)	Power (mW)
Silicon PV	0.0269	0.585	66	10.44	10.44
GaAs	0.0263	0.999	76	20.03	20.03

A repeatability test was conducted on a GaAs solar cell. The cell was tested under 1000 W/m^2 irradiance and 25° C. I-V curves were repeated 25 times and the results were recorded (Appendix A3). The GaAs result obtained in the first test is provided in Table 3.5. The average values of I_{sc}, V_{OC} and cell efficiency were found to be 0.0263 A, 0.999 V and 19.77%, respectively, and the standard percentage deviation are 0.03%, 0.01% and 6.97%.

3.2.4 PV Cell Temperature Test

The PV cell temperature test is very important to understand the temperature coefficient of the solar cell. The information that is gained from this test will be useful when the system is placed on the building rooftop and to see if a cooling system is needed to maintain the temperature of the solar cell under concentration. Moreover, knowing the maximum temperature that the solar cell can reach in a steady-state under the illumination of 1000 W/m^2 helps to calculate the percentage drop in power.

The test was carried out by placing the solar cell on a wood board to isolate the cell from surrounding material that could cool it down and could affect the test. Under 1 sun illumination, the thermocouple was attached to a copper slot adjacent to the solar cell. The copper slot is designed and bonded to a Printed Circuit Board (PCB) as the PCB has a less thermal conductivity which does not quickly dissipate the heat from the cell to the board. Figure 3.7 shows the experimental setup for testing the cell temperature and the results obtained over a period after the test started. The maximum temperature reached by silicon solar cell under the irradiance of 1000 W/m^2 is 63.11 °C, and it reached the steady-state value after approximately 1.5 hours from a starting temperature of 25 °C.

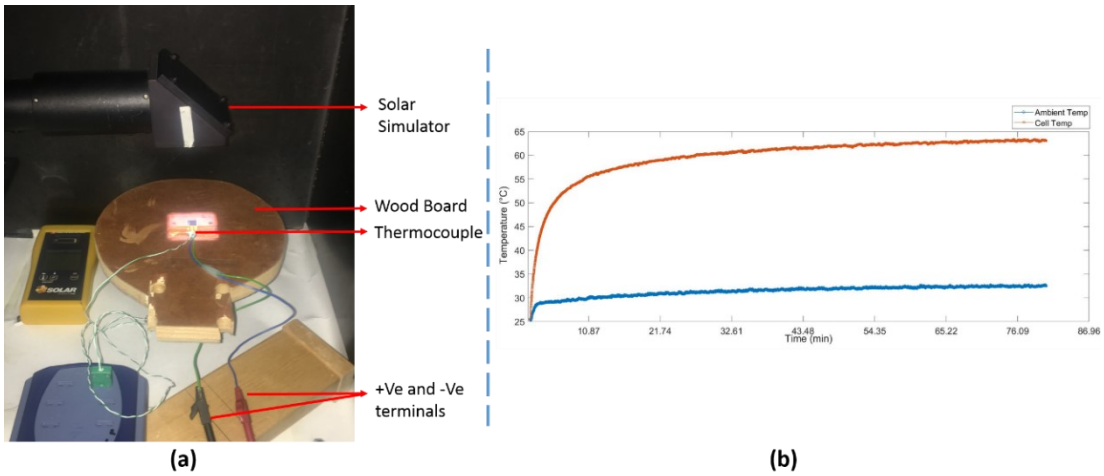

Figure 3.7: PV cell temperature test: (a) experimental setup of the test and (b) temperature of the silicon.

The solar cell power loss can be calculated as defined by [166] and was found to be a loss of 15.24% when the cell reaches a steady-state condition. Meanwhile, a temperature coefficient test was carried out to find the rate of change in the silicon solar cell parameters (I_{sc}, V_{OC} and P_{max}) with respect to temperature. The test was carried out under 1000 W/m^2 irradiance and the temperature was monitored using the Pico logger device. The I-V curves are measured at different temperatures with steps of approximately 5 °C starting from 25 °C to 63 °C.

Figure 3.8 shows the selected point of this test at a step of 10 °C for clarity.

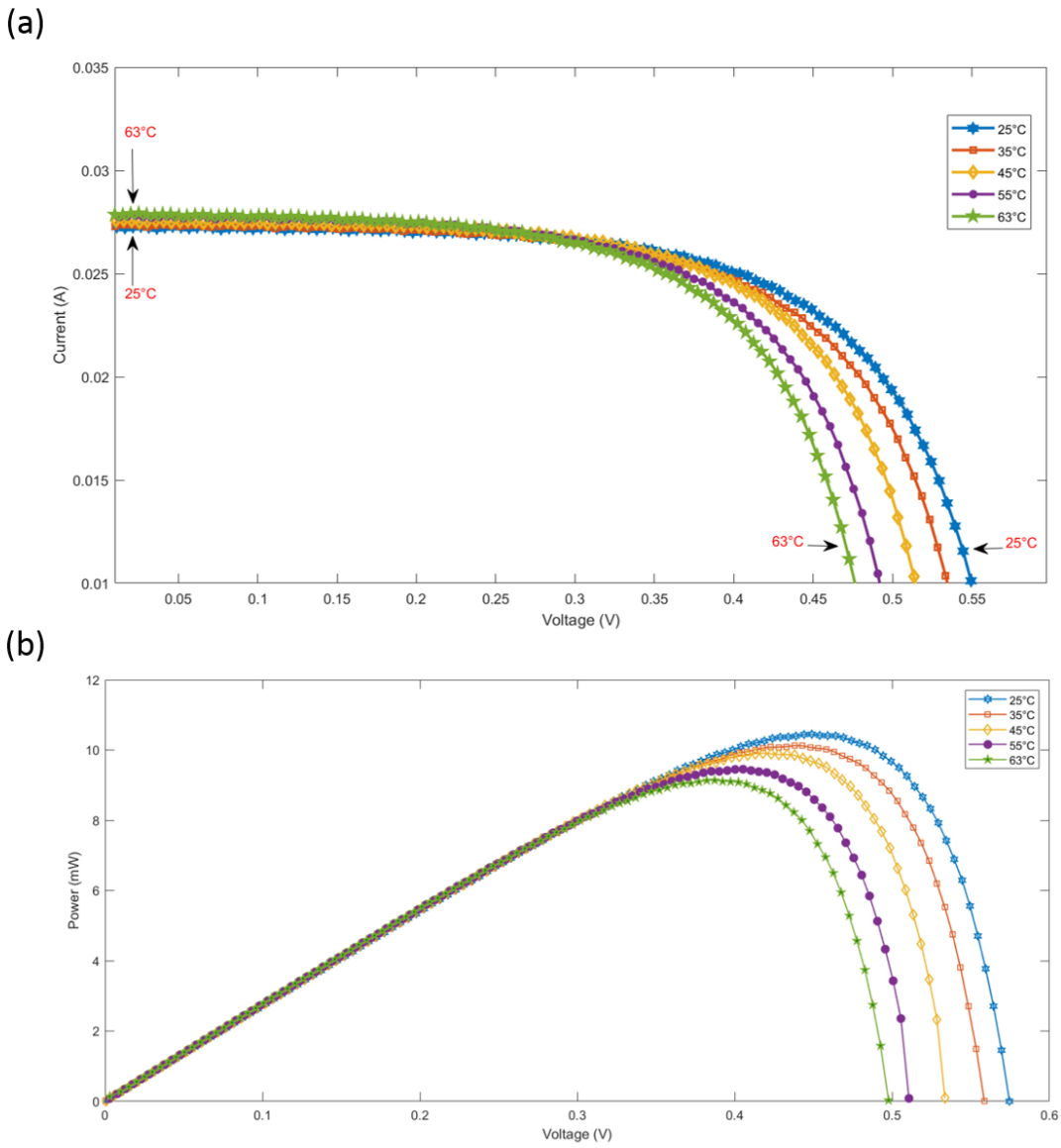

Figure 3.8: Temperature coefficient test for silicon cell: (a) I-V curve and (b) output power versus voltage.

It can be observed from the measured results that an increase in solar cell temperature has a significant effect on the open-circuit voltage and the output power as well, whereas the current increased slightly. This happens because an increase in the solar cell's temperature will reduce the bandgap of the semiconductor and thereby affect these parameters [167]. Table 3.6 shows a comparison for the bare silicon cell between temperatures of T=25 °C and at T= 63 °C.

Table 3.6: Electrical parameter of silicon cell at two different temperatures.

Temperature	I_{sc} (A)	V_{OC} (V)	I_{max} (A)	V_{max} (V)	P_{max} (mW)	FF (%)	η (%)
T= 25°C	0.0273	0.580	0.023	0.459	10.71	67%	10.71
T= 63°C	0.0279	0.498	0.024	0.387	9.14	66%	9.14

From Table 3.6, it can be seen that all of the electrical parameters of the cell drop except the short-circuit current increased slightly. The values of V_{OC} and V_{max} for the silicon solar cell decrease from 580 mV and 459 mV at 25 °C to 498 mV and 387 mV at 63.11 °C (approximately 14.13% and 15.68% for V_{OC} and V_{max}, respectively). The experimental temperature coefficient can be validated by comparing the results with the provided silicon datasheet (see Appendix A4). Figure 3.9 presents the analysed data obtained from Figure 3.8 for the experimental measurements of (a) I_{sc}, (b) V_{OC} and (c) P_{max} with respect to various temperature and the least square fit curve is obtained as per IEC 61215 standard clause 10.4 [168].

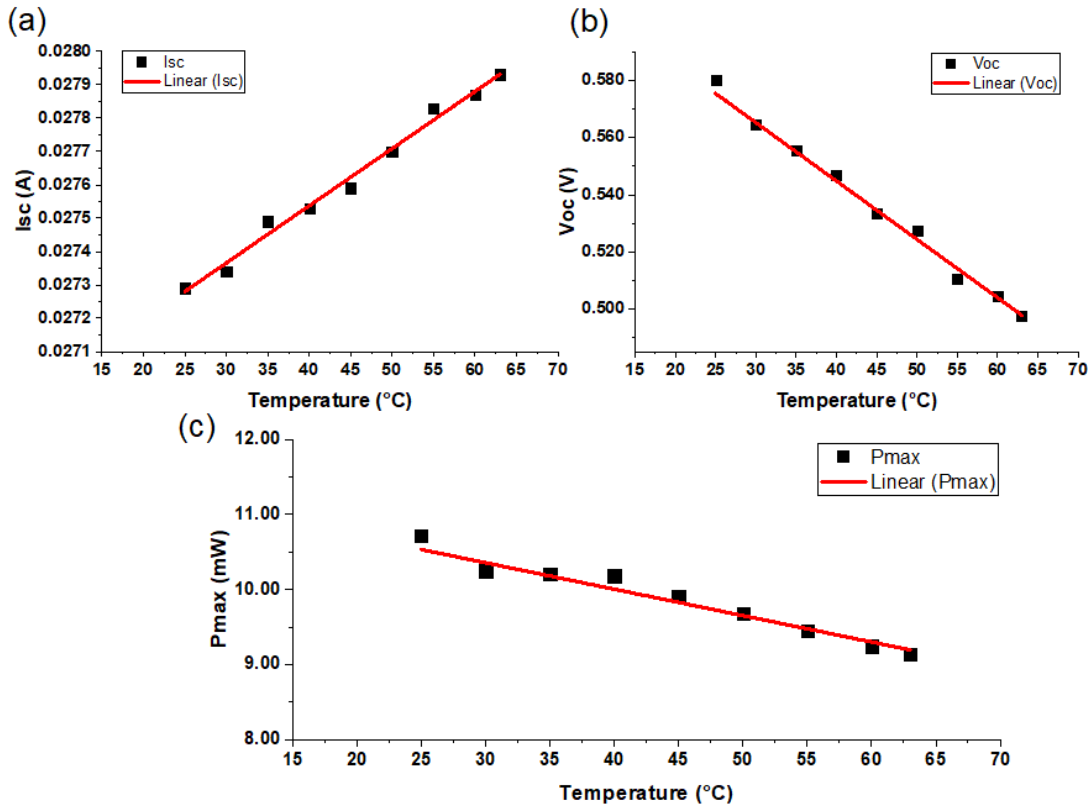

Figure 3.9: Silicon cell as a function of temperature: (a) I_{sc}, (b) V_{OC} and (c) P_{max}.

The temperature coefficient of the short-circuit current can be determined using the following equation [169]:

$$\alpha = \frac{1}{I_{sc_{ref}}} \text{ x } \frac{I_{sc} - I_{sc_{ref}}}{T - T_{ref}} \quad (3.2)$$

where, $I_{sc_{ref}}$ is the short-circuit current generated at the reference temperature. T_{ref} is the reference temperature of the solar cell, which is 25 °C in this study. The temperature coefficient of the short-circuit current for monocrystalline silicon (α) is found to be +0.00057 /°C.

Similarly, the temperature coefficient of the open-circuit voltage can be determined using the following equation [169]:

$$\beta = \frac{1}{V_{oc_{ref}}} \text{ x } \frac{V_{oc} - V_{oc_{ref}}}{T - T_{ref}} \quad (3.3)$$

where, $V_{oc_{ref}}$ is the open-circuit voltage generated at the reference temperature.

By using the data provided in Figure 3.9 (b), the temperature coefficient of the open-circuit voltage (β) is found to be -0.0037 /°C.

The temperature coefficient of the maximum power can be calculated using the following equation [170]:

$$\varepsilon = \frac{1}{P_{max}} \text{x } \frac{\Delta P_{max}}{\Delta T} \quad (3.4)$$

where, P_{max} is the maximum power generated by the solar cell. P_{max} is 10.71 mW at 25 °C and the ΔP_{max} was 1.57 mW. The temperature coefficient of the power coefficient is -0.38%/°C. The experimental temperature coefficients show a reasonable agreement with the published data for the silicon cell (α =+0.00045/°C, β=-0.0020/°C and ε =-0.40 % /°C for short-circuit current, open-circuit voltage and power, respectively, Appendix A4). This test provides important reference data for the design and understanding of the performance of the concentrator system, which will be described in the following chapters.

3.2.5 Solar Concentrator Uniformity Test

The uniformity of light distribution across the PV cell is crucial in the optical design of solar concentrators. In particular, non-uniformity leads to a reduction of the solar cell's efficiency due to an increase in the series resistance of the solar cell [171]. This work uses a spectroradiometer to characterise the non-uniformity of the fabricated concentrators.

In general, a spectroradiometer is used to measure the intensity of electromagnetic radiation over a wide range of wavelengths, including ultraviolet, visible and infrared spectrum. The spectroradiometer used in this work is supplied by Stellar Net [172]. The spectroradiometer comes with two separate instruments: a blue device for ultraviolet and visible light (UV-VIS), and a red device for infrared radiation light (IR). Both devices can be integrated and used as one unit, as shown in Figure 3.10 and 3.11. This type of spectroradiometer has been selected because it has the advantage of combining a wide range of electromagnetic spectra and creating a unified spectral graph. However, correctly displaying a single spectral graph over 200 nm to 1700 nm using both instruments requires a complex calibration procedure. Al-Najideen [173] has carried out intensive work on the appropriate setup and calibration of these instruments, which will help to ensure the proper function of the device for use in this work. The key specifications of the spectroradiometer are shown in Table 3.7.

Figure 3.10: A photograph of the blue (UV-VIS) and red (IR) instruments for measuring sunlight spectrum over a range of 200 nm to 1700 nm.

Table 3.7: Spectroradiometer specification.

Specifications	
Blue box range	200 to 1500 nm
Red box range	900 to 1700 nm
Detector integration	1ms to 65s
Power consumption	<100 mA via USB port
Fibre optic input	SMA905 0.22na single fibre

A schematic diagram showing the layout arrangement for the dual spectroradiometer device is given in Figure 3.11. The two devices are connected by a Y-shape fibre optic. The red device (NIR) requires a 5 Volts power supply because it coupled with a fan for cooling purposes. While the blue (UV-VIS) can be powered directly from the PC.

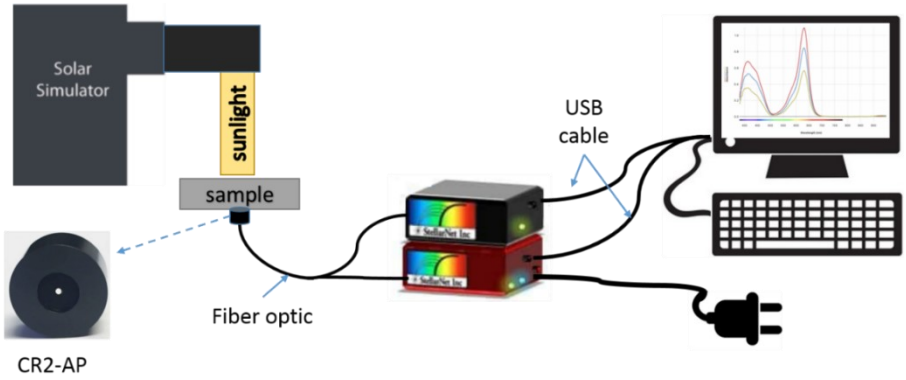

Figure 3.11: Schematic diagram of the spectroradiometer layout [173].

The solar simulator provides the source of light which is detected by CR2-AP detector to allow reading intensity measurements to be made of sources that are 10 times brighter. The CR2-AP is connected to both devices by a Y-shape optical fibre. The two instruments are connected to a PC via USB cable to provide a reading through the spectroradiometer software, which can provide a single spectral graph over a wavelength range of 200 nm to 1700 nm.

The setup described above is used to study the non-uniformity of light distribution at the exit area of the concentrators. During experiments, a thin copper sheet is placed at the exit area of the concentrators, which has a fixed size of 10 mm x 10 mm. This area is divided equally into nine sections, and each of these divisions has a 3 mm hole in the centre to allow the light to pass through to the detector. The experimental procedure and results of this experiment are presented in Chapter Five of this thesis.

3.3 Design and Construction of an Angular Response Testing Setup

The study of the angular response of the concentrators is an important aspect because it can determine the need for a tracking system. The concentrators with a wider angular response allow for cost reduction through using a simple tracker with less precision [174]. To investigate the angular response, it is necessary to design and construct a rotary stage to facilitate the change of the angle of the concentrator in respect to the incident light. The rotary stage should be able to hold the concentrator and the solar cell

and to rotate in a range from +90° to -90°. As discussed in Section 3.2.4 there is a need to maintaining the solar cell's temperature at STC because an increase in the solar cell's temperature leads to a reduction in the efficiency and power output of the solar cell. This led to the idea of a dual-function sample stage for cooling and rotation.

3.3.1 Rotary Stage

The rotating block is made of the aluminium (4.6 cm x 3.2 cm x 2.0 cm) with a heat exchanger for cooling incorporated in the design. The water channels are formed inside the rotating block through drilling as shown in Figure 3.12 (a) and (b). A photograph of the fabricated rotating stage is shown in Figure 3.12 (c) which can rotate ±90° in a step of 5° with a pointer indicator. The two holes that appear on the side of the rotating block as shown in the Computer Aided Drawing (CAD) in Figure 3.12 (a), were a result of drilling through the block to form a square path for the water circulation. Both holes were sealed after the channels were formed. The rotary stage consists of two parts: the rotating block/heat exchanger and an aluminium stand, which holds the rotating block and allows it to rotate. The aluminium stand has thin line grooves made at every 5°, with the corresponding angles marked in the unit of degree, as shown in Figure 3.12 (c).

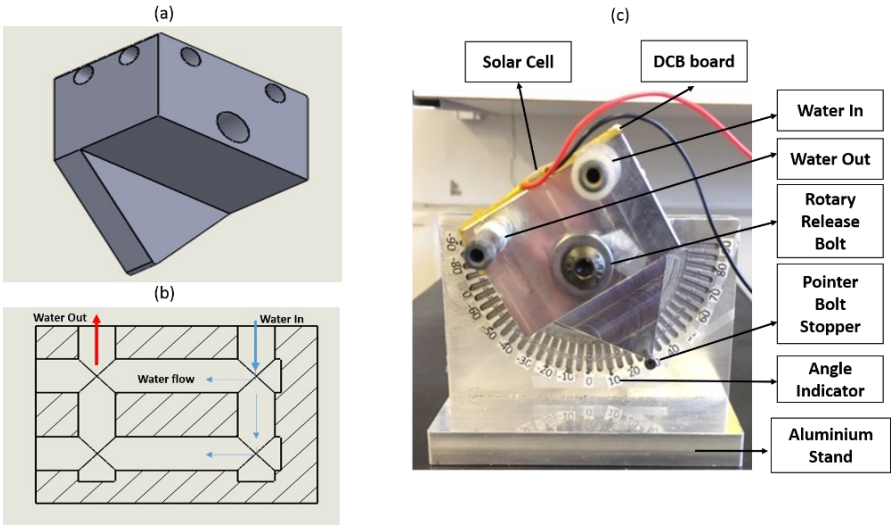

Figure 3.12: Rotary stage design: (a) CAD drawing (isometric view), (b) section view of water flow circulation and (c) a photograph of the fabricated dual-function rotary stage.

The top side of the rotary stage is designed to match the DCB board layout, which will be discussed in more detail in Section 3.6. The top side includes six holes: four holes with a diameter of 2 mm are used to secure the DCB board to the rotary stage, and the other two in the middle with a diameter of 4 mm are made to secure the concentrator on to the DCB board and rotary stage.

3.3.2 Experimental Setup

Once the illumination intensity is determined, the rotary stage is placed under one sun distance and the water pipes are connected before switching on the solar simulator. The inlet pipe is connected to a cold tap water next to the Faraday cage. Whereas the outlet pipe that drains the hot water is placed in the sink. Figure 3.13 shows a schematic diagram of the system (a) and a photograph of the rotary stage under solar illumination (b).

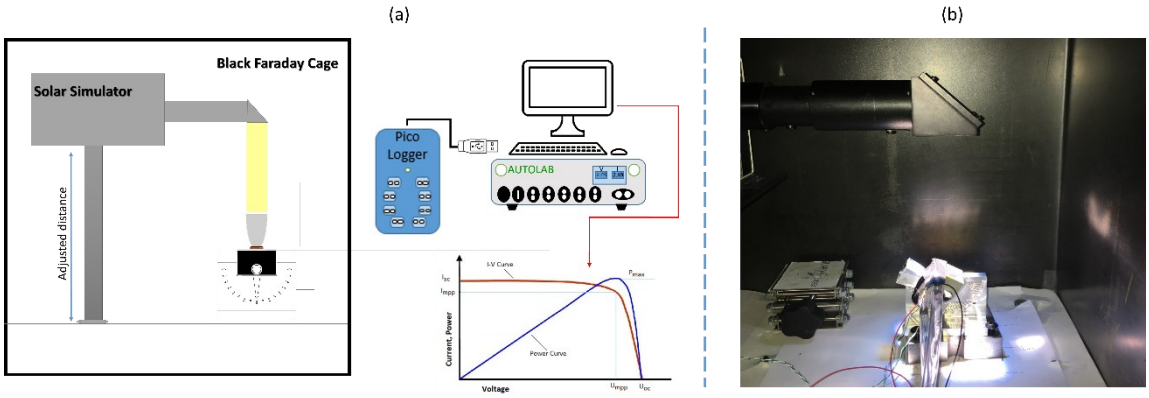

Figure 3.13: (a) Schematic diagram of the rotary stage components and (b) a photograph of a rotary stage under solar illumination.

3.3.3 Results

The angular response of a bare solar cell (i.e., without concentrator) was measured using this setup by moving the pointer at steps of 5 degrees, on both sides and recording the corresponding I-V curves. Figure 3.14 shows the short-circuit current and maximum power as a function of incline angles. The results show an identical representation of the data on both sides. These results demonstrate the functionality of the rotary stage required by the design.

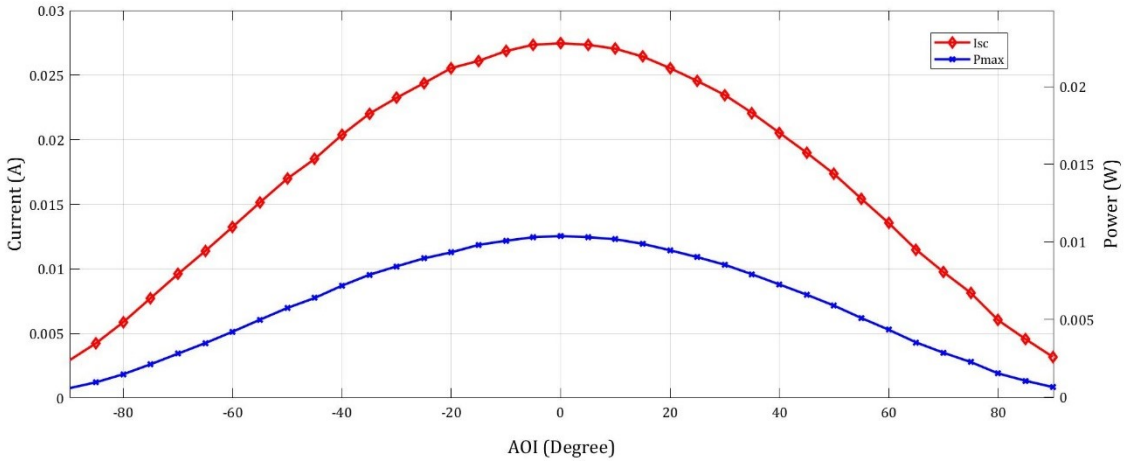

Figure 3.14: Angular response of I_{sc} and P_{max} for the bare silicon solar cell.

The simulator's shutter was closed after each measurement and the data was exported to an Excel file for processing. Two thermocouples were used, the first was used to measure the heat exchanger temperature (water in) and the second was used to measure the solar cell temperature to ensure that the I-V curve is taken at STC. The thermocouple's tip is placed on the copper underneath the cell. It is obvious from Figure 3.14 that the short-circuit current (I_{sc}) and the maximum power output (P_{max}) reach their maximum values at normal incidence, and these values decrease with an increase in the angle of incidence (AOI).

3.4 TracePro Simulation

Simulation is an essential part of this work because it provides useful insights into the modelling and design of the concentrators prior to their fabrication, which will save time and money. The optical performance of the concentrators is evaluated by using the ray-tracing technique. Many software packages are available for ray-tracing simulation. In this work, TracePro software has been selected because it is easy-to-use, powerful, fast and accurate. It has also been used widely by many authors in ray tracing of optical concentrators [118, 175, 176].

The ray-tracing simulation shows the optical behaviour of a concentrator by visually showing the detailed ray paths after they hit the inner surface of the optical system, where some of the reflected or refracted rays cannot be detected experimentally. The TracePro® software provided by LAMBDA research corporation [177] was employed to carry out the optical analysis in this project, which is based on a Monte Carlo ray-tracing simulation.

3.5 Development of Solar Concentrator Fabrication Procedures

One of the initial and essential objectives of this project is to fabricate a range of high-quality solar concentrators based on a specific design. Therefore, the design and the machine used to manufacture the concentrators should be selected carefully in terms of quality and cost-effectiveness. Once the concentrator is designed and created using SolidWorks software, the CAD file is saved and exported in a format that can be opened by the machine that fabricates the concentrator with a geometry according to the design. This section will discuss the two different types of LCPV concentrators produced by two different machines that are used in this project.

3.5.1 Acrylic Concentrator by 3D Printing

The 3D printing technique can deliver a design quickly, and with high quality and accuracy. This technique helps to reduce costs in terms of machine, labour and material cost. The first and main concentrator in this project is made from acrylic plastic, which is fabricated in-house by Form +1 3D printers supplied by Formlabs [178]. This technique is based on Stereolithographic (SLA) 3D technology, which uses a laser to cure the liquid instead of hard plastic wire. The material that has been used in this printer is a proprietary photopolymer clear/black/grey resin. A photograph of the 3D printer device is shown in Figure 3.15. The specifications of the Form +1 3D printer are provided in Table 3.8.

Figure 3.15: Form +1 3D Printer.

Table 3.8: Specification of Form +1 3D printer.

Specifications	
Layer thickness	25,50 or 100 microns
Min feature size	300 microns
Building size	12.5cm x 12.5cm x 16.5cm
Resin material	Liquid resin
Resolution	As low as 25 microns
Technology type	Stereo-lithography (SLA) technology

The process of printing combines software and hardware setups which are discussed in detail in the following section.

3.5.1.1 Software Setup

The designed file should be saved in one of the three formats: .obj, .sat or .stl. The file is then opened and imported by the dedicated Formlabs software, called "PreForm", which is available for download online. Once the file is imported, the selection of 3D printer type, resin type, and printing resolution is entered and now the visualisation of the file appears in the software design platform, as shown in Figure 3.16.

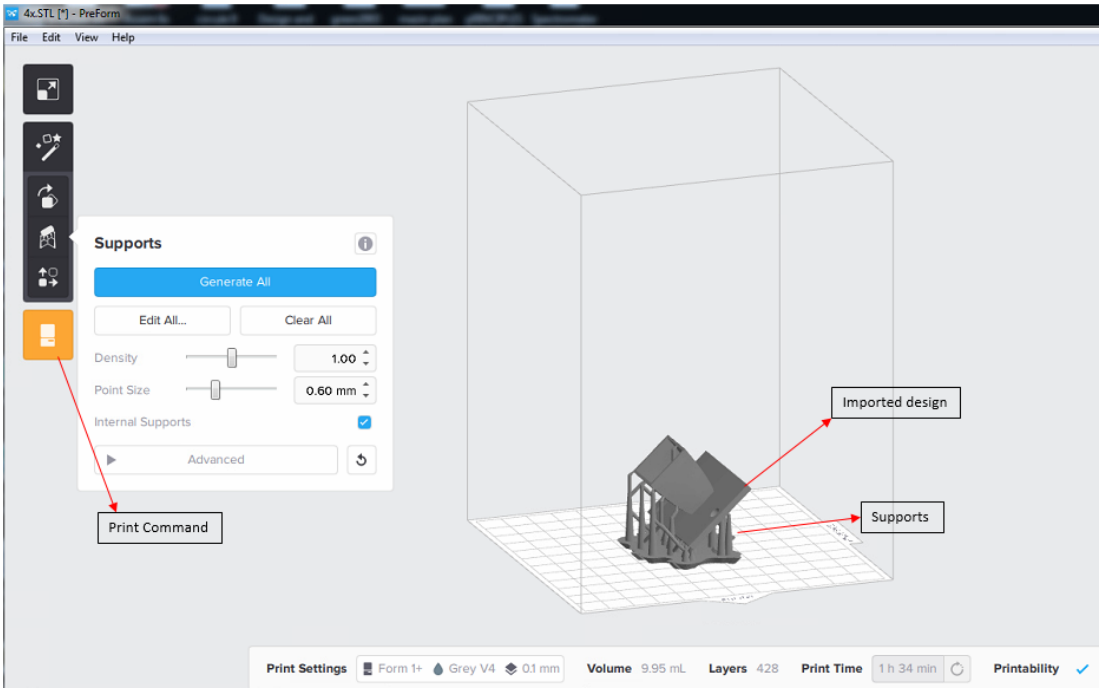

Figure 3.16: PreForm software characterisation.

The sample cannot be printed unless supports are applied to the imported design. The support consists of three components: rafts, scaffolding and touchpoints. The raft is the bottom part of the support (base), which is used to adhere the object to the build platform. The scaffolding is used to secure the printed design and the touchpoints are the contact part of the support component and the design. The size of the support can be adjusted and selected from the scale bar drop list under the supports button. After ensuring that all of the parameters are entered, the final step in the software setup is to press the orange button to start the printing process.

3.5.1.2 Hardware Setup

A hardware setup is also necessary in the process because it helps to correctly print the concentrator according to the design. The printer needs to be connected to the PC by a USB cable, while the PC should have PreForm software installed. The power cable should be attached to the power brick and plugged to the Form +1 power socket. The 3D printer works in such a way that a photosensitive liquid is filled in the resin tank and is exposed to an ultraviolet (UV) laser, which cures the resin filled in the tank at each layer. Due to light exposure, this causes a layer of resin to solidify. The resin should not exceed the upper line indicator as shown in Figure 3.17. The laser has the advantage of getting much finer details and produces a much higher quality object when compared to other 3D printer techniques. It is crucial to ensure that the build platform is inserted appropriately and secured by the handle, the resin tank should roll inside firmly, and we should ensure that exact type of filled resin is selected in the software.

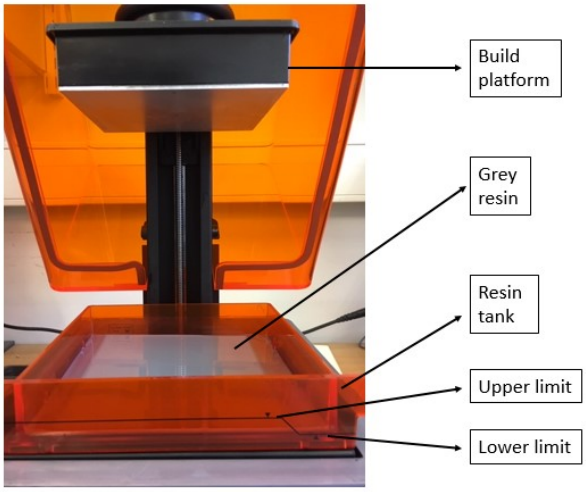

Figure 3.17: A photograph of the resin tank and build platform of a Form +1 3D printer.

The printer's cover must be closed before printing, otherwise, the printer will not start. After sending the command from the PreForm software, the power button on the device should be pressed to allow the printer to start the job.

3.5.1.3 Post-printing Treatment

After printing, the cover is opened and the build platform is pulled out. The device comes with a Form Finish Kit that contains the tools needed for the printing process. When the printing process is completed, a scraper is used to remove the sample gently. The two rinse tubes are half-filled with Isopropyl Alcohol (IPA). Treatment of the printed concentrator is carried out immediately after the printing process by immersing and shaking the concentrator in an IPA bath for 2 minutes, and then soaking it for 10 minutes in another bath to remove any contamination from the printing process. The printed concentrator is left to dry for about 1 hour before it is ready for the next stage. Figure 3.18 shows a photograph of a printed concentrator with supports while drying in air.

Figure 3.18: 3D printed CCPC with supports using Form +1.

3.5.1.4 Additional Adjustments

Even though the printer can produce a high-quality finish that has accurate geometry, some issues can occur during the print process that require additional adjustments. To guarantee a successful outcome, as specified by the design, the results need to be monitored and adjustments need to be made. The size of the concentrator after printing is not the same as the design because of some unknown factors during the printing process. It was found after several prints that the scale of the design needs to change from the default value 1.000 to 1.125 to ensure the exact size of the original file. Another issue is that sometimes the printer does not print the complete design, it often only prints the base of the supports on to the build platform. In this case, fine tuning is required to lower the build platform height, which can be done via the software. The scraper marks on the build platform could also affect the adherence of the printed parts and therefore

carefully removing the parts without making marks on the base is advised. Furthermore, foggy marks were also observed on the bottom of the resin tank. It was found that repeating the print in the same position can result in an unsuccessful print, which is often caused this foggy distribution at that exact position. To avoid this problem, regular cleaning and changing the position is required for each print. Finally, the 3D printer that was used offers good quality output for the designed parts and is considered the best for adding reflectors to its inner parts, but it was found that tiny bubbles appeared in the inner surface, which prevents a good finish. To ensure a smoother surface, another type of machine was explored, as discussed in the next section.

3.5.2 Aluminium Concentrator by CNC Machining

Another way to fabricate the concentrator is to use a Computer Numerical Control (CNC) machine. The vertical centre smart 430a [179] is a popular CNC machine that is available at Cardiff University's workshop and was used in this study to make a circular aluminium concentrator. The CAD file is inserted into the machine control system and the cutting process is carried out automatically. A photograph of the machine is shown in Figure 3.19.

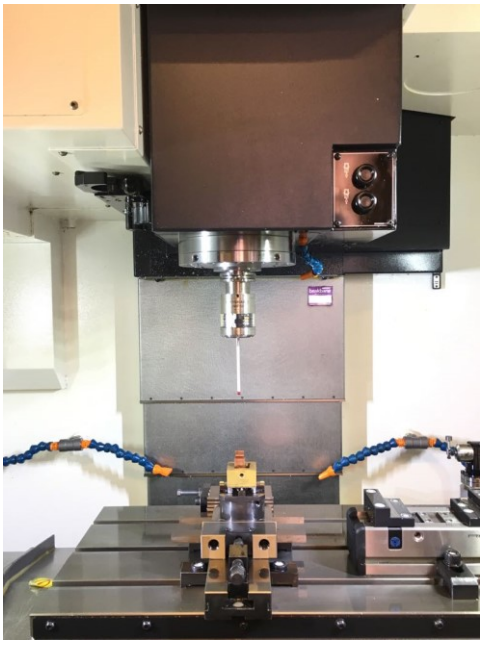

Figure 3.19: A photograph of a CNC machine.

A very high rigidity spindle is used for cutting with a maximum speed of 12000 rpm and motor output of 19kW/25.0hp. A block of aluminium is placed at the centre and the spindle moves down to cut and shape the aluminium block as per the required design.

The analysis of the cutting process and the remaining time are displayed on the control panel. Figure 3.20 shows the concentrator made by the CNC machine before adding the reflective coating. Clearly, the disadvantage of the method is incapable of making square entry concentrator as shown in Figure 3.18. A comparison between the two methods of manufacturing the CPC is made and the results are discussed in Chapter Four.

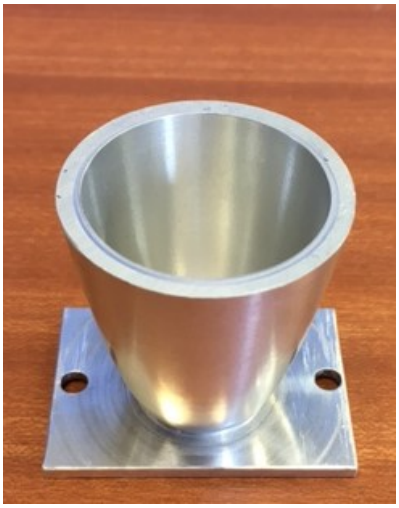

Figure 3.20: CPC design manufactured by a CNC machine.

3.6 Solar Cell Soldering Process

Monocrystalline silicon and GaAs cells were purchased in a wafer form without the output terminals, ready for direct connection to the testing instrument. Soldering of the solar cells is an important process that needs to be done carefully because it can affect their performance. Poor quality soldering can reduce solar cell efficiency because of bad wire joints, which result in high series resistance. The soldering and wire tabbing process was carried out in the laboratory. The first trial was to solder the tabbing wires directly on the both sides of the solar cell. Three silicon cells: silicon-1, silicon-2 and silicon-3, were tested under 1000 W/m^2 irradiance to obtain the I-V curves (see Appendix A5). The test was repeated three times for each cell and the average efficiencies achieved were 7.77%, 9.28% and 4.73%, which are significantly lower than the nominal efficiency of the solar cells. Therefore, this method produced unstable and inconsistent results due to the poor soldering on the back area. In addition, the soldering on the backside was not completely secure and was only in contact with a very small cell area. Moreover, the cells are fragile and can break easily using this method of soldering.

The problem of soldering quality can be minimised by using a DCB ceramic plate, together with the use of the hotplate for soldering at controlled temperature. This

process has proven to effective with repeatable and stable outputs (see Appendix A6). Three silicon cells were soldered on DCB and named DCB-1, DCB-2 and DCB-3. The solar cell is mounted on a thin copper layer located at the centre of the DCB board as shown in Figure 3.23, and heated using a hotplate (300 °C) after adding a little soldering lead to ensure a firm attached of the solar cell. Again, the test was repeated three times for the three DCB's and the average silicon cell efficiencies were 11.40%, 11.56% and 12.97%. These results show a stable electrical output after using the DCB compared to the first method. Moreover, the solar cell was found to be more secure in the middle of the DCB and easier to couple with the concentrator.

Several types of solar cells were discussed in the literature review (see Section 2.3) and based on the literature monocrystalline silicon solar cell LGBC has been used by many authors to investigate LCPV systems. The monocrystalline silicon cells to be used in this study were selected and purchased from Solar Capture Technology [82]. The cell size is 10 mm x 10 mm ±0.5 mm, wafer thickness of 200 μm ± 30 μm and the busbar width of 1.0 mm. The solar cells come without wire strips and with a single busbar, as shown in Figure 3.21.

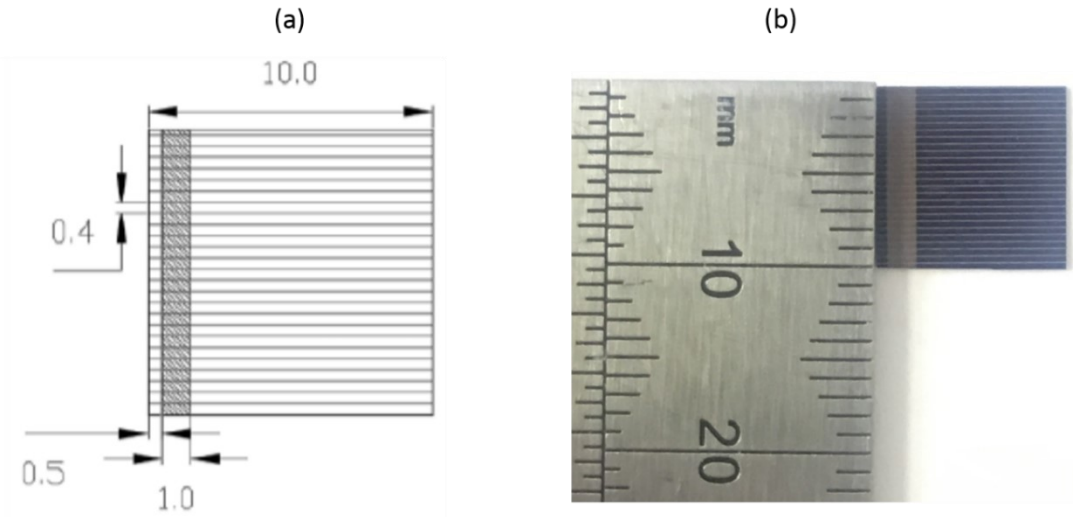

Figure 3.21: (a) Schematic diagram of silicon dimension and (b) a photograph of the actual silicon cell.

The DCB ceramic is used as a base for the silicon cell, which was supplied by Tianjin Century Electronics [180]. The DCB board is specially designed to match the concentrator base and the top side of the rotary stage to firmly secure the concentrator on the rotary stage for angular response testing. Figure 3.22 shows the design specifications, while more details are addressed in Appendix A7.

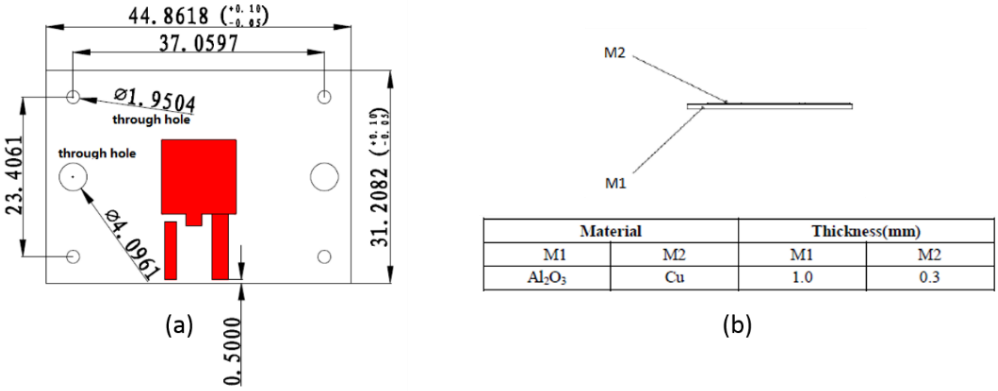

Material		Thickness(mm)	
M1	M2	M1	M2
Al_2O_3	Cu	1.0	0.3

Figure 3.22: DCB design: (a) top view of DCB dimensions and (b) side view of the DCB ceramic.

The advantage of using a DCB board over other types is its high thermal conductivity, which is around 24 ~ 28 W/m.K at 25°, and the electrical insulation that it provides. This is to enhance the cooling of the cell temperature with less water flow. A high-purified oxygen-free copper is firmly bonded onto the alumina ceramic substrates.

The process of mounting and soldering the solar cell is shown in Figure 3.23. The backside of the cell is directly attached to the copper surface (+Ve) terminal, while the busbar is soldered with a tabbing wire to be connected as a bridge with the (-Ve) terminal.

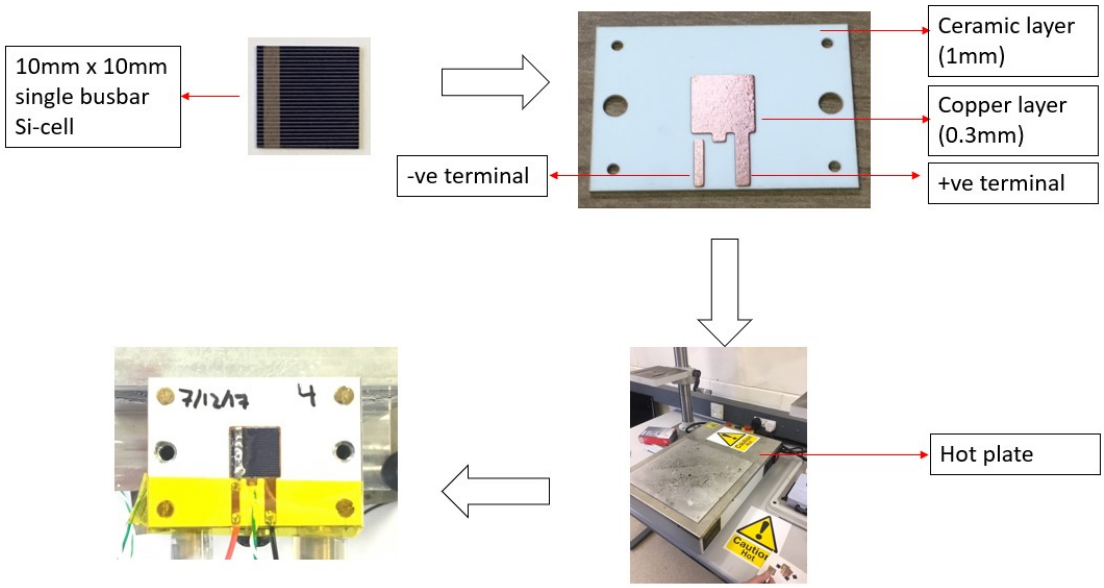

Figure 3.23: Drawing showing the solar cell soldering process in the DCB board.

A little soldering lead is applied to the copper surface and melted on the backside of the silicon cell and then stacked to the copper by using the hot plate at 300 °C. The soldering

of the solar cell was made using lead-free PV ribbons with a width of 0.1 mm. Soldering flux is applied to ease the process of the soldering and allow a better connection. It has been noticed that the flux pen helped to adhere to the connection. The last part is the soldering of the +Ve and –Ve wires to the DCB board copper end. The wired connections should be soldered with a minimum amount of solder because it can increase the series resistance of the solar cell.

3.7 Summary

The main techniques and methods required for use in this study were identified and experimental work was carried out to confirm the validity of these techniques and methods. An existing solar cell testing system was employed to carry out bench-mark testing using two types of solar cells (Si and GaAs) in order to demonstrate the suitability and capability required by this project. In addition, detailed testing on light uniformity, temperature dependence and light intensity were performed to ensure that the reliability and accuracy of the system meet the requirement of this project.

A rotary stage was specifically designed and constructed to investigate angular response, which also includes a heat exchanger to maintain the solar cell at a constant temperature during testing. This added additional capability to the existing solar cell measurement system to facilitate the study of angular response under a controlled temperature, which is a crucial setup for the experimental investigation that will be described in Chapter Five.

Methods and procedures for fabrication of concentrators were explored in an attempt to fabricate the high-quality concentrators that are required by this research. It is found that the method based on modern 3D printing (e.g., Form +1), together with the use of adhesive high reflective material, can conveniently produce high-quality prototype concentrators with different concentration ratios at laboratory scale, which is ideally suitable for the requirement of this research.

The method of attaching the solar cell to the DCB board is crucial because it can minimise the power loss caused by poor electrical connection and ensure good thermal contact to maintain temperature stability during the measurement. An effective procedure for securely mounting the solar cell onto the DCB board has been implemented and satisfactory electrical, thermal and mechanical properties required for successful characterisation were demonstrated.

Chapter Four: Design, Construction and Characterisation of a Cross Compound Parabolic Concentrator

4.1 Introduction

This chapter focuses on the design and development of a cross compound parabolic concentrator (CCPC) for possible applications in low-concentration photovoltaic systems. In particular, this chapter will describe the design, simulation, fabrication and testing of the five concentrators with the concentration ratios of 2.9x, 4.0x, 6.0x, 8.3x and 9.0x. A range of CCPC concentrators mostly with lower concentration ratios has been explored in the literature, and better to have concentrators with higher ratios that are not covered in the literature which will be explored in this thesis. A CCPC consists of four symmetrical reflectors of the same height and with square entry and exit apertures. In addition, a new type of CPC, which has a circular entry aperture and square exit aperture, was designed and tested, followed by a comparative study of all fabricated CCPCs in terms of power output and optical efficiency. The optical analysis was performed using TracePro® software to assist the design of CCPCs and predict the optical performance of the fabricated CCPCs, which proved to be an effective tool to achieve the best design, and also save time and costs. The concentrators were fabricated using a 3D printing technology and tested in an indoor testing setup.

4.2 Design of the CCPC

To achieve an optimal design of the concentrators, it is important to follow proper design techniques and procedures that ensure better results. A flow chart is devised for this project and is followed throughout the design and fabrication process until the optimised design is achieved, as shown in Figure 4.1.

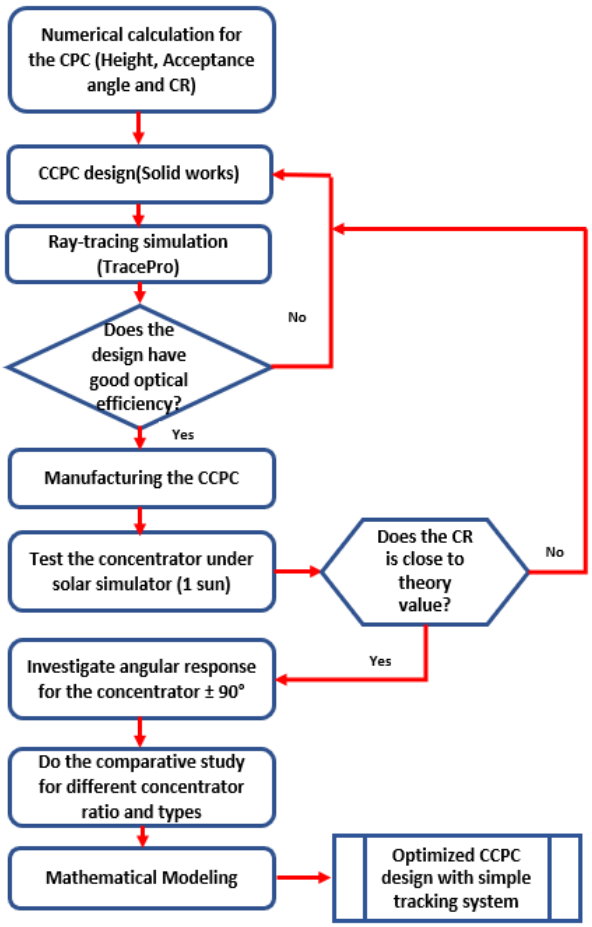

Figure 4.1: Flow chart for the design process of the optical concentrator.

As discussed in the literature [88], a CCPC consists of two symmetrical parabolic curves, which are able to reflect all the incident radiation to the absorber within its half acceptance angle. The four key variables for CCPC design are: input diameter (d1), output diameter (d2), half acceptance angle (Θ_c) and the height of concentrator (h). Figure 4.2 illustrates the four variables in (a) cross-sectional view, and (b) 3D view.

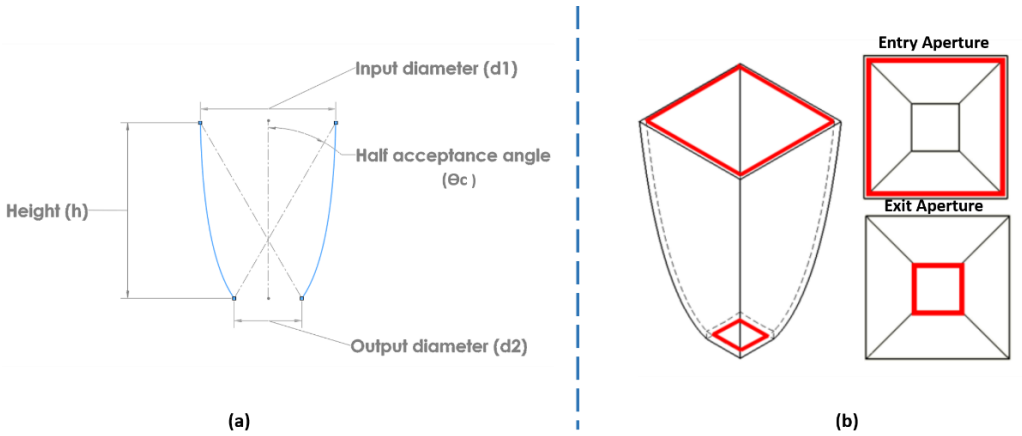

Figure 4.2: The compound parabolic concentrator variables in: (a) cross-sectional view and (b) 3D view.

The input and output diameters represent the dimensions of the entry and exit apertures of the CPC, as shown in Figure 4.2. For a given concentration ratio, there is a corresponding height. Despite being considered the most effective option for an ideal concentrator [181], a CPC is limited by its acceptance angle. The higher the concentration ratio, the narrower of its acceptance angle.

All of the incident rays entering through entry aperture d1 with an inclination smaller than the half acceptance angle will be reflected towards the receiver (exit aperture), where the absorber/solar cell is placed. However, the incident rays will be reflected back outside of the CPC if the incidence angle is more than the half acceptance angle. The analytical equations that were used to design the CPC will be discussed briefly in the next section, starting with determining the geometrical concentration ratio of the concentrator.

4.2.1 Design Variables

The primary input for designing an optical concentrator is to decide the concentration ratio required. Two different definitions of the concentration ratio are widely used, which are: the geometrical concentration ratio and the optical concentration ratio [182]. The geometrical concentration ratio is the ratio between the entry area and the exit area. The optical concentration ratio is defined as the light intensity at the receiver area divided by the light intensity at the entry area.

In this study, the receiver size is fixed to 10 mm x 10 mm because of the size of the monocrystalline silicon solar cell used, and therefore the geometrical concentration ratio will be decided by choosing the entry aperture area of the concentrator. In this work, five different concentration ratios of CCPC were chosen, and their optical performances were investigated. The selected concentration ratios are 2.9x, 4.0x, 6.0x, 8.3x and 9.0x.
The geometrical concentration ratio is given by the equation:

$$C_{geo} = \frac{Entry\ Area}{Exit\ Area} \tag{4.1}$$

In contrast to geometrical concentration, an effective concentration ratio is a term used after testing the concentrator, where this ratio should be less than the geometrical concentration ratio. The losses are due to many factors, such as the reflector material does not have an ideal surface reflectivity (ρ =1) and the imperfection of the geometry of the concentrator. Once the geometrical concentration ratio is selected, the half acceptance angle can be calculated.

The acceptance angle is another important parameter that needs to be considered. As discussed, the proper design of the concentrator will lead to the better performance of the system. The acceptance angle is the maximum angle that the incident rays entering inside the concentrator are reflected towards the receiver area. Where the incident angle of light is larger than the acceptance angle, the light can still enter the concentrator, but it will simply bounce back to the outside.

Figure 4.3 presents correlation between the half acceptance angle and the concentration ratios used in this study. It can be seen clearly from Figure 4.3 that the half acceptance angle decreases as the concentration ratio increases. A concentrator with lower concentration ratio has a larger half acceptance angle than that with a higher concentration ratio (e.g., they are 36° and 19.47° for 2.9x and 9.0x concentrators, respectively).

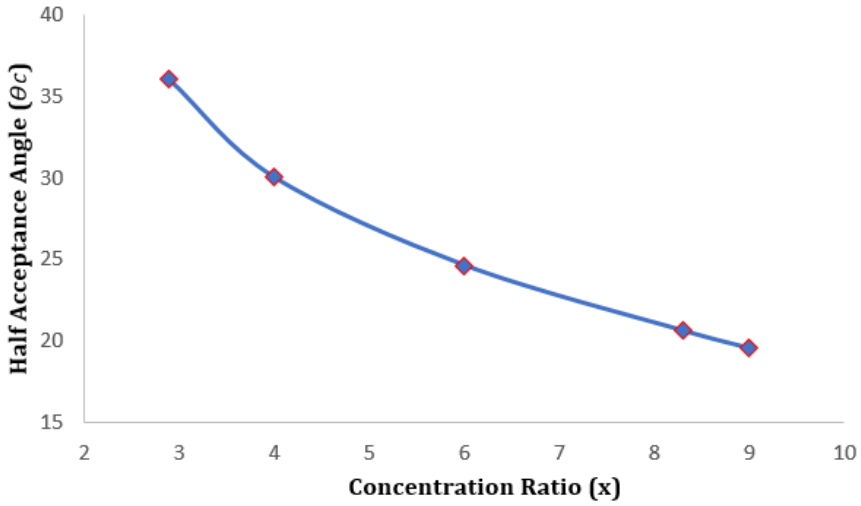

Figure 4.3: Calculated half acceptance angle trend for different concentration ratio.

The final procedure is to determine the height of the CCPC, which depends on the input area, output area and the half acceptance angle. A larger concentration ratio will result in a greater height and smaller angle of the concentrator [64].

To calculate the height of the CCPC, it is necessary to determine the focal point of the parabola, which can be calculated using equation,

$$f = a' (1+ \sin\theta_c) \tag{4.2}$$

where, a' is the absorber width and f is the focal point of the parabola curve. The height can then be derived by using equation [67],

$$h = \frac{f \text{ x } cos\ \theta_c}{sin^2\ \theta_c} \tag{4.3}$$

Table 4.1 lists the key design parameters for the five CCPCs, which were calculated using the procedures described above.

Table 4.1: Five concentrator design parameters.

CCPC parameters	2.9x	4.0x	6.0x	8.3x	9.0x
Exit area	10 mm x 10 mm				
Entry area	17 mm x 17 mm	20 mm x 20 mm	24.5 mm x 24.5 mm	28.4 mm x 28.4 mm	30 mm x 30 mm
Half acceptance angle	36.0°	30.0°	24.0°	20.6°	19.5°
Height	18.70mm	26.00 mm	38.60 mm	51.00 mm	56.00 mm

An Excel worksheet has been created to calculate the geometrical concentration ratio, the half acceptance angle and the height of the concentrator for any given entry aperture (Appendix B1).

4.2.2 Design Procedure in SolidWorks

Many tools can be used to draw the CCPC curve. The CCPC curve should be able to reflect all incidence light that falls at any point of the curve to the receiver ends. Many CCPC curves are available but not necessarily the perfect curve. If a designed curve is not correct, then optical losses will occur, and this will result in a poorly designed concentrator. The appropriate method employed to design the CCPC is in this study is discussed in detail in the following section.

4.2.2.1 Parabola Curve Equation

SolidWorks software is employed to create drawings for use by the 3D printer, as mentioned in Section 3.5. The reason for using the SolidWorks is that it is a popular and readily available software in Cardiff University, and it has the option of manually inserting a parametric equation of the parabolic curves using Equation Driven Curve (EDC) tap.

Prior to drawing a parabolic curve, the geometrical concentration ratio needs to be selected first using equation (2.7) described in Chapter Two. For example, to design a 4.0x concentrator in SolidWorks, two parameters should be entered to generate the

CCPC parabolic curve. The first parameter is the half acceptance angle expressed in radians, which is 0.5236 rad in this case. The second parameter is the receiver size in mm which is equal to 10 mm. The parabolic equation used in this study was proposed by Rincon et al. [183].

The coordinates x(t) and y(t) for plotting CCPC curves are given by:

$$x(t) = \frac{b\,(1+\sin\theta_c)\cos t}{1-\sin\,(t-\theta_c)} \tag{4.4}$$

$$y(t) = \frac{b\,(1+\sin\theta_c)\sin t}{1-\sin\,(t-\theta_c)} \tag{4.5}$$

where, b is the receiver size in mm, θ_c is the half acceptance angle of the concentrator, and t is a parameter that determines the curvature of the parabolic curve, which is related to half acceptance angle by,

$$t = \frac{\pi}{2} - \theta_c \tag{4.6}$$

where, π is equal to 3.1415. In case of 4.0x concentrator, the values inserted in SolidWorks for $t1$ and $t2$ are 0 and π/2 – 0.5236, respectively. After solving the parametric equation to plot the 4.0x parabolic curve, the next step is to create a new file in SolidWorks. To start the sketch, the front plane is selected as a drawing base plane for the design. Next, a drop list under Spline icon is clicked to select the Equation Driven Curve that both equation (4.4) and (4.5) are inserted. The parametric option is selected in SolidWorks to enter the x and y coordinates to generate a 4.0x CCPC as shown in Figure 4.4.

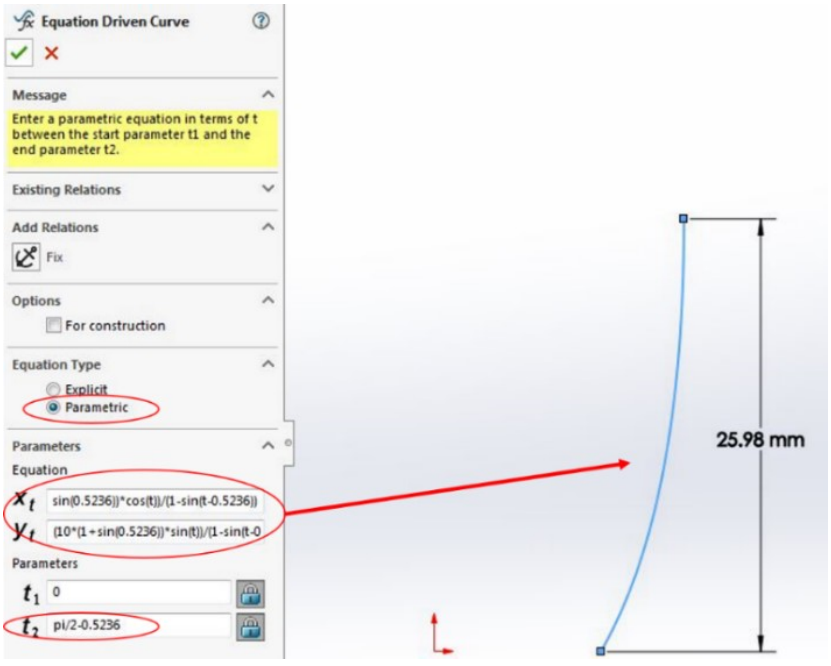

Figure 4.4: Illustration of 4.0x CPC curve created by using EDC in SolidWorks.

Once the equations are inserted in the specific block as shown in Figure 4.4, the software creates the CCPC curve. The CCPC curve will be displayed in the sketch section as shown in Figure 4.4 for 4.0x CCPC parabola. Then the centreline is used to draw a line between the curve focal point and middle of the receiver area, which represents the axis of the parabola. The next step is to duplicate this curve about the inserted centreline by using mirror feature to have a second curve as shown in Figure 4.5 (a). After having both left and right parabolic curves, the dimension of entry and exit area is taken to validate the equation 2.7 (Chapter Two) that provides the half acceptance angle of 4.0x CCPC as shown in Figure 4.5 (b).

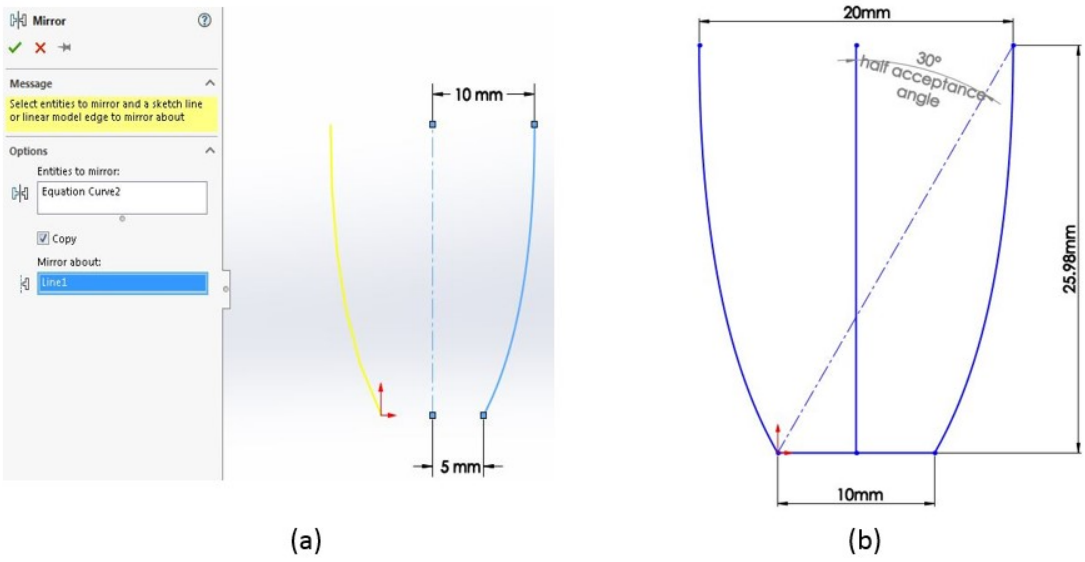

Figure 4.5: CCPC curve: (a) axis of parabola and mirror feature to draw the second parabola curve and (b) final 2D output of a 4.0x CPC design.

4.2.2.2 CCPC Design

A new sheet is created to convert the 2D design to obtain a 3D CCPC drawing. This is achieved by sweeping the CCPC curve along the four sides of the 2D concentrator, forming a three-dimensional shape, as illustrated in Figure 4.6. The design starts by creating two sketch planes: the first is for entry aperture with 20 mm x 20 mm (length x width) and the second sketch is for the exit aperture (receiver) 10 mm x 10 mm. The distance between the two sketches is the height of the parabolic curve, as shown by the step (1) of Figure 4.6. Then the parabolic curves created in Section 4.2.2.1 are copied and pasted into the newly created right and front plane, as shown by the step (2) of Figure 4.6. Now the parabolic curve is attached with the entry and exit apertures and the process of creating solid geometry remains to build the CCPC geometry. Step (3) in

Figure 4.6 represents the solid CCPC geometry after applying Lofted Boss/Base to the entry, exit and the four parabolic curves to form 3D CCPC shape. The last step in the design process is shown in step (4) of Figure 4.6, where the shell option is applied to the geometry to create a cavity and the thickness of the CCPC wall, which is set to 2mm to increase the rigidity of the concentrator. This thickness is applied to all of the concentrators used in this project.

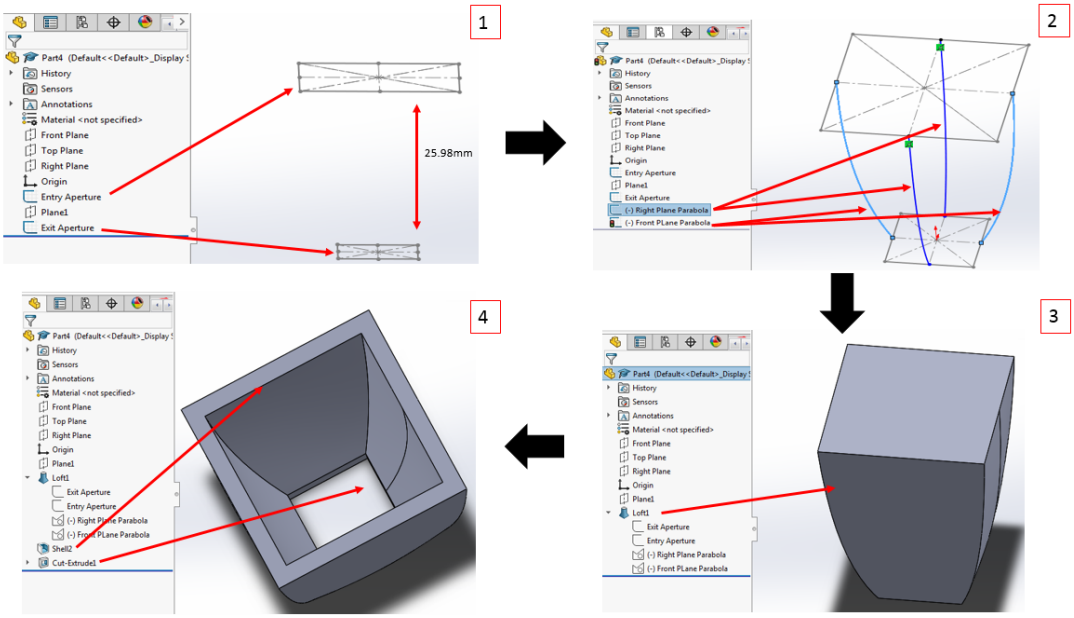

Figure 4.6: Design process for CCPC geometry.

A concentrator base is required to attach the CCPC securely to the rotary stage for testing. The dimension of the base was discussed in Section 3.5.2 because it is designed to match with the DCB ceramic. A modification was made to the base to include a terminal hole that was made to allow proper lay of solar cell wires and to avoid overstressing them. All the simulated results shown in this work were carried out for both of the CCPC concentrator and the base, which is printed as one part. Figure 4.7 illustrates the main parts of the designed system.

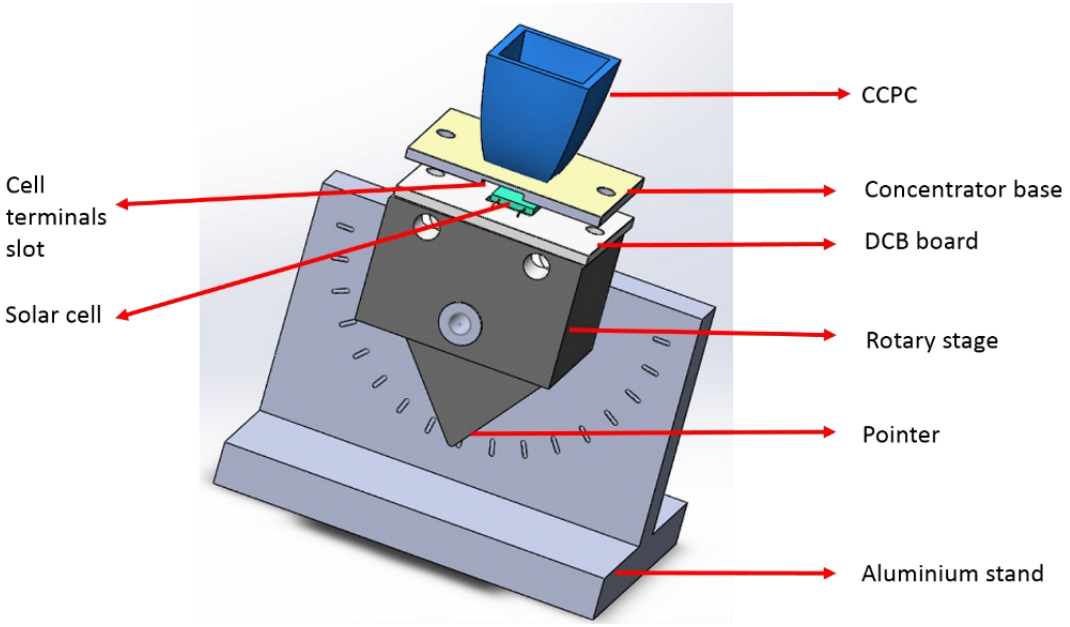

Figure 4.7: Assembly of the concentrator testing system with the main components.

The thickness of the base is the same as the thickness of the CCPC concentrator, which is 2 mm for all of the designed geometries. The mating feature has been used to join the base and the concentrator parts to form one part. Once the parts are assembled, the file is saved in STEP AP214 (.step) format to be exported and opened by the ray-tracing software which will be discussed in the following section.

4.3 Optical Modelling of the CCPC

TracePro simulation is used to provide the optical evaluation for the designed CCPC concentrators. This step is important because it checks the designed concentrators and ensures that the design requirements are met before fabrication. The optical efficiency of the concentrator is crucial because it is a measure of the quality of the concentrator [184]. TracePro is a powerful simulation tool that is based on the Monte-Carlo method to predict the ray's directional performance and the optical efficiency [185]. The ray-tracing study offers information on the optical ray behaviour inside the concentrator, actual concentration ratio, optical efficiency and flux distribution. Figure 4.8 shows the flowchart, indicating the steps followed in carrying out the optical ray-tracing simulation for the CCPC and other concentrators using TracePro.

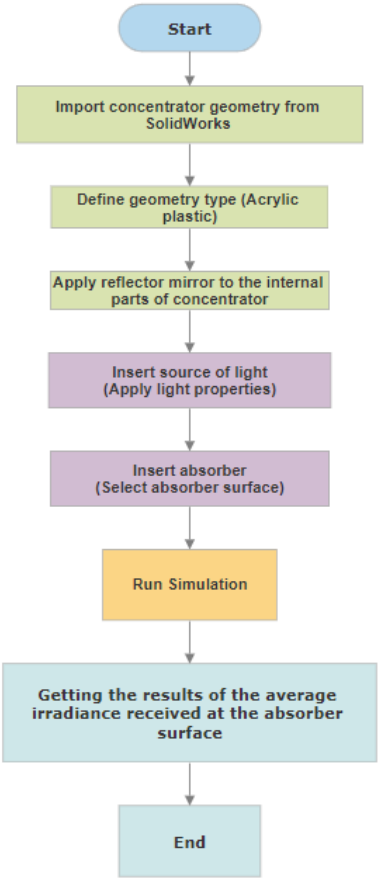

Figure 4.8: Flowchart of the steps of concentrator simulation.

4.3.1 Ray-tracing Parameters

A number of parameters must be input in TracePro to carry out the simulation. The material type selected for the concentrator body is acrylic plastic, which is the material used by the 3D printer in the laboratory. The internal surface of the concentrator is covered with a highly reflective mirror. The software provides two types of default reflectors: the perfect mirror and mirror, which have the specular reflectance of 100% and 95%, respectively. In addition, a variety of reflectors from several companies are also available. In this work, the reflector used is the *alanod* aluminium foil, which is not listed in the software. The *alanod* reflector has a specular reflectivity of 0.95, which indicates that 95% of the incident rays will be reflected and 5% of the rays absorbed by the reflector material (see Appendix B2). Once the material property is identified, the source of light is created and set to 1000 W/m^2. The simulation was carried out using a total number of rays of 10,000, with normal to surface angular distribution as shown in Figure 4.9 (a). Table 4.2 lists a comparison of a different number of rays generated for simulation of 4.0x CCPC and the corresponding simulation results collected from the receiver surface. It can be seen from Table 4.2 that 10,000 rays have a reasonable

execution time of 7 seconds compared to 12 minutes required by 1,000,000 rays, with little difference in the average flux and optical efficiency for both simulations of using a different number of rays.

Table 4.2: Comparison of the different generated number of rays to the 4.0x CCPC optical performance.

No. of rays	Execution time (min: sec)	Average flux (W/m^2)	Optical efficiency ($\eta_{optical}$)
100	0:1	3815.8	92.77
1000	0:5	3779.6	92.88
10000	0:7	3784.9	93.01
100000	1:14	3785.1	93.02
1000000	12:01	3785.5	93.03

Another essential step is to insert a block that acts as a receiver detector with a perfect absorber surface to ensure the collection of most of the rays. Once the simulation starts, the rays produced by the source strikes the surface of the concentrator and are reflected to the receiver area. The wavelength of the rays is set to 0.5461 μm because this number represents the mean value of the solar spectrum. Figure 4.9 (b) shows the light path of the CCPC using the ray-tracing simulation. It can be seen from Figure 4.9 (b) that the rays are reflected and concentrated to the received surface once they hit the CCPC's surface.

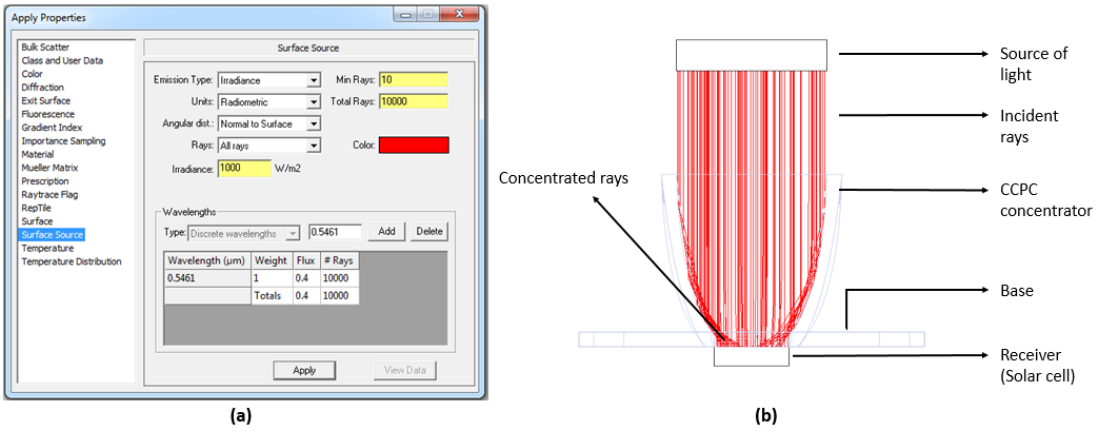

Figure 4.9: TracePro simulation: (a) light source parameters and (b) CCPC under light simulation.

4.3.2 Evaluation of the CCPC Concentration Ratio

The evaluation of the CCPC concentration ratio is the initial step to be carried out before any further investigation. This evaluation will determine how far the designed concentrator is from the original geometrical concentration ratio. The evaluation process in TracePro starts by ensuring the amount of power collected by the receiver

surface without concentrator is 1000 W/m², which is the same amount of power produced by the light source. Figure 4.10 shows the two cases of the ray-tracing simulation for the CCPC concentration ratio (a) without and (b) with the concentrator. It can be seen from Figure 4.10 (a) that the power intensity received by the collector without the concentrator shows an average intensity of 1000 W/m² which is the same as the intensity produced by the light source. Whereas Figure 4.10 (b) illustrates the case with the concentrator between the light source and the receiver surface, where the rays are reflected and concentrated at the receiver end.

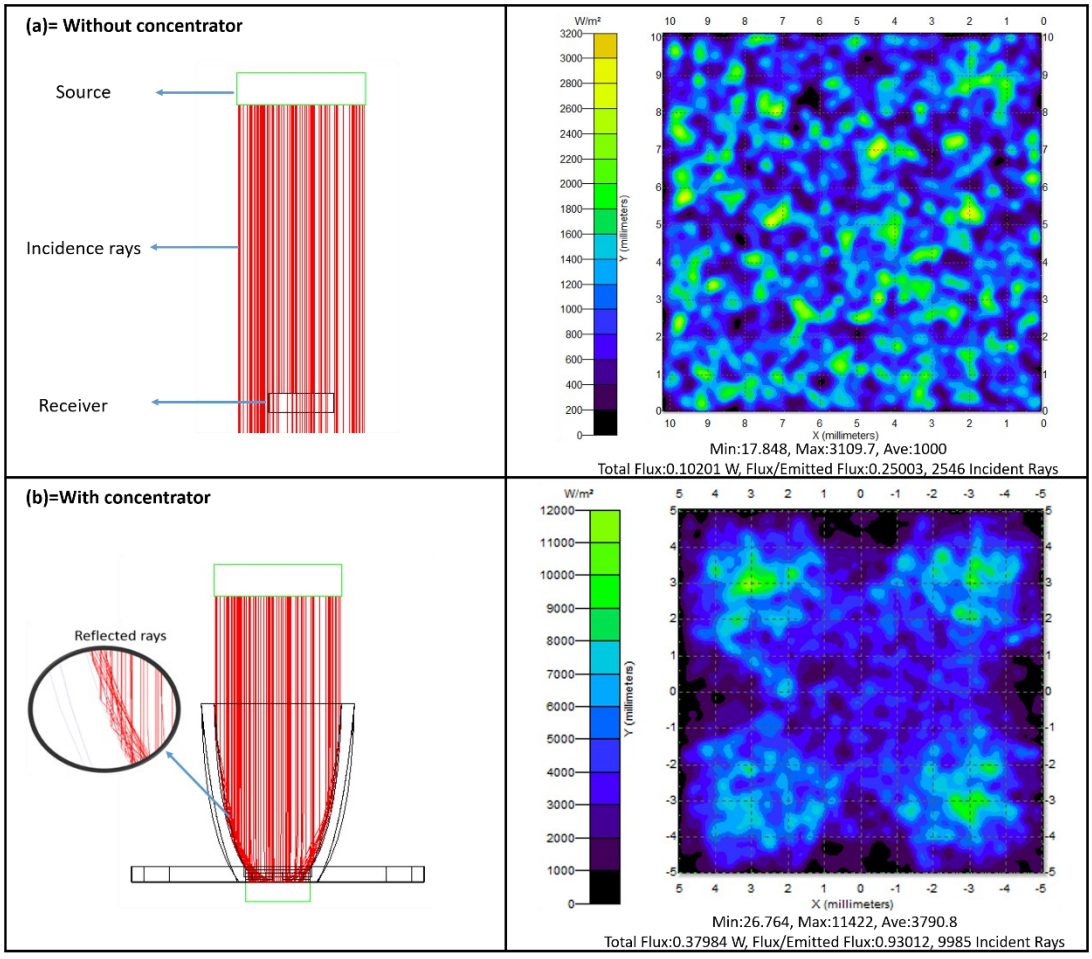

Figure 4.10: 4.0x CCPC evaluation with mirror reflector at two cases: (a) without concentrator and (b) with concentrator at 1000 W/m² irradiance.

The results of simulation show that the average illumination at the receiver surface of the 4.0x CCPC is 3790 W/m² compared to 1000 W/m² collected at the receiver surface when there is no concentrator. The simulated concentration ratio for the 4.0x CCPC can be calculated using the equation below,

$$CR = \frac{Average\ power\ with\ concentration}{Average\ power\ without\ concentration} = \frac{3790}{1000} \simeq \mathbf{3.8x} \qquad (4.7)$$

Comparing the simulated concentration ratio with the designed geometrical concentration ratio of the 4.0x CCPC, it is found that a loss of 5% occurred, which is arises because the mirror reflector has a surface reflectivity of 95%. The power obtained from the simulation is a light power and to compare these results with the experimental results which are electrical power, the cell efficiency should be taken into consideration. All of the simulated results are multiplied by 10% which is equivalent to the average efficiency of a silicon cell used in this work.

Figure 4.11 shows the 3D energy profiles of the concentrator with (a) a mirror of the reflectivity ρ =0.95 and (b) a perfect mirrors of the reflectivity ρ =1. The concentrator using the perfect reflector shows a good agreement with the geometrical concentration ratio because the average illumination obtained from the simulation is 3995.2 W/m^2. The results indicate that the parabolic curves created by the above-mentioned design procedures produce the expected results.

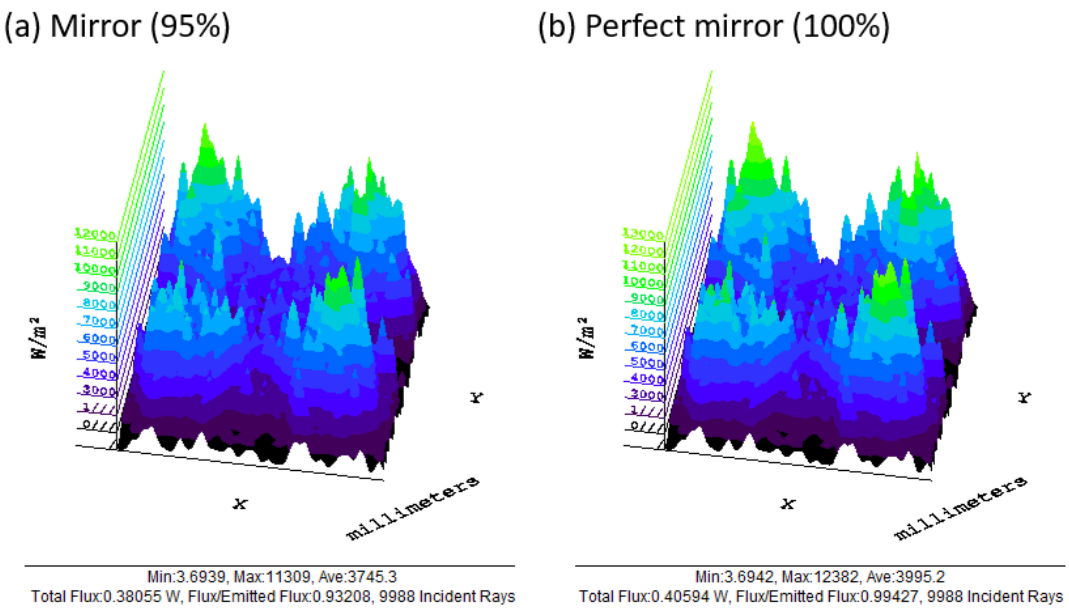

Figure 4.11: 3D view of 4.0x CCPC: (a) with a mirror reflector and (b) with perfect mirror reflector.

It can be seen from Figure 4.11 that the high intensity appears at the corners of the CCPCs receiver because it represents the focal point of the parabolic curves. It is to be noted that these high peaks increase with an increase in the reflectivity of the reflector surface. The average flux intensity appears in the irradiance map is 3995.2 W/m^2 for the case using the perfect mirror, compared to the average flux intensity of 3745.3 W/m^2 for the case using a mirror with a reflectivity of 95%. The optical efficiency of 4.0x CCPC is 99.4% using a perfect mirror compared to 93.2% after applying the non-perfect reflectors.

Although there is no huge difference in the flux distribution between the two types of mirror reflectors; however, the slight difference in the power output can be noticed. It can be seen from Figure 4.11 that the perfect mirror has more power output over a lower reflectivity surface. This demonstrates that the specular reflection of the reflector used has a major impact on the output power of the concentrator.

4.3.3 Simulation Results

The simulation results provide three main parameters that are useful for comparison with the experimental results. These parameters are the power collected at the receiver, optical efficiency and flux distribution. The optical efficiency (η_{optical}) of the CCPC concentrator was calculated according to the equation below [186]:

$$\eta_{\text{optical}} = \frac{\emptyset\, exit}{\emptyset\, entry} \tag{4.8}$$

where, $\emptyset\, exit$ is the flux reached at the exit aperture of the concentrator and $\emptyset\, entry$ is the flux enters at the entry aperture. The optical efficiency is automatically determined in TracePro simulation, and the results are displayed below the irradiance map that follows the term "Flux/Emitted Flux" in Figure 4.12.

The receiver surface is attached to the bottom of the CCPC, which is the exact location of the solar cell that was placed under the concentrator during the tests. Figure 4.12 shows the irradiance maps at (a) the focal plane of the 4.0x CCPC and (b) 2 mm below the focal plane, respectively. As mentioned in the CCPC design section of this chapter, because the thickness of the concentrator is 2 mm, the receiver surface (i.e., solar cell) is actually located at the 2 mm below the focal plane of the concentrator as shown in Figure 4.12 (b).

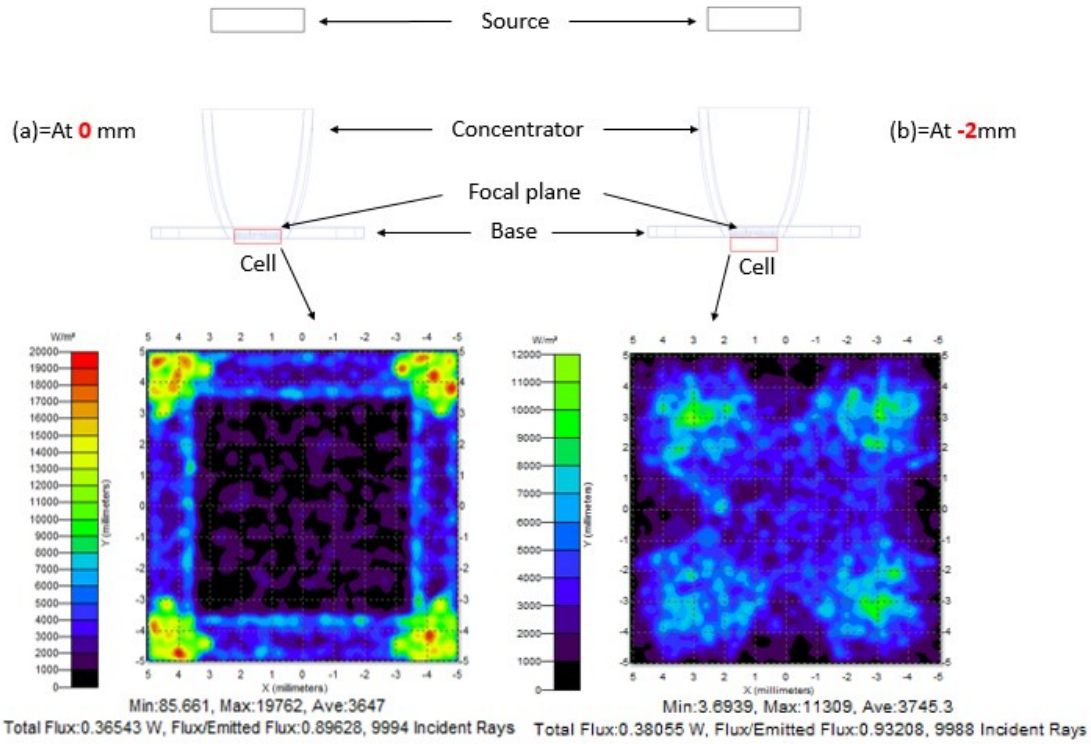

Figure 4.12: Receiver location under the CCPC concentrator: (a) at 0 mm and (b) at -2 mm.

The difference in light distribution between the two detector positions can be seen clearly from Figure 4.12. In the case of placing the detector at the focal plane (0 mm), the flux appears to be concentrated more at the four corners and hotspots (in red) occur. It can be seen from the irradiance bar that the flux can reach up to 20 times the flux of the incident rays. A low amount of flux is also collected at the centre of the detector. The optical efficiency and the electrical power output from solar cell (assuming 10% conversion efficiency of the solar cell) in this case are 89.6% and 36.5 mW, respectively. Whereas, when the detector is placed at 2 mm below the focal plane the flux appears to be more uniform than the previous case and the maximum flux can reach up to 12 times the flux at the incident rays. The optical efficiency and the power output obtained at 2 mm below the focal plane are found to be higher than that at the focal plane, which are 93.0% and 38.0 mW, respectively. The average flux received at the receiver surface for both focal plane and 2 mm below focal plane are 3647 W/m^2 and 3745 W/m^2, respectively. Although the flux distribution in this case is better than that from the focal plane, the flux distribution is uneven and this may affect the solar cell's efficiency. The concentrated flux has to be uniformly distributed across the receiver surface to deliver high cell performance. The flux uniformity across the receiver's surface will be investigated intensively in Chapter Five.

The simulation was carried out for the five concentrators to obtain their optical efficiencies. Table 4.3 lists the results of simulation for the solar cell placed at 2 mm below the focal plane and with light incidence at an angle normal to the plane.

Table 4.3: Simulated results for the five CCPC concentrators at 0° incidence angle.

CCPC (C_g)	Concentration ratio (C_r)	Optical efficiency ($\eta_{optical}$)	Entry aperture (mm)	Exit aperture (mm)	Total flux (mW)
2.9x	2.75	93.85	17 x 17	10 x 10	27.63
4.0x	3.78	93.01	20 x 20		38.00
6.0x	5.60	92.05	24.5 x 24.5		56.07
8.3x	7.51	91.38	28 x 28		75.33
9.0x	8.32	90.51	30 x 30		83.29

It can be seen from Table 4.3 that the optical efficiency decreases as the geometrical concentration ratio increases. This can be attributed to the fact that the optical losses increase with an increase in the height of the concentrator.

4.4 Fabrication and Testing of the Reflective CCPC

The fabrication process of the reflective CCPC concentrators was carried out using 3D printing technology, as discussed in Section 3.5.1. Three types of reflectors were compared to select the best reflector for use in this work. The details of this comparison are given in the reflector types section.

4.4.1 Acrylic Plastic CCPC

The steps of printing the concentrators were discussed earlier in section 3.5.1. Once the concentrator is printed using the Form +1 3D printer, the concentrator is kept dry before applying the reflector inside the internal surface of the concentrator. The process of applying the reflector material is applicable to other types of reflector material. An example of applying *alanod* aluminium reflector (Alanod GmbH, Germany) is illustrated. The steps are as follows:

- **Print out the shape of the parabola**

In SolidWorks software, print the 2D cross sectional CAD drawing of the concentrator in normal A4 paper size to a scale 1:1. This ensures that the printed drawing and marked parabola lines are consistent in size. The printed drawing can be seen in Figure 4.13.

- **Cut the printed paper along the marked parabola lines**

The printed parabola shape is then cut along the marked parabola lines. This process is repeated four times for the four parabola sides.

- **Stick the paper in an aluminium reflector**

The printed parabola shape is then attached to the backside of the aluminium reflector and the reflector is cut to match the printed drawing.

- **Apply the reflector inside the CCPC**

The final step is to apply “super glue” onto the backside of the aluminium reflector and the internal part of CCPC. Then, stick the four reflectors inside the CCPC interior surface. Figure 4.13 shows the process of applying aluminium reflector to the interior part of the printed CCPC concentrator.

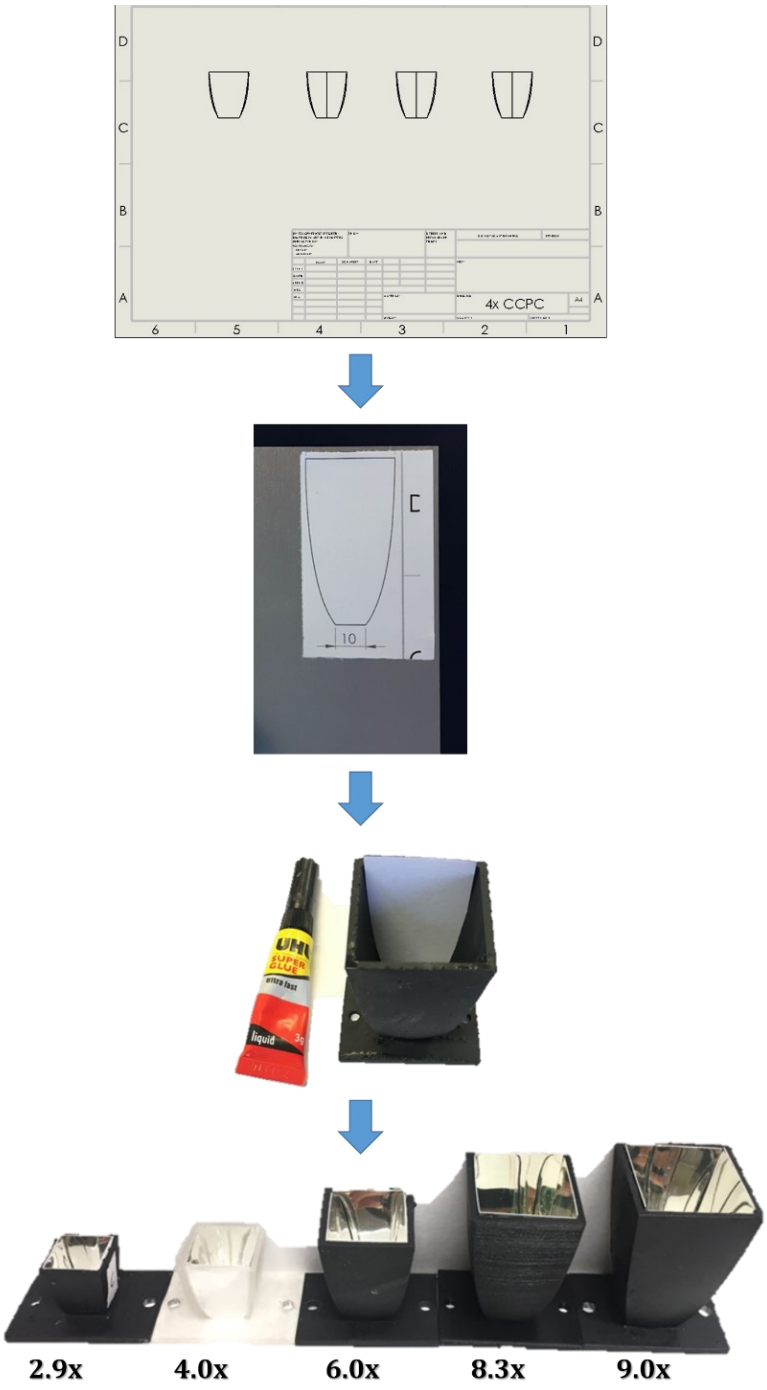

Figure 4.13: Steps of applying aluminium reflector in the internal surface of CCPC.

4.4.2 Reflector Types

The reflector material used for the CCPC concentrator plays an important role in ensuring that the efficiency of the concentrator is not reduced. To investigate the reflector impact on the overall concentrator performance, three commercial reflectors were used and compared to determine the outcome. The materials used in this study are 3M aluminium foil [187], adhesive aluminium reflector [188] and an *alanod* MIRO high-reflection sheet [189]. Figure 4.14 shows photographs of the three tested reflectors.

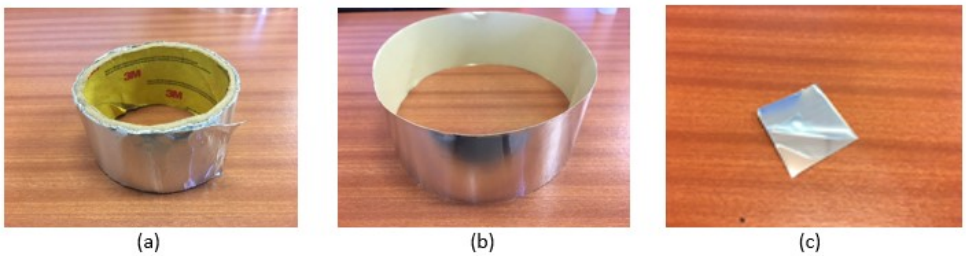

Figure 4.14: Different reflector types used: (a) 3M aluminium foil, (b) adhesive reflector tape and (c) *alanod* reflector sheet.

The reflectivity of the 3M aluminium foil and the adhesive aluminium reflector are not available from the manufacturers. Although the 3M aluminium foil seems to have a specular finish, its main drawback lies in the difficulty of applying the reflector to the CCPC's inner surface. This reflector is very soft, which can easily cause wrinkles when applied inside the concentrator, and this impedes the rays being reflected towards the cell. Meanwhile, the adhesive reflector tape is easier than the 3M foil when applied to the concentrator, but it does not have as good specular finish as the 3M aluminium foil. The three reflectors were applied to the inner surfaces of the 4.0x CCPC concentrators using the same procedure with maximal care. They were then tested under the standard testing condition described in Section 3.2.3. Figure 4.15 shows the I-V and P-V results for the three different reflectors.

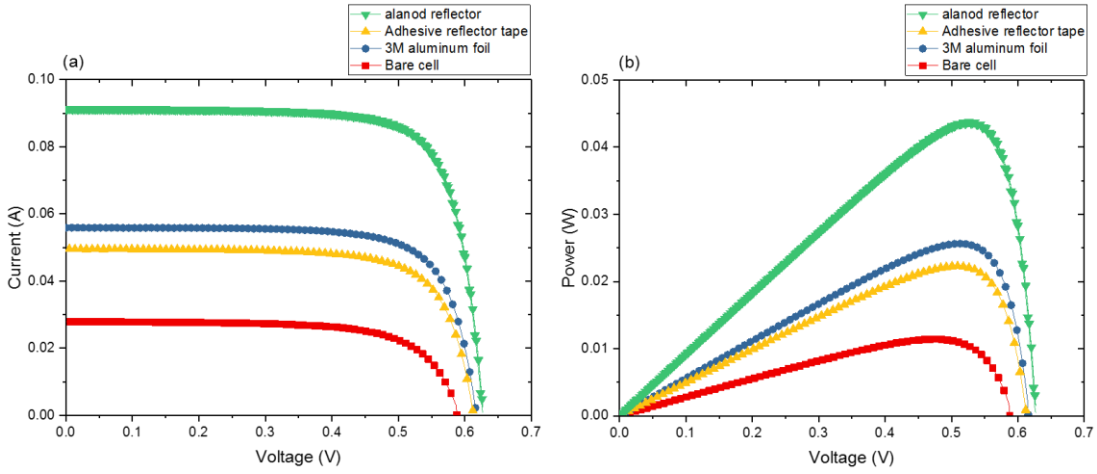

Figure 4.15: Comparison of the three tested reflectors: (a) I-V curves and (b) P-V curves.

It can be seen from Figure 4.15 (a) that the short-circuit current (I_{sc}) of the concentrator using *alanod* reflector is 0.090 A, while they are 0.055 A and 0.050 A for the 3M aluminium foil and adhesive reflector, respectively. Similarly, in Figure 4.15 (b) the maximum power output of the 4.0x CCPC using the *alanod* reflector is 0.045 W, which is

significantly higher than those using the 3M foil and adhesive reflector (0.026 W and 0.023 W, respectively). The drop in the maximum power output is about 42.2% when the 3M foil is used instead of *alanod* aluminium reflector. The optical efficiency decreases with a decrease in the reflectivity of the material used (adhesive reflector) and with the fabrication process (3M foil). Clearly, an appropriate selection of the reflector materials has significant influence on the optical efficiency of the fabricated concentrators. Based on the results, the *alanod* reflector has been selected to construct the acrylic CCPCs that were employed for the other studies in this project. In addition, this reflector has a constant reflectivity of 95% at different Angles of Incidence (AOI). Figure 4.16 shows the reflectivity of the *alanod* reflector as a function of wavelength for different AOIs [189].

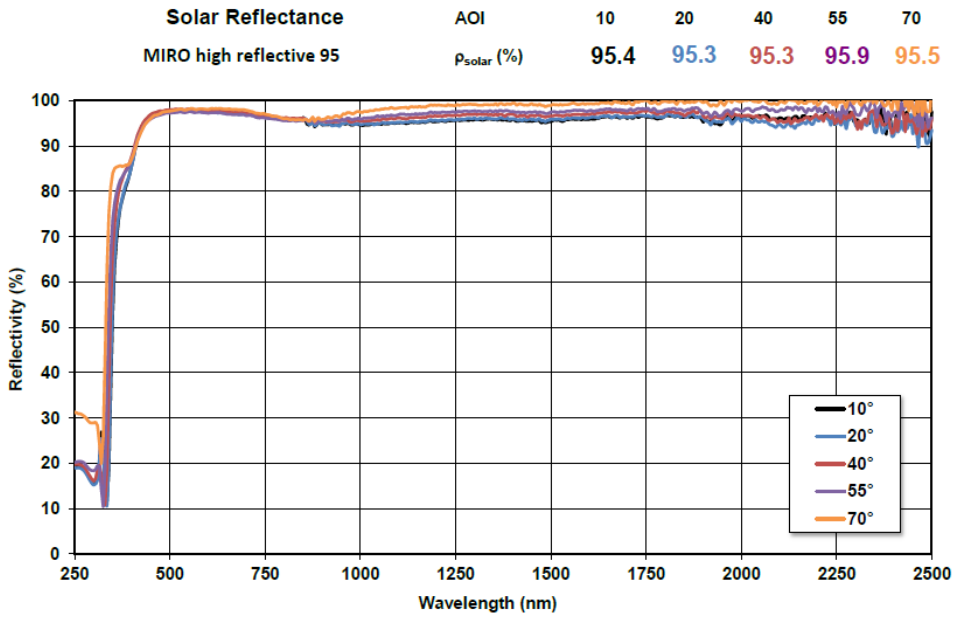

Figure 4.16: Miro film reflector as a function of wavelength [189].

4.4.3 Experimental Results of the Reflective CCPC

The testing of the fabricated concentrators was carried out and the electrical power output of the silicon solar cell was measured without and with the concentrator. The following steps were used to obtain the experimental results:

1- The solar simulator was switched on and a warm-up period of at least 20 minutes followed prior to starting the experiment to achieve a steady illumination of light across the illumination area.

2- Once the solar simulator was warmed up, the Solar Survey (apparatus for light intensity measurement) was switched on and placed in the middle of the light illumination area. Then, the solar simulator distance from the Solar Survey screen was adjusted until the Solar Survey displayed a reading of 1000 W/m^2.

3- The distance that corresponds to 1 sun between the solar simulator and the Solar Survey was measured using a ruler and the solar cell was placed at the same distance as measured from the solar simulator.
4- A thermocouple was attached near the solar cell to monitor the temperature of the solar cell and ensure to be remained at 25 °C.
5- The +Ve and -Ve terminals of the solar cell were connected to the inputs of the Autolab to obtain the I-V curves.
6- NOVA software was opened and the control screen of the Autolab was used to monitor the V_{OC} readings. The initial value of the open-circuit voltage (V_{OC}) was inserted into the Autolab procedure and the start button was clicked to generate the I-V curves of the solar cell.
7- Once the I-V curve was obtained, the data was exported and stored in an Excel sheet. Then, the simulator attenuator shutter was turned off.
8- The concentrator was placed on the top of the DCB ceramic and secured to it by screws to ensure the same 1 sun distance from the solar simulator to the entry aperture of the concentrator.
9- Steps 6 to step 7 were repeated to obtain I-V curves of the solar cell with the concentrator. The measurements were carried out three times for each test to ensure repeatability of the experiment and an average result is presented.

The simulated optical efficiency produced by TracePro was compared with the experimental optical efficiency. The experiment concentration ratio (C_{exp}) is obtained by dividing the short-circuit current of the solar cell with a concentrator ($I_{sc}\ with\ concentration$) by the short-circuit current of the bare cell ($I_{sc}\ without\ concentration$),

$$C_{\exp} = \frac{I_{sc}\ with\ concentration}{I_{sc}\ without\ concentration} \tag{4.9}$$

While the experimental optical efficiency ($\eta_{Exp,optical}$) is determined by dividing the experimental concentration ratio ($C_{\exp}$) by the geometrical concentration ratio (C_{geo}) multiplied by 100,

$$\eta_{\mathrm{Exp},optical} = \frac{C_{\exp}}{C_{geo}} \text{ x } 100 \tag{4.10}$$

where, C_{geo} is the geometrical concentration ratio defined in Section 4.2.1.

The same solar cell needs to be used for the tests with and without the concentrator. Also, the distance between the solar simulator and the concentrator has to be adjusted to ensure that an irradiance of 1000 W/m^2 is obtained at the entry aperture of the concentrator. Moreover, the temperature of the solar cell should be maintained at 25° C

because a variation of the cell's temperature leads to a change in the I_{sc} and V_{oc} . Figure 4.17 represents (a) I-V and (b) P-V curves for the five CCPC concentrators and the bare cell.

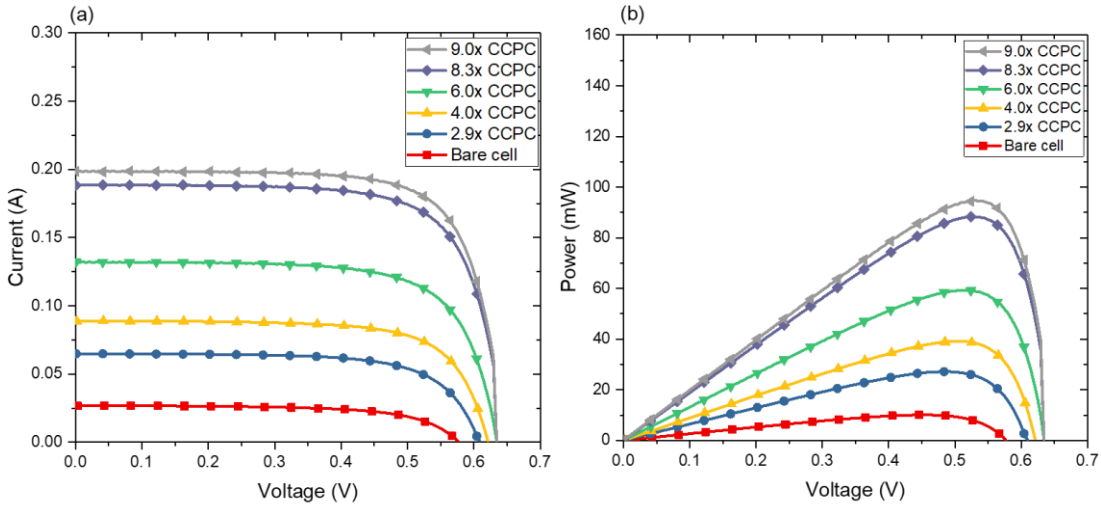

Figure 4.17: Solar cell characteristics under five CCPCs concentrator: (a) I-V curves and (b) P-V curves.

The short-circuit current of the solar cell under one sun condition (without concentrator) is 0.0270 A, which increased to 0.089 A using 4.0x CCPC. This gives an experimental concentration ratio of 3.33x and an optical efficiency of 83.0% ± 0.5% for the 4.0x CCPC, which has a geometrical concentration ratio of 4 times, as originally designed. The experimental optical efficiency is about 10% lower than the simulated optical efficiency of (93%). All five fabricated concentrators were investigated in detail. Figure 4.18 and Table 4.4 display the performances of the silicon cell as a function of different concentration ratios.

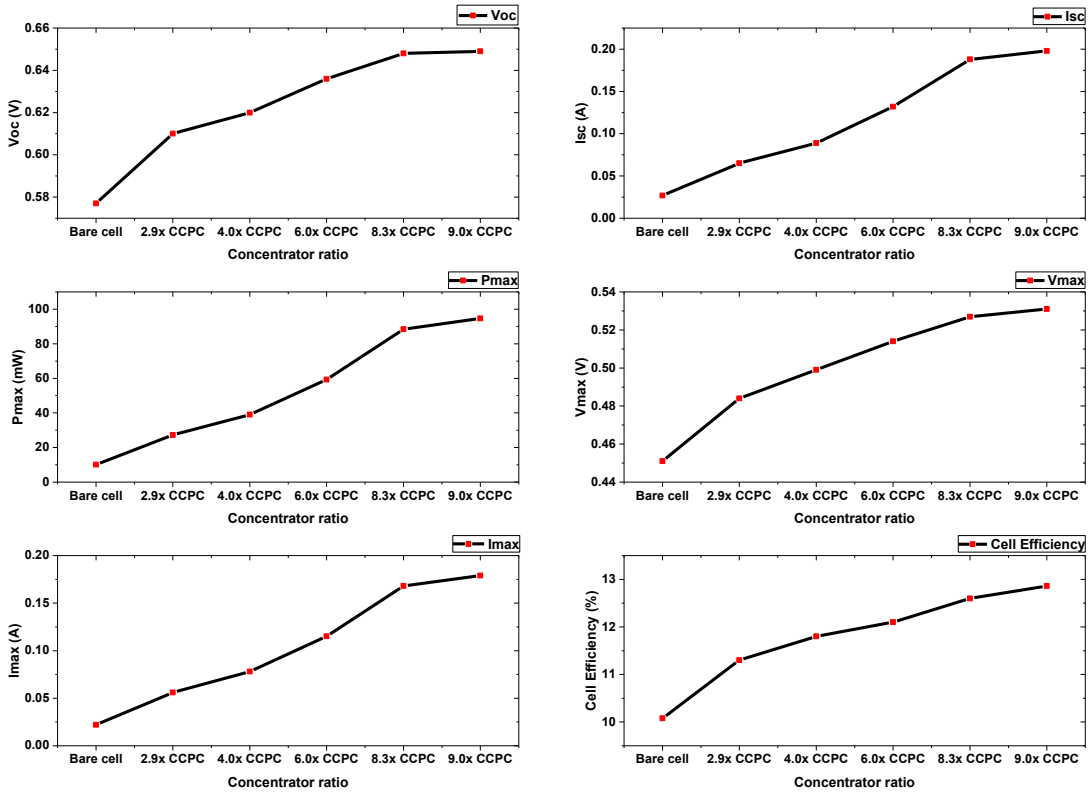

Figure 4.18: The cell parameter trends for the five CCPC concentrators.

It can be seen from Figure 4.18 that all of the cell parameters are improved with an increase in the concentration ratio. It can be seen from Figure 4.18 that the Voc curve show a slight variation with different concentration ratios. This is due to a slight difference in the cell temperature as the test was carried out in different days which make it very challenging to maintain the same water flow and temperature. The results from this work provide clear experimental evidence that the performance of photovoltaic system can be enhanced with concentration.

The deviation between the optical simulation and experimental results can be calculated by using the equation below [190]:

$$Dev\ (\%) = \left|\frac{EXP-SIM}{EXP}\right| \text{ x } 100 \qquad (4.11)$$

The deviation was calculated for the normal angle of incidence and the results are presented in Table 4.4.

Table 4.4: Experimental characteristics of five CCPCs under 1 sun illumination at normal incidence (0°).

CCPC ratio (x)	I_{sc} (A)	V_{OC} (V)	FF (%)	Cell efficiency (%)	Power (mW)	Actual optical efficiency (%)	Deviation in optical efficiency (%)
Bare Cell	0.027	0.577	65.0	10.1	10.1	-	-
2.9	0.065	0.610	68.7	11.3	27.2	83.5	12.4
4.0	0.089	0.620	69.7	11.8	39.0	83.0	12.1
6.0	0.132	0.636	70.7	12.1	59.3	82.0	12.3
8.3	0.188	0.648	72.0	12.6	88.4	84.5	8.1
9.0	0.198	0.649	73.0	12.8	94.7	82.0	10.4

The maximum optical efficiency of 84.50% was recorded for the 8.3x CCPC. The exit aperture of this concentrator was shrunk after the printing process and measured first by ruler and then using Coordinate Measuring Machine (CMM) to measure the exact dimensions of the exit aperture which found to have an area of 9.92 mm x 9.84 mm (Appendix B3). Consequently, the geometrical concentration of this concentrator becomes 8.3x. The concentrator was designed to have a geometrical concentration of 8.0x, but it ended up with 8.3x.

The optical efficiencies differ from one concentrator to another slightly and this is likely due to the manual method of applying the reflectors to the CCPC inner surfaces. It is to be noted that these in-house fabricated concentrators achieved higher optical efficiency compared to those reported in the literature (see Table 2.1). To my knowledge, the maximum optical efficiency for the same type of concentrators was reported to be 80% [104]. The results in Table 4.4 show the concentrators developed in this work represent the highest optical efficiency of the CCPCs known to date. It can be seen from Table 4.4 that I_{sc}, V_{OC} and FF are increased as the concentration ratio increases. This increase leads to an increase in the power output of all the concentrators compared the power output of the bare cell. For example, the 9.0x CCPC show a significant increase in the short-circuit current by 7.4 times compared with the bare cell. The open-circuit voltage was also increased from 0.578 V to 0.650 V. In addition, the FF increased from 65% to 73%. The FF for monocrystalline silicon is around 80% as per the manufacturer datasheet [82] under concentration, where the cell used in this research is found to vary from 65% to 67% under 1000 W/m^2, as discussed in Section 3.2.3. This leads to a significant increase in the power output of the solar cell with concentration, even though the actual optical

concentration ratio is only 7.4x due to various optical losses. It can be seen from Figure 4.17 (b) and Table 4.4 that the power output of 9.0x CCPC is 9.4 times higher than that of the bare cell (i.e., > geometrical concentration ratio). These results indicate that the gain in the power output due to concentration has over-compensated the optical losses in the concentrator because of increase in I_{sc}, V_{OC}, and FF with the concentration. This provides further evidence of the benefit of using concentrated solar power systems.

4.5 Fabrication and Testing of the Coated CPC

Another type of CPC concentrator was designed, constructed and experimentally tested. The 3D CPC is formed after rotating the 2D parabola curve around the concentrator axis (an imaginary midline which intersects the half of the absorber). The result of this revolving operation is a 3D CPC that has a circular entry and circular exit. Because silicon cells are commonly supplied in a square shape, this brought an idea of investigating a circular CPC entry with a square exit that fits with the silicon monocrystalline solar cell with a size of 10 mm x 10 mm. This unique modification on the original CPC design was fabricated and tested to compare the power output and the optical efficiency between the circular and square concentrators. This investigation will explore if there are any advantages of the circular CPC over the CCPC type. Figure 4.19 illustrates the CAD design of the CPC with the circular entry and square exit aperture. The parabolic curve of this concentrator has been taken from Edmund CPC design which available online [191]. This CPC is designed to have a geometrical concentration ratio of 7.0x and it was designed in the earlier stage of this project before designing the square CPC. The consideration of employing this type of the geometry is considered because this shape can be readily fabricated using lathe machine tools.

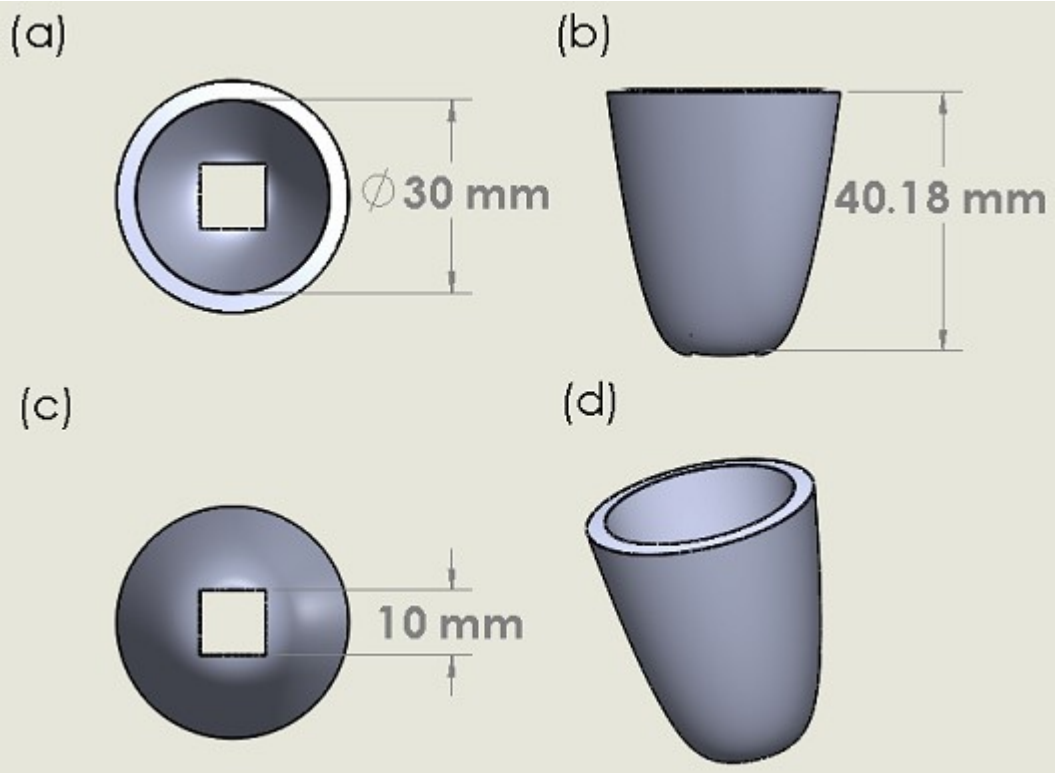

Figure 4.19: CAD design views of the 3D CPC concentrator shape and dimension in mm: (a) top view, (b) right view, (c) bottom view and (d) isometric view.

The area of the entry aperture of the circular concentrator is given by,

$$A_{\text{entry}} = \pi r^2 \tag{4.12}$$

where, r is the radius of the entry area of the circular CPC and π is 3.1415. The geometrical concentration ratio of this CPC is determined by,

$$C_{\text{geo}} = \frac{A_{\text{entry}}}{A_{\text{exit}}}$$

After designing the concentrator in SolidWorks, the CAD file of the CPC is exported to TracePro software for optical study of the concentrator.

4.5.1 Simulation Study of Circular CPC

Following the same process of simulation described in Section 4.3, the circular CPC is optically analysed and evaluated. This design differs from that of the CCPC as its exit area was cut to a square shape instead of a normal circle exit. This cut affects the performance of the concentrator and leads some incident rays to be reflected away from the receiver outside the CPC as shown in Figure 4.20.

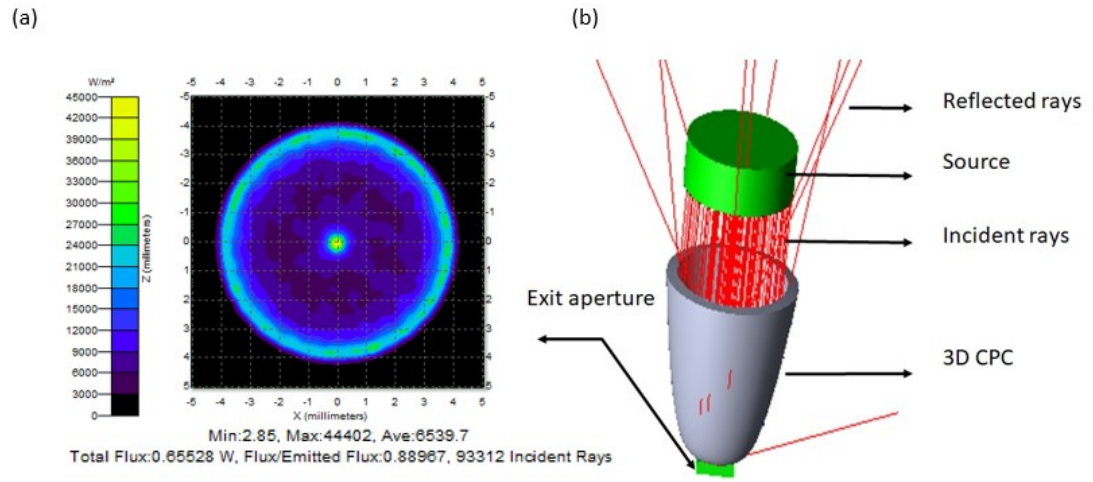

Figure 4.20: 3D CPC simulation: (a) irradiance map for the exit aperture and (b) the ray-tracing of the 7.0x CPC concentrator.

In TracePro software, a circular object has been inserted as a source surface for the 7.0x CPC with the same diameter of the entry aperture of the concentrator. Although the exit aperture of the circular concentrator is square, the irradiance map shows a circular flux intensity distribution. This is due to the circular curvature of the concentrator which is different from the CCPC that has four corners as explained by Cooper et. al. [142].

The optical evaluation process that was used in Section 4.3.2 is followed with the 7.0x circular design. The simulation shows that the design has a concentration ratio, optical efficiency and power output of 6.5x, 88.9% and 65 mW, respectively. The uniformity distribution of light in the circular 7.0x concentrator shows a circular image of the entry aperture, and no light is received at the corners of the detector surface. From the simulation, it can be seen that the circular design suffers from non-uniform distribution flux at the receiver's surface.

4.5.2 Coating of the CPC

It was found that applying an aluminium reflector to a circular CPC is much more difficult due to internal curvature and the size of the aluminium reflector. Consequently, the coating appears to be the only viable solution for this type of concentrators. For this particular design, a CNC machine (described in Section 3.5.2) was used to fabricate the concentrator to have a fine and smooth finish prior to the coating stage. After machining, the fabricated aluminium concentrator was sent to CIR Electroplating [192] for gold plating. The gold plating was employed to produce a specular surface. The concentrator was polished, zincated, copper flashed, silver-plated and finally gold plated (0.5 microns, 23ct). Figure 4.21 shows the CPC before and after coating. The CPC concentrator was

then experimentally investigated using a silicon solar cell to validate the simulation results. The two concentrators were tested under STC and the I-V and P-V curves were obtained to identify the difference between the coated and not coated concentrator (Appendix B4). The maximum power output (P_{max}) obtained for the non-coated concentrator at normal incidence is 33.7 mW (about 60%) of that obtained with the coated concentrator which found to be 55.4 mW.

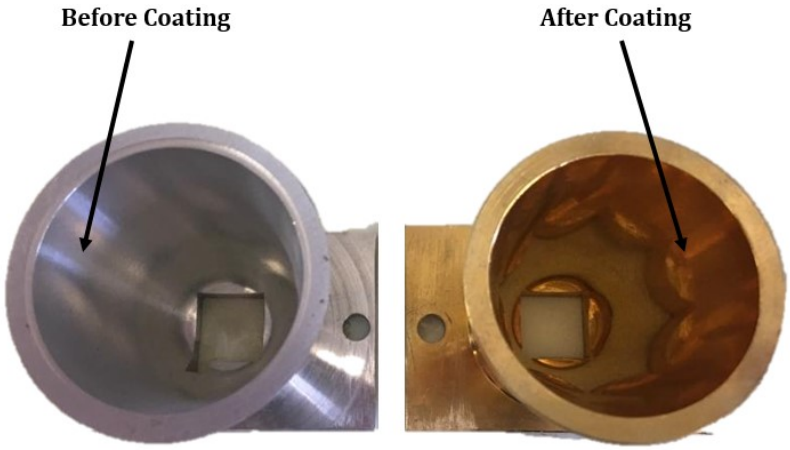

Figure 4.21: 7.0x CPC concentrator before and after coating.

4.5.3 Experimental Results of the Coated CPC

Prior testing of the coated CPC concentrator, a square 7.0x CCPC was designed and fabricated for comparative study. Figure 4.22 shows the I-V curves and P-V curves for both concentrators, and the bare cell under the illumination of 1000 W/m^2. The short-circuit current increased from 0.027 A (bare cell) to 0.126 A and 0.145 A for the circular and square CPCs, respectively. Similarly, the open-circuit voltage increased from 0.577 V (bare cell) to 0.631 V and 0.638 V for the circular and the square CPCs, respectively. In addition, the FF has shown a boost from 66% (bare cell) to 70% for both 7.0x circular and square concentrators. As a result, the cell efficiency has also increased from 10.00% (bare cell) to 11.80% and 12.00% for the circular and square CPCs, respectively. The P-V curves shown in Figure 4.22 (b) shows a 14% increase in power for the square 7.0x compared with the circular 7.0x concentrator. The advantage of the square design over the circular design is that it increases the area of collected irradiance when connected in an array and it optimises the use of solar cells when they are cut in square shape compared to a circular shape [104].

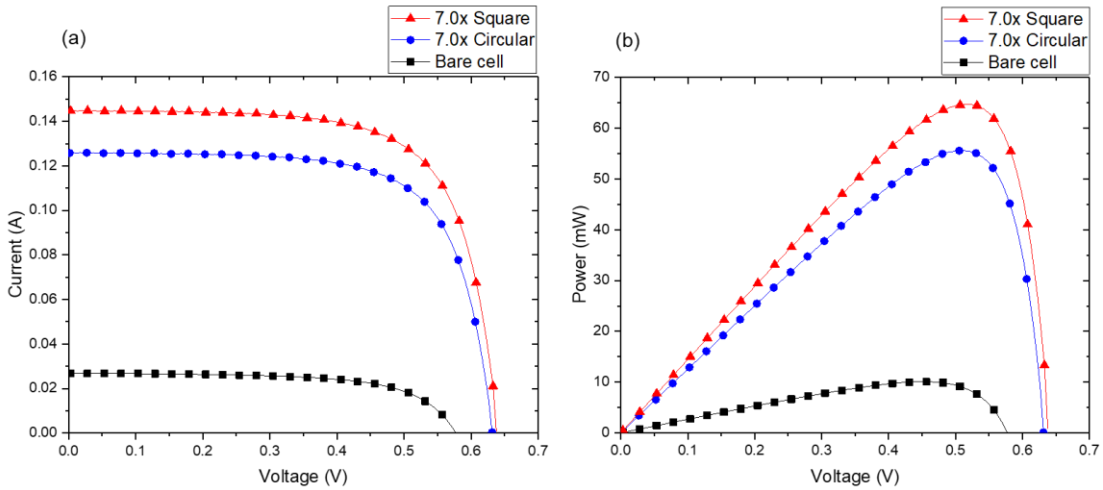

Figure 4.22: 7.0x square, 7.0x circular and the bare cell electrical output: (a) I-V curve and (b) P-V curve.

The experimental results (EXP) of the circular CPC and square CCPC were compared with the simulation results (SIM) in terms of the optical efficiency and the power output. Figure 4.23 presents comparison between the circular 7.0x CPC and the square 7.0x CCPC in terms of (a) optical efficiency and (b) power output.

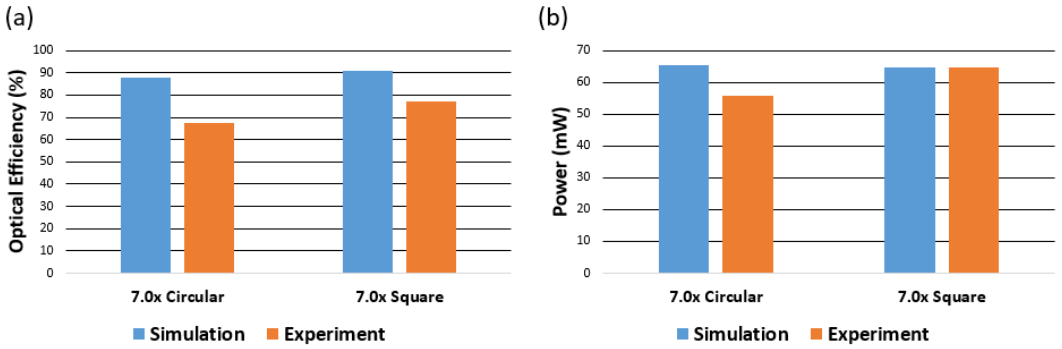

Figure 4.23: Simulation and experimental comparison for 7.0x CPC and 7.0x CCPC for: (a) optical efficiency and (b) power output.

It can be seen clearly from Figure 4.23 (a) that the simulated (blue bars) optical efficiency of the square concentrator is slightly higher than the optical efficiency of the circular concentrator, which are 91% and 88%, respectively. The difference is more significant based on the results from the experiments (Orange bars). This is probably due to the poorer coating finish of the circular concentrator compared to the aluminium reflector used in the square concentrator. It is worth to notice that the curve used in the circular concentrator was not made by using the parametric equation, which has been explained in the first section of Chapter Four (square CCPC). As the curve used in the circular concentrator was used in the very early stage of the project before discovering the best

equation to draw the CPC curve. The cause of variation in the experimental results is due to the reflectivity surface of the two concentrators. Figure 4.23 (b) shows that the simulated power outputs of the two concentrators are almost the same (approximately 65 mW). Whereas the experiment power outputs are found to be 55.70 mW and 64.75 mW for the circular and square concentrators, respectively. It appears that the square 7.0x CCPC has higher optical efficiency due to higher reflectivity of reflector material than that of the coated 7.0x CPC. In addition, there appears to be more losses in the circular 7.0x CPC due to the mismatch between the circular entry aperture and square exit aperture.

4.6 Summary

An effective procedure has been developed for the design, fabrication and characterisation of high-quality low-concentration solar concentrators. The design follows the established theoretical framework and is assisted using TracePro simulation, while 3D printing is employed for accurate implementation of the concentrator geometry and the highly reflective surfaces are formed by covering the surfaces with high reflectivity mirror materials. The quality of the concentrators is evaluated in terms of the optical efficiency by I-V and P-V curves of the photovoltaic systems constructed using a silicon solar cell and the fabricated concentrators.

Using this fabrication process, a high-quality concentrator (8.3x) has been developed that has an optical efficiency of 84.5%. To my knowledge, this is the highest value reported to date. Furthermore, the experimental results show that the increases in the power outputs of 8.3x and 9.0x CCPCs are higher than their respective geometrical concentration ratios, even though optical losses exist in the concentrators. This is a surprising result but can be explained by the fact that the efficiency of the solar cell increases with increasing the light intensity, offering a further advantage for using solar concentrators.

A set of concentrators with geometrical concentration ratios of 2.9x, 4.0x, 6.0x, 8.3x, and 9.0x have been fabricated and characterised, which display optical efficiencies in a range of 82% to 84%, representing the highest optical efficiencies reported to date. These concentrators were designed and fabricated for the study of angular response in the following chapter.

A new concentrator geometry that has a circular entry area and square exit area was designed, implemented and investigated experimentally. The advantage of this type of geometry is that it can be fabricated using the lathe machines, which are readily available in many workshops. However, the experimental results show that its optical efficiency is lower than its CCPC counterpart.

Chapter Five: Angular Response and Light Uniformity of Concentrators

5.1 Introduction

The investigation of the angular response of a concentrator is important to examine its capability and limitation for solar energy harvesting under real operating conditions where the incidence angle of sunlight changes with time. This study focuses on experimental determination of the angular response of the five fabricated CCPC concentrators (2.9x, 4.0x, 6.0x, 8.3x and 9.0x). The knowledge obtained from this investigation will provide useful insights into the necessity and the use of an appropriate tracking system for maximum energy production over the period between sunrise and sunset. In this study, the non-uniformity of light distribution across the solar cell's surface due to the use of the concentrator, its effect on the power output of the concentrated systems are also investigated to demonstrate the importance of the uniformity in concentrator design. In addition, the possibility of increasing the acceptance angle of a given concentration ratio is explored, which could have important implications for efficiency and cost of concentrated systems.

5.2 Angular Response

The angular response study aims to determine the dependence of the output power of a concentrator on the incidence angle. The test was carried out by pointing the concentrator normal to the solar simulator light and then changing the incidence angle in increments of 5° clockwise and anticlockwise. Many authors used the term 'normal incidence' to describe the incidence rays that are perpendicular to the entry aperture of the concentrator (middle of the concentrator) or to the PV surface [2, 116, 193, 194]. The in-house fabricated rotary stage described in Section 3.3 was used to study the angular response by setting the concentrator at different angles, and obtaining the corresponding I-V curves of the solar cell mounted on the receiver area of the concentrator. This chapter focuses on investigating the angular response of the following specific CCPC concentrators (2.9x, 4.0x, 6.0x, 8.3x and 9.0x) and the 4.0x rectangular CCPC.

5.2.1 Simulation

A ray-tracing simulation was used to carry out the optical analysis of concentrators and to investigate the optical efficiency of each concentrator at a different Angle of Incidence (AOI) before conducting the experimental test. In order to match the experimental test conditions, the simulation was carried out by tilting both the concentrator and the receiver surface from +90° to -90° at increments of 5°, while the source surface was fixed. Figure 5.1 shows the simulation setup of 4.0x CCPC under the light source, and the receiver's irradiance map at four selected AOI (0°, 15°, 30° and 45°). The irradiance map shows the light distribution (also referred to as flux distribution) on the receiver's surface and the colour scale beside the map indicates the intensity level: red for high intensity, blue for low intensity and black for no flux received. The receiver surface used in the simulation has an area of 10 mm x 10 mm that matches the exit aperture of the concentrator. The receiver's surface is assumed to be a perfect absorber of the incoming solar irradiance and the reflector is assumed to have a specular reflectivity of 95%. It can be seen from the figure below that the light distribution on the receiver surface changes with the change in incidence angle. At the normal incidence (0°), all the rays are concentrated on the receiver surface and result in optical efficiency of 93.0%, as shown in Figure 5.1 (a). This percentage indicates that the concentrator at normal AOI can reflect the majority of the rays falling on the concentrator to the exit aperture area, with only 7.0% of the rays are lost. In the simulation, the optical efficiency is found to be 86.4% when the incidence angle is at 15° and the loss is more likely due to the blockage of light on the left-edge due to the tilt as shown in Figure 5.1 (b). Figure 5.1 (c) shows the direction of the rays when the concentrator is at its half acceptance angle (30°). This angle represents the maximum incidence angle where the blockage is due to the tilt of the concentrator and the light on the right side of the concentrator surface reflected out after multiple reflections inside the concentrator wall. The electrical power output collected at the receiver surface when the AOI is at 30° is 0.5 mW compared to 38.0 mW received at normal incidence. Consequently, the optical efficiency at this angle is only 1.30%, resulting in a reduction of 91.7% in the optical efficiency from that at the normal incidence. Figure 5.1 (d) shows the simulated rays at an incidence angle of 45°, which is beyond the half acceptance angle of the concentrator. It is evident that the rays are not reaching the receiver's surface and are lost outside the concentrator.

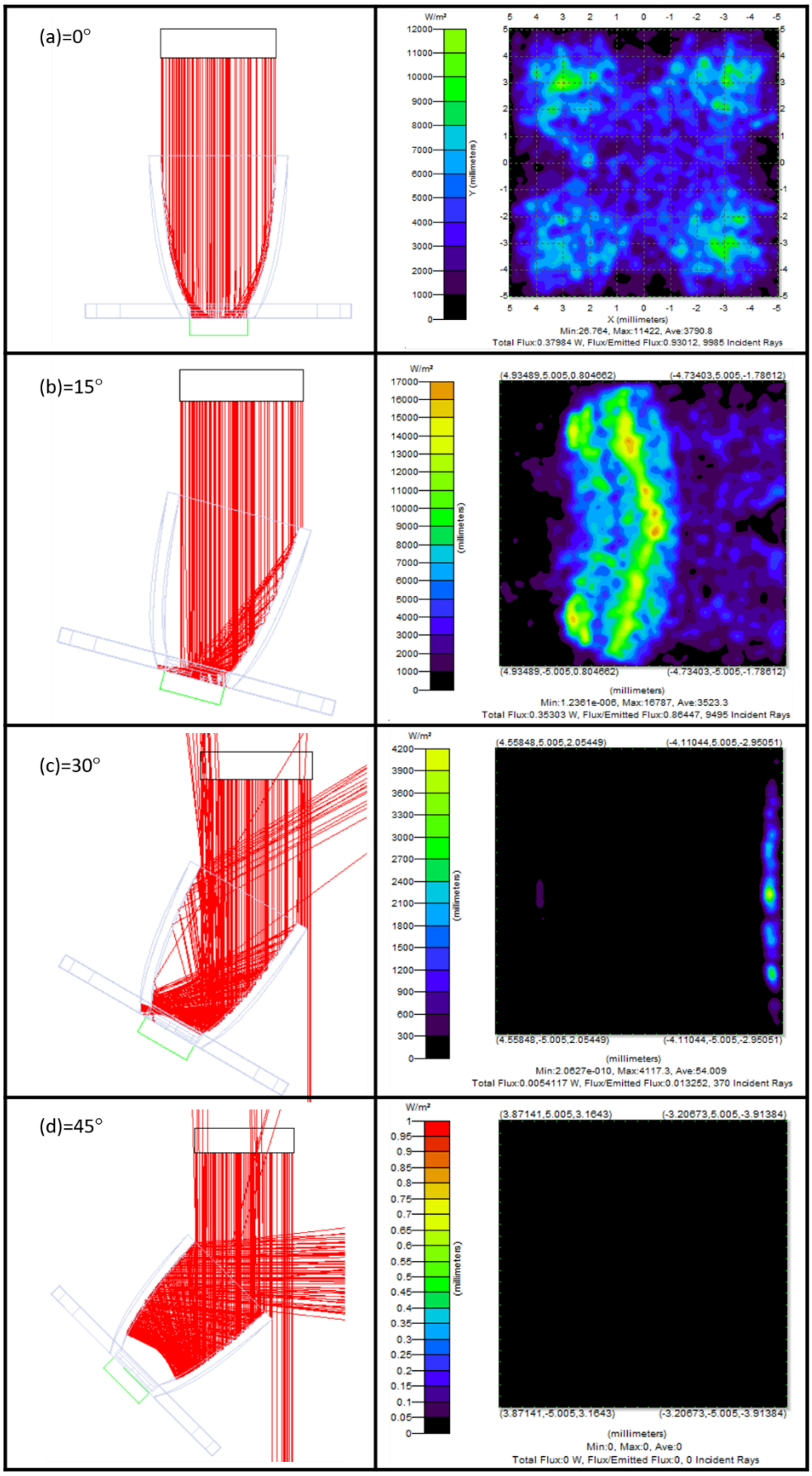

Figure 5.1: Irradiance maps showing the light distribution for 4.0x CCPC at four incidence angles: (a) 0°, (b) 15°, (c) 30° and (d) 45°.

It is to be noted that the simulation results are conducted along an East-West (E-W) direction (from right to left). Because the concentrator is symmetrical and has both square entry and exit apertures, the result will be the same for a North-South (N-S) direction. This result shows that the CCPC produces the maximum power output when the rays are at normal incidence (0°) and that the power reduces dramatically with an increase in the incidence angle.

Figure 5.2 compares the simulated results of the angular response of the bare cell (red) with the 4.0x CCPC (blue) for angles within ±90°. The angular response of the bare cell was simulated using the source and the receiver only. The source is set to produce 1000 W/m^2 and the receiver surface collects the total amount of rays directly from the source without using the concentrator. The receiver surface was then tilted from -90° to +90° at increments of 5°. The angular response of the 4.0x CCPC was simulated using the same procedure, except the concentrator was inserted between the light source and the receiver. All the simulated results are converted to electrical power (assuming 10% conversion efficiency of the solar cell) by multiplying the optical power by 10% which is equivalent to the average efficiency of a silicon cell used in this work.

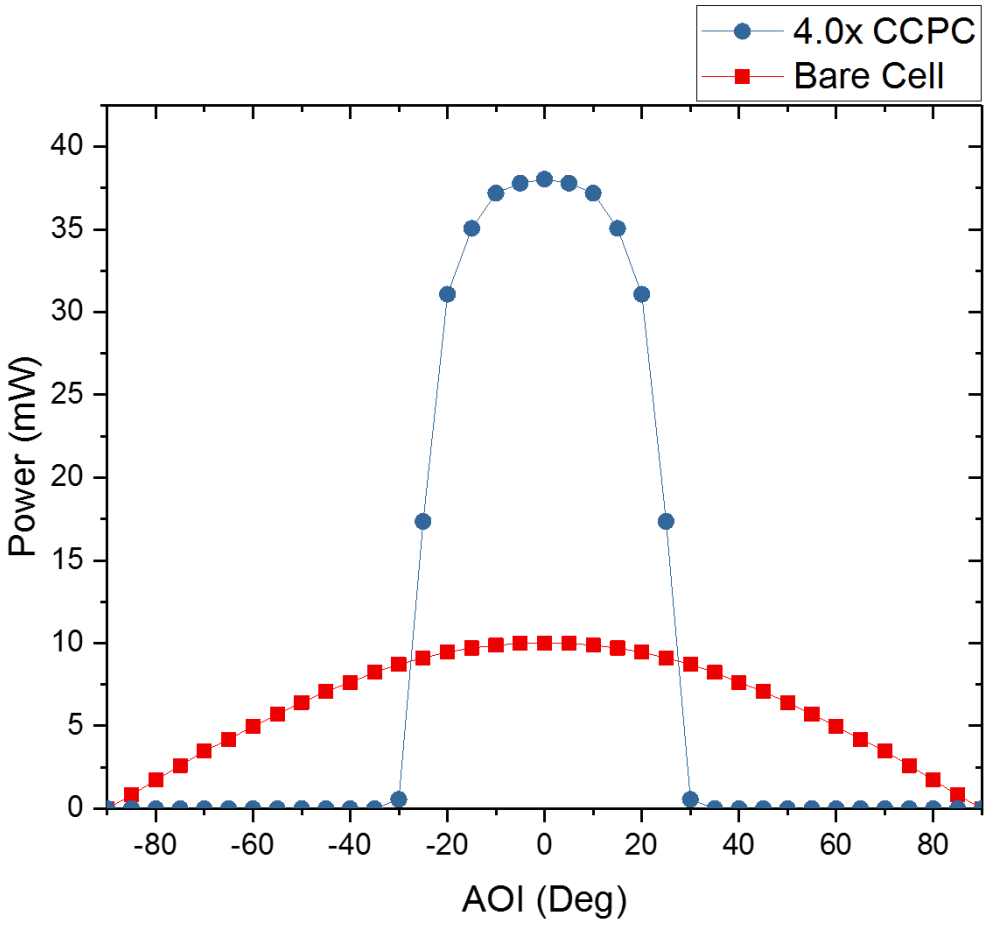

Figure 5.2: The power output variation of the 4.0x CCPC and the bare cell at a different AOI.

The peak power for the bare cell is 10 mW at normal incidence when the cell is placed horizontally and perpendicular to the solar simulator light. The power output reaches 50% of its peak power with an AOI ±60°. A bare cell is thus shown to have a gradual reduction in its output power in response to AOI. The maximum simulated power output for 4.0x CCPC is also achieved when the light is perpendicular to the solar cell surface (normal incidence). The concentrator generates a peak power of 38 mW, compared to 10 mW with no concentration, delivering a maximum power ratio of 3.8. However, the 4.0x CCPC power output reduces to more than 50% of its peak value when the AOI varies in the range of 25°, and this continues to decrease with the increase of incidence angle. In addition, it can be seen that the power produced by the 4.0x CCPC is always higher than the one provided by the bare cell when the AOI is within ±25°, after this angle the power is 0 mW, while the bare cell can still absorb rays beyond 30° because the acceptance angle is 180° in this case.

Figure 5.3 shows the simulated power output (a) and optical efficiency (b) as a function of different incidence angles for five concentrators: 2.9x, 4.0x, 6.0x, 8.3x and 9.0x. It can be seen from Figure 5.3 (a) that when the incidence angle is 0° the concentrators with a higher concentration ratio have a higher power output than that of the lower concentration (e.g., they are 83.0 mW and 27.7 mW for 9.0x and 2.9x concentrators, respectively). However, the concentrators with higher concentration ratio have lower power output when the incidence angle is close to the half acceptance angle of the concentrator than that of lower concentration ratio.

Figure 5.3 (b) shows that the concentrators with a lower concentration ratio have a higher optical efficiency than that of the higher concentration (e.g., they are 94% and 90% for 2.9x and 9.0x concentrators, respectively). Different optical losses occurred due to the different height of the concentrators, as the rays' pathway is longer in higher concentration CCPCs than in the lower concentration CCPCs.

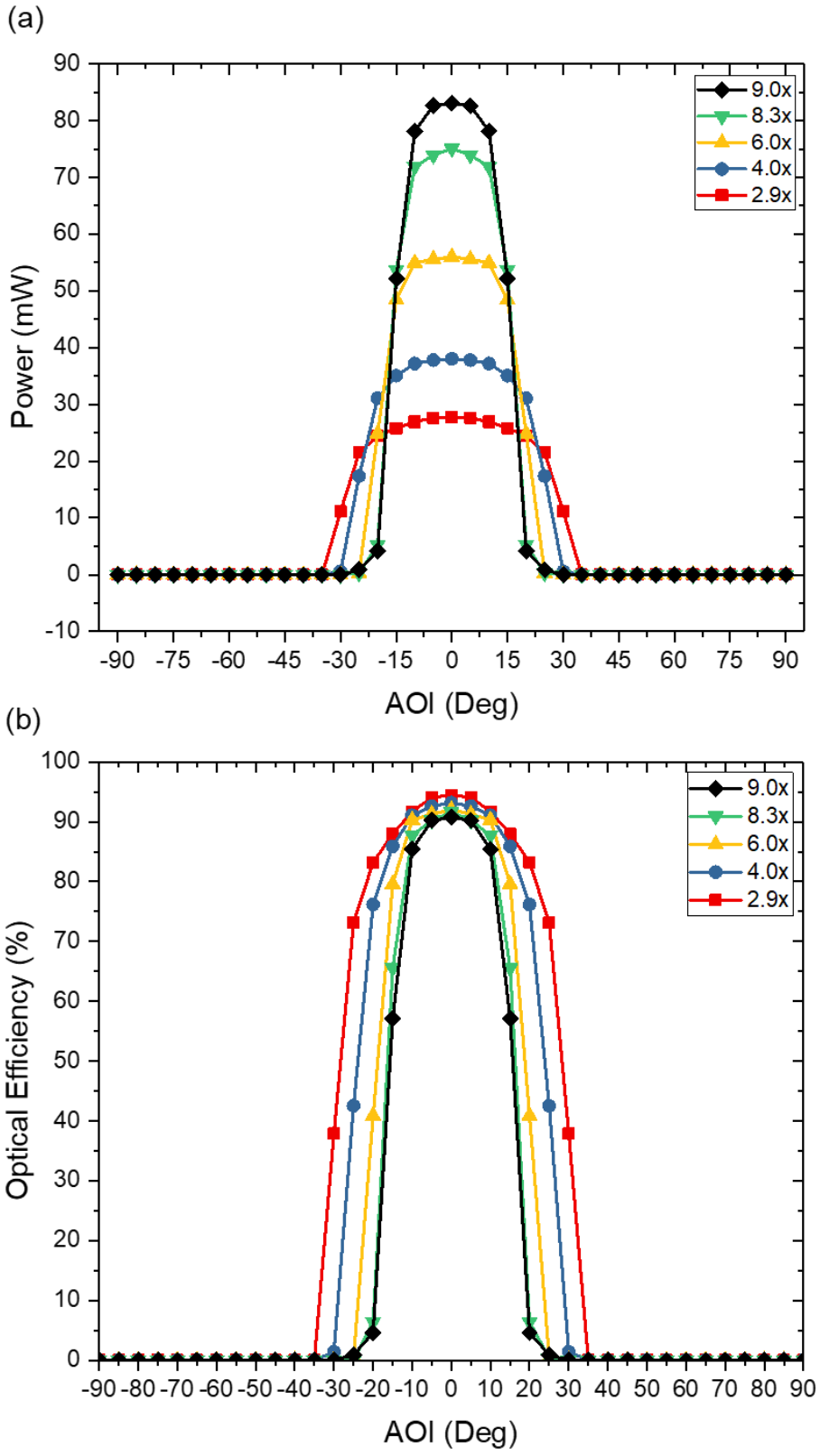

Figure 5.3: Simulated variation of: (a) power output and (b) optical efficiency with incidence angle for the five concentrators, 2.9x, 4.0x, 6.0x, 8.3x and 9.0x.

All five concentrators simulated here have the same receiver size but possess different entry aperture, concentration ratio, height and half acceptance angle. It can be seen that

the half acceptance angle of these CCPCs decreases as the concentration ratio increases. It can be seen from Figure 5.3 (b) that the 2.9x CCPC has a wider half acceptance angle (36.00°) compares to the 9.0x CCPC, which has a half acceptance angle of 19.47°. Nevertheless, the concentrator with a higher concentration ratio is capable of gaining more power than those of low concentration ratios. However, a tracking system is required to harvest power for a long period due to the narrow half acceptance angle of high concentration CCPCs. These simulated results will be validated by experimental investigation, as described in the next section.

5.2.2 Experimental Results and Discussion

For the experimental tests, the rotary stage is placed at the centre of the solar simulator illumination area and the pointer is adjusted at 0°, indicating that the incident light from the solar simulator is perpendicular to the aperture area of the solar concentrator. This position provides the maximum power to be collected at the receiver area of the concentrators. Figure 5.4 shows a photograph for the angular response experiment of the 4.0x CCPC concentrator at normal incidence.

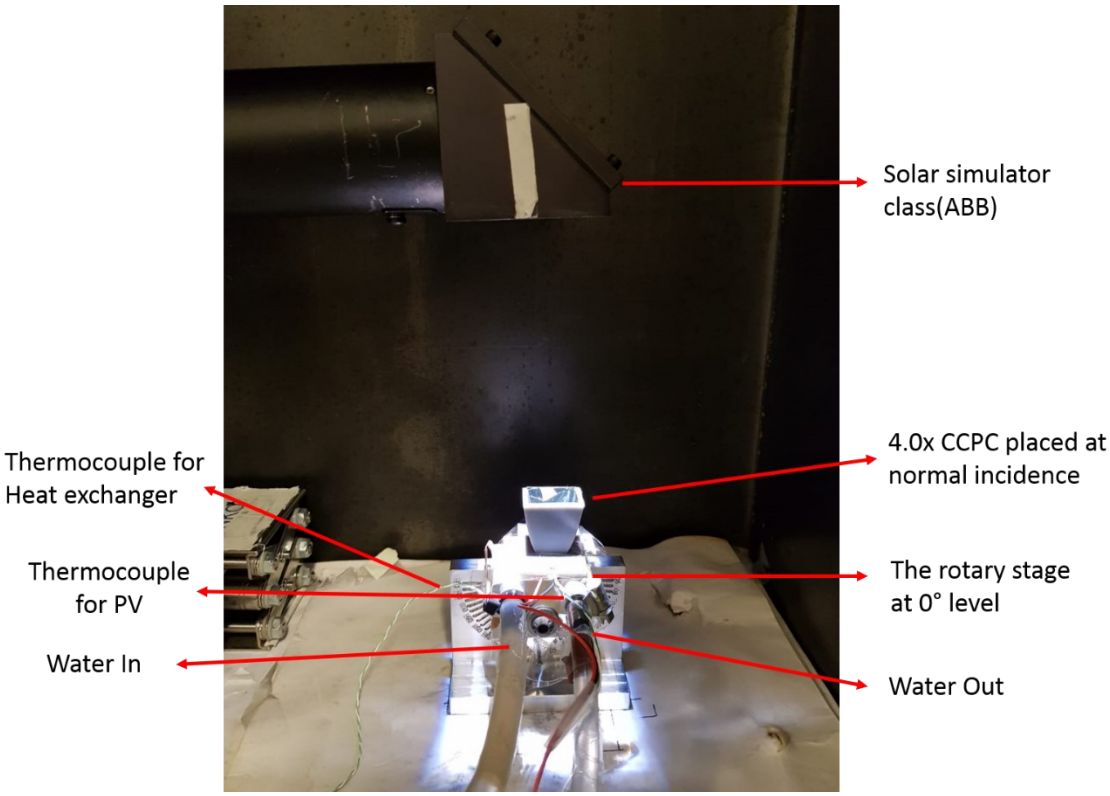

Figure 5.4: 4.0x CCPC layout under normal incidence illumination.

The rotary stage is tilted to a given incidence angle manually to study the angular response with and without the concentrators. The angles were varied between 0° and

45° because the maximum half acceptance angle is 36° for the 2.9x CCPC and narrower for other tested CCPC concentrators. The rotary stage is rotated in an increment of every 5° and the I-V curve is obtained for each angle. I-V curves were taken when the cell temperature reaches 25 °C (±1 °C) to meet the Standard Test Condition (STC) of PV cell testing. An initial test is conducted using a bare cell at the light intensity of 1000 W/m^2, which is measured using the Solar Survey [161]. The distance between the solar simulator and the cell surface is adjusted to ensure one sun irradiance at solar cell surface. After the angular test is completed for the bare cell, a concentrator is mounted on the top of the cell and secured firmly to the rotary stage, to ensure the stable rotation of the concentrator without falling down and to provide cooling to the solar cell at the same time. The distance is adjusted again to achieve one sun irradiance on the entry aperture of the concentrator. Figure 5.5 shows the comparison between the simulation (SIM) and experimental (EXP) results for the 4.0x CCPC. The tests were repeated three times and the average values are presented with error bars shown in Figure 5.5. It can be seen that the experiment results of the 4.0x CCPC show a good agreement with the ray-tracing simulation results, with an average deviation of the power output of 1.5% for angles between 0° to 15°. A dramatic drop in power output appears at AOI 15° for both sets of data.

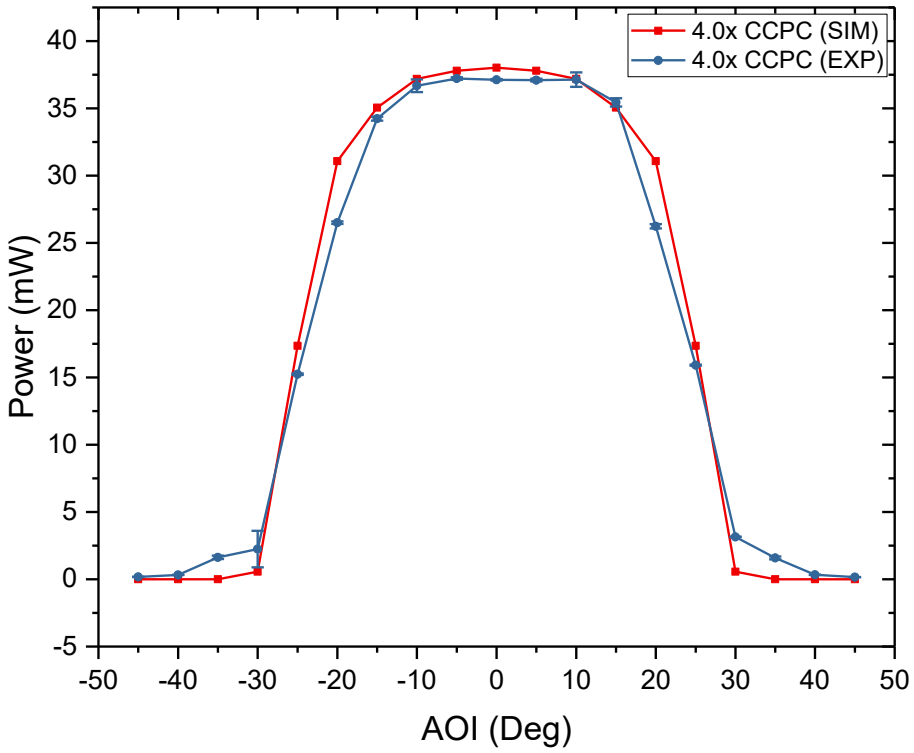

Figure 5.5: Comparison between simulation and experimental result of 4.0x CCPC.

Further analysis was carried out to examine the changes in the I-V and P-V curves at different incidence angles. Figure 5.6 (a) shows that the short-circuit current (I_{sc}) and the maximum power (P_{max}) at normal irradiance have the highest values which are 0.084 A and 0.039 W, respectively. The fill factor can also be determined from the I-V, which is 0.72. Figure 5.6 (b) shows a slight drop of the short-circuit current (I_{sc}) to 0.0782 A and the maximum power (P_{max}) to 0.034 W at A0I of 15°. The fill factor also decreases slightly to 0.71. The I-V curve shows a significant drop of the short-circuit current (I_{sc}) when the AOI is 30°. This angle is theoretically the half acceptance angle of the 4.0x CCPC, and the short-circuit current is reduced to 0.01 A and the maximum power is reduced to 0.003 W, and the fill factor to 0.59. The power output reduces to almost 0 when the angle is greater than the half acceptance angle of the concentrator as shown in Figure 5.6 (d), where most of the rays falling onto the surfaces of the concentrator are reflected back to outside of the concentrator.

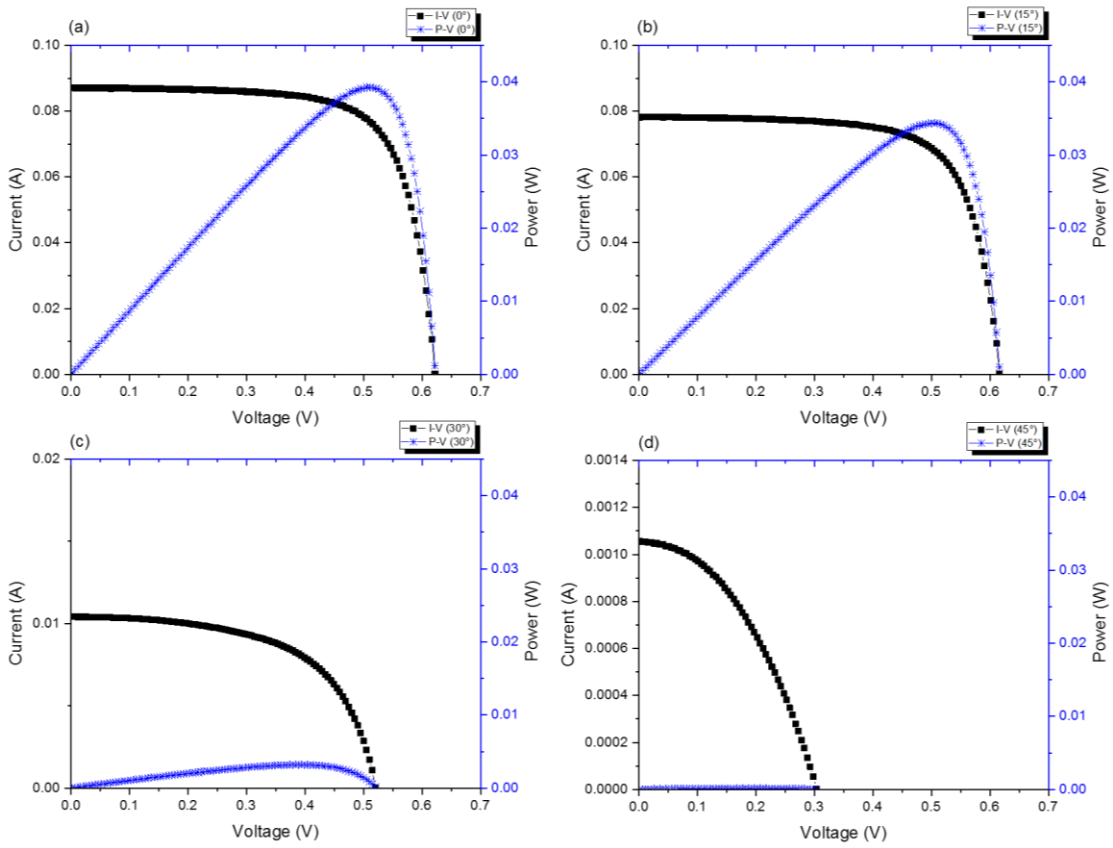

Figure 5.6: I-V and P-V curves for the 4.0x CCPC at different angles: (a) 0°, (b) 15°, (c) 30° and (d)45°.

Figure 5.7 presents the angular response of the power data collected for 2.9x, 4.0x, 6.0x, 8.3x and 9.0x CCPCs. The experimental power output from the bare cell decreases gradually when the AOI increases as shown in Figure 5.7. This gradual reduction is due to the cosine effect [195], which can be explained by the fact that the solar cell surface

area under the illumination of the sunlight decreases with the cosine of the AOI (normal to surface). In addition, the experimental results show that the concentrators with lower concentration ratio have a wider half acceptance angle than that of the higher concentration ratios, as predicted by the simulation.

The 4.0x CCPC has a maximum power output of 38.00 mW at normal incidence, and a power ratio of 3.8 when compared with a bare cell. The power ratio is determined from the power output of the solar cell with a concentrator divided by the power output of the bare cell [113].

The results show that the angular response of the 4.0x CCPC is narrower compared to the 2.9x CCPC. The 6.0x CCPC has a maximum power output of 59.80 mW at normal incidence, with a rapid decrease in power for AOI larger than 5°. It can be seen, for example, that the power output of 6.0x CCPC is reduced to 55% of its peak value when the AOI is 15°. Despite the higher power output of 8.3x and 9.0x CCPCs, at 75.00 mW and 89.70 mW, respectively, these concentrators have poor angular response compared to the concentrators of lower concentration ratio as shown in Figure 5.7. This explains why a tracking system is needed for the concentrators with a higher concentration ratio.

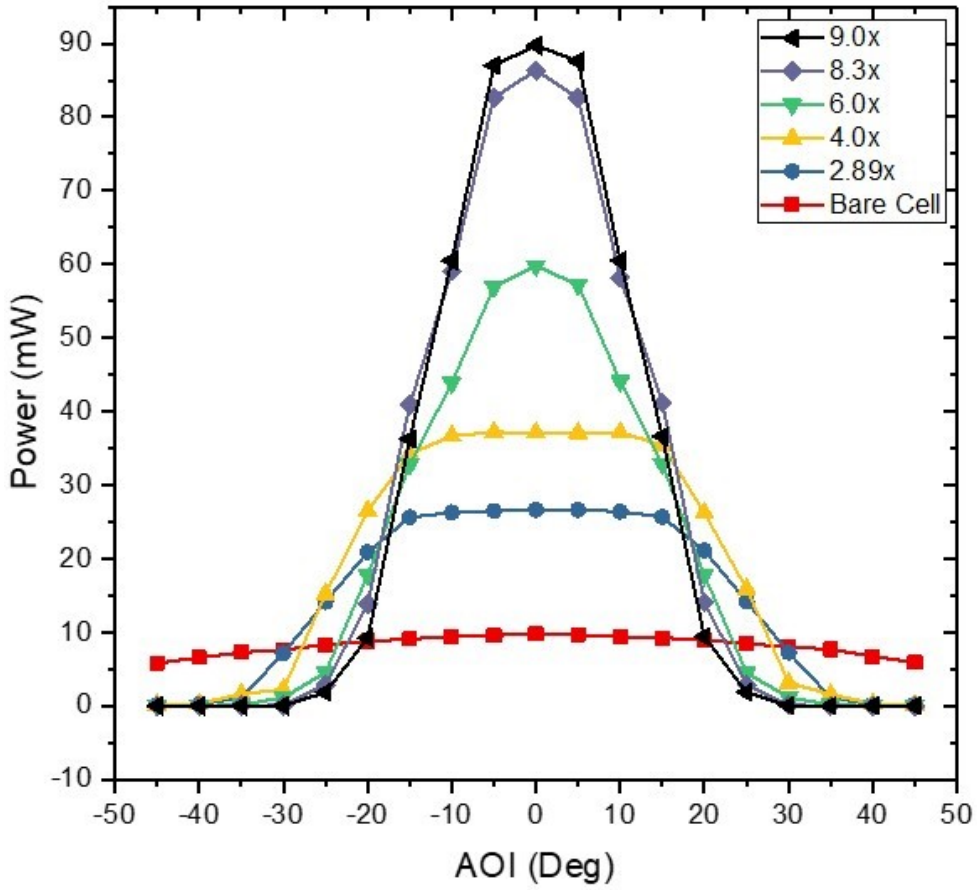

Figure 5.7: Variation of the experimental power output for concentrating CCPCs and non-concentrating with different incidence angles.

5.3 Uniformity

The uniformity of light distribution on the PV cell is an important parameter in the design of the PV system, as the non-uniform illumination over the solar cell decreases the solar cell's performance. The uniform distribution of the light on the solar cell results in reducing the hot spots on the receiver areas [195]. The light distribution in the solar cell can differ from one concentrator to another, which depends on many factors, including the concentrator geometry, imperfections of optics and errors in the reflector surface [79]. Moreover, at different incident angles, there will be different light distributions at the receiver side. As discussed in the literature, non-imaging concentrators do not reflect the image of the source in a single-point; this is considered an advantage over imaging concentrators because a single-point focus can cause hotspots and thus malfunctioning of the solar cell. However, the light distribution in the non-imaging concentrator, especially the CCPC, is not uniform across the solar cell. As the concentration ratio of the CPV system increases, the non-uniform distribution increase as well and it becomes more difficult to maintain uniformity. This section aims to explore the possibility of

improving uniformity of light distribution in the solar cell under the fabricated concentrators in this research.

5.3.1 Simulation

The non-uniformity was initially investigated using the ray-tracing simulation to map the distribution of the reflected light over a receiver area of 10 mm x 10 mm, which is divided into nine sections (blocks) of equal size, as shown in Figure 5.8.

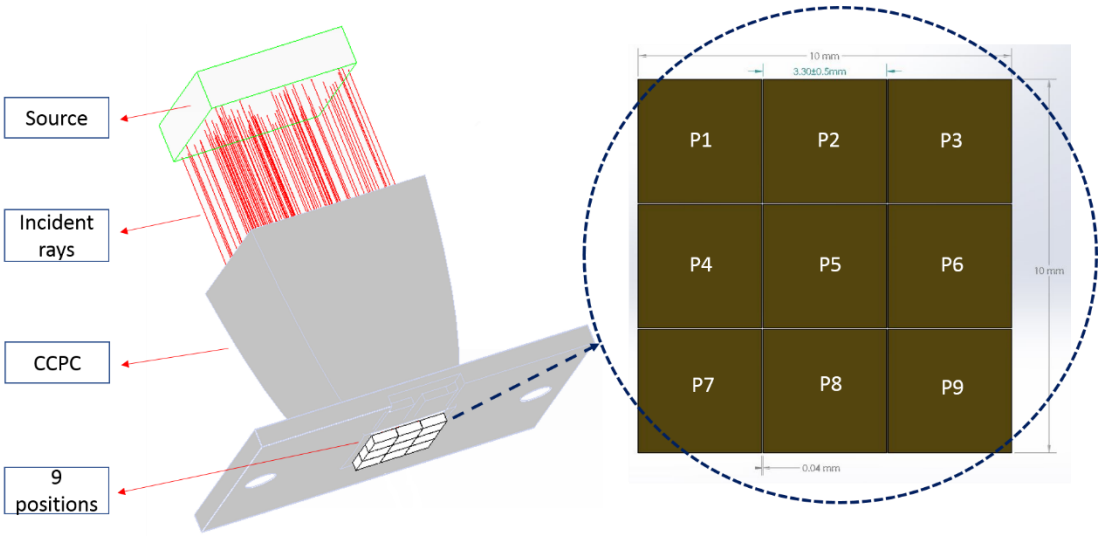

Figure 5.8 Nine positions of the receiver area for uniformity simulation using TracePro.

The nine sections are numbered as shown in Figure 5.8. The section width is 3.33 mm and the distance between each section is approximately 0.04 mm. As mentioned in Section 4.3.3, the default position of the receiver surface is at 2 mm below the concentrator end. The same setup is used in this simulation, except that the light radiation is changed from 1000 W/m^2 to 115 W/m^2. This change is necessary because the spectroradiometer employed for experimental validation has an upper limit of 1.5 suns. The spectroradiometer was used experimentally to validate the simulated results of the non-uniformity test and these results will be discussed in the next section. As an example, the flux distribution of the 4.0x CCPC with a height of 25.9 mm is displayed in Figure 5.9 (b) showing a higher power intensity on the four corners of the receiver.

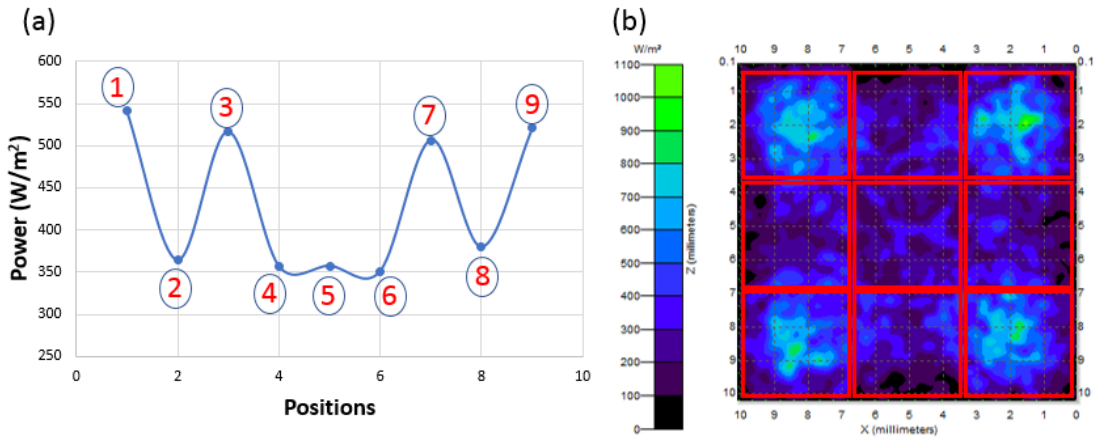

Figure 5.9: 4.0x CCPC uniformity test: (a) the average flux at nine sections for the given incidence of 115 W/m² and (b) the corresponding irradiance map showing the flux distribution across the nine sections.

Applying 115 W/m² at the source side, it can be seen clearly that the peak flux is focused at the corners of the receiver (i.e., the positions of 1, 3, 7 and 9 in Figure 5.9). The power value in these positions is greater than 500 W/m², while the power values in other positions (2, 4, 5, 6 and 8) range from 350 W/m² to 375 W/m². The actual concentration ratio of this 4.0x CCPC can be determined using the average flux over the nine positions, which is 3.7x. The corresponding optical efficiency is 93%. Figure 5.10 shows the simulated power distributions for the five concentrators and the contour plots correspond to each concentrator at the nine positions. The irradiance maps shown in the figure represents the uniformity of the full cell area of five different concentrators. It can be seen clearly from Figure 5.10 that the 2.9x and 4.0x have almost the same non-uniformity distribution and the hotspots appear at the corners. The 6.0x, 8.3x and 9.0x, are shown to have a different light distribution due to different concentration ratios. The varying intensity levels appear to be focused at the edges.

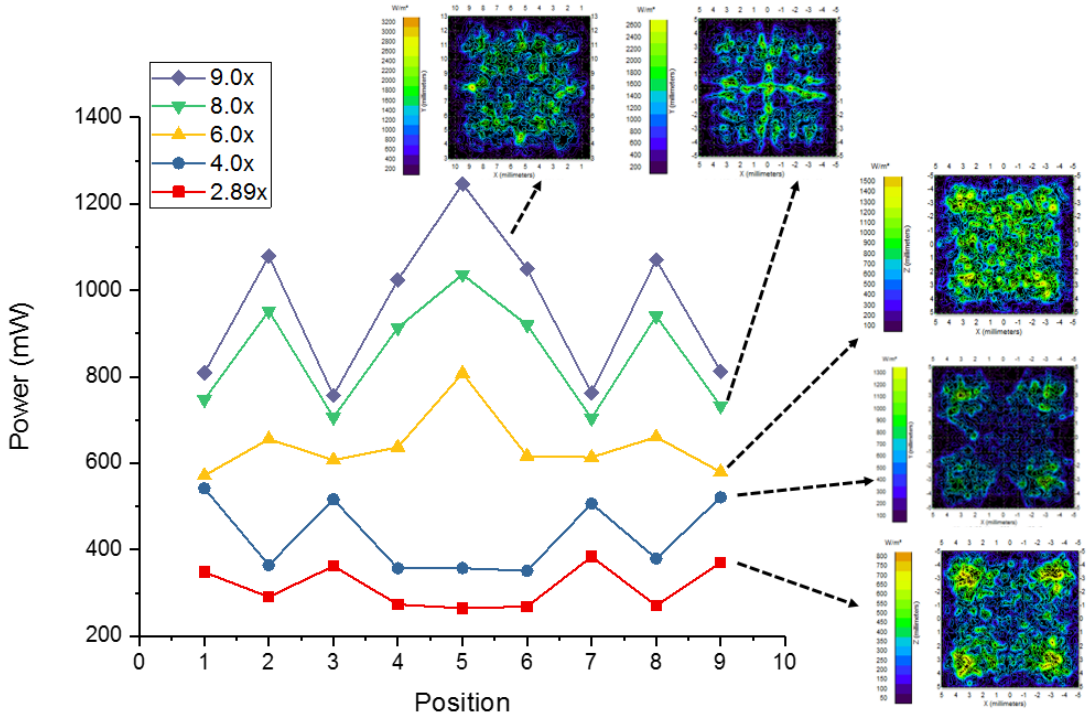

Figure 5.10: Power flux distribution for the five concentrators at the nine positions and their corresponding contour plot.

It is important to understand the flux distribution and its effect on the performance of solar cells. The non-uniformity can be calculated based on IEC60904-9 by measuring the minimum and maximum flux over the tested area [165]. Using the simulation results for the 4.0x CCPC at the receiver location of -2 mm, the non-uniformity over the nine sections under normal irradiance can be calculated by:

$$Non-uniformity\ (\%) = \frac{541-350}{541+350}\ \text{x}\ 100\% = 21.4\%$$

This corresponds to a uniformity of 78.6%. Ahmed et al proposed another method to evaluate the uniformity [196] by defining the Concentrator Uniformity Factor (CUF), which is determined by:

$$\text{CUF} = [1 - (\frac{Maximum\ received\ irradiance - Average\ received\ irradiance}{Maximum\ received\ irradiance})]\text{x}\ 100 \qquad (5.1)$$

The values obtained using this method are very similar to the first method. Therefore, in this study, the uniformity of the received irradiance on the receiver is computed using the standard (first) method.

5.3.2 Experimental Validation

A spectroradiometer has a small sensing area that enables measurement of the light intensity of the section area shown in Figure 5.8 and is, therefore, employed to determine the light distribution over the solar cell surface. The spectroradiometer consists of two

devices that measure the UV-VIS and NIR ranges, respectively, so as to cover a wide range of 300 nm to 1700 nm. To ensure constant and repeatable testing, a copper plate is used and mounted on an adjustable aluminium stage. The aluminium stage has nine holes to secure the CR2-AP receptor and only the middle hole is used for this test as it is kept in the middle of the light illumination area as shown in Figure 5.11. The copper sheet has a thickness of 0.6 mm with nine circular holes drilled within a 10 mm x 10 mm area (i.e., the same size of the solar cell area). The holes are evenly spaced and the diameter of the holes is 3 mm, which matches the aperture of the Cosine Receptor CR2-AP of the spectroradiometer. The holes are numbered in the same manner as shown in Figure 5.8. The light from the solar simulator is detected by the CR2-AP receptor, which is connected to the two devices by Y-shape fibre optics. The outputs of both instruments are connected to a PC that processes and displays spectral graph from the measured data. Figure 5.11 shows the experimental setup for the non-uniformity test.

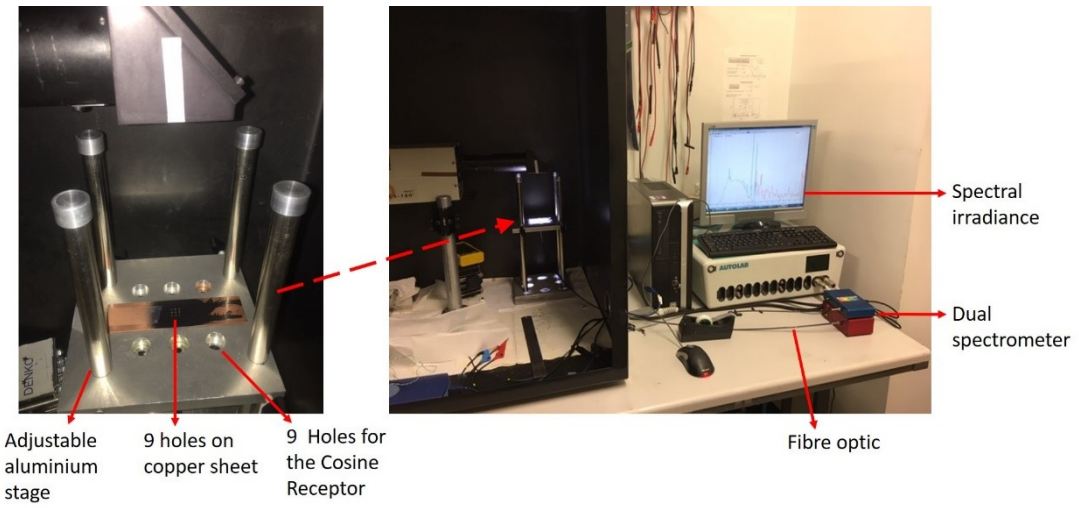

Figure 5.11: Experimental setup for the non-uniformity test.

The copper sheet is painted with black paint to avoid light reflecting on the sheet and to avoid further concentration within the internal wall of the holes. The spectroradiometer needs to be tested prior of using it to ensure that it functions properly. A standard practice before using the device is to take dark reference by blocking the fibre optic aperture so there is no light entering into the sensor. Then, the solar simulator is switched ON and the tests were recorded for three different intensity levels, which was achieved by changing the distance between the solar simulator and the fibre optic aperture, corresponding to 7, 7.1 and 8 inches, respectively. The intensity of 1000 W/m^2 (1 sun) is found to be at the distance of 7.1-inch. This test was carried out without using the copper sheet and the concentrator. Figure 5.12 shows the spectral irradiance at three

different levels. This test was repeated three times for each level and the maximum standard deviation of 1% was found between the three tests.

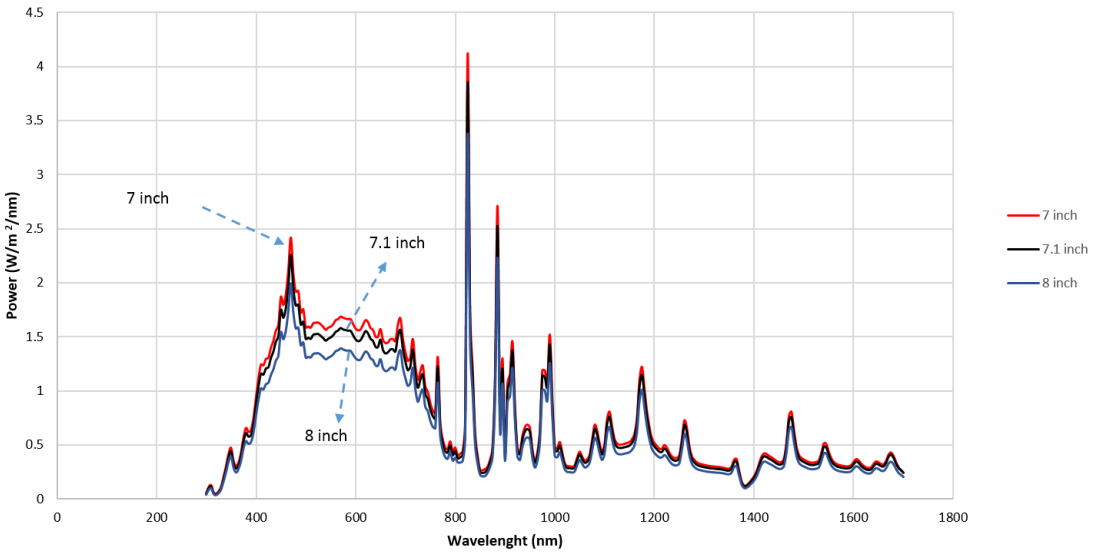

Figure 5.12: Spectral irradiance for different intensity levels.

The results shown in Figure 5.12 were taken at the centre of the illumination area (i.e., position 5) through the holes of the aluminium stage (Figure 5.11), where the Cosine Receptor (light sensor) is attached.

Table 5.1 displays the experimental data collected from the spectroradiometer at one sun irradiance (7.1 inches).

Table 5.1: Experimental data collected by the spectroradiometer at one sun irradiance.

Electromagnetic wave	From	To	Irradiance (W/m²)	%
UV-VIS	300	750	541	53.55%
IR	750	1700	473.42	46.86%
Total	300	1700	1010.27	100%

Another two tests have been carried out before testing the concentrator uniformity at exit aperture. These tests made to check the uniformity of the nine positions separately, and to investigate the effect of the copper sheet before using the concentrator. The normal spectral irradiance was measured without the copper plate, and then the plate was introduced to calculate the effect on the non-uniformity that plate has, and the results are shown in Figure 5.13.

(a)

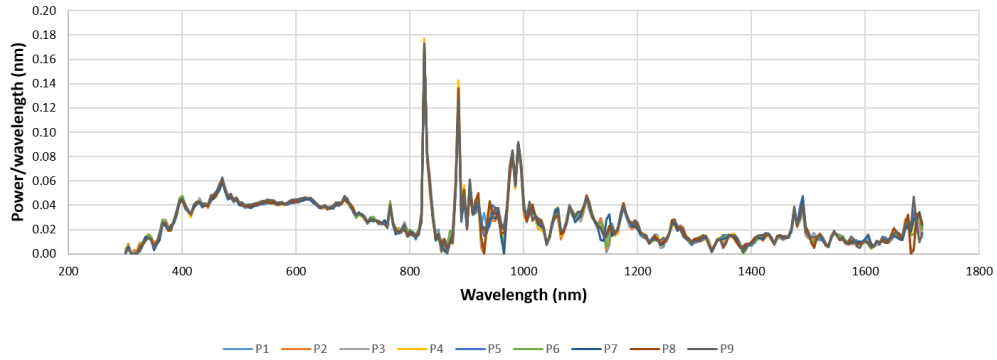

(b)

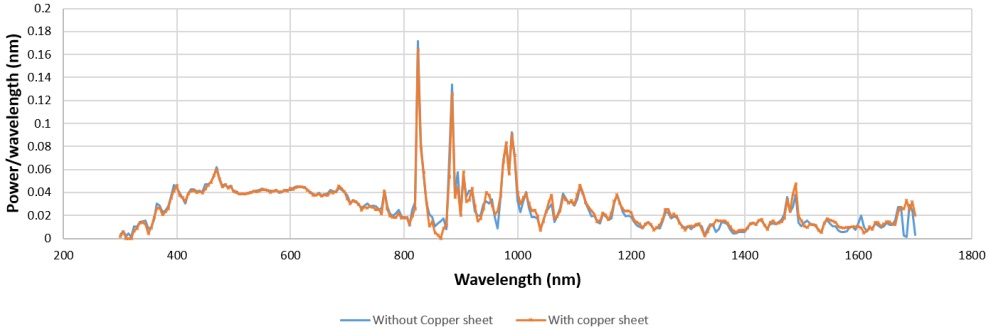

Figure 5.13: Spectral irradiance by using a spectroradiometer for: (a) nine positions uniformity test and (b) with and without a copper sheet.

As shown in Figure 5.13 (a), the differences in the spectral irradiance among the nine positions are very small. The average standard deviation among the nine positions is 0.18%, while the maximum deviation is 1.57% at 1685 nm. Figure 5.13 (b) shows the measured spectral irradiances with and without the copper sheet, respectively. The maximum standard deviation is 2.25% at 1685 nm, indicating that the use of the copper sheet should not introduce significant error. The CR2-AP was fixed at the central hole of the aluminium stage (i.e., the middle of the illumination area). A tape was used to attach the concentrator to the copper sheet and then the concentrator was moved on the top of the fixed CR2-AP detector to record the light intensity at each of the nine holes at the exit aperture of the concentrator. The spectral irradiance of each hole was taken at a time. Figure 5.14 presents the results of this test for 2.9x CCPC. Each point represents the total intensity summarised over the range from 300 nm to 1700 nm as shown in the table of Figure 5.14 (a), in the unit of W/m^2. It can be seen that position 1 has higher power, as also indicated by the spectral graph (dark blue) of Figure 5.14 (a). Meanwhile, position 5 has lower spectral irradiance, and this can also be seen in Figure 5.14 (a). The flux uniformity is shown in Figure 5.14 (b), and is approximately in agreement with the simulated results for 2.9x, as seen in Figure 5.10.

(a)

P1	P2	P3	P4	P5	P6	P7	P8	P9
420.87	321.94	387.83	203.69	202.14	204.29	359.62	321.58	374.7

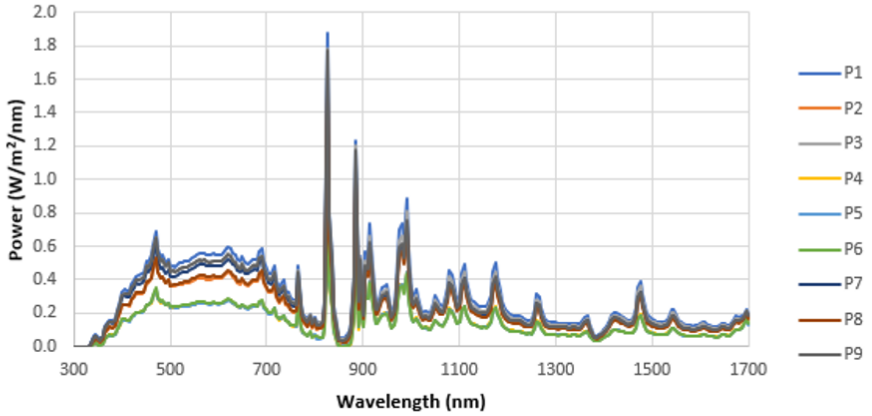

(b)

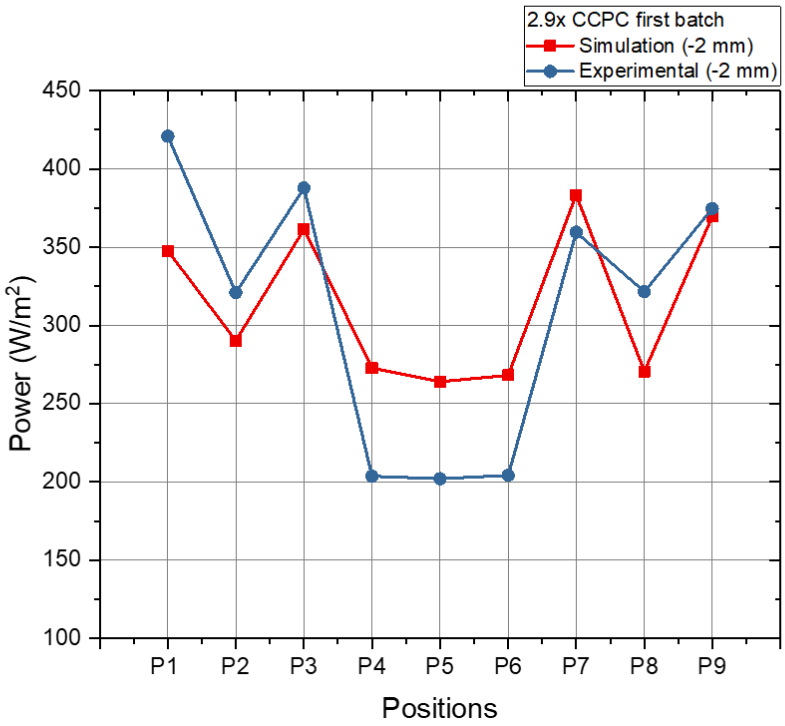

Figure 5.14: Simulated and experimental results of 2.9x CCPC at nine positions for: (a) experimental spectral irradiance and (b) simulated and experimental uniformity distribution.

5.3.3 Improved Design

It was noticed that the flux distribution on the receiver's surface was not uniform when the receiver was located at the default position, 2 mm below the focal plane, as discussed in Section 4.3. This observation led to an investigation of the flux uniformity on the receiver surface at different distance to the focal plane and its effect on the power output of the solar cell. The study was carried out initially by simulation and then by experimental validation. As a result of this study, a new batch of concentrators was made and they are referred to as the 'improved design'.

5.3.3.1 Simulation of the Improved Design

The uniformity of flux distribution was investigated by changing the distance between the receiver and the concentrator. As explained earlier (Section 4.3.3), -2mm is the default position to place the solar cell underneath the exit surface of the concentrator, as this is the thickness of the concentrator wall. This thickness was found to be rigid for a robust concentrator after printing. It was found that this gap can significantly affect the power output of the solar cell. Several positions were examined to achieve the best performance from the CCPCs. The flux distribution on the receiver surface as a function of the distance from the focal plane was investigated systematically by varying the distance from 0 mm to 6 mm below the focal plane at an interval of 0.5mm. Figure 5.15 shows the uniformity distribution as a function of detector positions.

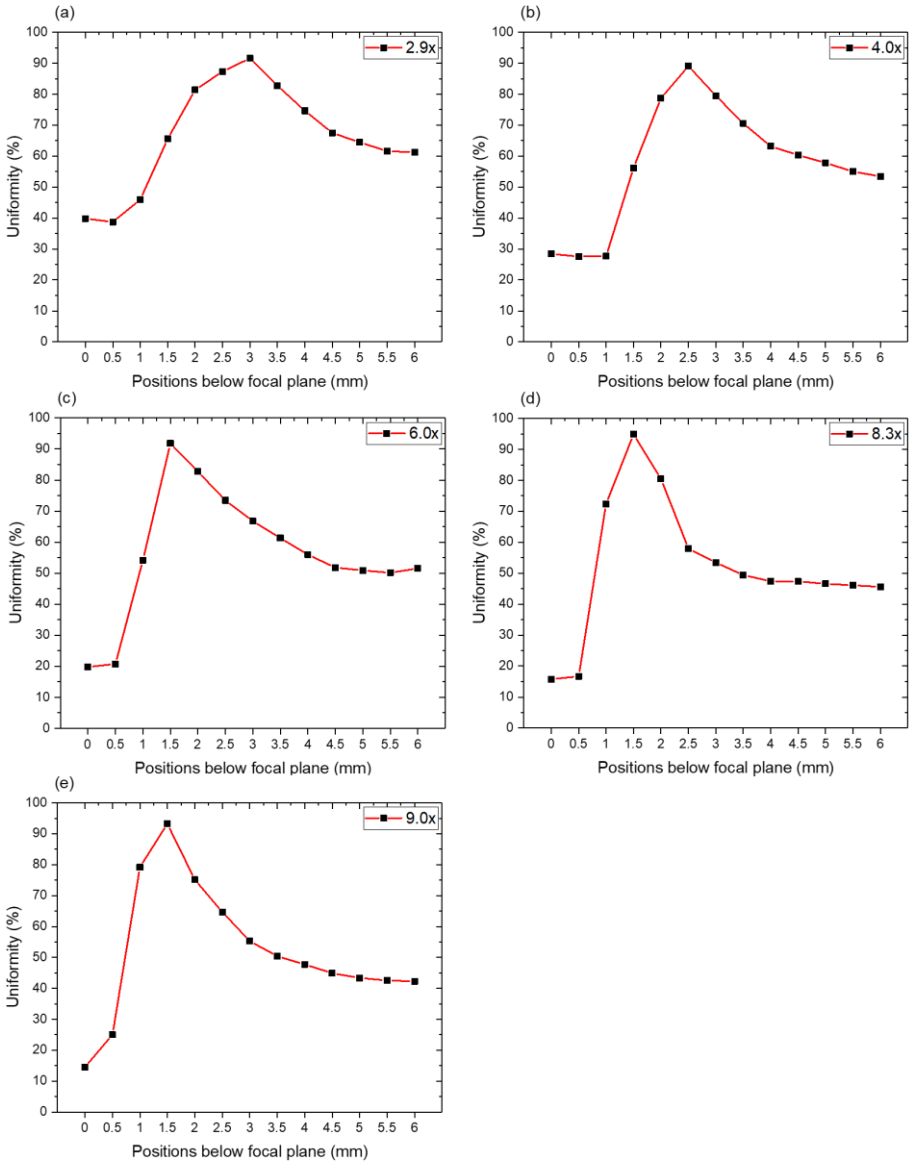

Figure 5.15: Uniformity distribution of light as a function of detector positions: (a) 2.9x CCPC, (b) 4.0x CCPC, (c) 6.0x CCPC, (d) 8.3x CCPC and (e) 9.0x CCPC.

It can be seen that the distance from the focal plane of the concentrator to the top surface of the solar cell has a significant effect on the concentrator uniformity. The solar cell positioned at 0 mm (focal plane) has the lowest uniformity among all the positions. The uniformity increases initially with increasing the distance from the focal plane and reaches the highest uniformity at an optimal position, and then decreases as the distance further increases. However, the optimal value is different for the concentrator with a different concentration ratio. The position of -2 mm is the default position for all five concentrators where the top surface of the solar cell is placed exactly on the bottom surface of the concentrator. The uniformity at this position appears to be 80% for all concentrators investigated, as shown in Figure 5.15. For the 2.9x CCPC, the highest uniformity is found at -3 mm, at which the uniformity reached 91.6 %. For the 4.0x CCPC, the highest uniformity of 89.0 % is achieved at -2.5 mm, which is 0.5 mm below the default position). For the 6.0x, 8.3x and 9.0x CCPCs, the highest uniformity is found to be at the position of -1.5 mm.

Figure 5.16 shows the simulated flux distributions of the 4.0x CCPC for four different receiver positions. It can be seen from Figure 5.16 that there is a noticeable difference in the flux distribution between the default position and the optimal position.

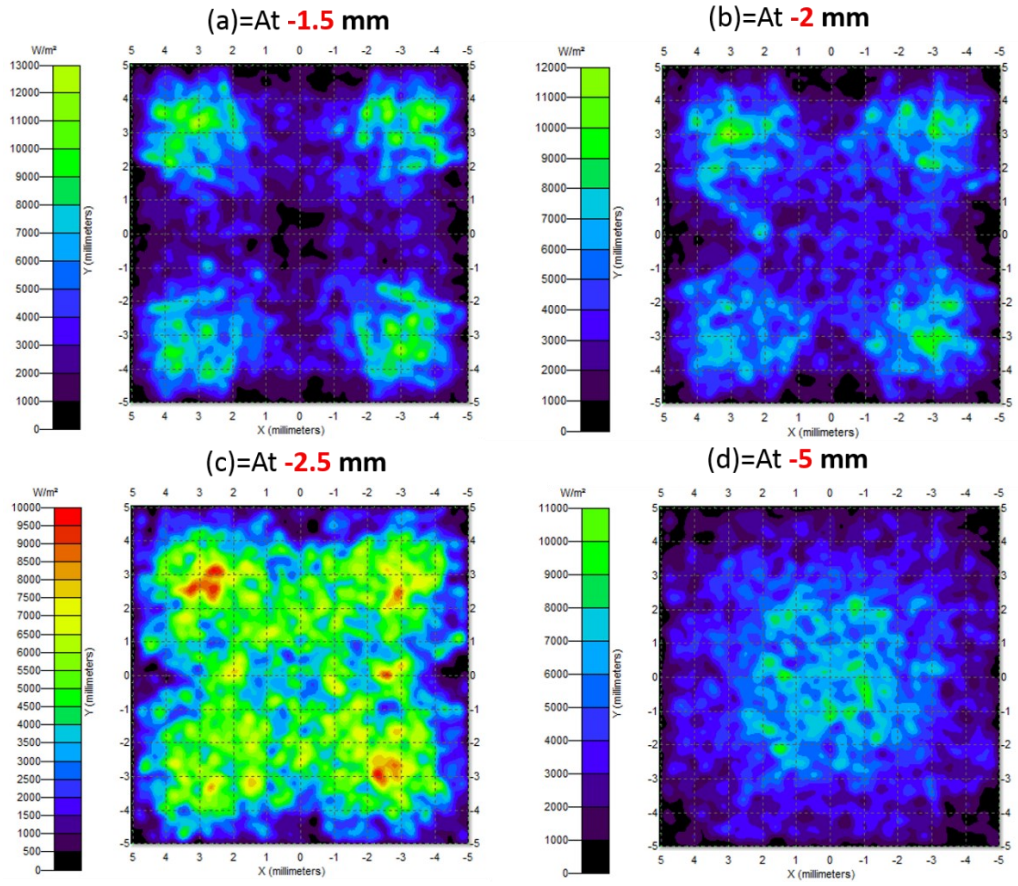

Figure 5.16: Comparison of four different positions for the 4.0x CCPC flux distribution.

It can be seen from Figure 5.16 (a) that the hotspots are focused at the corners and the central area has a lower intensity. Figure 5.16 (b) shows the flux distribution at the default position (-2 mm) where the four hotspots also appear at the corners, but with lower intensity than that at -1.5 mm. When the solar cell is lowered by 0.5 mm downwards from the default position (-2.0 mm), the uniformity of the flux is displayed in Figure 5.16 (c), which shows a more homogenous distribution across the solar cell. The contrast between the hotspots and central area is less significant compared to that at the position of -2.0 mm. Figure 5.16 (d) displays the irradiance map at -5 mm from the focal plane of the concentrator, which shows higher light intensity in the central area, which is the opposite to the cases shown in Figures 5.16 (a), (b) and (c).

The light intensity at nine positions (see Figure 5.8) of the improved design is compared to the old design. The results are shown in Figure 5.17 (a)-(e) for 2.9x, 4.0x, 6.0x, 8.3x and 9.0x CCPCs, respectively. A clear improvement is evident. For example, the results of the 2.9x CCPC displayed in Figure 5.17 (a) show that the data spread across the nine positions for improved design (-3 mm) are significantly smaller than those of the old design (-2 mm). Similar conclusions can also be drawn from Figure 5.17 (b)-(e) for the CCPCs of 4.0x at position of -2.5 mm, 6.0x, 8.3x and 9.0x at position of -1.5 mm.

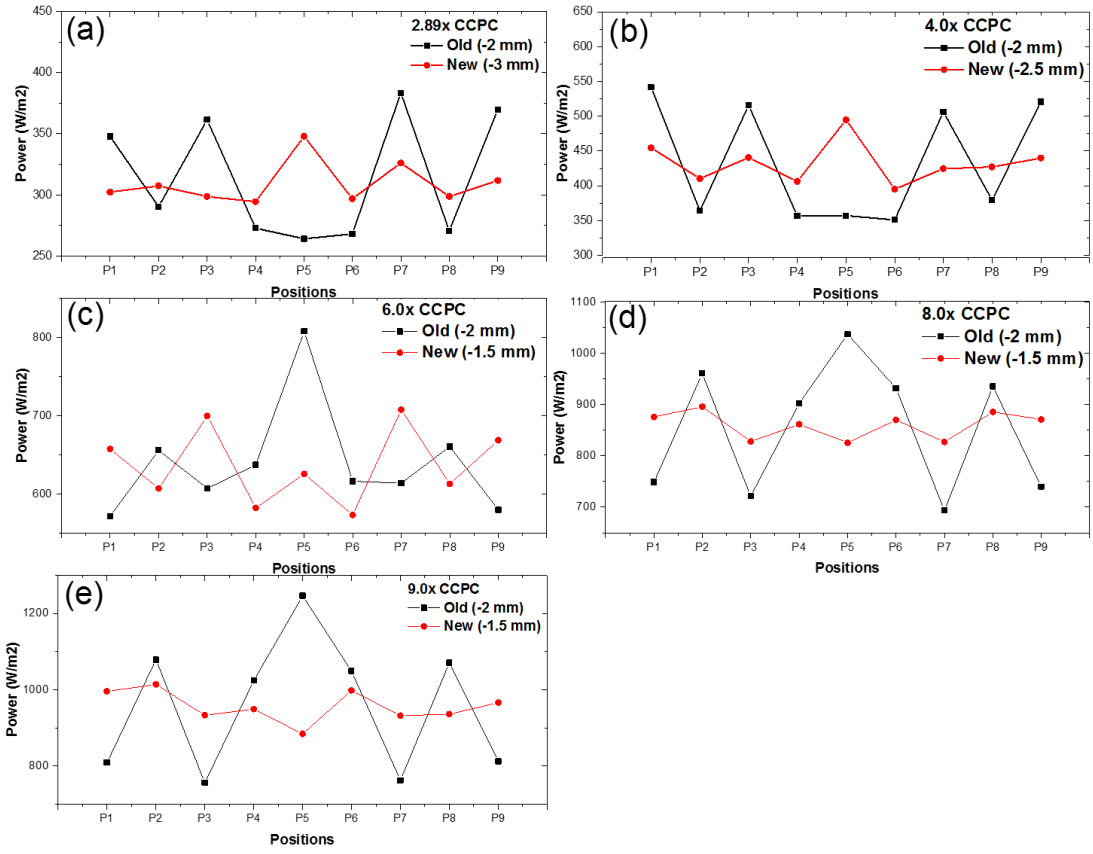

Figure 5.17: Simulation results for the nine position blocks of the improved design for: (a) 2.9x CCPC, (b) 4.0x CCPC, (c) 6.0x CCPC, (d) 8.3x CCPC and (e) 9.0x CCPC.

5.3.3.2 Experimental Validation of the Improved Design

After carrying out the simulation study of the solar cell position, the design of the CCPCs was modified in SolidWorks according to the optimal positions and the second batch of the concentrators (improved design) were fabricated. Figure 5.18 shows the photographs of the fabricated second batch of concentrators with a modification in the cell position, which involved reducing the thickness of the base plate of some of the concentrator, such as 6.0x and 9.0x.

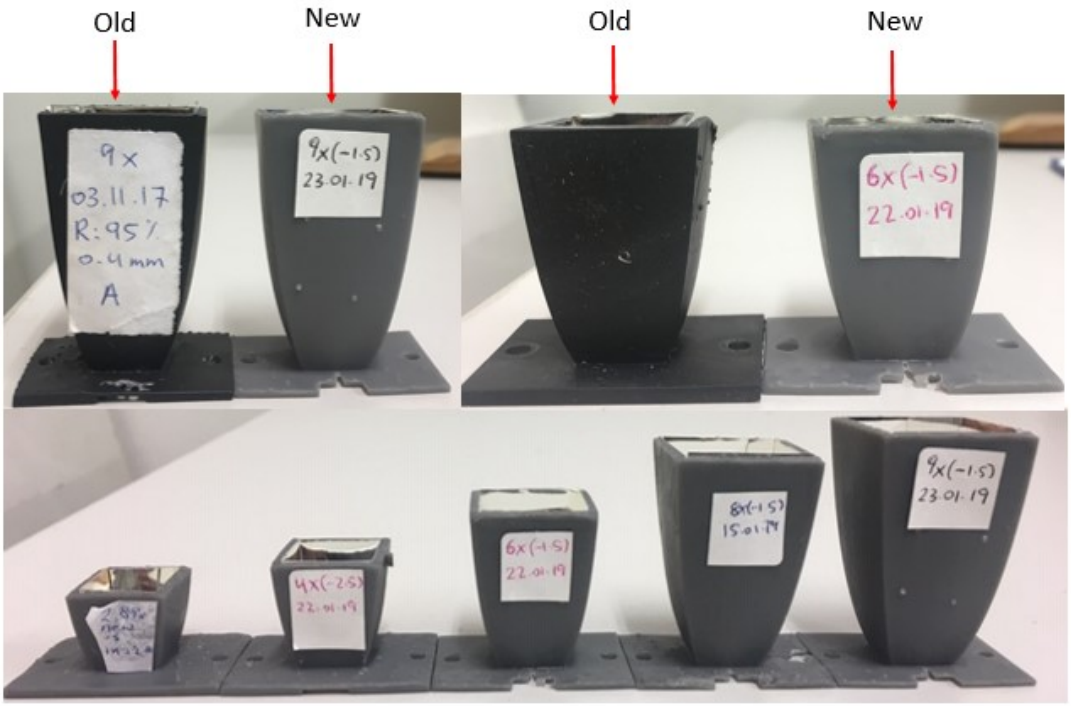

Figure 5.18: The second batch of the CCPC concentrators with improved design.

The new batch of concentrators was fabricated using the same fabrication process and the same aluminium reflector of 95% reflectivity as the first batch in order to see the effect of the solar cell position. It is noticed from Figure 5.18 that the thickness of the base plate of 6.0x and 9.0x CCPC in the new batch of concentrators is reduced by 0.5 mm.

The new batch of concentrators was first tested under one sun irradiance using the same solar cell, the same test conditions and processes that were used to obtain the I-V curves of the first batch. The old designs were also tested immediately following the completion of the first tests on the new batch to ensure the testing conditions as consistent as possible for fair comparison. Figure 5.19 displays the I-V curves for the bare cell, the old and the new batches of the CCPCs obtained at STC and under normal incidence (0°). The experiment results of the improved CCPC design show a marginal improvement over the

old design. This confirms the importance of the uniformity in concentrator design for obtaining large power output. Table 5.2 lists the performance parameters of the solar cell obtained from the bare cell, and those with the old and improved design of CCPCs. An increase in the power output of the solar cell can be seen clearly from all the concentrators in the new design.

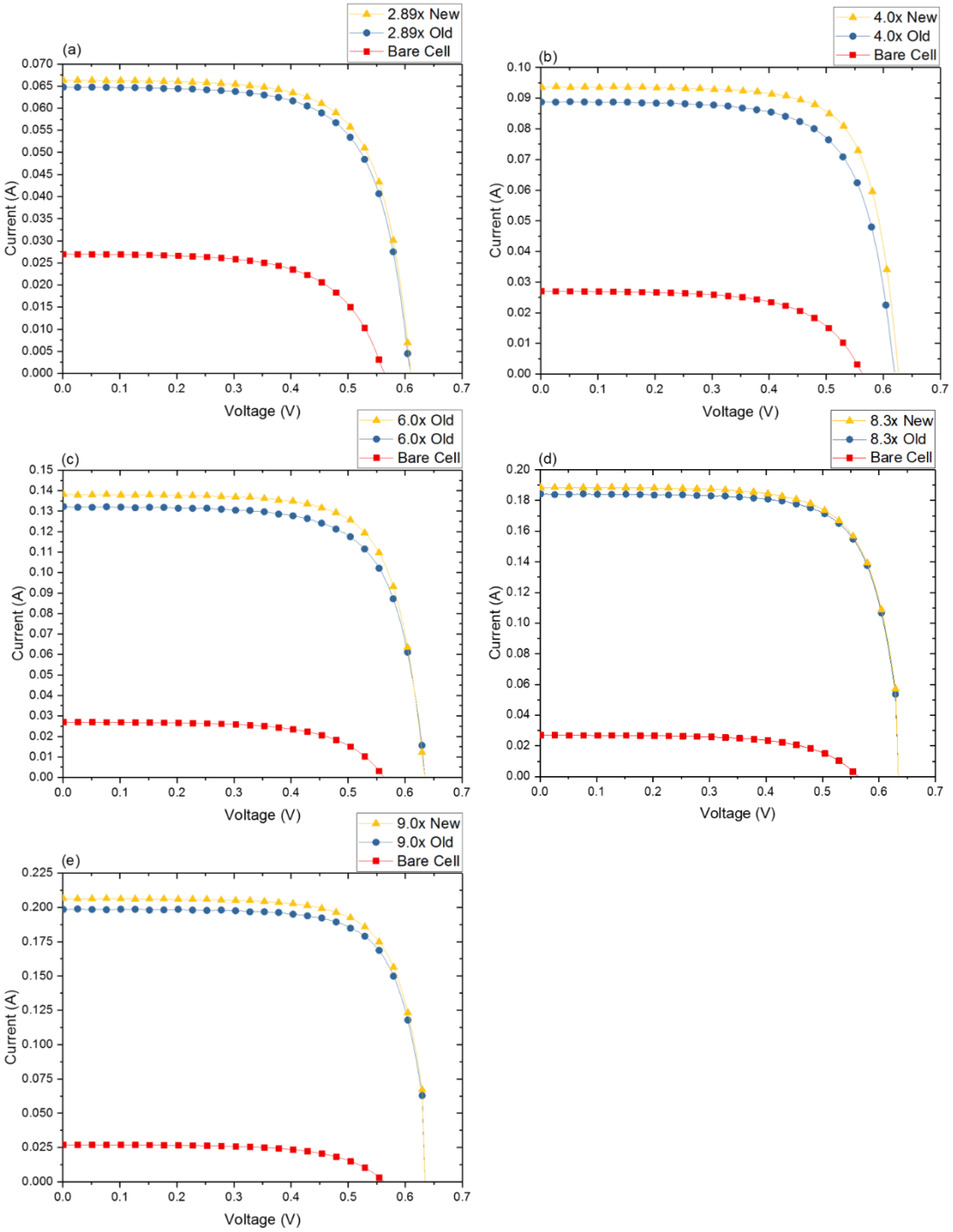

Figure 5.19: I-V curves comparison between the old and new designed batches.

Table 5.2: Electrical characteristics of the old and new design.

	Old design				New design			
CCPC (C_g)	**I_{sc} (A)**	**Cell effic. (%)**	**FF (%)**	**Power (mW)**	**I_{sc} (A)**	**Cell effic. (%)**	**FF (%)**	**Power (mW)**
Bare Cell	0.0270	9.55	63.00	9.55	—			
2.9x	0.0648	11.33	68.70	27.18	0.0664	11.50	70.30	28.30
4.0x	0.0889	11.70	69.70	38.50	0.0940	12.42	73.00	43.00
6.0x	0.1323	12.10	70.70	59.30	0.1383	12.40	72.00	63.50
8.3x	0.1843	12.65	72.90	87.30	0.1886	12.80	74.00	88.35
9.0x	0.1989	12.86	73.00	97.70	0.2066	12.88	73.40	98.55

The flux distribution was investigated experimentally again using the spectroradiometer with the nine holes in the copper sheet. Figure 5.20 shows the comparison of light distribution between the simulated and experimental results for the 2.9x concentrator only. The results show a good agreement between the simulation and experiment. Figure 5.20 shows the simulated and experimented power at -3 mm positions (improved design). The test was repeated three times and the average results is presented. The experimental uniformity for -3 mm is 86.89%. The difference between the two sets of data is that the simulation represents the average flux collected over the whole area of each section whereas the experimental data was obtained from a single point within the corresponding section. Table 5.3 shows the simulated results for an old and new design for the five CCPCs.

This experiment reveals that significant error could exist in determining the concentration ratio based on measuring the short-circuit currents due to the effect of non-uniformity. For accurate determination, the spectroradiometer should be employed.

Table 5.3: Simulated results for an old and new design for the five CCPC's using TracePro.

CR (x)	Avg. flux old (%)	Uniformity old (%)	Std.Dev old (%)	Avg. flux new (%)	Uniformity new (%)	Std.Dev new (%)
2.9x	314.24	85.58	48.46	309.34	91.68	17.21
4.0x	432.49	79.34	84.97	432.58	88.81	29.84
6.0x	638.81	82.85	70.30	638.50	92.61	33.72
8.3x	850.20	80.88	126.99	860.20	95.91	26.68
9.0x	956.65	75.05	175.08	956.55	93.16	41.15

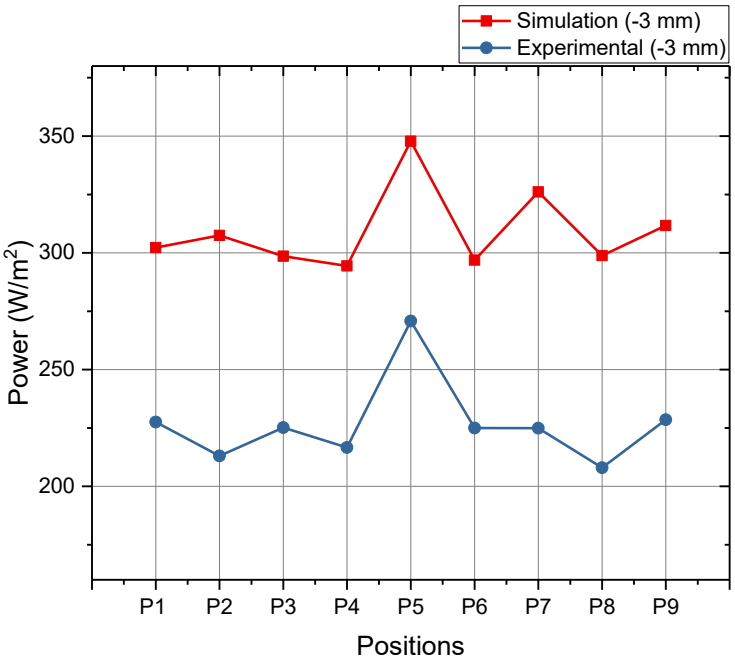

Figure 5.20: Simulated and experimental power as a function of the position for the 2.9x CCPC.

5.4 Rectangular Cross Compound Parabolic Concentrator (RCCPC)

The standard Cross Compound Parabolic Concentrator (CCPC) is a square shape for both entry area and exit area. A new type of CCPC was designed and investigated in this section, which has a square exit area but rectangular entry area. This new type of CCPC is referred to as the Rectangular Cross Compound Parabolic Concentrator (RCCPC). The purpose of this study is to investigate the angular response of the RCCPC in comparison with the standard CCPC, aiming to improve the angular response of the CCPCs with the same concentration ratio. The RCCPC has two different parabolic profiles and hence two different half acceptance angles in the east-west (E-W) and north-south (N-S) directions as shown in Figure 5.21.

5.4.1 RCCPC Design

The RCCPC was designed to have a rectangular entry aperture and square exit area with a geometrical concentration of 4.0x, which will be compared later with a square 4.0x CCPC. The same CCPC profile that was used to design the standard 4.0x CCPC (as explained in Chapter Four) is used for the 4.0x RCCPC. The changes were made on the entry aperture for both sides while keeping the same height. Consequently, the curve differs from the standard 4.0x CCPC (with a half acceptance angle of Θ_c= 30°), resulting

in a wide half acceptance angle of Θ_{c1}= 33.97° along the long side and a narrow half acceptance angle of Θ_{c2}= 26.59° along the short side, as illustrated in Figure 5.21.

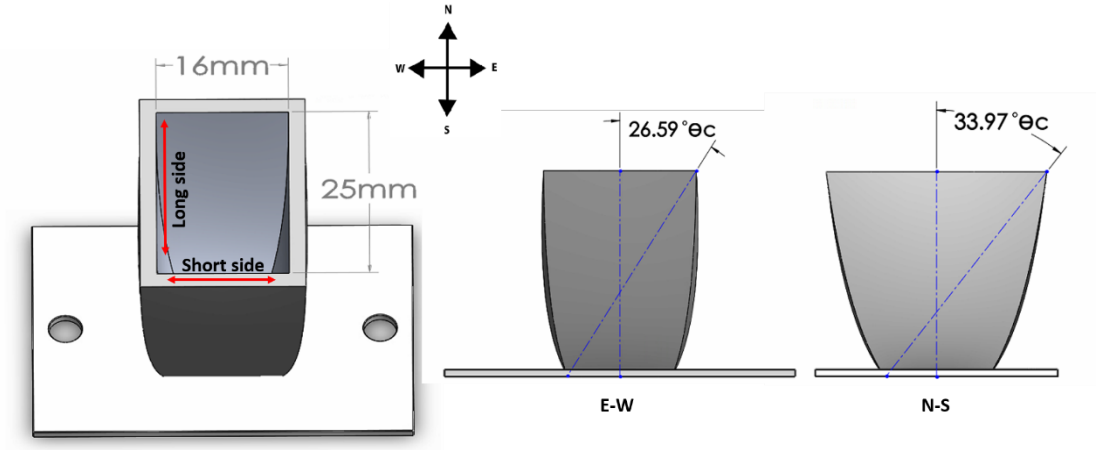

Figure 5.21: CAD design of the 4.0x RCCPC with long and short sides dimensions.

It can be seen in Figure 5.21 that the entry aperture of the RCCPC has a dimension of 16 mm on the short side and 25 mm on the long side, and the solar cell at the receiver end remains as 10 mm x 10 mm. This gives a geometrical concentration ratio of 4.0x. The angular response can be investigated along E-W (short side) and N-S (long side) direction, as shown in Figure 5.21.

5.4.2 Simulation

A ray-tracing simulation using the TracePro was performed to study the effect of the 4.0x RCCPC on its angular response due to the two different half acceptance angles and to compare it with the original 4.0x CCPC. This time, the source was applied in a rectangular shape to match the entry aperture of the asymmetric concentrator. Figure 5.22 shows the simulated optical efficiency for the E-W and N-S directions as a function of the incidence angle between 0° and ±45°.

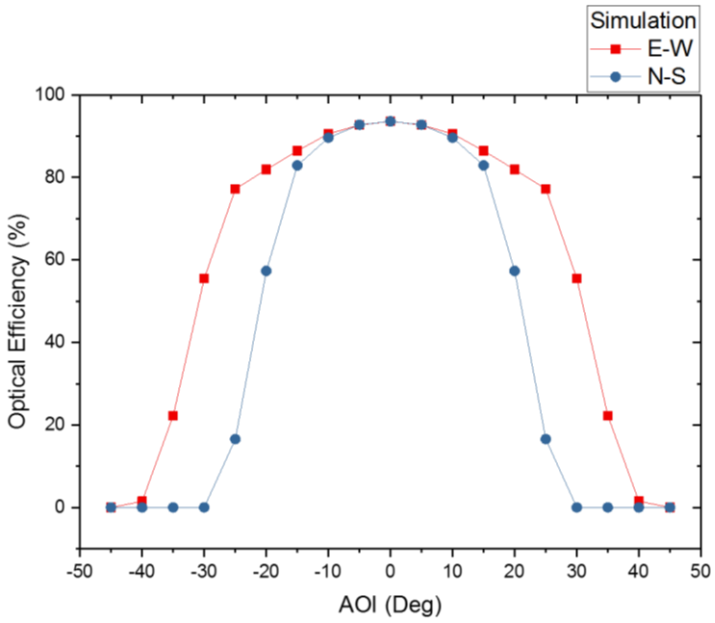

Figure 5.22: Simulated optical efficiency for the 4.0x RCCPC for both E-W and N-S directions.

The graph shows a wider angular response for the RCCPC in the E-W direction (short side) and a narrower angular response in the N-S direction (long side). This is an unexpected result but can be explained by the fact that the second reflection of the rays by the parabolic surface of the short-side walls fall back to the exit area, resulting a significant increase in half acceptance angle in the E-W direction. In the N-S direction, the rays from the second reflection are all coming out of the concentrator from the entry aperture. Only the rays from first reflection are able to fall onto the exit aperture. Figures 5.23 and 5.24 show the irradiance maps of the 4.0x RCCPC for different incidence angles along the E-W and N-S directions, respectively. It can be seen from Figure 5.23 that the rays falling onto the exit area at 30° and beyond are those subjected to the second reflection. It is clear that the increase in the half acceptance angle is due to the second reflection in a favourable direction.

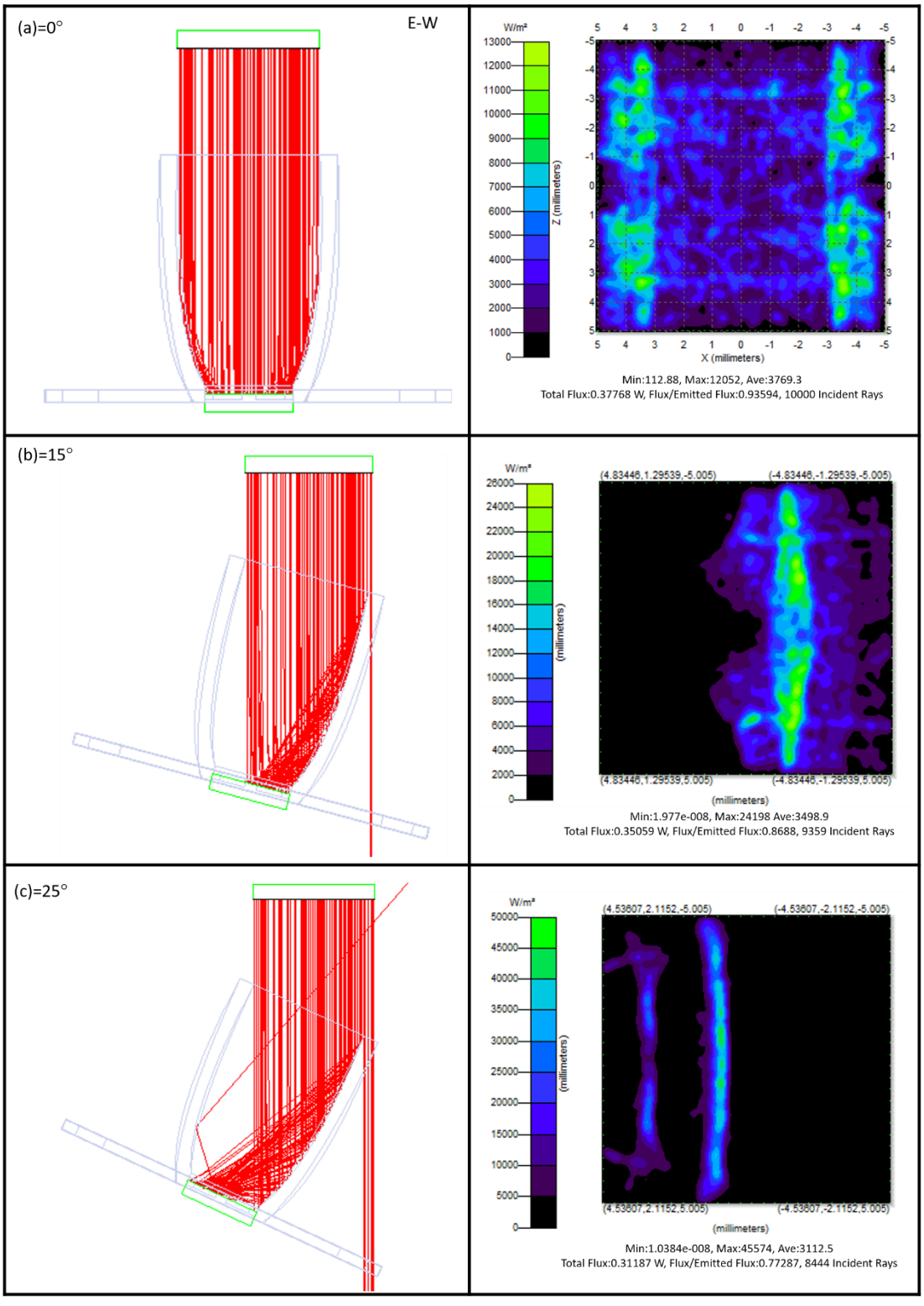
(a)=0°
E-W
W/m²
13000
12000
11000
10000
9000
8000
7000
6000
5000
4000
3000
2000
1000
0
Z (millimeters)
X (millimeters)
Min:112.88, Max:12052, Ave:3769.3
Total Flux:0.37768 W, Flux/Emitted Flux:0.93594, 10000 Incident Rays
(b)=15°
W/m²
26000
24000
22000
20000
18000
16000
14000
12000
10000
8000
6000
4000
2000
0
(millimeters)
(4.83446,1.29539,-5.005)
(-4.83446,-1.29539,-5.005)
(4.83446,1.29539,5.005)
(-4.83446,-1.29539,5.005)
(millimeters)
Min:1.977e-008, Max:24198 Ave:3498.9
Total Flux:0.35059 W, Flux/Emitted Flux:0.8688, 9359 Incident Rays
(c)=25°
W/m²
50000
45000
40000
35000
30000
25000
20000
15000
10000
5000
0
(millimeters)
(4.53807,2.1152,-5.005)
(-4.53807,-2.1152,-5.005)
(4.53807,2.1152,5.005)
(-4.53807,-2.1152,5.005)
(millimeters)
Min:1.0384e-008, Max:45574, Ave:3112.5
Total Flux:0.31187 W, Flux/Emitted Flux:0.77287, 8444 Incident Rays

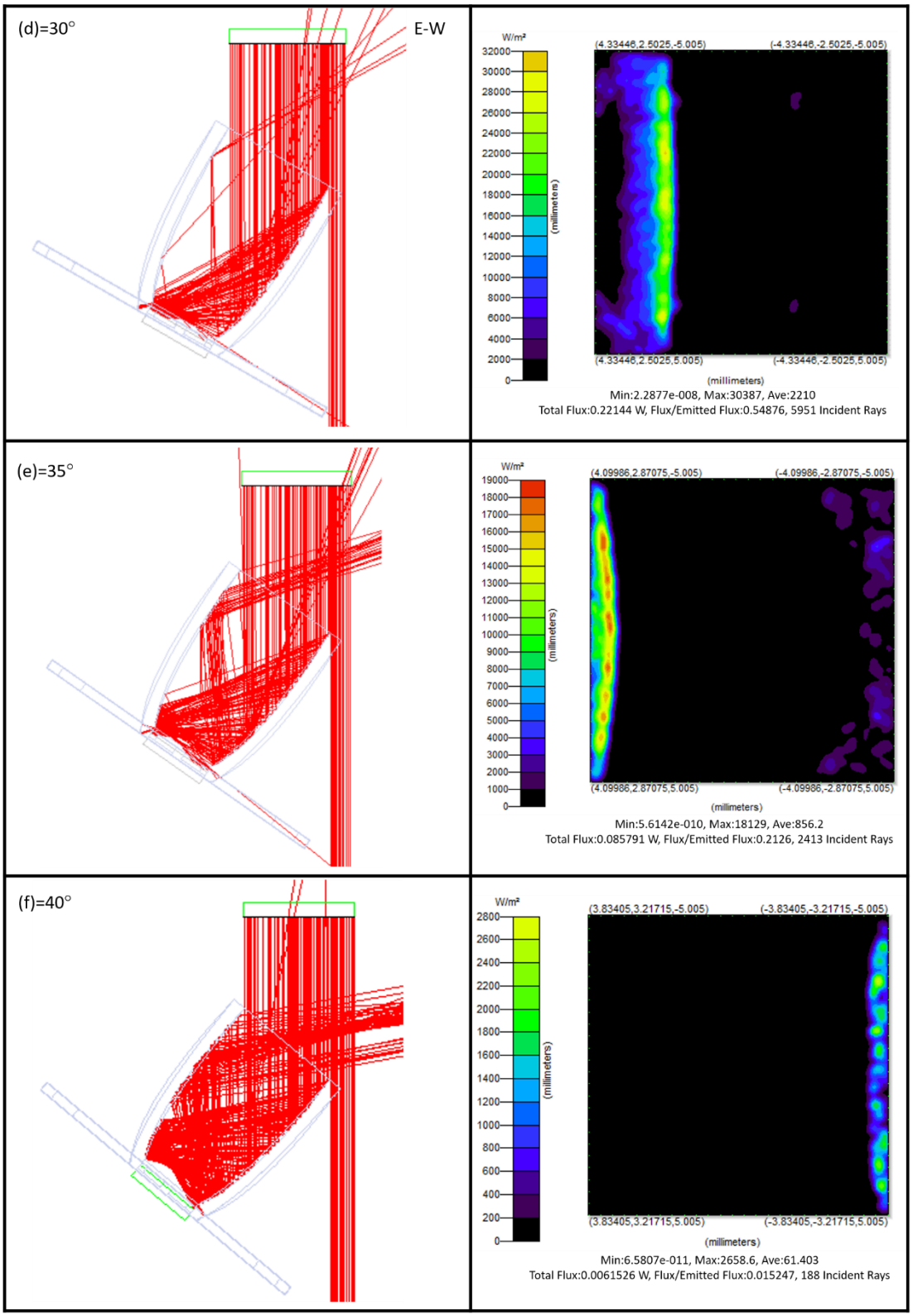

Figure 5.23: Simulated irradiance maps for the 4.0x RCCPC along E-W direction at: (a) AOI= 0°, (b) AOI= 15°, (c) AOI= 25°,(d) AOI= 30°, (e) AOI= 35°, (f) AOI= 40°.

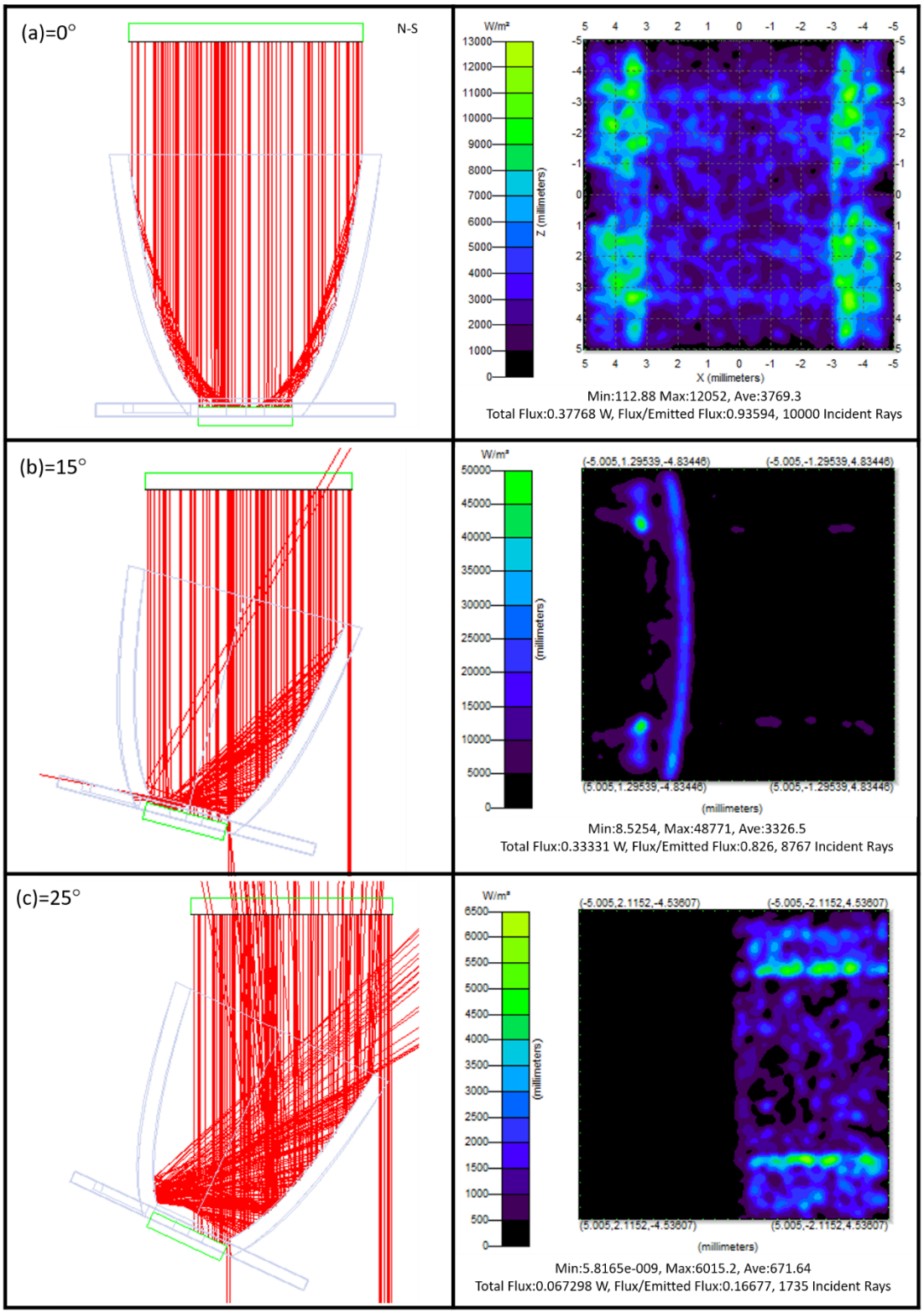
(a)=0°
N-S
W/m²
13000
12000
11000
10000
9000
8000
7000
6000
5000
4000
3000
2000
1000
0
Z (millimeters)
X (millimeters)
Min:112.88 Max:12052, Ave:3769.3
Total Flux:0.37768 W, Flux/Emitted Flux:0.93594, 10000 Incident Rays
(b)=15°
W/m²
50000
45000
40000
35000
30000
25000
20000
15000
10000
5000
0
(millimeters)
(-5.005,1.29539,-4.83446)
(-5.005,-1.29539,4.83446)
(5.005,1.29539,-4.83446)
(5.005,-1.29539,4.83446)
(millimeters)
Min:8.5254, Max:48771, Ave:3326.5
Total Flux:0.33331 W, Flux/Emitted Flux:0.826, 8767 Incident Rays
(c)=25°
W/m²
6500
6000
5500
5000
4500
4000
3500
3000
2500
2000
1500
1000
500
0
(millimeters)
(-5.005,2.1152,-4.53607)
(-5.005,-2.1152,4.53607)
(5.005,2.1152,-4.53607)
(5.005,-2.1152,4.53607)
(millimeters)
Min:5.8165e-009, Max:6015.2, Ave:671.64
Total Flux:0.067298 W, Flux/Emitted Flux:0.16677, 1735 Incident Rays

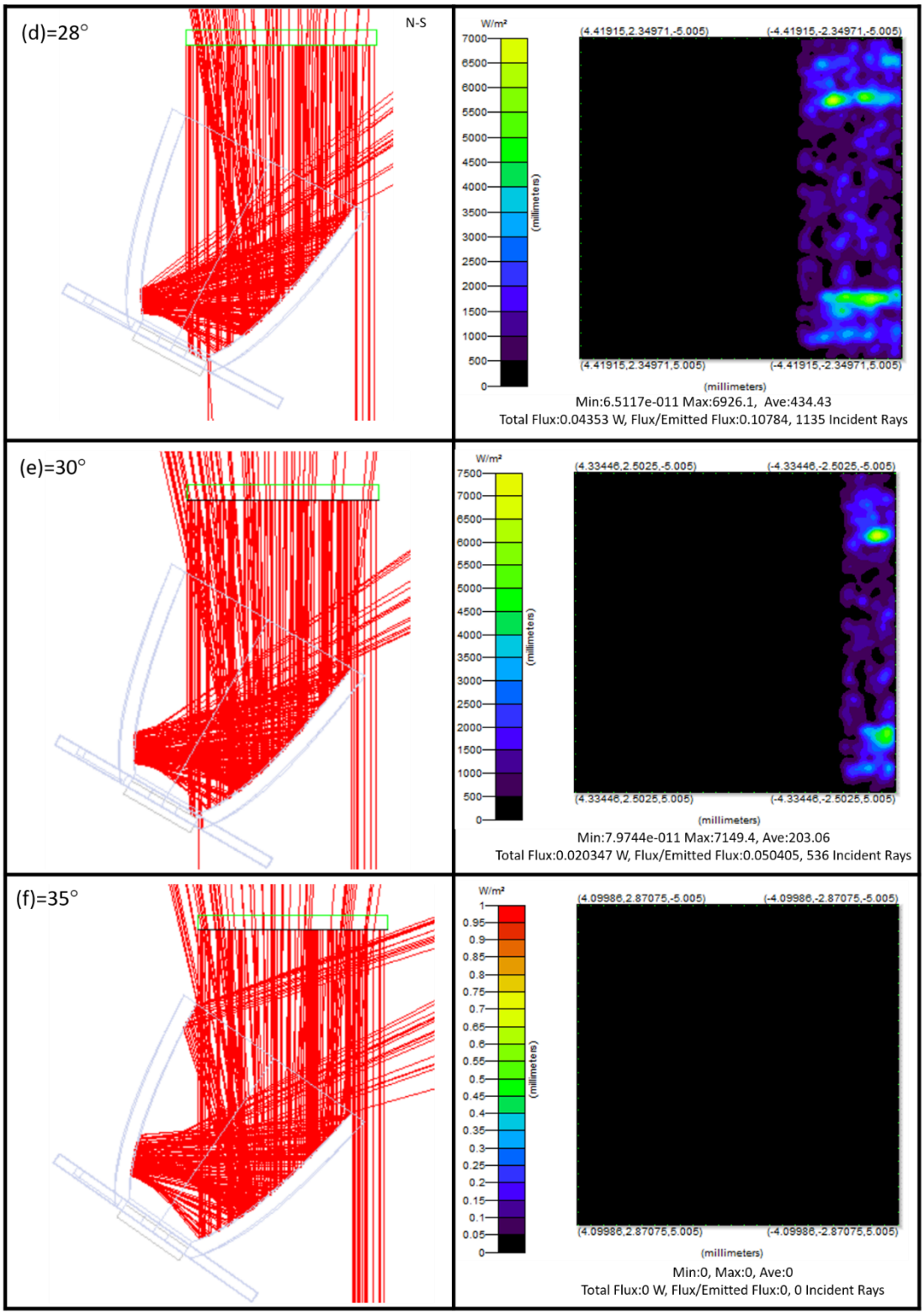

Figure 5.24: Simulated irradiance maps for the 4.0x RCCPC along N-S direction at: (a) AOI= 0°, (b) AOI= 15°, (c) AOI= 25°, (d) AOI= 28°, (e) AOI= 30° and (f) AOI= 35°.

A detailed inspection of Figure 5.23 shows that the receiver's surface collects all of the incoming rays at a normal incidence angle (0°) and the average flux received is 3769 W/m^2. For AOI at 15°, some incoming rays are still able to shine onto the receiver surface

directly while other of incoming rays reach the receiver surface after one reflection as shown in Figure 5.23 (b). The corresponding average flux is reduced to 3498.9 W/m^2 due to a decrease of the effective entry area. For AOI at 25° (Figure 5.23 (c)), all incoming rays that reach the receiver surface are reflected once and the average flux collected decreases further to 3112.5 W/m^2. For AOI at 30° and 35° (Figure 5.23 (d)-(F)), all incoming rays are reflected twice before reaching the receiver surface and the average flux is reduced to 2210 W/m^2 and 856.2 W/m^2, respectively. As the AOI increases further, the effective entry area reduces further and more rays that have entered the concentrator are reflected out until no rays are able to reach the receiver's surface, which corresponds to an AOI > 40° as shown in Figure 5.23 (f).

The angular response of the RCCPC along N-S direction exhibits a similar trend, except that the second reflection in this direction cannot reach the receiver surface. Instead, all incident rays after the second reflection are reflected out of the concentrator. It can be seen that the simulated half acceptance angle in this direction is very close to the theoretical value of 33.97°. It is interesting to note that the simulated half acceptance angle in the E-W direction is approximately 40°, which is significantly larger than the theoretical value of 26.59°. Moreover, the large half acceptance angle is obtained without causing any reduction in the concentration ratio and optical efficiency. This result provides an important insight into the possibility of achieving improved half acceptance angle through geometrical design by considering the second reflection.

Finally, it is to be noted that the light distribution becomes increasingly non-uniform as AOI increases and the uniformity becomes worse for the RCCPC than for the standard CCPC. As demonstrated in the previous section, the non-uniformity degrades the performance of the solar cells. In addition, it may lead to cell deterioration, due to operating under highly inhomogeneous light intensity across the cell surface.

Based on the irradiance maps in Figure 5.23 and Figure 5.24, the average light intensity as a function of the AOI can be calculated. The results are presented in Figure 5.25 for both E-W and N-S directions. It can be seen that the highest light intensity of 3769.3 W/m^2 is obtained at AOI=0° and it decreases as the AOI increases. However, the average light intensity decreases much faster in the N-S direction than in the E-W direction once the AOI is larger than 20°.

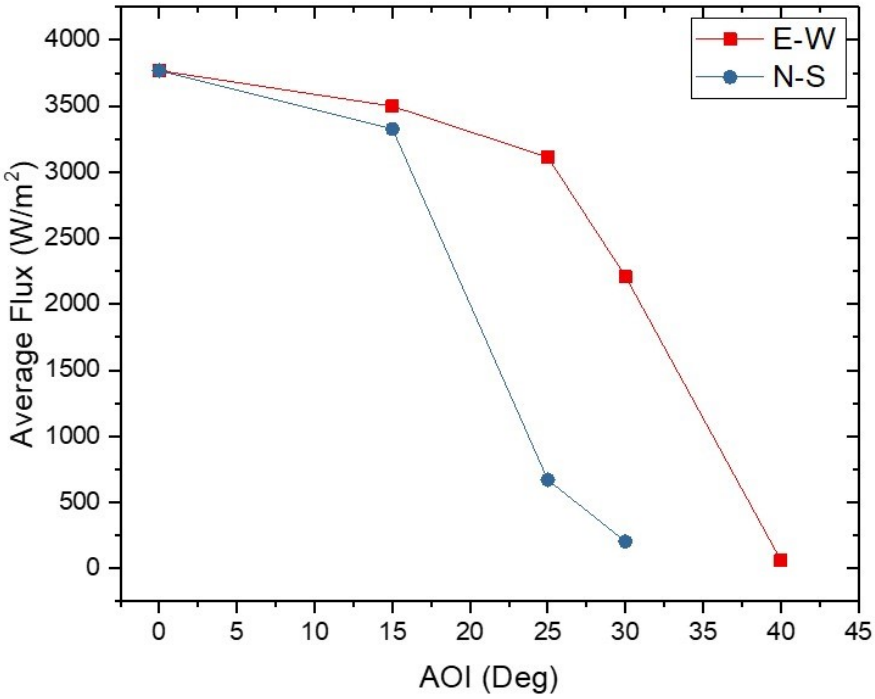

Figure 5.25: Average flux incidence on the receiver surface for E-W and N-S directions at different incident angles.

5.4.3 Experimental Result and Discussion

The experimental work is conducted to validate the findings of the simulation study. The concentrator was fabricated using a 3D printer, as described in Section 3.5.1. The same reflector material with specular reflectivity of 95% is applied to the internal surface of the concentrators. Figure 5.26 shows a photograph of the printed 4.0x RCCPC.

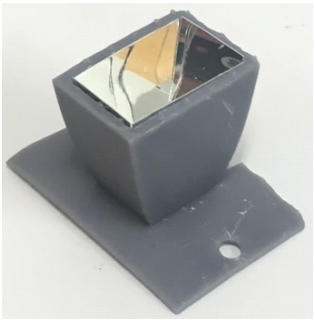

Figure 5.26: A photograph of the fabricated 4.0x RCCPC.

The tests were carried out using the measurement system described in Chapter Three. The temperature of the solar cell was maintained at 25° and the I-V curves were taken at a different incidence angle, which varied from 0° to 45°. Each test was repeated three times. Figure 5.27 shows the average values of the power output obtained from the three experiments (in black) compared with the power output of the simulated results (in red).

The average deviation between the simulation and experimental is 3.1% for the concentrator rotating along the E-W direction with the AOI varying from 0° to 25°, while the average deviation for the N-S direction is 9.0% for the same angles. Clearly, the simulation and experiment are in a good agreement.

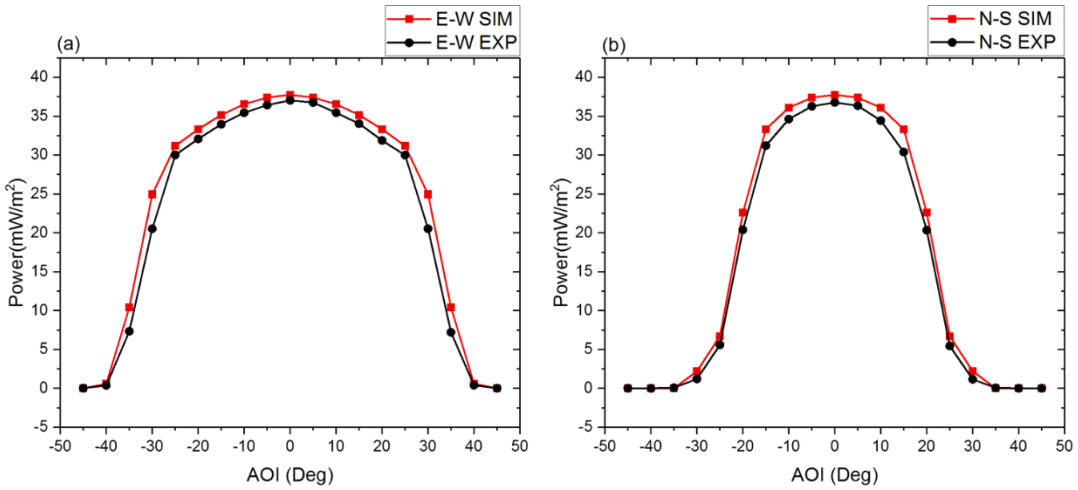

Figure 5.27: Simulation and experimental results of the power output of the 4.0x RCCPC.

The possibility to improve the angular response of the standard CCPCs was also investigated. Previously, the angular response was determined by positioning a CCPC with its sides in parallel to the sides of the base of the rotary stage as shown in Figure 5.28 (a). In this experiment, the test was carried out by positioning a standard 4.0x CCPC with its sides at 45 degrees in respect to the sides of the base of the rotary stage as shown in Figure 5.29 (b). The angular response was then determined by rotating the rotary stage as shown in Figure 5.28 (d). Figure 5.28 (e) shows a photograph of the experimental setup.

Figure 5.29 shows the experimental results of the angular responses obtained from a standard 4.0x CCPC positioned in parallel position and 45° position, respectively. The experimental results from a 4.0x RCCPC along E-W and N-S directions are also included for comparison. It can be seen from Figure 5.29 that the angular response is improved slightly by positioning the standard 4.0x CCPC at 45° (blue line), compared to the standard 4.0x CCPC positioned in parallel (black line). However, a significant improvement is achieved by using the 4.0x RCCPC in E-W direction (red line), although the power output at lower angles appears to be slightly lower than that of the standard 4.0x CCPC. It is anticipated that a RCCPC can produce more total energy than a standard CCPC when used in stationary operation. Meanwhile, the RCCPCs have a narrower

angular response in the N-S direction. It is crucial to ensure that the RCCPCs are operated in the E-W direction to obtain the maximum benefits.

The usefulness and potential benefit of a concentrator with improved angular response is to reduce the number of movements of the tracking system, which will be demonstrated in Chapter Six.

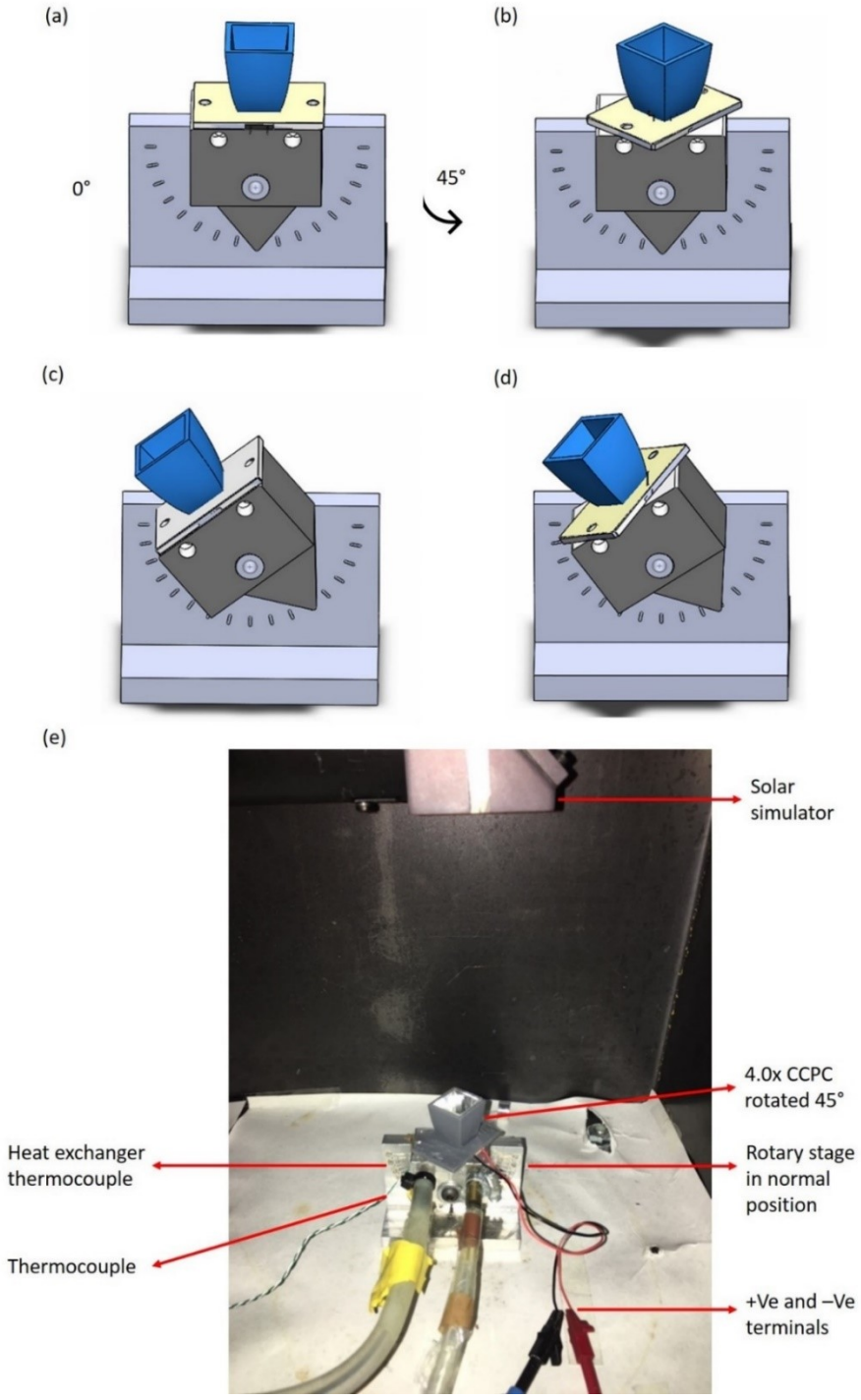

Figure 5.28: Illustration of angular response experiments in two different positions: (a) standard position at AOI=0°, (b) 45° position at AOI=0°, (c) standard position at AOI=30°, (d) 45° position at AOI=30°, and (e) a photograph of the experimental setup.

Figure 5.29 shows a power output comparison between the original 4.0x CCPC, the 4.0x CCPC rotated at 45°, and the 4.0x RCCPC at E-W and N-S.

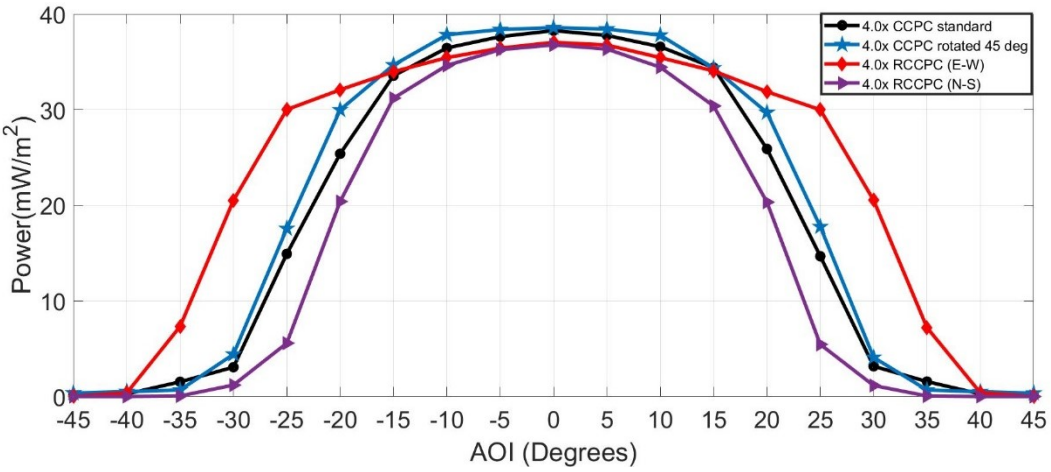

Figure 5.29: Experimental results for the 4.0x CCPC normal, 4.0x CCPC rotated at 45° and 4.0x RCCPC at E-W and N-S directions.

5.5 Summary

The main objectives for this chapter are to investigate the angular response of the concentrators developed in Chapter Four and to explore the possibility of further improvement. The angular responses of the five CCPCs of different concentration ratios were determined and the results show that the half acceptance angle of the CCPCs decreases as the concentration ratio increases, as predicted by TracePro simulation.

An attempt was made to improve the uniformity of the light distribution of the CCPCs, which were shown to have a noticeable effect on the power output of the solar concentrator system. A systematic study reveals that the uniformity is very sensitive to the distance between the exit aperture of the concentrator and the top surface of the solar cell. High uniformity over 90% can be achieved by placing the solar cell at an optimal position that ranges from 1 mm to 3 mm below the exit aperture of the concentrators, depending on the concentration ratio of a specific concentrator.

The possibility of improving the angular response for a given concentration ratio was explored. One method is to simply rotate a standard CCPC by 45° in the horizontal plane. The experimental result using the 4.0x CCPC shows that the light intensity has been increased within the angles of 15° and 25°, compared with those of the standard setup. A much larger improvement was found by using a rectangular CCPC operating in E-W direction. In this case, both the half acceptance angle and the light intensity within the

range of 15° and 40° are substantially improved. The simulation results indicate that the improvement happens because a significant amount of light after second reflection fall onto the exit aperture even when the incidence angle is larger than the half acceptance angle. To my knowledge, this result is the first experimental evidence to demonstrate that the angular response of CCPCs can be improved by including multiple light reflections in a geometrical design.

Chapter Six: Energy Production Optimisation

6.1 Introduction

This chapter describes the calculation of the daily energy production of the fabricated CCPCs when they are used in non-stationary solar concentrator systems. A tracking system can be employed to maximise the collection of solar radiation, whose incident angle changes with time. The optimal tracking movement for each concentrator is determined in order to minimise the number of tracking movements and thus reduce the cost of the tracking system. The calculations were initially performed under a fixed solar radiation of 1000W/m^2, and then under a varied radiation based on real solar data. Finally, the costs analysis and economic viability are discussed.

6.2 Tracking Model for CPV

The objective of carrying out the energy calculation is to identify the amount of energy that produced by the cell coupled with the concentrator in a day and the corresponding optimal tracking movements that deliver the highest energy production with the least number of tracking movements. In principle, in order to obtain the maximum energy production, constant tracking is needed to ensure that the angle of incidence (AOI) of the rays is always perpendicular to the entry aperture of the concentrator.

6.2.1 Fixed Radiation

The calculation of the optimal tracking movements was first carried out under a fixed solar radiation, using the energy results obtained from the angular response indoor experiments of the fabricated concentrators. In this case, solar radiation is generated from a solar simulator and, thus, the following assumptions were made.

6.2.1.1 Assumptions

The assumptions that were made to calculate the energy production under a fixed solar radiation are:

1. A fixed solar radiation of 1000 W/m^2 is used to approximate the real solar radiation, so that the data from indoor experiments on the angular response can be employed directly.
2. The sky is clear with no clouds and diffuse radiation (ideal case).

6.2.1.2 Fixed Radiation Calculation Procedures

The calculation procedure is the same for all concentrators of different concentration ratios, except for some minor deviations in the procedure depending on the number of movements and the overlap condition. The procedure is demonstrated as follows using an example based on the 4.0x CCPC, but it is valid for all of the other concentration ratios.

Procedure for Calculating Energy Production at 5° Intervals

1. The power output against the solar incidence angle is collected at intervals of 5° using the results of angular response experiments (the units of power were converted from mW to W).
2. The length of time that corresponds to the solar incidence change needs to be determined. It is known that the sun moves 15° per hour [197]. Therefore, it takes 20 minutes for the sun to move 5°.
3. The energy produced over every 20 minutes can be calculated using the average power output between the two angles of 5° difference to multiplying the length of time (20 minutes) and then convert it to hour.
4. The calculation will cover the angular change from 0° to 180° that corresponds to the sun movement from sunrise to sunset.

Case1: No Movement

In the case of no movement, the concentrator was positioned with its axis aligned vertically (i.e., in parallel to 90°) and the sunlight can only reach the solar cell within the full acceptance angle of the concentrator. For the 4.0x CCPC, this is between 60° and 120°, as shown in Figure 6.1. Table 6.1 lists the power output as a function of the solar radiation incidence angle for 4.0x CCPC, which were determined in Chapter Five, and corresponding energy production over every 5°, which were calculated based on the procedure described above. The total energy production in a day using the 4.0x CCPC is the sum of 12 points, which gives 0.11 Wh.

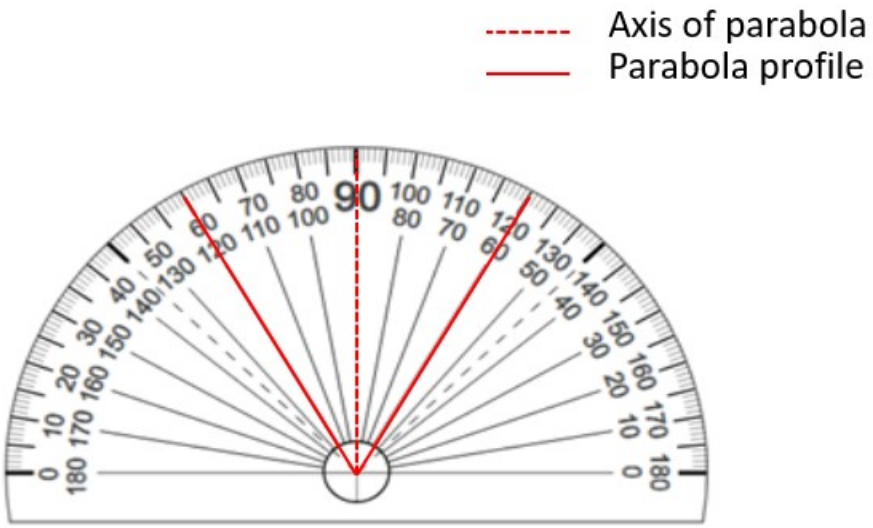

Figure 6.1: No movement case protractor representation for the 4.0x CCPC.

Table 6.1: Power output as a function of the solar radiation incidence angle for 4.0x CCPC.

File of View 180°	60°	65°	70°	75°	80°	85°	90°	95°	100°	105°	110°	115°	120°
Rotary stage angles	-30	-25	-20	-15	-10	-5	0	5	10	15	20	25	30
Power (mW)	3.077	14.924	25.389	33.551	36.451	37.636	39.264	37.76	36.582	34.391	25.898	14.678	3.175
Power (W)	0.003	0.015	0.025	0.034	0.036	0.038	0.039	0.038	0.037	0.034	0.026	0.015	0.003

Number of Points	1	2	3	4	5	6	7	8	9	10	11	12
Angle	(60°-65°)	(65°-70°)	(70°-75°)	(75°-80°)	(80°-85°)	(85°-90°)	(90°-95°)	(95°-100°)	(100°-105°)	(105°-110°)	(110°-115°)	(115°-120°)
Energy (Wh)	0.0030	0.0067	0.0098	0.0117	0.0123	0.0128	0.0128	0.0124	0.0118	0.0100	0.0068	0.0030

Figure 6.2 shows the energy produced by the 4.0x CCPC at 12 points (intervals) within the full acceptance angle. Because the concentrator is stationary in a vertical position, the best angles that can harvest the maximum energy are the angle between 85° and 90°, and the one between 90° and 95°, which correspond to interval 6 and 7 (circled in red), respectively. In Table 6.1, it can be seen that the energy collected during intervals 6 and 7 is 0.0128 Wh, while it is only 0.0030 Wh during the intervals 1 and 12, thus providing that tracking can improve the energy collection.

It is to be noted that the number of intervals is different for the concentrators with different full acceptance angles. For a concentrator of known full acceptance angle, the number of points can be calculated using the formula below:

$$\text{Number of intervals} = \frac{Full\ acceptance\ angle}{5} \qquad (6.1)$$

where, 5 represents a change of 5°.

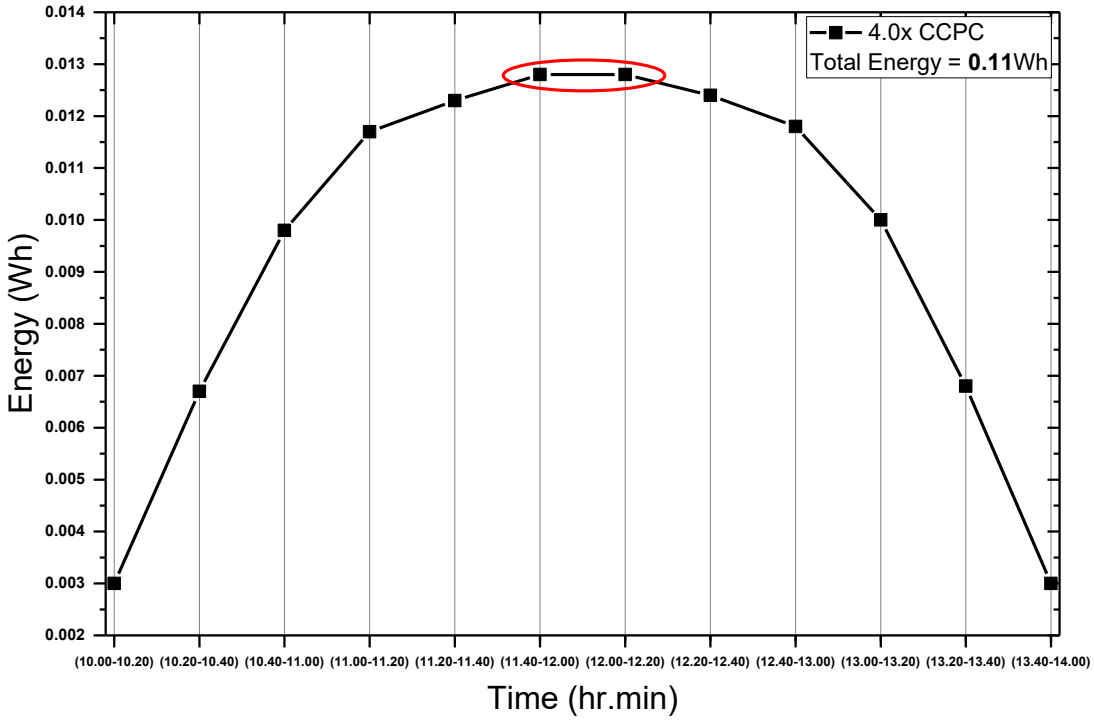

Figure 6.2: Energy collected using the 4.0x CCPC during 12 intervals against the time of the day.

Case 2: One Movement

To increase the energy collection for the 4.0x CCPC, the concentrator was initially positioned by aligning its axis at 60° to the horizontal plane and then making one movement to 120° in response to the sun's movement, as shown in Figure 6.3 (a). Based on the assumption of fixed solar radiation (i.e., the light intensity does not change with the incident angles) and no overlap between the two positions, the total energy collected in this case is simply twice that of Case 1.

Case 3: Two Movements

Because the 4.0x CCPC has a full acceptance angle of 60°, it can be used to cover 180° by two movements without any overlap as shown in Figure 6.3 (b). In this case, the concentrator is initially positioned with its axis at 30°, and it moves to 90° and 150° in response to the sun's movement. Based on the same assumptions as described in Case 2, the total energy collected in this case is three time of Case 1.

Overlap occurs when two sets of data share the same points. For a concentrator that has a full acceptance angle of θ, the overlap will definitely occur if,

$$\theta(n+1) > 180° \tag{6.2}$$

where, n is the movement without causing overlap. Clearly, the overlap will happen for the 4.0x CCPC if n>2.

Case 4: Three Movements

This case describes three movements that led to the overlap. For the 4.0x CCPC, overlap occurs after three movements. When the number of movements increases, the intervals producing the least energy on the angular response curves are removed from the dataset (i.e., points 1 and 12 in Figure 6.2), which are used to calculated energy collected at large light incidence angles. Appropriate arrangement of overlaps can eliminate the data points that contribute least to energy production. Consequently, the points with higher energy values remain. In this case, an effective acceptance angle can be defined and used for energy production calculation. For a concentrator operation that satisfies equation 6.2, the effective acceptance angle, Θ_e, of a concentrator can be calculated using,

$$\Theta_e = \frac{180}{n+1} \tag{6.3}$$

using equation (6.3), the effective acceptance angle of the 4.0x CCPC for n=3 will be reduced from 60° to 45°. Consequently, the number of intervals required for energy production calculation will be reduced to 9, as indicated by equation (6.1). Figure 6.3 (c) shows the arrangement of the tracking movements for this case. It can be seen that the least productive intervals in the angular response of the 4.0x CCPC becomes irrelevant. In the energy production calculation, only intervals 2 to 10 were used, and intervals 1, 11 and 12 were discarded.

Case 5: Eight Movements and More

The calculation of eight movements of the 4.0x CCPC follows the same process described in Case 4. Using equation (6.1) and (6.3), the results show that the effective acceptance angle for n=8 is 20° and the number of intervals needed for energy production calculation is 4. Figure 6.3 (d) illustrates the arrangement for eight tracking movements of the 4.0x CCPC with an effective acceptance angle of 20° and four intervals for each movement. The same process may be performed with 17 movements and 35 movements, as shown in Figure 6.3 (e) and (f), respectively. When the number of movements of the concentrator increases, the overlap between the acceptance angles of the concentrator increases and the effective acceptance angle becomes narrower. This leads to the removal of more intervals of low energy value and, consequently, only the highest interval for energy production remains for the case with 35 movements.

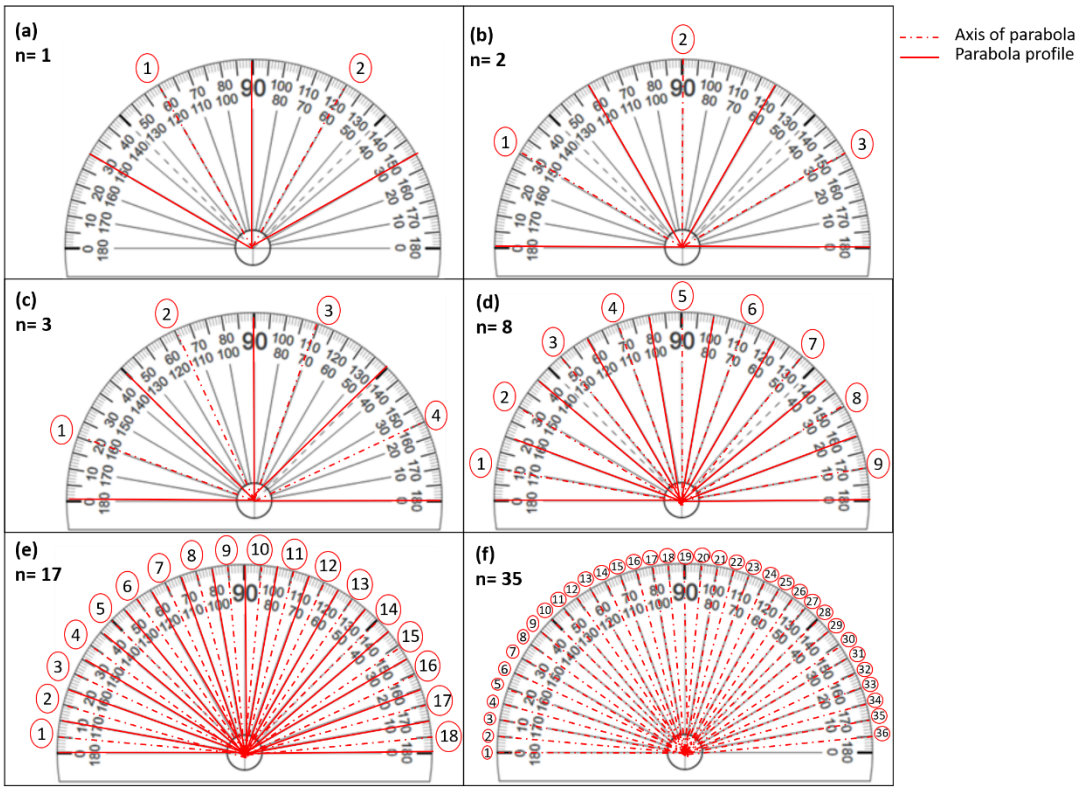

Figure 6.3: 4.0x CCPC movements: (a) 1 movement, (b) 2 movements, (c) 3 movements, (d) 8 movements, (e) 17 movements, and (f) 35 movements.

For each tracking arrangement, the energy produced using the 4.0x CCPC can be calculated using this method. Figure 6.4 presents the daily energy production as a function of the tracking movements using the 4.0x CCPC. The amount of energy produced increases with an increase in tracking movements. Moreover, the energy increases rapidly for the first four movements and it then approaches saturation after the fifth movement. This result indicates that an optimal tracking movement exists, which represents a trade-off between the maximum energy collection and the minimum tracking movements. For the 4.0x CCPC, the optimal tracking number is found to be five, because an increase in the tracking movements from 5 to 35 only leads to an increase from 0.443 Wh to 0.462 Wh, which is a percentage increase of less than 5%. An important implication of this result is that a significant increase in daily energy production can be obtained by a few simple tracking movements. This can lead to a substantial reduction in the cost of tracking systems.

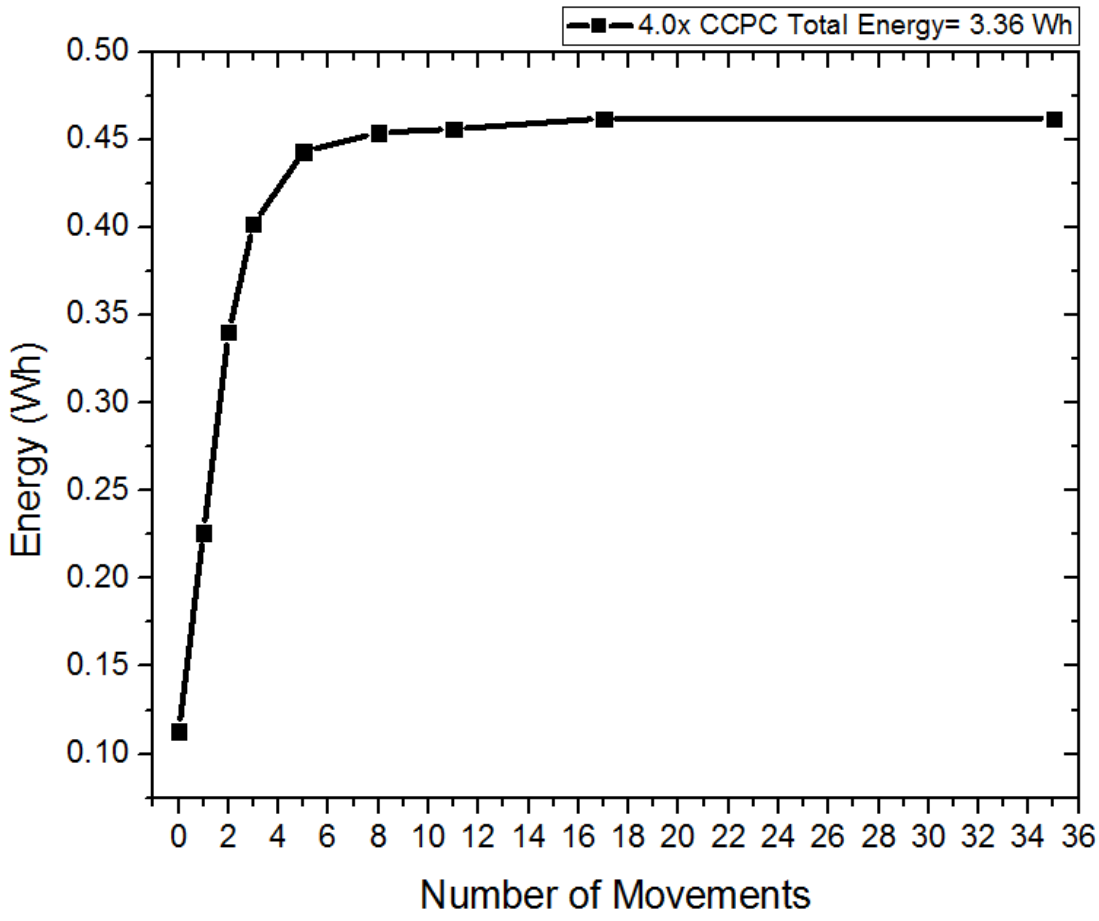

Figure 6.4: The number of tracking movements and the corresponding energy (Wh) production using the 4.0x CCPC.

Tracking Calculation Procedure for 9.0x CCPC

This calculation follows exactly the same procedure as described earlier for the 4.0x CCPC, except for using the angular response data of the 9.0x CCPC obtained in Chapter Five. Because this concentrator has a full acceptance angle of 40°, it can produce power from 70° to 110° when it is positioned vertically in a stationary operation (Figure 6.5), which corresponds to a period from 10:40 hrs to 13:20 hrs. Figure 6.5 shows the energy production at each interval of 5°, which was calculated based on the experimental data of the angular response of the 9.0x CCPC under fixed solar illumination. There are eight intervals in total, due to the narrower full acceptance angle of the 9.0x CCPC, compared with the 4.0x CCPC that has 12 intervals. The intervals that produce the maximum amount of energy are points 4 and 5, which corresponds to the time from 11.40 hrs to 12.20 hrs.

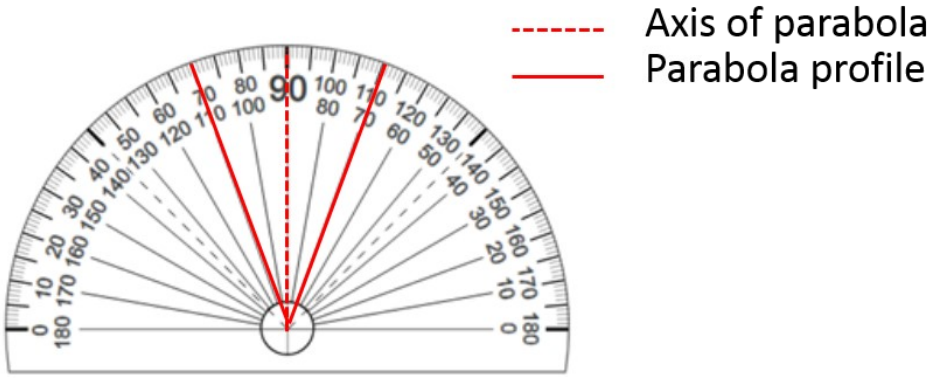

Figure 6.5: 9.0x CCPC concentrator full acceptance angle representation with no movement using a protractor.

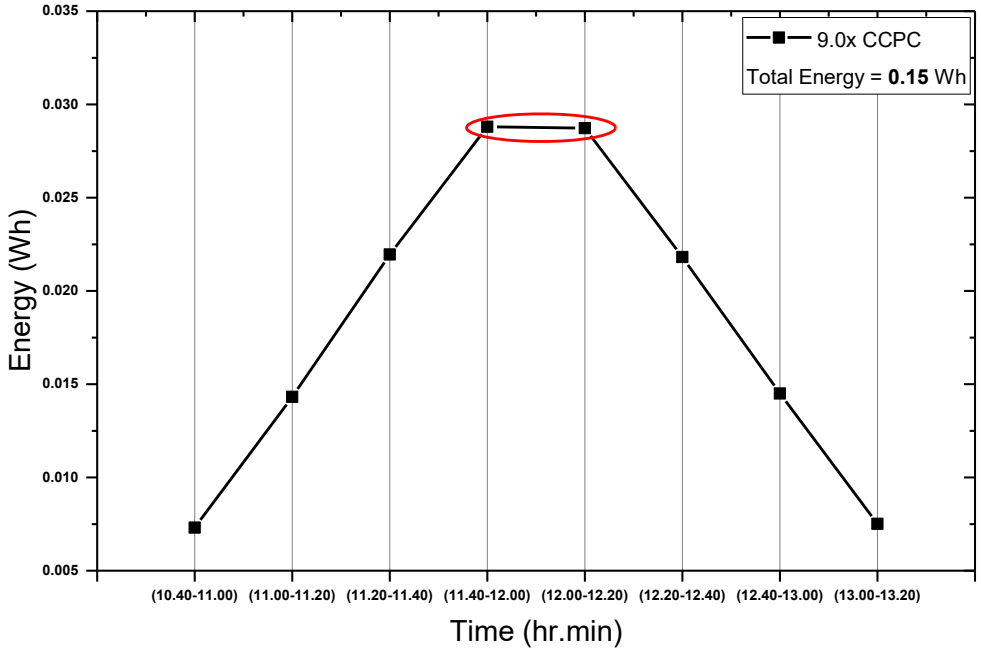

Figure 6.6: Energy-Time graph for the 9.0x CCPC within its full acceptance angle.

For this concentrator, the overlap can be avoided if the number of tracking movement is n < 4 because its full acceptance angle is 40°. However, the overlap will start to occur if $n \geq 4$. With four movements, the calculation of energy production of this concentrator will involve seven intervals, with either the first or last point being discarded. With increasing tracking movement, more points that are less productive will be discarded, which results in an increase in total daily energy production.

6.2.1.3 Results

The same procedure as described earlier for the 4.0x CCPC and the 9.0x CCPC was applied to the other concentrators investigated in this work, in order to determine the optimal tracking movement. Table 6.2 summaries the key characteristics of the angular response

of all of the concentrators investigated in this research. It can be observed from Table 6.2 that the lowest concentration ratio (i.e., 2.9x) has more intervals to collect the sunlight and hence a longer period for energy production. This is due to a wide full acceptance angle of 70°, while the highest concentration ratio (i.e., 9.0x) has less intervals and thus a shorter period where the concentrator is capable of collecting sunlight. This is due to a narrow full acceptance angle of approximately 40°.

Table 6.2: Number of intervals and effective operating period, and the angles of each concentration ratio.

Concentration ratio (x)	No. of energy points	Time range (hr. min)	Angle range (from 0° to 180°)
2.9	14	10.00 – 14.20	60° – 125°
4.0	12	10.20 – 14.00	65° – 120°
6.0	10	10.40 – 13.40	70° – 115°
8.3	8	11.00 – 13.20	75° – 110°
9.0	8	11.00 – 13.20	75° – 110°

The daily energy production as a function of tracking movements were calculated for all five concentrators using the method explained earlier. The results are shown in Figure 6.7, with the optimal number of tracking movements marked by a black circle for each concentrator. The optimal number was determined based on a trade-off between the maximum energy production and minimum tracking movements. For the 2.9x CCPC, the optimal number of tracking movements is three, which gives a daily energy production of 0.283 Wh. The optimal number of tracking movements for the 4.0x CCPC is five, which corresponds to a daily energy production of 0.443 Wh. Similarly, the optimal numbers of tracking movements for the 6.0x, 8.3x and 9.0 CCPCs are 8, 11 and 11, and their corresponding daily energy productions are 0.641 Wh, 0.941 Wh and 0.954 Wh, respectively. Clearly, the optimal tracking movement increases with the increasing concentration ratio of the concentrators, due to the fact that the acceptance angle decreases with an increase in the concentrator ratio. Concentrators with a low concentration ratio only require a few tracking movements in a day but will result in a significant improvement in daily energy production compared with the stationary operation.

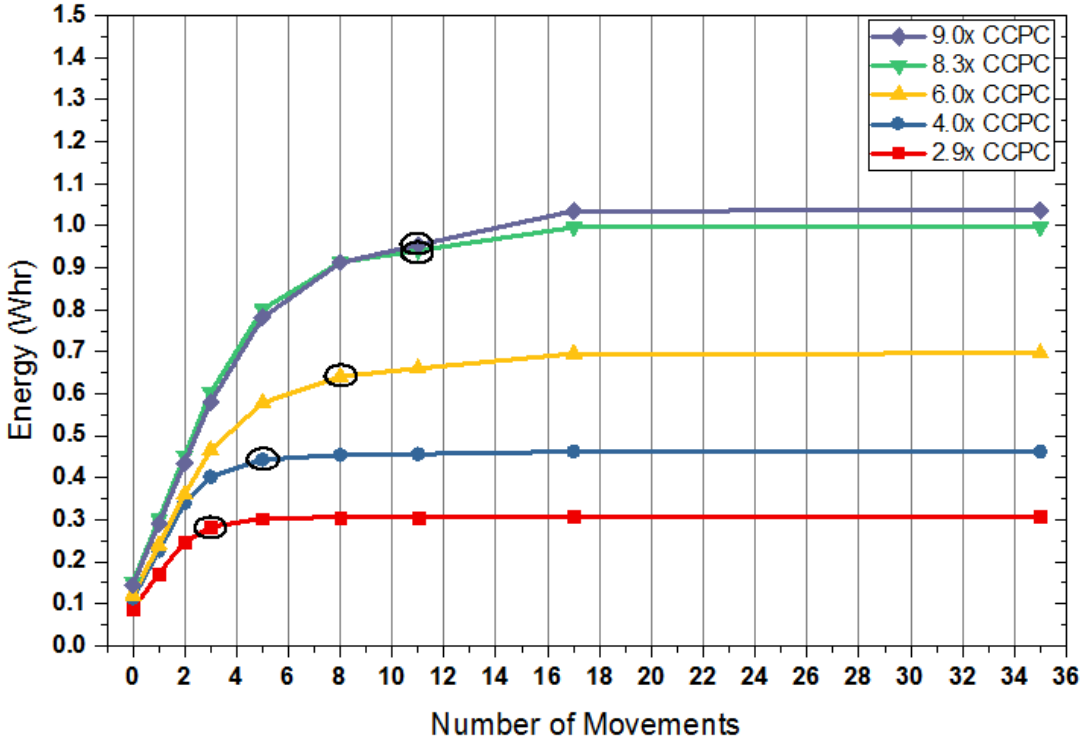

Figure 6.7: Energy collected at different tracking movement for the five CCPC concentrators.

The results obtained in Figure 6.7 show a significant difference in the energy output among the five concentrators due to their different concentration ratios. All of the concentrators have the same exit aperture of 10 mm x 10 mm, but they have different entry apertures. For example, the 9.0x CCPC has an entry aperture of 30 mm x 30 mm, while the 2.9x CCPC has an entry aperture of 17 mm x 17 mm. This results in a maximum energy production of the 9.0x CCPC being about 3.36 times larger than that of the 2.9x CCPC. However, more tracking movements are required for the high concentration concentrators to reach the maximum energy production points. The higher the concentration ratio of a concentrator, the more tracking movements are required to approach their maximum value of energy production. This is demonstrated clearly in Figure 6.8, which displays the normalised energy production as a function of tracking movement.

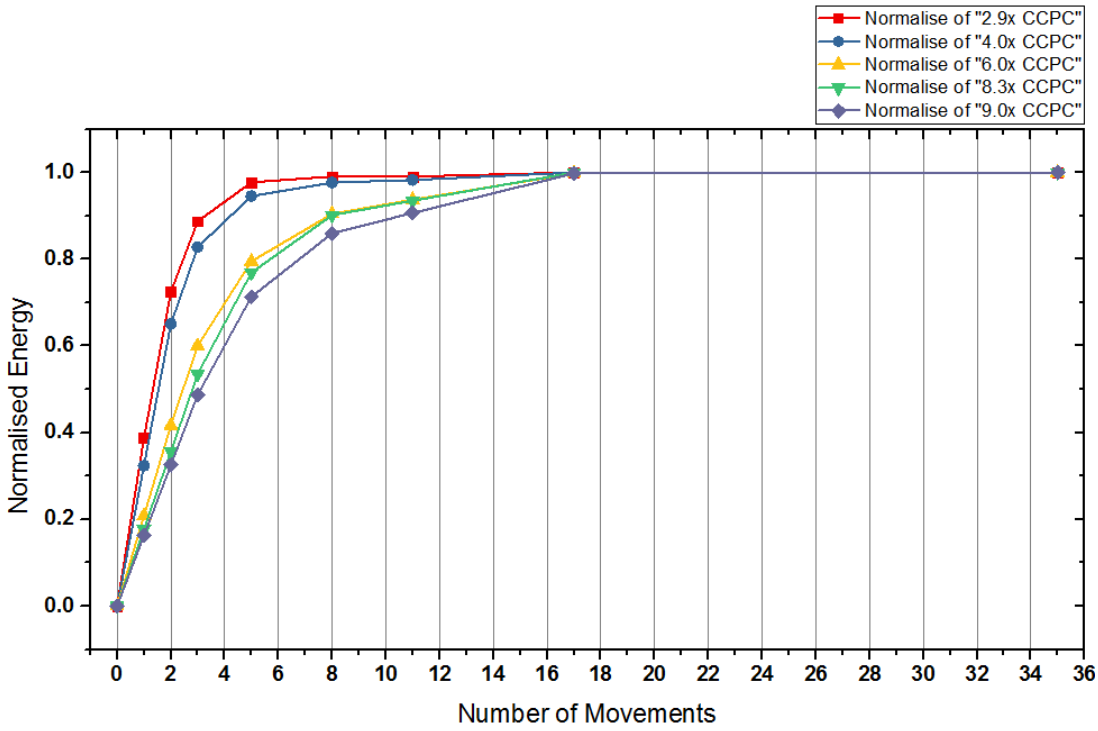

Figure 6.8: Normalised energy production of the five concentrators as a function of the number of tracking movements.

Up to this point, the results discussed above have been obtained from standard CCPCs, which have square entry and square exit apertures. A comparison with a rectangular CCPC (RCCPC), which has rectangular entry and square exit apertures, has also been investigated because it has been shown in Chapter Five that the RCCPC has wider angular response in E-W direction and thus may have an impact on the number of tracking movements. Figure 6.9 shows an energy production comparison between a standard 4.0x CCPC and a 4.0x RCCPC operating in the E-W direction. It can be seen that the 4.0x RCCPC requires only three movements to approach its maximum value while the 4.0x CCPC require five movements, although the maximum value for the 4.0x CCPC is slightly higher than that of the 4.0x RCCPC (possibly due to the slightly lower optical efficiency of this concentrator). Consequently, a significant reduction in the tracking movements can be achieved without the expense of the concentration ratio. These results demonstrate the benefit of developing novel concentrators with a wide angular response.

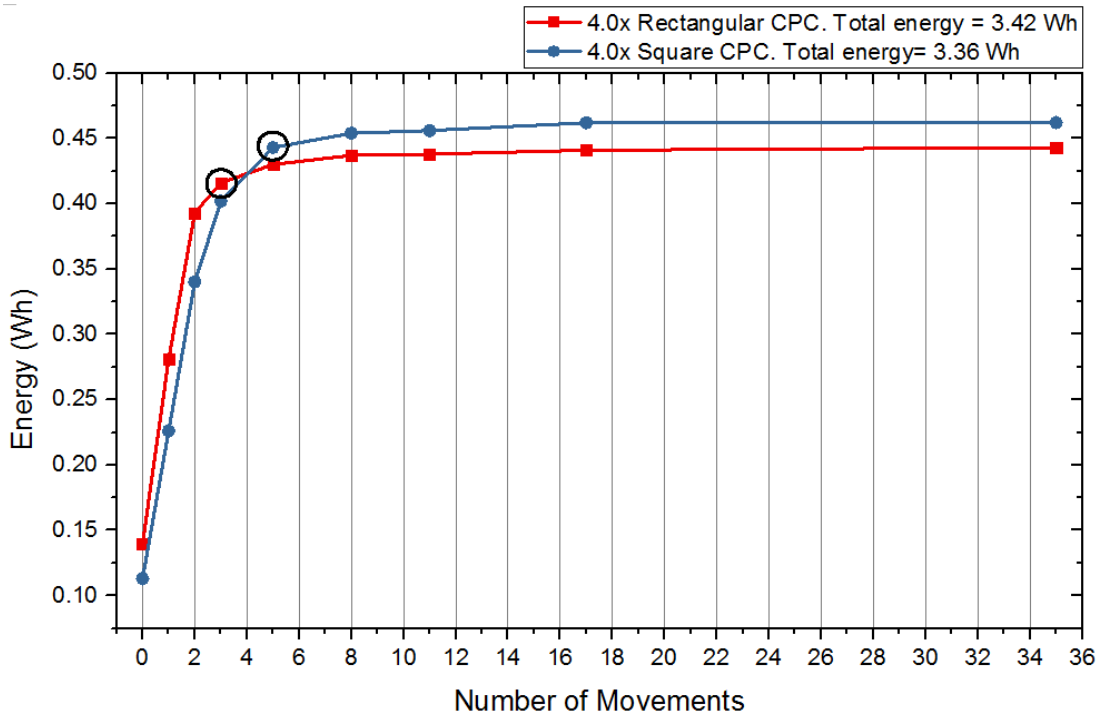

Figure 6.9: Comparison between the 4.0x CCPC and 4.0x RCCPC (E-W) in terms of the energy production as a function of the number of tracking movements.

6.2.2 Tracking Model Based on Realistic Solar Radiation

In the previous section, the calculation was carried out based on a fixed solar radiation intensity of 1000 W/m^2, which does not vary with time. In this improved model, the real solar intensity will be employed. Due to the motion of the earth, the sun's position varies daily and annually. Thus, solar radiation varies from sunrise to sunset, and also from one location to another. Solar radiation changes with seasonal shift, in addition to other factors such as clouds, pollution and dust. Solar intensity at any location depends on many factors, such as the latitude and longitude of that location.

6.2.2.1 Calculation Using Real Solar Data

To carry out a calculation using the real sun data, a specific location needs to be selected. The location selected for this study is Muscat, Oman, which is located in northern Oman and whose coordinates are 23.5880° latitude and 58.3829° longitude. The formulae that are used to analyse the metrological data are extracted from Duffie and Beckman's book (solar engineering of thermal processes) [67] in which the declination (δ), slope (β), surface azimuth angle (γ), hour angle (ω), angle of incidence (Θ_i), zenith angle(Θ_z), sun rising hour (ω_r), sun set hour (ω_s), solar altitude angle (α_s) and solar azimuth angle (γ_s) are calculated. These angles are illustrated in Figure 6.10.

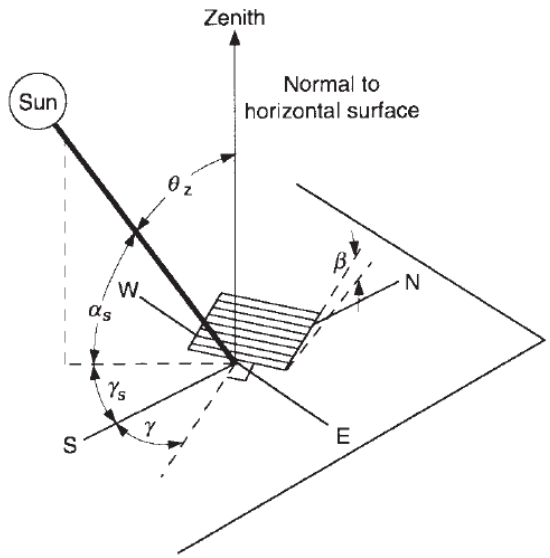

Figure 6.10: Solar angles for the position of the sun relative to a plane [67].

Four particular days—21 March, 21 June, 21 September and 21 December—were selected to represent spring, summer, autumn and winter, which are designated as n=80, n=172, n=264 and n=355, respectively. To obtain the solar radiation data for Muscat, two sub-models were built independently using MATLAB Simulink (the solar radiation angle model and the Iqbal model) and then connected to produce the results, as follows:

- Solar radiation angle model

  This model is responsible for calculating the solar angles and considered as an input model in which the latitude, longitude, number of the day (n) and the instant time are inserted to output the relative solar angles.
- Iqbal model

  This model is responsible for providing the direct, diffuse, beam and global radiation based on the provided information from the first model [198].

A capture of the model is provided in Appendix D1.

6.2.2.2 Results

Before conducting the simulation of the real solar data in Simulink, it is necessary to specify each concentrator's capability to harvest radiation as a function of time. Figure 6.11 shows the sunlight harvesting hours of the five CCPCs when they are in a stationary position. It is observed that the 2.9x CCPC has a longer harvesting period because it can collect the sunlight from 09.40 hrs to 14.20 hrs, which makes a total collection time of 4 hours and 40 minutes. The higher the concentration ratio, the shorter the harvesting period because the acceptance angle decreases with an increase in concentration ratio. Consequently, the harvesting period for the 9.0x CCPC is only 2 hours and 50 minutes,

which starts at 10.40 hrs and ends at 13.20 hrs and is approximately 2 hours less than the 2.9x CCPC.

Figure 6.11: The sunlight harvesting period of five CCPCs at stationary condition.

The calculated results of the solar radiation on the four selected dates (21 March, 21 June, 21 September and 21 December) from 06.00 hrs to 18.00 hrs at Muscat are shown in Figure 6.12. It can be seen that there is a huge difference in the solar radiation intensity between summer (red line) and winter (green line). The maximum and minimum values of the solar radiation intensity that can be collected in summer and winter at solar noon are 1120 W/m^2 and 447 W/m^2, respectively. In contrast, the solar radiation intensity is very similar for spring and autumn,

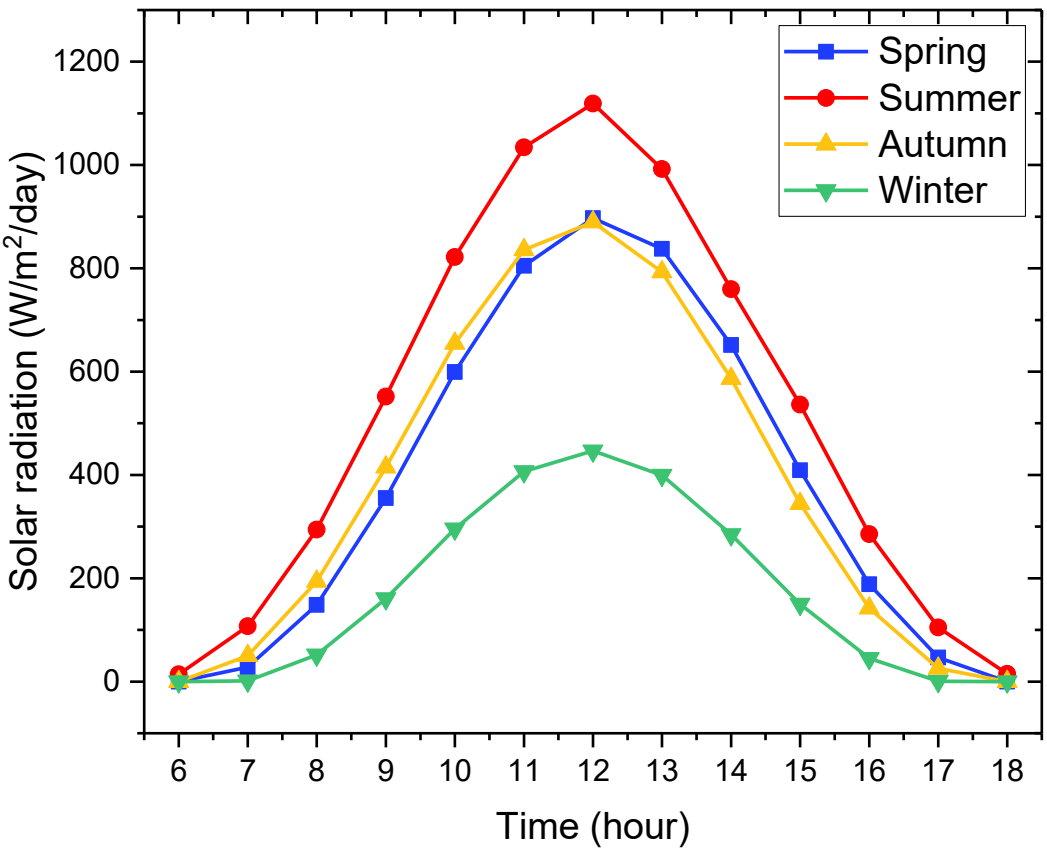

Figure 6.12: Solar radiation incident for Muscat on the 21 March (spring), 21 June (summer), 21 September(autumn) and 21 December (winter).

To validate the solar radiation results obtained by Simulink, the "day hour" (about 13 hours on 21 June) was calculated to compare with the published data. The radiation in Wh/m^2 was added for each hour and was then divided by 1000. The result obtained for this particular day is 6.5 kWh/m^2, which compares to the NASA metrological data from the same day (taken from 22-year average data for a monthly average insolation incident on a horizontal surface), which was 6.9 kWh/m^2/day [199]. Clearly, this result confirms the validity of the data.

A similar calculation to Case 1 (see Section 6.2.1.2) was carried out using the real solar radiation data (Figure 6.12), instead of using the fixed radiation of 1000 W/m^2. The purpose of this calculation is to see if there is a significant difference between the realistic calculation (based on the real solar radiation data) and the simplified calculation (based on a fixed radiation data). Figure 6.13 shows the results from this calculation for the 4.0x CCPC at the four selected dates, compared to the result of the simplified calculation shown in Figure 6.2 (the results for other concentrators are presented in Appendix D2). It can be seen that the solar radiation from 10.40 to 12.40 hrs in summer is higher than that collected from the solar simulator during the same time, although for the other hours the radiation is less than the solar simulator. Meanwhile, the energy collected by the concentrator during the winter season is significantly different from that collected using the solar simulator. For example, the energy collected by solar simulator from 11.40 to 12.00 hrs is 2.2 times higher than that collected during the same time in winter. The energy collected in spring and autumn is very similar and is less than that obtained from the solar simulator. Consequently, the results calculated using the fixed radiation data are slightly lower than these based on the real solar data from the summer. The results calculated using the fixed radiation data are moderately higher than those based on the real solar data from the spring and autumn. For the calculation based on the real solar data from the winter, the results are considerably lower than those calculated using the fixed radiation data.

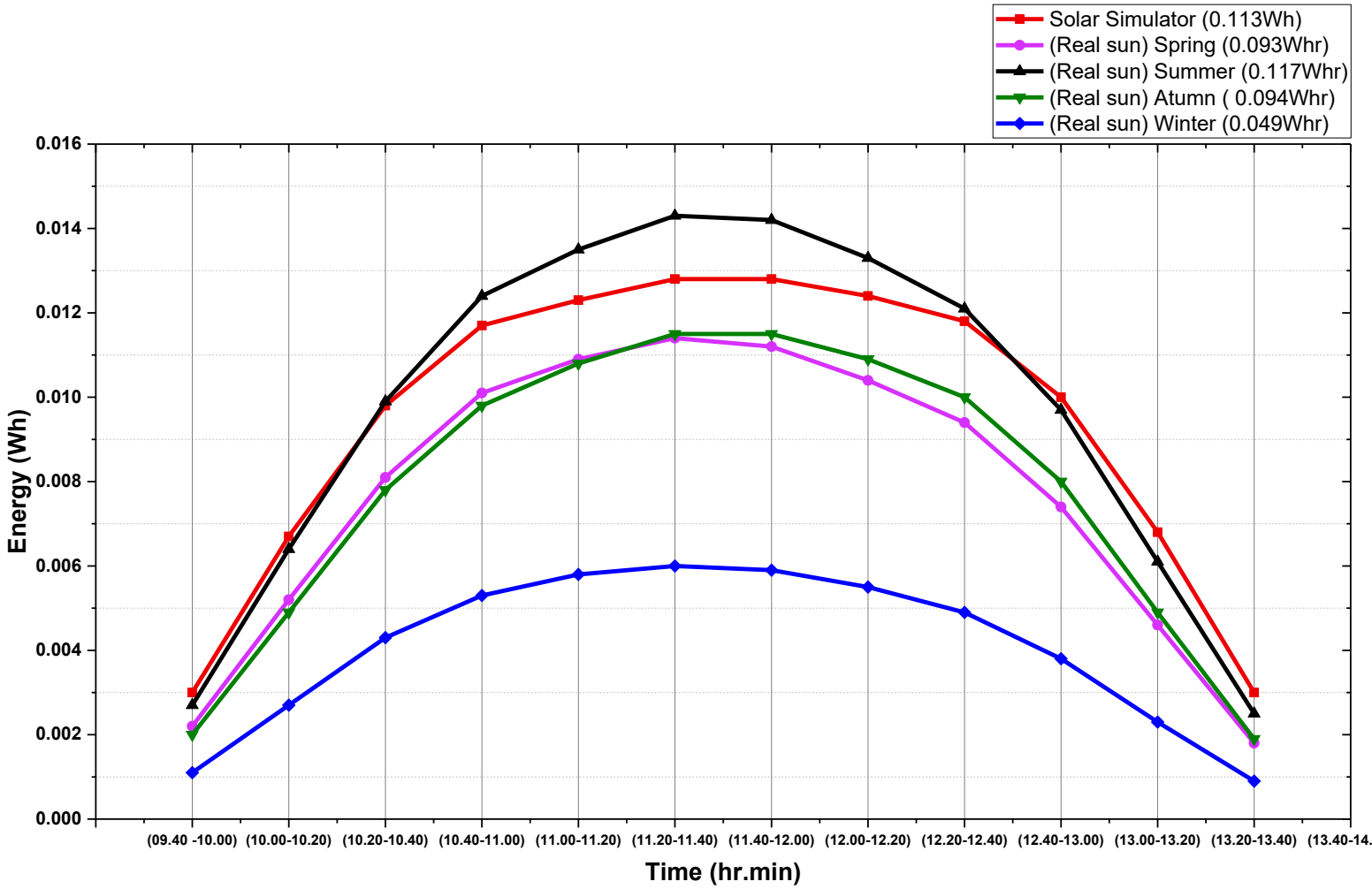

Figure 6.13: Energy production in an interval of 5° using the 4.0x CCPC under stationary operation for four seasons and for the fixed radiation.

Using the results shown in Figure 6.13, the daily energy production as a function of the tracking movement can be calculated using the real solar radiation data of four seasons. Figure 6.14 shows the results that were calculated using the 4.0x CCPC. The data obtained from the fixed radiation data (Figure 6.4) are also presented for comparison. It can be seen that the variation of sunlight intensity among the different seasons does not seem to affect the optimal tracking movements, which is five for all seasons. In contrast, the daily energy production varies significantly with the change of the seasons, in a similar manner to those shown in Figure 6.13. Nevertheless, the yearly average of the energy production per day based on the realistic calculation is only about 18% lower than the values predicted using the simplified calculation. Furthermore, the results in Figure 6.14 show that the daily energy production can be significantly increased with a few simple tracking movements, which is five for the 4.0x CCPC. This result raises a question about the currently accepted view of CCPC's suitability for stationary application. It is true that a CCPC can collect more solar radiation than other types of concentrators at stationary operation. However, the use of a tracking system with CCPCs will bring a further substantial increase in energy production, as shown in Figure 6.14. A key advantage of the tracking system for CCPCs is its simplicity and low cost, due to the fact that it involves only a few movements and is extremely tolerant to tracking error.

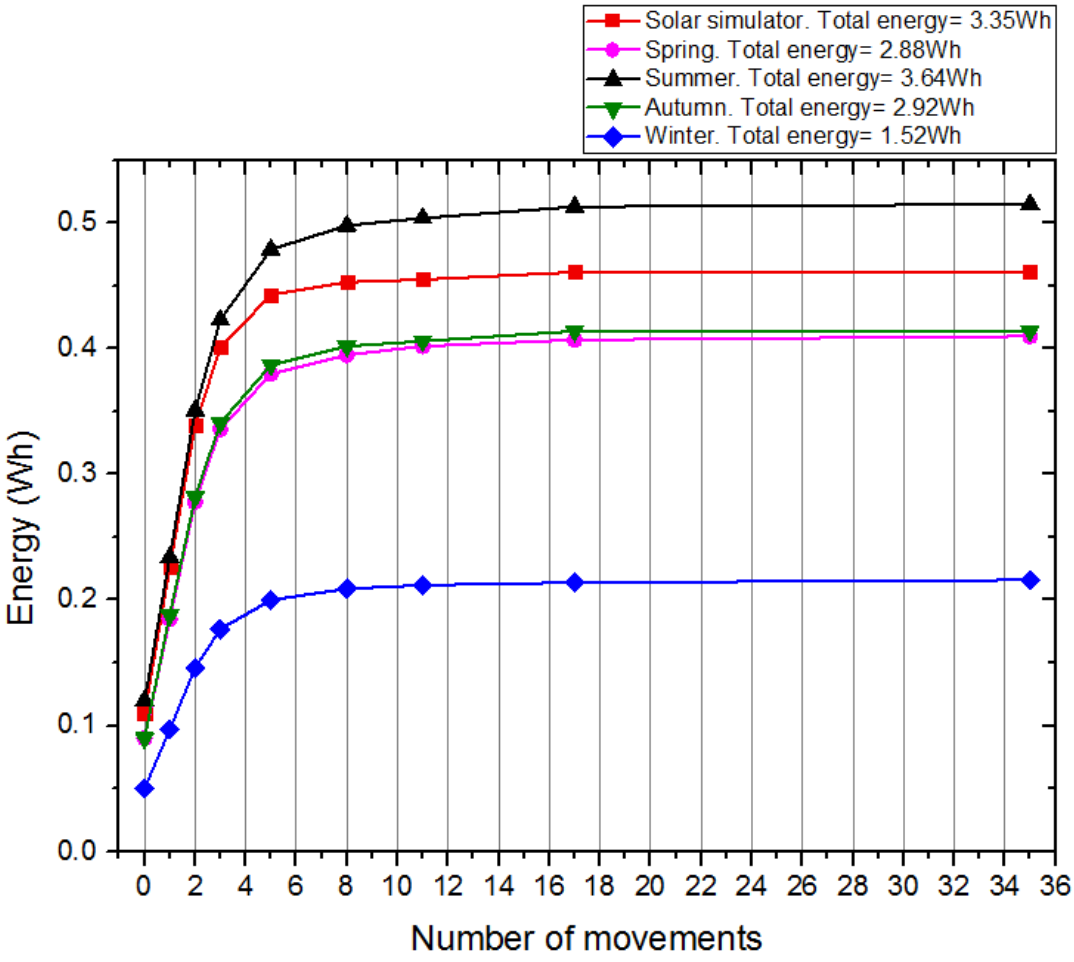

Figure 6.14: The daily energy production of the four seasons as a function of tracking movements using the 4.0x CCPC, compared with the data obtained using the fixed radiation data.

6.3 Economic Viability

This section provides a detailed breakdown of the manufacturing costs of the CCPC concentrators produced in the laboratory and it aims to predict the manufacturing cost of CCPC solar power systems in large scale production. A conventional PV solar panel will be employed as a reference for comparison in order to investigate their economic potential.

6.3.1 Cost Analysis

Table 6.3 lists the cost of the materials and components that are used to construct the concentrators used in this study. These materials and components were purchased in small quantities and the manufacturing costs that are calculated based on these prices represent the real production cost of prototypes on laboratory scale. Two single cell concentrating systems, one based on a silicon cell and one based on a GaAs cell, were estimated and the results are presented in Table 6.4. The concentrators were fabricated

using 3D printing and the power output used for cost analysis is the actual experimental data obtained under indoor testing. The labour cost involving the design and fabrication of the concentrator is neglected, as is the cooling system and water used in the testing.

Table 6.3: Cost of the materials and components used for fabrication of the CCPCs of this study.

Sr.No	Material	Quantity	Dimension	Unit Cost	Total Cost + Freight
1	LGBC silicon cell	100	10 mm x 10 mm	£2.50	£300
2	GaAs solar cell	10	10 mm x 10 mm	£12	£120
3	DCB ceramic	32	46 mm x 32 mm	£4	£171
4	*Alanod* reflector	1 A4 sheet	210 mm x 297 mm	£13.81	£13.81
5	3D printer resin	1 Litre	–	£120	£151.80
6	Heat sink compound	1	–	£5.56	£6.67
7	Solder wire + bus wire+ flux pen	1	–	£4.15	£9.34
8	Tabbing wire	1 Roll	–	£1.29	£1.29

Table 6.4: Cost of the prototype concentrating system fabricated in laboratory for this study.

Material	2.9x	4.0x	6.0x	8.3x	9.0x
Silicon solar cell	10 x 10 mm^2	10 x 10 mm^2	10 x 10 mm^2	10 x 10 mm^2	10 x 10 mm^2
	£2.5	£2.5	£2.5	£2.5	£2.5
GaAs solar cell	10 x 10 mm^2	10 x 10 mm^2	10 x 10 mm^2	10 x 10 mm^2	10 x 10 mm^2
	£12	£12	£12	£12	£12
DCB ceramic	46 x 32 mm^2	46 x 32 mm^2	46 x 32 mm^2	46 x 32 mm^2	46 x 32 mm^2
	£4	£4	£4	£4	£4
3D printer Resin	0.0099 L	0.0108 L	0.0147 L	0.0187 L	0.0206 L
	£1.20	£1.30	£1.80	£2.25	£2.50
Alanod reflector	12.30 cm^2	20.00 cm^2	36.20 cm^2	54.80 cm^2	64.00 cm^2
	£0.26	£0.40	£0.80	£1.20	£1.40
Total Cost Silicon	**£7.96**	**£8.20**	**£9.10**	**£9.95**	**£10.40**
Total Cost GaAs	**£17.46**	**£17.70**	**£18.60**	**£19.45**	**£19.90**

The manufacturing cost shown in Table 6.4 is very high because they were fabricated in laboratory using materials and components that were purchased or fabricated in small quantities. Clearly, this cost can be significantly reduced if they are produced in large quantities on an industrial scale. The potential for cost reduction based on industrial-scale production is explored next.

- Concentrator

The cost of printing the concentrators on a laboratory scale is between £1.20 and £2.50 for each of the fabricated concentrators. In reality, we can use different materials and manufacture processes at significantly reduced costs. According to a quotation obtained from Huzhou Dear Industry [200], the price of producing the 9.0x CCPC on a large scale is as low as £0.056.

- Direct Bonded Copper (DBC) ceramic substrate

The ceramic DCB is custom made and it has been designed especially for this project. The DCB was purchased from Tianjin Century Electronics [180] and the price was £4/piece based on a laboratory scale (32 pieces). The estimated price from the same company based on a large quantity (> 10,000 pieces) is £2/piece.

- Reflector cost

The cost of the aluminium reflector purchased from '*alanod*' Company [189] based on a laboratory scale is £13.81/sheet. The reflector cost that is used for the 9.0x CCPC based on the laboratory scale is £1.40. Similar reflectors can be supplied by FastArriver in China [201] at a mass production cost of £5.62/m^2. This reduces the reflector cost of the 9.0x CCPC to only £0.036.

- Solar cell cost

The monocrystalline silicon solar cells of a size of 10 mm x 10 mm with a single bus bar (LGBC) type were purchased from Solar Capture Technologies [82]. The quoted price is £2.50/cell based on a laboratory scale. While a mass produced silicon solar cell could be supplied by DS New Energy [202] at an estimated price of £0.53/piece.

The GaAs solar cell was quoted by Arima Photovoltaic & Optical Corp [203] in China on a laboratory scale at £12/cell (with a minimum order of 10 cells). This price can be reduced to £8/cell for large quantities. It is to be noted that the costs presented here are based on recent currency conversion rate, which may vary in the future.

The manufacturing cost of a CCPC concentrating solar power unit similar to those developed in this study can be estimated using the prices based on industrial-scale production. Using the 4.0x CCPC and the 9.0x CCPC as examples, the estimated cost is shown in Table 6.5. Clearly, the cost of these concentrating solar power units can be reduced dramatically if they are manufactured in large quantities on an industrial scale. For example, a cost reduction of 74.80% can be achieved for a silicon-based unit with a 9.0x CCPC concentrator, and a reduction of 49.25% can be achieved for the GaAs based unit.

Table 6.5: Manufacturing cost of the 4.0x CCPC and 9.0x CCPC concentrating solar power unit based on industrial-scale production.

Material	4.0x CCPC	9.0x CCPC
Silicon solar cell	(10 x 10) mm^2	(10 x 10) mm^2
	£0.53	£0.53
GaAs solar cell	(10 x 10) mm^2	(10 x 10) mm^2
	£8	£8
DCB ceramic	(46 x 32) mm^2	(46 x 32) mm^2
	£2	£2
Concentrator	(25.98 x 20 x 2) mm^2	(58.34 x 30 x 2) mm^2
	£0.029	£0.056
Aluminium reflector	20.00 cm^2	64.00 cm^2
	£0.011	£0.036
Total cost with silicon	**£2.56**	**£2.62**
Total cost with GaAs	**£10.04**	**£10.10**

6.3.2 Comparison Between a Flat PV Panel and a Concentrated Silicon System

A commercial monocrystalline PV panel from Solar BP [204] is selected for the comparative study because it is the most cost-effective panel that we have identified to date. Brief details of this commercial PV panel follow:

Model: SOLAR WATT 60M high power
Max. Power: 300 Wp
Solar cells: 60 monocrystalline solar cells
Cell dimension: 156 x 156 mm^2
Efficiency: 18.8%
Price: £275

A conceptual concentrated solar panel using the 9.0x CCPC concentrator is envisaged for this comparative study to investigate the economic impact of concentrators on the solar panels. The maximum power output produced using the 9.0x CCPC coupled with a LGBC silicon cell at normal incidence is 105 mW. In order to produce a comparable power output of 300 W, a total of 2,857 solar cells would be needed if 9.0x CCPCs are employed.

Alternatively, we could scale up the concentrator to accommodate the large-area solar cells (156 mm x 156 mm) that are employed in the commercial panel. For an exit aperture area of 156 mm x 156 mm, the scaled-up 9.0x CCPC will need an entry aperture

area of 468 mm x 468 mm. Based on this dimension, a scaled-up 9.0x CCPC was designed using CAD and simulated by TracePro. The results of the simulation indicate that the properties of the concentrators can be scaled-up linearly (see Appendix D3 for details). Assuming that all of the parameters are scalable linearly, a concentrator unit that consists of a scaled-up 9.0x and a 156 x156 mm^2 silicon solar cell will be able to generate a power output of 49.5 W. Therefore, a panel that has six of these unit will be able to produce a power output of 297 W. In this study, the cost of making this system was estimated and compared to the commercial system. The results are shown in Table 6.6. In the calculation, it is assumed that the cost of silicon cells is 50% of the cost of the entire system [57]. Therefore, the "Total Cost" shown in Table 6.6 represents the cost of the silicon cells only for the commercial system and the cost of the concentrator units only for the concentrator system. The costs of the other parts (e.g. the frames, covers, and wiring etc.) are not included because they are expected to be more or less the same. It can be seen from Table 6.6 that the total cost of the concentrator units is actually slightly higher than the cost of the silicon cells in the commercial panel. The results indicate that there is no advantage to use the concentrator system with silicon cells if the purpose is to reduce the cost because the silicon cells are now extremely cheap and is comparable to the cost of the concentrators.

Table 6.6: Comparison between a 9.0x CCPC scaled-up system and the commercial panel. In this calculation, it is assumed that the cost of silicon cell is 50% of the total cost of the system [57].

Material	PV Panel	9.0x CCPC Scaled-up
Area	1.46 m^2	1.31 m^2
Power output	300 Wp	297 Wp
No. of cells	60	6
Cell size	156 x 156 mm^2	156 x 156 mm^2
No. of Concentrator	_	6
Aluminium reflector cost	_	£8.75 x 6=£52.5
Concentrator cost	_	£13.6 x 6 = £81.6
Silicon cell cost	_	£ 2.3 x 6 = £ 13.8
Total cost	**£138**	**£ 148**

Using this data, the break-even point of the solar cell cost is £2.48/cell (156 mm x156 mm). Based on the assumption that the solar cell cost is 50% of the total cost of the panel, the cost of silicon cells in the commercial panel is £2.30/cell (156 mm x 156 mm). It can be seen that the solar cell cost in this commercial system is actually slightly lower than the break-even point. Consequently, there is no benefit for using the concentrators in this

case. In the other hand, mass production of PV panels should be addressed as it reduces the cost of the PV panels when compared to concentrator fabrication. Although the concentrator shows higher price compared to the PV panel, it has an advantage of reducing the total area as shown in Table 6.6, which consequently reduce the amount of PV material compared to the PV panel and replace them by the scaled-up concentrator. This will also lead to reducing the waste of PV material and recycling process after their life expectancy.

However, it should be noted that the concentrator will be beneficial for solar cells, which are more expensive than silicon solar cells. This is the case for all of the other types of solar cells.

6.3.3 Comparison Between a Flat PV Panel and a Concentrated GaAs System

A conceptual flat panel using GaAs cells and a conceptual concentrated GaAs panel were envisaged to study the possibility of cost reduction using the concentrated system for GaAs cells. The panels were designed to produce a power output that is comparable to the commercial silicon panels (i.e., 300 W). Since GaAs cells are available in a dimension of 10 mm x 10 mm, the conceptual panels were designed based on this dimension and using the 9.0x CCPC fabricated in this project. The results of the cost analysis are shown in Table 6.7. The cost of the commercial silicon panels is also included for comparison.

Table 6.7: The cost of the solar cells employed in a commercial silicon panel, a conceptual GaAs flat panel and a conceptual concentrated GaAs panel.

Material	PV panel	GaAs	GaAs coupled with 9.0x CCPC
Area	1.46 m^2	1.45 m^2	1.45 m^2
No. of cells	60	14,508	1612
Cell size	156 x 156 mm^2	10 x 10 mm^2	10 x 10 mm^2
Power output	300 W	290.2 W	320 W
Total cost	**£138**	**£116,064**	**£12,896**

The cost of silicon cells is estimated by assuming that the cost of the solar cells is 50% of the total cost of the panel, which is £2.30/cell (156 mm x 156 mm). The cost of GaAs cells is £8.00/cell (10 mm x 10 mm), which comes from a recent quotation based on large quantity purchasing. It can be seen from Table 6.7 that a reduction by an order of magnitude is possible by using the concentrated panel for GaAs cells. This is very different from the case for silicon cells. For GaAs cells, the concentrated system will have a huge benefit in terms of cost reduction because the cost of GaAs cells is substantially

more expensive than the cost of the concentrators. Unfortunately, even with concentration, the GaAs panels are still far more expensive than the silicon panels.

6.4 Summary

The limitation of the acceptance angle of the CCPCs leads to deployment of tracking system in order to maximise the sunlight collection from sunrise to sunset. A calculation procedure was developed based on the angular response data obtained in the laboratory, which enabled an estimation of daily energy production as a function of the tracking movements of the concentrator. Consequently, the optimal number of tracking movements was determined for the fabricated concentrators. It is found that only a few tracking movements are needed to reach the maximum daily energy production, which indicates that a simple and low-cost tracking system is sufficient for CCPC concentrated solar power systems. The calculation shows that the optimal number of tracking movements for the 2.9x, 4.0x and 6.0x CCPCs are three, five and eight movements, respectively. While the optimum number of tracking movements for both 8.3x and 9.0x CCPCs is 11 movements. The calculation procedure was first carried out based on an assumption of a constant solar radiation of 1000 W/m^2 and then an improved calculation was performed using real solar radiation, whose intensity changed during the day. The results obtained from the real solar radiation display a similar trend to those obtained under constant solar radiation, but the values change significantly with the seasons during the year. The calculation also shows that a novel rectangular entry 4.0x RCCPC can reach its maximum energy production with fewer tracking movements, due to its wide angular response along the E-W direction. This will further improve the simplicity and reduce the cost of the tracking system.

A cost analysis of using concentrators with both silicon and GaAs cells was performed to evaluate the impact on cost reduction. The result obtained from a conceptual 9.0x CCPC GaAs system shows that a substantial reduction in system cost can be achieved for the same power output. Although this system is not yet economically viable, the advantage of using the concentrator system is clearly demonstrated. The result obtained from a conceptual silicon concentrator system indicates that there is no benefit for using concentrators with silicon cells because the cost of silicon cells is almost the same as the cost of the concentrators. For other types of solar cells, it is likely that the cost reduction can be achieved by using concentrators if the cost of solar cells cost more than £2.48/cell (156 mm x 156 mm). There are other factors need to be considered such as space taken, weight and durability as well as cost.

Chapter Seven: Conclusions and Future Works

7.1 Introduction

This thesis describes a systematic experimental and simulation study of the design, fabrication, characterisation and evaluation of Cross Compound Parabolic Concentrators (CCPCs) for solar power generation application. The project began by developing a fabrication process for in-house manufacturing of low concentration CCPCs using a state-of-the-art 3D printing technique. A parametric equation was used to define the geometry of the concentrators in SolidWorks. TracePro was used for optical simulation and validation of the design. A set of standard CCPCs with concentration ratios of 2.9x, 4.0x, 6.0x, 8.3x and 9.0x were fabricated. In addition, concentrators with new geometry, including a rectangular CCPC and a circular CPC, were created for comparative study and to explore performance improvement. To provide crucial data to calculate the daily power generation of concentrated solar power systems, the angular response of the fabricated concentrators was investigated using the TracePro simulation and was then validated by experiment. The uniformity of light distribution on the exit aperture of the concentrators and its effect on the power generation of concentrated solar power systems was also investigated. Finally, the daily energy output of a concentrated solar power system for different tracking arrangements was estimated and the potential economic benefit of using the concentrators developed in this project was evaluated.

7.2 Main Conclusions

1. A method of fabricating CCPCs was developed, which facilitated the successful construction of a prototype concentrator with an optical efficiency of 84.5%. To my knowledge, this is the highest optical efficiency of a CCPC reported to date. This success can be attributed to: 1) the use of high precision 3D printing (Form 1+ 3D Printer) to accurately implement the geometrical design in practice; 2) a simple process that enables the formation of highly reflective concentrator surfaces using the state-of-the-art mirror film of 95% reflectivity; and 3) an appropriate distance between the exit aperture of concentrator and the surface of the solar cell for the best uniformity. The fabrication process is reliable and repeatable and has been employed in the fabrication of a number of CCPCs with different concentration

ratios, including 2.9x, 4.0x, 6.0x, 8.3x and 9.0x. All of which have an optical efficiency in the range of 82%–84%.

2. A rotary stage with cooling capability was designed and fabricated to study the angular response of the CCPCs. This enabled successful experimental investigation of the angular response of five CCPCs with different concentration ratios. The experimental results from the five CCPCs show that concentrators with higher concentration have a narrower angular response, while these with lower concentration ratios have a wider angular response. The results are in good agreement with the simulation by the TracePro, with an average deviation of 11.10% at normal incidence (0°). Furthermore, this work provides essential experimental data and a validated simulation model for the following system optimisation study to identify the appropriate tracking movement.

3. Non-uniform light distribution will decrease the power output of a concentrated solar power system and create hotspots, which can affect the long-term stability of the solar cell. A systematic experimental investigation and simulation was carried out to study the uniformity of light distribution across the solar cell surface of a concentrated solar power system. The results of this investigation reveal that the uniformity of the light distribution is very sensitive to the distance between the exit aperture of the concentrator and the top surface of the solar cell. The optimal position depends on the concentrator's concentration ratio. For the concentrators that have been investigated in this study, a high uniformity of over 90% can be achieved by placing the solar cell at optimal positions of -3mm and -2.5mm for the 2.9x and 4.0x CCPCs, respectively. The optimal cell positions for the 6.0x, 8.0x and 9.0x CCPCs is -1.5 mm. A maximum increase by 11.68% in the power output was demonstrated experimentally using an improved design of the 4.0x CCPC.

4. The experimental results show that uniformity at the exit aperture of a concentrator can significantly affect the short-circuit current (I_{sc}) of the solar cell. Inevitably, the measured short-circuit current varies for the concentrators of different uniformity, even though they have the same concentration ratio. This result indicates that significant errors may occur when the concentration ratio is determined using the measured short-circuit currents, which is currently

employed for experimental determination of the concentration ratio. Clearly, this method is only valid for concentrators with good uniformity. In the absence of the knowledge on the uniformity, a more accurate method for determining the concentration ratio is the one initiated in this research, which uses the spectroradiometer with a small-area sensor to map the solar cell surface. An additional advantage of this technique is that it also provides information on spectral change, if any.

5. A unique design of a rectangular 4.0x CCPC (RCCPC) that has a rectangular entry aperture and square exit aperture was fabricated to explore the possibility of improving the angular response of the CCPCs. The results of this investigation produced an unexpected result – the half acceptance angle of this 4.0x RCCPC in E-W is much wider than the theoretical value. Furthermore, the angular response of this 4.0x RCCPC is clearly wider than a standard 4.0x CCPC that has a square entry aperture and square exit aperture of the same concentration ratio. The TracePro simulation results reveal that the improvement is due to a favourable outcome of the second reflection (neglected in design theory), which reflects the initially reflected light onto the exit aperture when the incidence angle is larger than the theoretical half acceptance angle. To my knowledge, this result is the first experimental evidence to show that the angular response of CCPCs can be improved by including multiple light reflections in the geometrical design, offering important insights into future development of wide acceptance angle CCPCs. This study also shows that the angular response of the concentrator can be improved, albeit less significantly, by simply rotating a standard CCPC by 45 degrees in the horizontal plane (compared to the typical arrangement of the concentration orientation). This provides further insight into the possibility of improving the angular response by geometry modification.

6. A new concentrator geometry (i.e., circular CCPC) that has a circular entry aperture and a square exit aperture was designed, fabricated and investigated experimentally. The rationale of this design is that a concentrator of such shape can be conveniently manufactured using lathe machines, which are widely available in many factories and workshops. However, the results of experiment and simulation show that the optical efficiency of this design is slightly lower than that of a standard square CCPC.

7. Due to the limitation of the acceptance angle of the CCPCs, a tracking system can be employed to maximise the daily power generation in response to changing positions of the Sun during the day. A calculation procedure was developed to determine the minimum movements of tracking, while obtaining the maximum daily energy production of a CCPC solar power system. Using this procedure together with the angular response data from experiments, the optimal number of tracking movements for the concentrators studied in this project was calculated and the results show that only a few movements are needed, indicating that a simple and low-cost tracking system is sufficient. The optimal number of movements for the 2.9x, 4.0x and 6.0x CCPCs are 3, 5 and 8 movements, respectively, while it is 11 for both 8.3x and 9.0x CCPCs. The calculation was initially performed based on the assumption of a constant solar radiation intensity of 1000 W/m^2. An improved calculation was then performed using real solar radiation data, whose intensity changes in a day. The results show that the tracking movements in the case of the constant solar radiation is very similar to those of the real solar radiation in summer in Oman, while it is different for the case in the winter season.

8. A cost analysis of using concentrators was performed and their economic viability was evaluated based on both laboratory-scale and industrial-scale production processes. A comparison was carried out between a flat PV panel and a concentrated solar power system that consists of a monocrystalline silicon cell and a scaled-up 9.0x CCPC. It is found that a reduction of the total area by 10.30% can be achieved using the concentrators in a 300 W system. A total number of 60 cells is used in the 300 W flat PV system, while only six cells are required in the 9.0x concentrated system for the same power output. However, the economic benefit is not obvious due to the substantially lower price of silicon cells in recent years. On the other hand, the advantage of using the concentrators with GaAs cells is clearly demonstrated because of the high cost of GaAs cells. A substantial reduction in the system cost by a factor of 9 can be achieved by using the 9.0x concentrator system, compared to the corresponding flat panel.

9. In addition to the data obtained from the CCPCs, this work also generates a large amount of experimental data of solar cells under different testing conditions. These data include the solar cell's parameters (typically the short-circuit current, open-circuit voltage, fill factor, maximum power output, and conversion

efficiency) as a function of the concentration ratio, the angular response, and the temperature dependence of I-V characteristics. For instance, the I-V characteristics of a solar cell was found to change significantly with its temperature. Therefore, the incorporation of a water-cooling capability in the rotary stage enables us to control the temperature of the solar cell during testing, and hence determine of the temperature coefficient of the solar cell. The experimental results show that the temperature coefficients of the silicon cell used in this work are α =+0.00057/°C, β=-0.0037/°C and ε =-0.38 % /°C for short-circuit current, open-circuit voltage and power, respectively.

10. It is known that the concentration ratio of a concentrator will always be smaller than its geometrical concentration ratio due to inevitable optical losses. However, the ratio of the power output of a concentrated solar power system can be larger than the geometrical concentration ratio, due to the fact that the all of the parameters of the solar cell that determine the power output (including the short-circuit current, open-circuit voltage, and fill factor) increase as the concentration ratio increases. The results from this work provide direct experimental evidence. It can be seen that the 9.0x CCPC has a designed geometrical concentration ratio of 9, while the actual concentration ratio of the fabricated concentrator is 7.4, which gives an optical efficiency of 82%. However, the power output of the concentrated system using this concentrator with a monocrystalline silicon cell produces 9.7 times more power than a bare cell—note that this value is larger than the geometrical concentration ratio.

7.3 Future Works

1. The results from the angular response of the novel RCCPC show that the angular response can be significantly improved by taking into account the second reflection in the concentrator design. This discovery opens a new avenue to explore the possibility of improving the angular response beyond theoretical predication of current model. However, in-depth investigations are needed to identify and understand how the geometrical shape of the reported 4.0x RCCPC could improve the angular response through the second reflection, while maintaining the same concentration ratio. An enhanced understanding of this result may help to discover more favourable concentration geometries that may lead to further improvement in the angular response.

2. The experiment on improving the angular response of a standard 4.0x concentrator by rotating 45° in horizontal plane demonstrated a marginal but noticeable improvement. This result is not yet fully understood. Therefore, an in-depth study into the mechanisms that are responsible for the improvement may lead to further improvement by modifying the concentrator's geometry in the horizontal plane.

3. A significant improvement in the uniformity of 8.3x and 9.0x CCPCs by changing the solar cell position to their optimal position is predicted by the simulation. However, the improvement obtained from the experiments is less significant when compared to the results of other concentrators. Therefore, further investigations are needed to understand the reasons for the observed difference between simulation and experiment, which may offer valuable insights into the role of uniformity in "higher concentration" concentrators.

4. The power output of a concentrated solar power system decreases as the incidence angle increases because the effective light collection area of the concentrator becomes smaller for a larger incidence angle. Another factor that might also contribute to the reduction of power output is non-uniformity. The simulation results show that the light distribution on the solar cell in a concentrated system for large angle incidence is highly non-uniform. Therefore, a further investigation is needed to identify if the non-uniformity at large angle incidence contributes to significant power reduction, and consequently seek for the appropriate solutions to the problem.

5. An experimental investigation should be designed and performed to validate the model that has been developed to predict the optimal numbers for the tracking movement for different CCPCs. An experimental validation of the model is a crucial step prior to the model being used for the design of future concentrated solar power system to achieve the maximum energy production at minimum cost.

6. Outdoor testing of a concentrated solar power system under real operating conditions on a building's rooftop should be considered. The system should be designed and constructed using an array of optimised CCPCs with appropriate

solar cells. The performance of the optimised concentrated solar power system should be investigated in comparison with an equivalent flat panel system.

7. Heat generation is an increasingly severe problem in a concentrated solar power system. Therefore, a detailed thermal analysis should be conducted, and solutions for the utilisation and dissipation of heat should be sought. In particular, hybrid systems that co-generate electricity and heat will be explored.

8. An in-depth cost analysis should be performed to evaluate the possibility of improving the economic viability of the concentrated solar power systems using GaAs and InP solar cells, which are currently expensive. The investigation will be aimed to identify the key factors and solutions that can lead to the economic application of a concentrated solar power system that has the potential to compete with standard flat silicon panels.

References

1. (IEA), I.E.A.g., *World Energy Outlook 2016, Executive Summary*. 2016. p. 13.
2. Shanks, K., S. Senthilarasu, and T.K. Mallick, *Optics for concentrating photovoltaics: Trends, limits and opportunities for materials and design.* Renewable and Sustainable Energy Reviews, 2016. **60**: p. 394-407.
3. Jakhar, S., M.S. Soni, and N. Gakkhar, *Historical and recent development of concentrating photovoltaic cooling technologies.* Renewable and Sustainable Energy Reviews, 2016. **60**: p. 41-59.
4. Iea. *Solar PV - Tracking Power*. [cited 12.01.2020]; Available from: https://www.iea.org/fuels-and-technologies/solar.
5. Iea. *Renewables 2019 Fuel report - October 2019*. [cited 12.01.2020]; Available from: https://www.iea.org/reports/renewables-2019.
6. Akisawa, A., M. Hiramatsu, and K. Ozaki, *Design of dome-shaped non-imaging Fresnel lenses taking chromatic aberration into account.* Solar Energy, 2012. **86**(3): p. 877-885.
7. Sgouridis, S., et al., *Comparative net energy analysis of renewable electricity and carbon capture and storage.* Nature Energy, 2019.
8. Princiotta, F.T. and D.H. Loughlin, *Global climate change: The quantifiable sustainability challenge.* Journal of the Air & Waste Management Association, 2014. **64**(9): p. 979-994.
9. FORUM, W.E. *Fossil fuels will still dominate energy in 20 years despite green power rising*.[Accessdate03.06.2019];Availablefrom:https://www.weforum.org/agenda/2017/10/fossil-fuels-will-dominate-energy-in-2040/.
10. Secretariat, U. *Report of the Conference of the Parties on its twenty-first session, held in Paris from 30 November to 13 December 2015*. in *United Nations Framework Convention on Climate Change*. 2015.
11. Schellnhuber, H.J., S. Rahmstorf, and R. Winkelmann, *Why the right climate target was agreed in Paris.* Nature Climate Change, 2016. **6**(7): p. 649.
12. Prasartkaew, B., *Mathematical Modeling of an Absorption Chiller System Energized by a Hybrid Thermal System: Model Validation.* Energy Procedia, 2013. **34**: p. 159-172.
13. Agency, I.R.E. *Renewable Generation Capacity by Energy Source - 2018*. 2018 [cited 09.05.2019]; Available from: https://www.irena.org/Search?keywords=&irena_topic=440b8182ba8941d291b9aefac97fef47.
14. Nayak, P.K., et al., *Photovoltaic solar cell technologies: analysing the state of the art.* Nature Reviews Materials, 2019. **4**(4): p. 269-285.
15. Kannan, N. and D. Vakeesan, *Solar energy for future world: - A review.* Renewable and Sustainable Energy Reviews, 2016. **62**: p. 1092-1105.
16. Chen, C.J., *Physics of solar energy*. 2011: John Wiley & Sons.
17. Kalogirou, S.A., *Solar energy engineering : processes and systems.* 2014.
18. Boyle, G., *Renewable Energy: Power for a Sustainable Future*. 2012: OUP Oxford.

19. Zahedi, A., *Review of modelling details in relation to low-concentration solar concentrating photovoltaic.* Renewable and Sustainable Energy Reviews, 2011. **15**(3): p. 1609-1614.
20. Eicker, U., *Solar Technologies for Buildings*. 2003: Wiley.
21. Ramakumar, R. and J. Bigger, *Photovoltaic systems.* Proceedings of the IEEE, 1993. **81**(3): p. 365-377.
22. Shah, A., et al., *Photovoltaic technology: the case for thin-film solar cells.* science, 1999. **285**(5428): p. 692-698.
23. Mekhilef, S., R. Saidur, and M. Kamalisarvestani, *Effect of dust, humidity and air velocity on efficiency of photovoltaic cells.* Renewable and Sustainable Energy Reviews, 2012. **16**(5): p. 2920-2925.
24. Yadav, A., A.P.P.K. , M. Tech (ECE),, and M. RPSGOI, *ENHANCEMENT IN EFFICIENCY OF PV CELL THROUGH P&OALGORITHM.* International Journal For Technological Research In Engineering, 2015. **Volume 2**.
25. Manjot Kaur and H. Singh, *A REVIEW: COMPARISON OF SILICON SOLAR CELLS AND THIN FILM SOLAR CELLS.* International Journal Of Core Engineering & Management (IJCEM). **Volume 3**(Issue 2).
26. Augustin McEvoy, L.C., Tom Markvart, *Solar Cells: Materials, Manufacture and Operation*. 2012.
27. Markvart, T. and L. CastaÑer, *IIa-1 - Principles of Solar Cell Operation*, in *Practical Handbook of Photovoltaics*, T. Markvart and L. Castañer, Editors. 2003, Elsevier Science: Amsterdam. p. 71-93.
28. Zhang, X., et al., *Review of R&D progress and practical application of the solar photovoltaic/thermal (PV/T) technologies.* Renewable and Sustainable Energy Reviews, 2012. **16**(1): p. 599-617.
29. Öztürk, S., et al., *Operating principles and practical design aspects of all SiC DC/AC/DC converter for MPPT in grid-connected PV supplies.* Solar Energy, 2018. **176**: p. 380-394.
30. PVinsights. *Principle of solar energy: The Photovoltaic effect* 2019 [cited 16.04.19]; Available from: http://pvinsights.com/Knowledge/Principle.php.
31. Chapin, D.M., C.S. Fuller, and G.L. Pearson, *A new silicon p-n junction photocell for converting solar radiation into electrical power [3].* Journal of Applied Physics, 1954. **25**(5): p. 676-677.
32. Masters, G.M., *Renewable and Efficient Electric Power Systems*. 2004.
33. Chao, K.-H., S.-H. Ho, and M.-H. Wang, *Modeling and fault diagnosis of a photovoltaic system.* Electric Power Systems Research, 2008. **78**(1): p. 97-105.
34. Priyanka, M. Lal, and S.N. Singh, *A new method of determination of series and shunt resistances of silicon solar cells.* Solar Energy Materials and Solar Cells, 2007. **91**(2): p. 137-142.
35. Mammo, E.D., N. Sellami, and T.K. Mallick, *Performance analysis of a reflective 3D crossed compound parabolic concentrating photovoltaic system for building façade integration.* Progress in Photovoltaics: Research and Applications, 2013. **21**(5): p. 1095-1103.
36. Qi, B. and J. Wang, *Fill factor in organic solar cells.* Physical Chemistry Chemical Physics, 2013. **15**(23): p. 8972-8982.
37. Fraas, L.M. and L.D. Partain, *Solar cells and their applications*. Vol. 236. 2010: John Wiley & Sons.

38. Sharma, S., K.K. Jain, and A. Sharma, *Solar Cells: In Research and Applications—A Review.* Materials Sciences and Applications, 2015. **06**(12): p. 1145-1155.
39. Fraunhofer, *PHOTOVOLTAICS REPORT*. 2019.
40. Newswire, P.R.P. *Thin Film Photovoltaics Market, 2017 - 2030*. 2017 [cited 18.04.19]; Available from: https://markets.businessinsider.com/news/stocks/thin-film-photovoltaics-market-2017-2030-1002199960.
41. Saga, T., *Advances in crystalline silicon solar cell technology for industrial mass production.* Npg Asia Materials, 2010. **2**: p. 96.
42. *SOLARQUOTES*. 2009 [cited 18.04.19]; Available from: https://www.solarquotes.com.au/panels/photovoltaic/monocrystalline-vs-polycrystalline/.
43. NREL. *Best Research-Cell Efficiency Chart*. [cited 16.04.19]; Available from: https://www.nrel.gov/pv/cell-efficiency.html.
44. Green, M.A., *Crystalline and thin-film silicon solar cells: state of the art and future potential.* Solar Energy, 2003. **74**(3): p. 181-192.
45. Fraunhofer Institute for Solar Energy Systems, I., *PHOTOVOLTAICS REPORT*. 2016.
46. Sharaf, O.Z. and M.F. Orhan, *Concentrated photovoltaic thermal (CPVT) solar collector systems: Part I–Fundamentals, design considerations and current technologies.* Renewable and Sustainable Energy Reviews, 2015. **50**: p. 1500-1565.
47. Bagnall, D.M. and M. Boreland, *Photovoltaic technologies.* Energy Policy, 2008. **36**(12): p. 4390-4396.
48. *Solar Thin Films 5MW Amorphous Silicon Module Manufacturing Plant*. 2014 [cited 21.04.19]; Available from: http://www.spacedaily.com/reports/Solar_Thin_Films_5MW_Amorphous_Silicon_Module_Manufacturing_Plant_999.html.
49. Dimroth, F. and S. Kurtz, *High-efficiency multijunction solar cells.* MRS bulletin, 2007. **32**(3): p. 230-235.
50. Hirst, L.C. and N.J. Ekins-Daukes, *Fundamental losses in solar cells.* Progress in Photovoltaics: Research and Applications, 2011. **19**(3): p. 286-293.
51. Makham, S., M. Zazoui, and J. Bourgoin, *Analysis of multijunction solar cells: electroluminescence study.* MJ Condens Matter, 2004. **5**: p. 181-5.
52. Hörantner, M.T., et al., *The potential of multijunction perovskite solar cells.* ACS Energy Letters, 2017. **2**(10): p. 2506-2513.
53. Roldan-Carmona, C., et al., *High efficiency single-junction semitransparent perovskite solar cells.* Energy & Environmental Science, 2014. **7**(9): p. 2968-2973.
54. Zanesco, I. and E. Lorenzo, *Optimisation of an asymmetric static concentrator: the PEC-44D.* Progress in Photovoltaics: Research and Applications, 2002. **10**(5): p. 361-376.
55. Mallick, T.K. and P.C. Eames, *Design and fabrication of low concentrating second generation PRIDE concentrator.* Solar Energy Materials and Solar Cells, 2007. **91**(7): p. 597-608.
56. Homes, S.E.F. *Solar Concentrators Are The Future of Renewable Energy*. [cited 2019 25.04.2019]; Available from: http://www.solar-energy-for-homes.com/solar-concentrator.html.
57. Tang, R. and X. Liu, *Optical performance and design optimization of V-trough concentrators for photovoltaic applications.* Solar Energy, 2011. **85**(9): p. 2154-2166.
58. Chemisana, D., *Building integrated concentrating photovoltaics: A review.* Renewable and Sustainable Energy Reviews, 2011. **15**(1): p. 603-611.

59. Sellami, N., T.K. Mallick, and D.A. McNeil, *Optical characterisation of 3-D static solar concentrator.* Energy Conversion and Management, 2012. **64**: p. 579-586.
60. Lee, S. *Thermal challenges and opportunities in concentrated photovoltaics*. in *2010 12th Electronics Packaging Technology Conference, EPTC 2010*. 2010.
61. Assadi, M.K., et al., *Enhancing the efficiency of luminescent solar concentrators (LSCs).* Applied Physics A: Materials Science and Processing, 2016. **122**(9).
62. Zhang, L., et al., *Concentrating PV/T hybrid system for simultaneous electricity and usable heat generation: A review.* International Journal of Photoenergy, 2012. **2012**.
63. Rabl, A., *Comparison of solar concentrators.* Solar Energy, 1976. **18**(2): p. 93-111.
64. Welford, W.T. and R. Winston, *The optics of nonimaging concentrators: light and solar energy*. 1978: Academic Press.
65. Chaudhari, V.A. and C.S. Solanki, *From 1 sun to 10 suns c-si cells by optimizing metal grid, metal resistance, and junction depth.* International Journal of Photoenergy, 2009. **2009**.
66. Proise, F., *Study and realisation of micro/nano photovoltaic cells and their concentration systems*. 2014, Paris 6.
67. Duffie, J.A., *Solar engineering of thermal processes*. 4th ed. ed, ed. W.A. Beckman. 2013, Hoboken, N.J.: Wiley.
68. Ochieng, R.M. and F.N. Onyango, *Some techniques in configurational geometry as applied to solar collectors and concentrators.* Solar Collectors and Panels, Theory and Applications: Sciyo, 2010: p. 357-378.
69. Xie, W.T., et al., *Concentrated solar energy applications using Fresnel lenses: A review.* Renewable and Sustainable Energy Reviews, 2011. **15**(6): p. 2588-2606.
70. Mroczka, J. and K. Plachta. *Modeling and analysis of the solar concentrator in photovoltaic systems*. in *Proceedings of SPIE - The International Society for Optical Engineering*. 2015.
71. Zacharopoulos, A., et al., *Linear Dielectric Non-Imaging Concentrating Covers For PV Integrated Building Facades.* Solar Energy, 2000. **68**(5): p. 439-452.
72. Castro, M., I. Antón, and G. Sala, *Pilot production of concentrator silicon solar cells: Approaching industrialization.* Solar Energy Materials and Solar Cells, 2008. **92**(12): p. 1697-1705.
73. Y. Tripanagnostopoulos, M.S., S. Tselepis, V. Dimitriou, Th. Makris, *DESIGN AND PERFORMANCE ASPECTS FOR LOW CONCENTRATION PHOTOVOLTAICS*, in *20th European Photovoltaic Solar Energy Conference and Exhibition*. 2005: Barcelona, Spain. p. 4.
74. Baig, H. and T. Mallick, *Challenges and opportunities in concentrating photovoltaic research.* Mod Energy Rev, 2011. **3**(2): p. 20-26.
75. Belessiotis, V., S. Kalogirou, and E. Delyannis, *Chapter Six - Indirect Solar Desalination (MSF, MED, MVC, TVC)*, in *Thermal Solar Desalination*, V. Belessiotis, S. Kalogirou, and E. Delyannis, Editors. 2016, Academic Press. p. 283-326.
76. Welford, W.T., *The optics of nonimaging concentrators : light and solar energy*, ed. R. Winston. 1978, New York London: New York London : Academic Press.
77. Madala, S., *Stationary Nonimaging Concentrators–A Comprehensive Study and Design Improvements.* 2016.
78. Khamooshi, M., et al., *A review of solar photovoltaic concentrators.* International Journal of Photoenergy, 2014. **2014**.
79. Baig, H., K.C. Heasman, and T.K. Mallick, *Non-uniform illumination in concentrating solar cells.* Renewable and Sustainable Energy Reviews, 2012. **16**(8): p. 5890-5909.

80. Concentration, E.U.S.P.a. *Introducing Concentrating Solar Power*. [cited 06.05.2019]; Available from: https://www.e-education.psu.edu/eme812/node/646.
81. solartronenergy. *HCPV Solar Parabolic Solar Concentrator Technology*. 10/07/2020]; Available from: https://www.solartronenergy.com/hcpv-solar/.
82. *Mildura Solar Power Station SHARE* [cited 10/07/2020; Available from: https://www.power-technology.com/projects/mildura-solar-power-station/.
83. Dreger, M., et al. *Development and investigation of a CPV module with Cassegrain mirror optics*. in *AIP Conference Proceedings*. 2014. American Institute of Physics.
84. Ullah, I., *Development of Fresnel-based concentrated photovoltaic (CPV) system with uniform irradiance.* Journal of Daylighting, 2014. **1**(1): p. 2-7.
85. Segev, G. and A. Kribus, *Performance of CPV modules based on vertical multi-junction cells under non-uniform illumination.* Solar Energy, 2013. **88**: p. 120-128.
86. Tien, N.X. and S. Shin, *A novel concentrator photovoltaic (CPV) system with the improvement of irradiance uniformity and the capturing of diffuse solar radiation.* Applied Sciences, 2016. **6**(9): p. 251.
87. Canavarro, D., *Advances in the design of solar concentrators for thermal applications.* 2014.
88. Winston, R., *Principles of solar concentrators of a novel design.* Solar Energy, 1974. **16**(2): p. 89-95.
89. Mgbemene, C.A., et al., *Electricity generation from a compound parabolic concentrator coupled to a thermoelectric module.* Journal of Solar Energy Engineering, Transactions of the ASME, 2010. **132**(3): p. 0310151-0310158.
90. Dai, G.-L., et al., *Numerical investigation of the solar concentrating characteristics of 3D CPC and CPC-DC.* Solar Energy, 2011. **85**(11): p. 2833-2842.
91. Su, Y., et al., *A novel lens-walled compound parabolic concentrator for photovoltaic applications.* Journal of Solar Energy Engineering, Transactions of the ASME, 2012. **134**(2).
92. Abu-Bakar, S.H., et al., *Rotationally asymmetrical compound parabolic concentrator for concentrating photovoltaic applications.* Applied Energy, 2014. **136**: p. 363-372.
93. Hossain, E., et al. *Solar cell efficiency improvement using compound parabolic concentrator and an implementation of sun tracking system*. in *2008 11th International Conference on Computer and Information Technology*. 2008.
94. Hatwaambo, S., et al., *Angular characterization of low concentrating PV–CPC using low-cost reflectors.* Solar Energy Materials and Solar Cells, 2008. **92**(11): p. 1347-1351.
95. Mallick, T.K., et al., *The design and experimental characterisation of an asymmetric compound parabolic photovoltaic concentrator for building façade integration in the UK.* Solar Energy, 2004. **77**(3): p. 319-327.
96. Mallick, T.K., P.C. Eames, and B. Norton, *Non-concentrating and asymmetric compound parabolic concentrating building façade integrated photovoltaics: An experimental comparison.* Solar Energy, 2006. **80**(7): p. 834-849.
97. Guiqiang, L., et al., *Experiment and simulation study on the flux distribution of lens-walled compound parabolic concentrator compared with mirror compound parabolic concentrator.* Energy, 2013. **58**: p. 398-403.
98. Guiqiang, L., et al., *Design and investigation of a novel lens-walled compound parabolic concentrator with air gap.* Applied energy, 2014. **125**: p. 21-27.

99. Li, G., et al., *Optical evaluation of a novel static incorporated compound parabolic concentrator with photovoltaic/thermal system and preliminary experiment.* Energy Conversion and Management, 2014. **85**: p. 204-211.
100. Su, Y., S.B. Riffat, and G. Pei, *Comparative study on annual solar energy collection of a novel lens-walled compound parabolic concentrator (lens-walled CPC).* Sustainable Cities and Society, 2012. **4**: p. 35-40.
101. Welford, W.T., *High collection nonimaging optics*. 2012: Elsevier.
102. Tripanagnostopoulos, Y., et al., *CPC Solar Collectors With Flat Bifacial Absorbers.* Solar Energy, 2000. **69**(3): p. 191-203.
103. Tan, M.-H., K.-K. Chong, and C.-W. Wong, *Optical characterization of nonimaging dish concentrator for the application of dense-array concentrator photovoltaic system.* Applied optics, 2014. **53**(3): p. 475-486.
104. Sellami, N. and T.K. Mallick, *Optical efficiency study of PV Crossed Compound Parabolic Concentrator.* Applied Energy, 2013. **102**: p. 868-876.
105. Baig, H., et al. *Indoor characterization of a reflective type 3D LCPV system*. in *12th International Conference on Concentrator Photovoltaic Systems, CPV 2016*. 2016. American Institute of Physics Inc.
106. Sweet, T.K., et al. *Scalable solar thermoelectrics and photovoltaics (SUNTRAP)*. in *AIP Conference Proceedings*. 2016. AIP Publishing.
107. Baig, H., et al., *Conjugate refractive–reflective based building integrated photovoltaic system.* Materials Letters, 2018. **228**: p. 25-28.
108. Baig, H., et al., *Conceptual design and performance evaluation of a hybrid concentrating photovoltaic system in preparation for energy.* Energy, 2018. **147**: p. 547-560.
109. Winston, R. and J.M. Enoch, *Dielectric compound parabolic concentrators.* Applied Optics, 1976. **15**(2): p. 291-292.
110. Mohr, A., et al. *Silicon concentrator cells designed for a direct mounting on compound parabolic concentrator*. in *3rd World Conference onPhotovoltaic Energy Conversion, 2003. Proceedings of*. 2003. IEEE.
111. Sarmah, N., B.S. Richards, and T.K. Mallick, *Evaluation and optimization of the optical performance of low-concentrating dielectric compound parabolic concentrator using ray-tracing methods.* Applied Optics, 2011. **50**(19): p. 3303-3310.
112. Baig, H., et al., *Enhancing performance of a linear dielectric based concentrating photovoltaic system using a reflective film along the edge.* Energy, 2014. **73**: p. 177-191.
113. Baig, H., et al., *Performance analysis of a dielectric based 3D building integrated concentrating photovoltaic system.* Solar Energy, 2014. **103**: p. 525-540.
114. Baig, H., N. Sellami, and T.K. Mallick, *Trapping light escaping from the edges of the optical element in a Concentrating Photovoltaic system.* Energy Conversion and Management, 2014. **90**: p. 238-246.
115. Yew, T.-K., K.-K. Chong, and B.-H. Lim, *Performance study of crossed compound parabolic concentrator as secondary optics in non-imaging dish concentrator for the application of dense-array concentrator photovoltaic system.* Solar Energy, 2015. **120**: p. 296-309.
116. Baig, H., N. Sellami, and T.K. Mallick, *Performance modeling and testing of a Building Integrated Concentrating Photovoltaic (BICPV) system.* Solar Energy Materials and Solar Cells, 2015. **134**: p. 29-44.
117. Rabl, A., *Optical and thermal properties of compound parabolic concentrators.* 1975.

118. Schuetz, M.A., et al., *Design and construction of a ~7 × low-concentration photovoltaic system based on compound parabolic concentrators.* IEEE Journal of Photovoltaics, 2012. **2**(3): p. 382-386.
119. Abu-Bakar, S.H., et al., *Performance analysis of a novel rotationally asymmetrical compound parabolic concentrator.* Applied Energy, 2015. **154**: p. 221-231.
120. Shell, K.A., et al. *Design and performance of a low-cost acrylic reflector for a ~7x concentrating photovoltaic module*. in *High and Low Concentrator Systems for Solar Electric Applications VI*. 2011. San Diego, CA.
121. Li, W., et al., *Six-parameter electrical model for photovoltaic cell/module with compound parabolic concentrator.* Solar Energy, 2016. **137**: p. 551-563.
122. Baig, H., et al. *Outdoor performance of a reflective type 3D LCPV system under different climatic conditions*. in *AIP Conference Proceedings*. 2017. AIP Publishing.
123. Chong, K.-K., et al., *Dense-array concentrator photovoltaic prototype using non-imaging dish concentrator and an array of cross compound parabolic concentrators.* Applied energy, 2017. **204**: p. 898-911.
124. Ferrer-Rodríguez, J.P., et al., *Development, indoor characterisation and comparison to optical modelling of four Fresnel-based high-CPV units equipped with refractive secondary optics.* Solar Energy Materials and Solar Cells, 2018. **186**: p. 273-283.
125. Mathur, R.K., et al., *Thermal non-uniformities in concentrator solar cells.* Solar Cells, 1984. **11**(2): p. 175-188.
126. Chenlo, F. and M. Cid, *A linear concentrator photovoltaic module: analysis of non-uniform illumination and temperature effects on efficiency.* Solar Cells, 1987. **20**(1): p. 27-39.
127. Herrero, R., et al., *Concentration photovoltaic optical system irradiance distribution measurements and its effect on multi-junction solar cells.* Progress in Photovoltaics: Research and Applications, 2012. **20**(4): p. 423-430.
128. Meng, X.L., et al., *A novel absorptive/reflective solar concentrator for heat and electricity generation: An optical and thermal analysis.* Energy Conversion and Management, 2016. **114**: p. 142-153.
129. Cuevas, A. and S. López-Romero, *The combined effect of non-uniform illumination and series resistance on the open-circuit voltage of solar cells.* Solar Cells, 1984. **11**(2): p. 163-173.
130. Luque, A., G. Sala, and J. Arboiro, *Electric and thermal model for non-uniformly illuminated concentration cells.* Solar Energy Materials and Solar Cells, 1998. **51**(3-4): p. 269-290.
131. Batzelis, E.I., P.S. Georgilakis, and S.A. Papathanassiou, *Energy models for photovoltaic systems under partial shading conditions: a comprehensive review.* IET Renewable Power Generation, 2014. **9**(4): p. 340-349.
132. Siaw, F.-L., K.-K. Chong, and C.-W. Wong, *A comprehensive study of dense-array concentrator photovoltaic system using non-imaging planar concentrator.* Renewable energy, 2014. **62**: p. 542-555.
133. Franklin, E. and J. Coventry, *Effects of highly non-uniform illumination distribution on electrical performance of solar cells.* 2002.
134. Lu, Z., et al. *The effect of non-uniform illumination on the performance of conventional polycrystalline silicon solar cell*. in *Proceedings of ISES World Congress 2007 (Vol. I–Vol. V)*. 2008. Springer.
135. Andreev, V., et al., *Effect of nonuniform light intensity distribution on temperature coefficients of concentrator solar cell*. 2003. 881-884 Vol.1.

136. Chen, J., et al., *Optimization of a uniform solar concentrator with absorbers of different shapes.* Solar Energy, 2017. **158**: p. 396-406.
137. Perez-Enciso, R., et al., *A simple method to achieve a uniform flux distribution in a multi-faceted point focus concentrator.* Renewable Energy, 2016. **93**: p. 115-124.
138. Esparza, D. and I. Moreno. *Solar concentrator with diffuser segments*. in *22nd Congress of the International Commission for Optics: Light for the Development of the World*. 2011. International Society for Optics and Photonics.
139. Parretta, A., et al. *Modelling of CPC-based photovoltaic concentrator*. in *19th Congress of the International Commisssion for Optics Optics for the Quality of Life*. 2003. Firenze.
140. Cotfas, D.T., et al. *Study of combined photovoltaic cell/thermoelectric element/solar collector in medium concentrated light*. in *2017 International Conference on Optimization of Electrical and Electronic Equipment (OPTIM) & 2017 Intl Aegean Conference on Electrical Machines and Power Electronics (ACEMP)*. 2017. IEEE.
141. O'Gallagher, J. and R. Winston, *Maximally concentrating optics for solar electricity generation*, in *Intersol Eighty Five*. 1986, Elsevier. p. 1669-1673.
142. Cooper, T., et al., *Performance of compound parabolic concentrators with polygonal apertures.* Solar Energy, 2013. **95**: p. 308-318.
143. McConnell, R. and V. Fthenakis, *Concentrated photovoltaics*, in *Third Generation Photovoltaics*. 2012, IntechOpen.
144. Maike Wiesenfarth, D.S.P.P., Dr. Andreas W. Bett,Kelsey Horowitz, Dr. Sarah Kurtz, *CURRENT STATUS OF CONCENTRATOR PHOTOVOLTAIC (CPV) TECHNOLOGY*, V. 1.3, Editor. 2017.
145. Seshan, C. *CPV: Not just for hot deserts!* in *2010 35th IEEE Photovoltaic Specialists Conference*. 2010.
146. Tyagi, V.V., S.C. Kaushik, and S.K. Tyagi, *Advancement in solar photovoltaic/thermal (PV/T) hybrid collector technology.* Renewable and Sustainable Energy Reviews, 2012. **16**(3): p. 1383-1398.
147. Kurtz, S. and J. Geisz, *Multijunction solar cells for conversion of concentrated sunlight to electricity.* Optics express, 2010. **18**(101): p. A73-A78.
148. Vu, N.H. and S. Shin, *Flat concentrator photovoltaic system with lateral displacement tracking for residential rooftops.* Energies, 2018. **11**(1).
149. POWER, V.G. *The Benefits of Solar Trackers*. 2015 [cited 25.05.2019]; Available from: http://www.valldoreix-gp.com/the-benefits-of-solar-trackers/.
150. Bellos, E. and C. Tzivanidis, *Development of analytical expressions for the incident angle modifiers of a linear Fresnel reflector.* Solar Energy, 2018. **173**: p. 769-779.
151. Wang, J., et al., *Analysis of operating characteristics for tracking system of parabolic trough solar collector.* Taiyangneng Xuebao/Acta Energiae Solaris Sinica, 2016. **37**(12): p. 3125-3131.
152. Xiao, G., et al., *A model-based approach for optical performance assessment and optimization of a solar dish.* Renewable Energy, 2017. **100**: p. 103-113.
153. Renzi, M., et al., *Experimental investigation and numerical model validation of a 2.5 kWt concentrated solar thermal plant.* Applied Thermal Engineering, 2018. **133**: p. 622-632.
154. Mousazadeh, H., et al., *A review of principle and sun-tracking methods for maximizing solar systems output.* Renewable and Sustainable Energy Reviews, 2009. **13**(8): p. 1800-1818.

155. Hong, T., et al., *A Preliminary Study on the 2-axis Hybrid Solar Tracking Method for the Smart Photovoltaic Blind.* Energy Procedia, 2016. **88**: p. 484-490.
156. Burhan, M., et al., *Solar to hydrogen: Compact and cost effective CPV field for rooftop operation and hydrogen production.* Applied Energy, 2017. **194**: p. 255-266.
157. Gleckman, P. *A high concentration rooftop photovoltaic system*. in *Proceedings of SPIE - The International Society for Optical Engineering*. 2007.
158. Cooperation, N. *Small Area Solar Simulators*. 2019 [cited 15.05.2019]; Available from: https://www.newport.com/f/small-area-solar-simulators.
159. Standard, A., *E927-19, Standard Classification for Solar Simulators for Electrical Performance Testing of Photovoltaic Devices1, ASTM International, West Conshohocken, PA, USA*. 2019.
160. Autolab, M. *Autolab PGSTAT302N - High Performance*. 20.05.2019]; Available from: https://www.metrohm-autolab.com/Products/Echem/NSeriesFolder/PGSTAT302N.
161. SEAWARD. *Solar Survey Multifunction Solar Irradiance Meters*. 2019 [cited 15.05.2019]; Available from: http://www.seawardsolar.com/products/solar-irradiance-meter?ref=seaward.co.uk.
162. ZONEN, K. *CMP10 Pyranometer*. 2019 [cited 2019 16.05.2019]; Available from: https://www.kippzonen.com/Product/276/CMP10-Pyranometer#.XN0r_BRKiM9.
163. Technology, p. *Thermocouple Data Logger*. 2019 16.05.2019]; Available from: https://www.picotech.com/data-logger/tc-08/usb-tc-08-manuals.
164. Rolley, M.H., *Systems Integration of Concentrator Photovoltaics and Thermoelectrics for Enhanced Energy Harvesting*, in *School of Engineering*. 2018, Cardiff University.
165. IEC, *Photovoltaic Devices: Part 9. Solar Simulator Performance Requirements ed 2.0, IEC 60904-9 (Geneva,Switzerland: International Electrotechnical Commission)*.
166. Niclas. *Measuring the temperature coefficient of a PV module*. [cited 25.05.2019]; Available from: https://sinovoltaics.com/solar-basics/measuring-the-temperature-coefficients-of-a-pv-module/.
167. Chikate, B.V. and Y. Sadawarte, *The factors affecting the performance of solar cell.* International journal of computer applications, 2015. **1**(1): p. 0975-8887.
168. edition, I.S., *Crystalline silicon terrestrial photovoltaic (PV) modules –Design qualification and type approval* in *IEC 61215*. 2005-04, International Electrotechnical Commission: Geneva 20, Switzerland.
169. Naman, G.Z., *Design and development of symmetric reflective compound parabolic concentrator (SRCPC) for power generation*. 2016, Heriot-Watt University.
170. Radziemska, E., *The effect of temperature on the power drop in crystalline silicon solar cells.* Renewable energy, 2003. **28**(1): p. 1-12.
171. Herrero, R., et al., *Concentration photovoltaic optical system irradiance distribution measurements and its effect on multi-junction solar cells.* Progress in Photovoltaics: Research and Applications, 2012. **20**(4): p. 423-430.
172. Inc, S. *Dual-Detector Super Range (DSR) Spectrometer Systems*. 1991-2019 [cited 16.05.2019]; Available from: https://www.stellarnet.us/stellarnet-downloads/dual-detector-super-range-spectrometers-systems/.
173. Al-Najideen, M., M. Al-Shidhani, and G. Min. *Optimum design of V-trough solar concentrator for photovoltaic applications*. in *AIP Conference Proceedings*. 2019. AIP Publishing.
174. Schriemer, H., et al. *Refractive concentrator optics architectures, tracker precision, and cumulative energy harvest*. in *2015 IEEE 42nd Photovoltaic Specialist Conference (PVSC)*. 2015. IEEE.

175. Shell, K.A., et al. *Performance of a low-cost, low-concentration photovoltaic module*. in *7th International Conference on Concentrating Photovoltaic Systems, CPV-7*. 2011. Las Vegas, NV.
176. Jing, L., et al., *Design of uniform-irradiance concentrator for concentration photovoltaics system.* Guangxue Xuebao/Acta Optica Sinica, 2014. **34**(2).
177. CORPORATION, L.R. *TracePro®* [cited 17.05.2019]; Available from: https://www.lambdares.com/tracepro/.
178. formlabs. *The Form +1*. [cited 20/12/2016]; Available from: https://formlabs.com/3d-printers/form-1-plus/.
179. Mazak. *VERTICAL CENTER SMART 430A*. [cited 23.05.2019]; Available from: https://www.mazak.com.vn/vertical-center-smart-430a/.
180. CEC. *Direct Copper Bonded (DCB) Ceramic Substrates*. 23.05.2019]; Available from: https://www.china-rectifier.com/result.aspx?KeyWord=DCB.
181. Winston, R., J.C. Miñano, and P.G. Benitez, *Nonimaging optics*. 2005: Elsevier.
182. Sun, P.F.T. *Concentrator Optics*. [cited 13.05.19]; Available from: https://www.powerfromthesun.net/Book/chapter08/chapter08.html.
183. Rincón, E., M. Durán, and A. Lentz. *New solar air heater based on non-imaging optics for high temperature applications*. in *Proceedings of the ASME 3rd International Conference on Energy Sustainability 2009, ES2009*. 2009.
184. Paul, D.I., *Symmetric compound parabolic concentrator with indium tin oxide coated glass as passive cooling system for photovoltaic application.* Journal of Solar Energy, 2016. **2016**.
185. Wang, X.-d. and O.S. Wolfbeis, *Fiber-optic chemical sensors and biosensors (2013–2015).* Analytical chemistry, 2015. **88**(1): p. 203-227.
186. Sellami, N. and T.K. Mallick, *Optical characterisation and optimisation of a static Window Integrated Concentrating Photovoltaic system.* Solar Energy, 2013. **91**: p. 273-282.
187. Supplies, E.T. *3M Aluminium Foil Tape - 425 -*. [cited 25.05.19]; Available from: https://embossingtapesupplies.com.au/3m-aluminium-foil-tape-425.html.
188. Rapid. *Ultratape Rhino Aluminium Foil Tape 50mm x 45.7m*. [cited 18.04.18]; Available from: https://www.rapidonline.com/Ultratape-Rhino-Aluminium-Foil-Tape-50mm-x-45-7m-87-1900?IncVat=1&pdg=pla-353758740462:kwd-353758740462:cmp-757438067:adg-44804851896:crv-207912323492:pid-87-1900:dev-c&gclid=Cj0KCQjw0brtBRDOARIsANMDykYcRewaU4V5ZDaOgQ1zEuOrsqy4sGjW59AxF_WnXZ6miK7jhRzCgWgaAsbKEALw_wcB.
189. alanod, *MIRO® – Don't settle for less*. 2018.
190. Embaye, M., R. Al-Dadah, and S. Mahmoud, *Thermal performance of hydronic radiator with flow pulsation–Numerical investigation.* Applied Thermal Engineering, 2015. **80**: p. 109-117.
191. Optics, E. *Compound Parabolic Concentrator*. [cited 03.01.2020]; Available from: https://www.edmundoptics.com/p/25deg-434mm-output-dia-compound-parabolic-concentrator/17843/.
192. Electroplating. *Gold Plating Services*. [cited 24.06.2019]; Available from: http://www.cirelectroplating.co.uk/gold-plating-services/.
193. Mokhtar, G., B. Boussad, and S. Noureddine, *A linear Fresnel reflector as a solar system for heating water: Theoretical and experimental study.* Case Studies in Thermal Engineering, 2016. **8**: p. 176-186.

194. Hatwaambo, S., et al., *Angular characterization of low concentrating PV-CPC using low-cost reflectors.* Solar Energy Materials and Solar Cells, 2008. **92**(11): p. 1347-1351.
195. Al-Shohani, W.A.M., et al., *Optimum design of V-trough concentrator for photovoltaic applications.* Solar Energy, 2016. **140**: p. 241-254.
196. Daabo, A.M., S. Mahmoud, and R.K. Al-Dadah, *The effect of receiver geometry on the optical performance of a small-scale solar cavity receiver for parabolic dish applications.* Energy, 2016. **114**: p. 513-525.
197. Wang, J.-M. and C.-L. Lu, *Design and implementation of a sun tracker with a dual-axis single motor for an optical sensor-based photovoltaic system.* Sensors, 2013. **13**(3): p. 3157-3168.
198. Wong, L. and W. Chow, *Solar radiation model.* Applied Energy, 2001. **69**(3): p. 191-224.
199. Center, A.S.D. *Processing, archiving and distributing Earth science data at the NASA Langley Research Center* [cited 25.08.2018]; Available from: https://eosweb.larc.nasa.gov/.
200. *Huzhou Dear Indusrtry Co., Ltd.* 2019 [cited 01.12.19]; Available from: https://hzdear.en.alibaba.com/.
201. FASTARRIVER Henan Fastarriver Industrial Co., L. *Polished Mirror Aluminum Coil/Sheet*. [cited 09.09.2019]; Available from: http://www.fastarriver.com/product_silver_mirror_aluminum.html.
202. *DS New Energy*. [cited 05.12.19]; Available from: https://www.dsneg.com/.
203. group, A. *Solar Energy*. [cited 15/07/2019]; Available from: http://www.arima.com.tw/en/about3.php.
204. future, W.S.p.t. *Solarwatt Framed Panels*. [cited 07/08/2019]; Available from: http://www.windandsun.co.uk/products/Solar-PV-Panels/Solarwatt-PV-Panels/Solarwatt-Framed-Panels#.XUrzPvJKiM8.

Appendix

A1: Monocrystalline LGBC solar cell datasheet

```
12:05
\\ws7.lboro.ac.uk\WS-PVMAD\Data\J-V\Mustafa\2019-10-17_Cardif-Mazin\Second run\Monocrtstalline_light_1.txt
Measurement Time (secs)         1.000000E+1
Number of Points                1.000000E+2
Fraction of points to  use in calculating rough parameters              5.000000E+0
Cell Area               1.000000E+0
Irradiance              1.000000E+3
Voltage Start (V)               -2.000000E-1
Voltage Stop (V)                8.000000E-1
Current Compliance              5.000000E-2
4 Wire          1.000000E+0
Voltage Settling Tiime (ms)             1.000000E+1
Voc (V)         5.698883E-1
Jsc (mA/cm²)            -2.628389E+1
FF              6.880917E-1
Efficiency (%)          1.030684E+1
Isc (mA)                -2.628389E+1
Vmp (V)         4.565000E-1
Imp (mA)                -2.257797E+1
Pmp (W)         1.030684E-2
Rs (Ohms)               5.278185E-1
Rsh (Ohms)              1.193637E+3
```

A2: GaAs Datasheet

SOLAR CELL

Arima Photovoltaic & Optical Corp.

III-V Single-Junction Solar Cell

Product Features

- Single Junction GaAs solar cell,
- Front and back contacts are weldable or solderable,
- Cells are fully tested under illumination
- Various sizes including 2.5 x 2.5, 4 x 4, 5.5 x 5.5, 7 x 7, 10 x 10 mm^2 and 26 cm^2 available

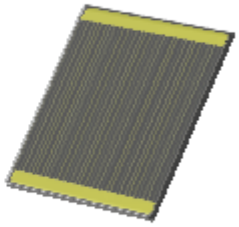

Typical Cell Characteristics

Product	Size Aperture Area	I_{sc} [mA]	V_{oc} [V]	I_{mp} [mA]	V_{mp} [V]	P_{mp} [mW]	FF [%]	EFF [%]
T1JM1F100A	10mm x 10mm 1.006 cm^2	27.9	1.0	26.4	0.89	23.5	84.6	23.4

Typical I-V Characteristics

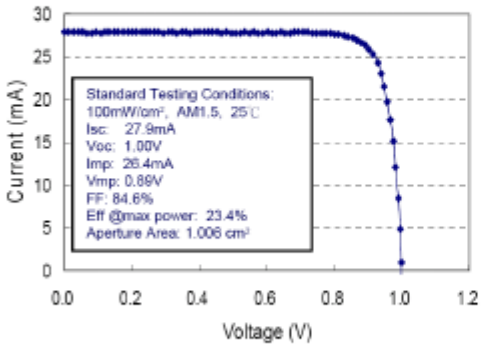

External Quantum Efficiency

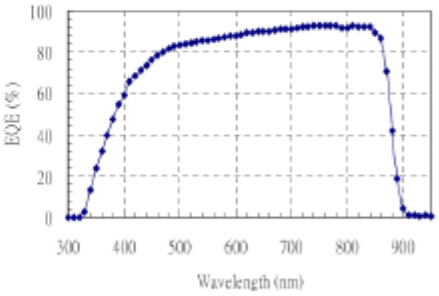

Arima PV&O W: www.arima.com.tw T: +886-3-4699768 F: +886-3-4699771 E: info-PV@arima.com.tw

A3: Repeatability test (25 I-V curves)

GaAs solar cell

Test No.	V_{OC} (V)	I_{sc} (A)	Efficiency (%)
1	0.9995	0.0263	19.98
2	0.9991	0.0263	19.93
3	0.9988	0.0263	19.86
4	0.9998	0.0263	19.81
5	0.9998	0.0263	19.79
6	0.9995	0.0263	19.81
7	0.9991	0.0264	19.8
8	0.9998	0.0263	19.76
9	0.9995	0.0263	19.78
10	0.9991	0.0262	19.7
11	0.9991	0.0263	19.75
12	0.9995	0.0263	19.74
13	0.9995	0.0263	19.78
14	0.9995	0.0264	19.79
15	0.9995	0.0263	19.84
16	0.9995	0.0263	19.77
17	0.9995	0.0263	19.75
18	0.9995	0.0263	19.7
19	0.9995	0.0263	19.71
20	0.9991	0.0262	19.74
21	0.9991	0.0262	19.71
22	0.9995	0.0262	19.69
23	0.9988	0.0262	19.73
24	0.9995	0.0262	19.73
25	0.9998	0.0262	19.7
Average	**0.9994**	**0.0263**	**19.77**

A4: Temperature Coefficient of Monocrystalline silicon Cell

solar capture TECHNOLOGIES

SPC002 Concentrator Cells

PHYSICAL CHARACTERISTICS	Dimension	10 mm x 10 mm ± 0.5 mm
	Wafer Thickness	200 µm ± 30 µm
	Front (-)	One 1.5 mm busbar (silver) with selective emitter, acid texturized surface with blue silicon nitride AR Coating.
	Rear (+)	Silver plated rear, aluminium back surface field.

METALISATION PATTERNS

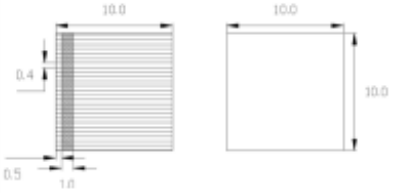

TYPICAL ELECTRICAL CHARACTERISTICS

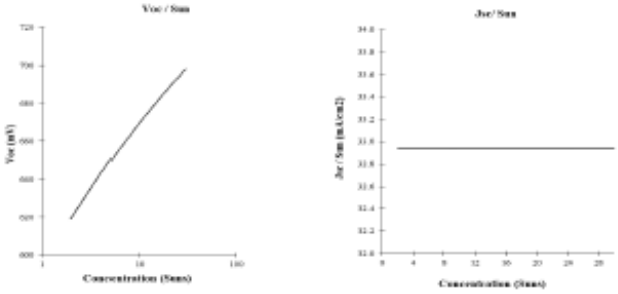

TYPICAL TEMPERATURE COEFFICIENTS	Voltage	-2.08	mV/k
	Current	+4.58	mA/K
	Power	-0.40	%/K

TYPICAL SPECTRAL RESPONSE

TYPICAL EFFICENCY RESPONSE

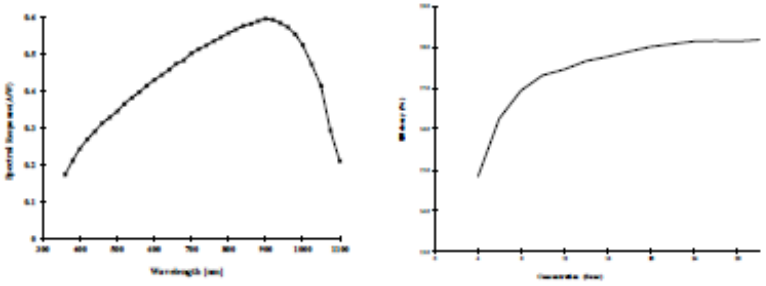

World leaders in photovoltaic innovation

A5: Silicon Solar Cells Soldering Without DCB Ceramic

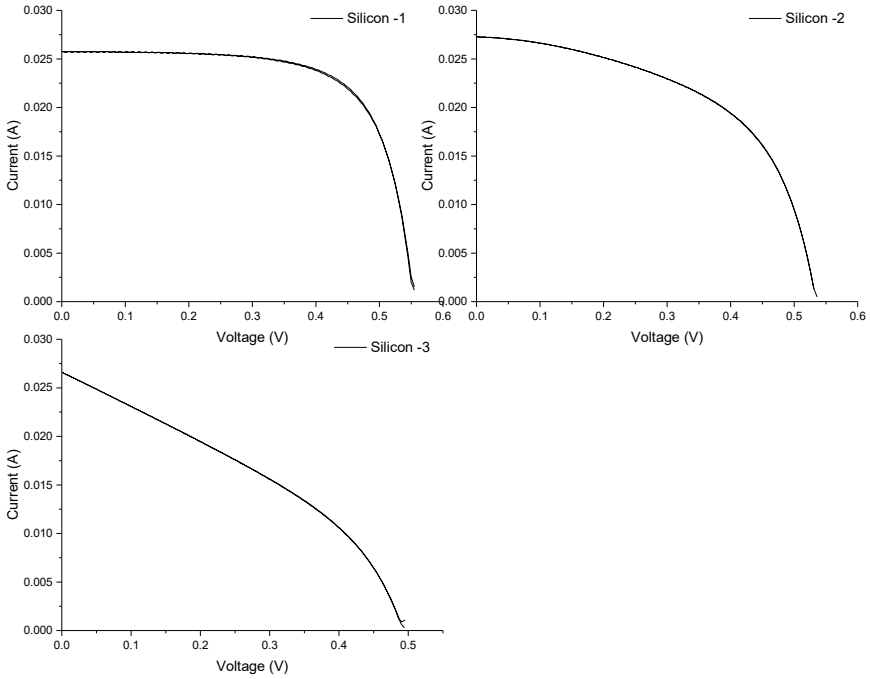

A6: Silicon Solar Cells Soldering With DCB Ceramic

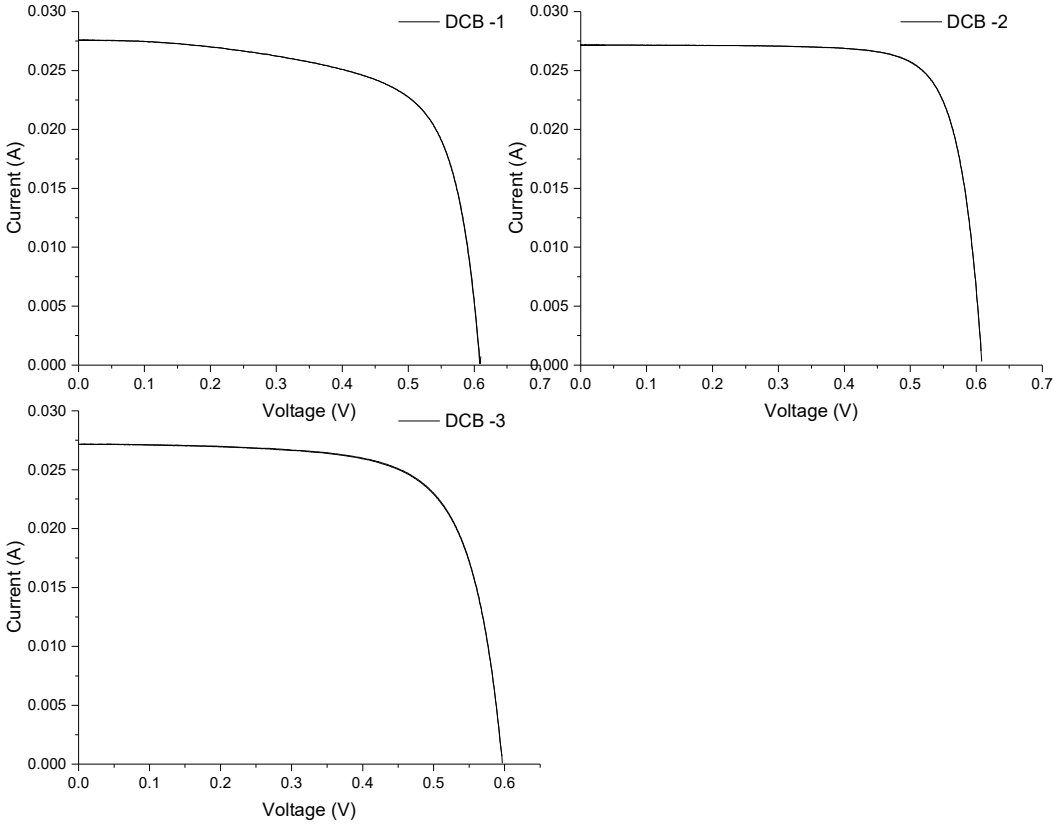

A7: DCB Specification

Direct Copper Bonded (DCB) Ceramic Substrates

Features
- Fine Mechanical strength
- Fine Adhesion and Corrosion Resistent
- Excellent Electrical Insulation and Thermal Conductive Properties
- High Reliability
- Lower Thermal Expansion Coefficient
- Etchable to Various Graphs

Applications
- Power Semiconductor Modules
- Power Hybrids
- Power Control Circuits
- Solid-state Relays
- Semiconductor Refrigerators
- Electronic Devices for Automobile
- Intelligent Power Assemblies
- Solar Cell Board

Characteristics of Material

Item		Unit	Value	
Ceramic	Content	%	96Al_2O_3	96AlN
	Thickness	mm	0.25, 0.38, 0.5, 0.63(std.), 0.76, 1.0	
	Dielectric Constant (at 25℃,1MHz)		9.4	8.9
	Dielectric Loss Angle (at 25℃,1MHz)	$\times 10^{-4}$	3	3
	Dielectric Strength	kV/mm	>14	>14
	Thermal Conductivity (at 25℃)	W/m.K	24~28	150
Copper layer	Thickness	mm	0.3	
	Thermal Conductivity	W/m.K	385	
DCB	Dimension (max.)	mm×mm	127×198	75×57
	Thermal Expansion Coefficient	10^{-6}/℃	7.4(25~200℃)	5(50~500℃)
	Bounding Force	N/mm	>6	>3
	Bending	μ m/mm	<150/50	
	Operating Temperature (inert atmosphere)	℃	-55~+850	
	Plating		Au or Ni plated or bare Cu	
Note: Dimension and etching graph of DCB substrate can be produced according to customers' requirements.				

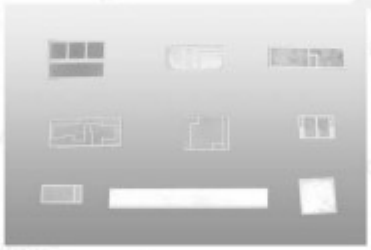

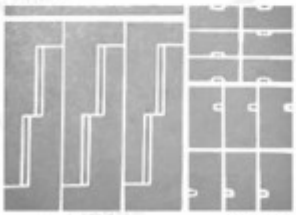

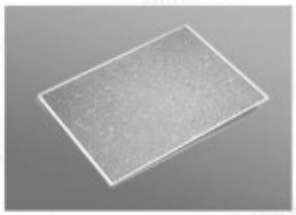

Various DCB ceramic substrates

Tianjin Century Electronics Co., Ltd

B1: Excel sheet used to calculate the CCPC concentration ratio

				Focal Point														
				10.5														
														θ i	θ i			
														Winston				
θc (half acceptance)	θt	θ (angular half acceptance)	a	a'	C2D	C3D		height 2	Winston Equation	height 3	height 4	height 5	F	θt	Htruncate	Htruncated		
30	41.8	48.59037789	20	10	2	4		25.98	25.98076	36.37307	51.9615	51.96152	15	-88.4292	13.19605	115.376238		
								mm										
30											COTx= 1/TAN							

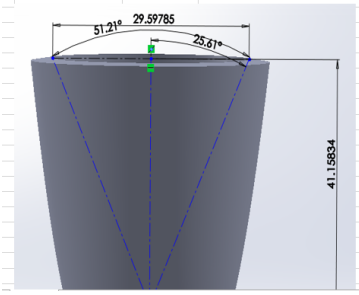

3.225401

θ

To create parabola shape in solidworks

1- enter half entry dimension.
2- Enter full entry dimension
3- enter the legth of parabola
4- enter the half acceptance angle

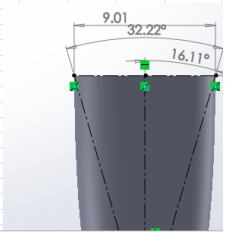

B2: Alanod Reflector Datasheet

Product data sheet

Product: **1095AG**
MIRO® high reflective 95

alanod SOLAR
4700/0259/001/08.13

Alloy	[1]	1050 or purer	
Hardness	[2]	hard	
Treatment front side	(S1)	brightened, anodised and PVD-coated	
Treatment reverse side	(S2)	anodised	
Coating system	(S1)	PVD - based on AG 99,95	
Iridescence assessment	(S1)	absolutely free of interference colours	
Delivery options			
in form of		Coil, strip, sheet, blanks	
Thickness from/to	[mm]	0,20 - 0,50	
Width up to	[mm]	1250,00	
Optical Values			
Total light reflection	[%]	≥ 98	DIN 5036-3 (U-Globe) (8°)
Brightness 60° along	[-]	≥ 93	ISO 7668 (60°)
Brightness 60° across	[-]	≥ 92	ISO 7668 (60°)
Solar reflection	[%]	≥ 95	ASTM G 173
Solar weighted spec. reflectance	[%]	≥ 92	ASTM G 173
Mechanical Properties			
Yield strength Rp 0,2	[MPa]	140 - 190	
Tensile strength Rm	[MPa]	160 - 200	
Elongation A50	[%]	≥ 2	
Deformation/Bending/Bending radius		≥ 1,5 x gauge of material	
Tolerances			
Thickness from/to	[mm]	0,20 - 0,50 ± 0,04	
Width/Coil up to	[mm]	+ 3,00 / - 0,00	
Width Slit Coil	[mm]	± 0,20 standard	
Longitudinal Curvature	[mm]	≤ 1,00 on a measuring length of 1000 mm	
Length	[mm]	0 - 600 + 1,00 / - 0,00	
	[mm]	601 - 1500 + 1,50 / - 0,00	
	[mm]	1501 - 2500 + 2,50 / - 0,00	
	[mm]	2501 - 3500 + 3,50 / - 0,00	
Flatness	[%]	1 % of wavelength, max. 8 mm	
Transversal Divergency	[mm]	≤ 1,5 (D1-D2)	
		other tolerances on request	
Protective Film			
Protective Film Type	[-]	PE - Film	
Protective Film Thickness	[µm]	50 - 60	

[1] based on DIN EN 573-3 (Aluminium), DIN EN 13599 (Copper) resp. Rolling mill standard
[2] based on DIN EN 485-2 (Aluminium), DIN EN 1652 (Copper) resp. Rolling mill standard
13.08.2018 09:33:53 Valid only on print date

1 of 1

B3: Exit aperture dimension of 8.3x CCPC

19-Jul-2018 16:14 Start Template Page 1

(mm)	ACTUAL	NOMINAL	LO-TOL	HI-TOL	DEVIATION	GRAPHIC	ERROR
Y_DISTANCE							
Point:PNT1--Point:PNT2							
Lengthavg	9.924	10.000	-0.100	+0.100	-0.076	-*-+---	
Point:PNT11--Point:PNT22							
Lengthavg	9.922	10.000	-0.100	+0.100	-0.078	-*-+---	
Point:PNT111--Point:PNT222							
Lengthavg	9.924	10.000	-0.100	+0.100	-0.076	-*-+---	
X_DISTANCE							
Point:PNT3--Point:PNT4							
Lengthavg	9.831	10.000	-0.100	+0.100	-0.169	<--+---	-0.069
Point:PNT33--Point:PNT44							
Lengthavg	9.848	10.000	-0.100	+0.100	-0.152	<--+---	-0.052
Point:PNT333--Point:PNT444							
Lengthavg	9.848	10.000	-0.100	+0.100	-0.152	<--+---	-0.052

Duration 5 mins 5 secs FAIL in:3 out:3 End of Report

B4: I-V and P-V curves for 7.0x circular CPC with and without coating

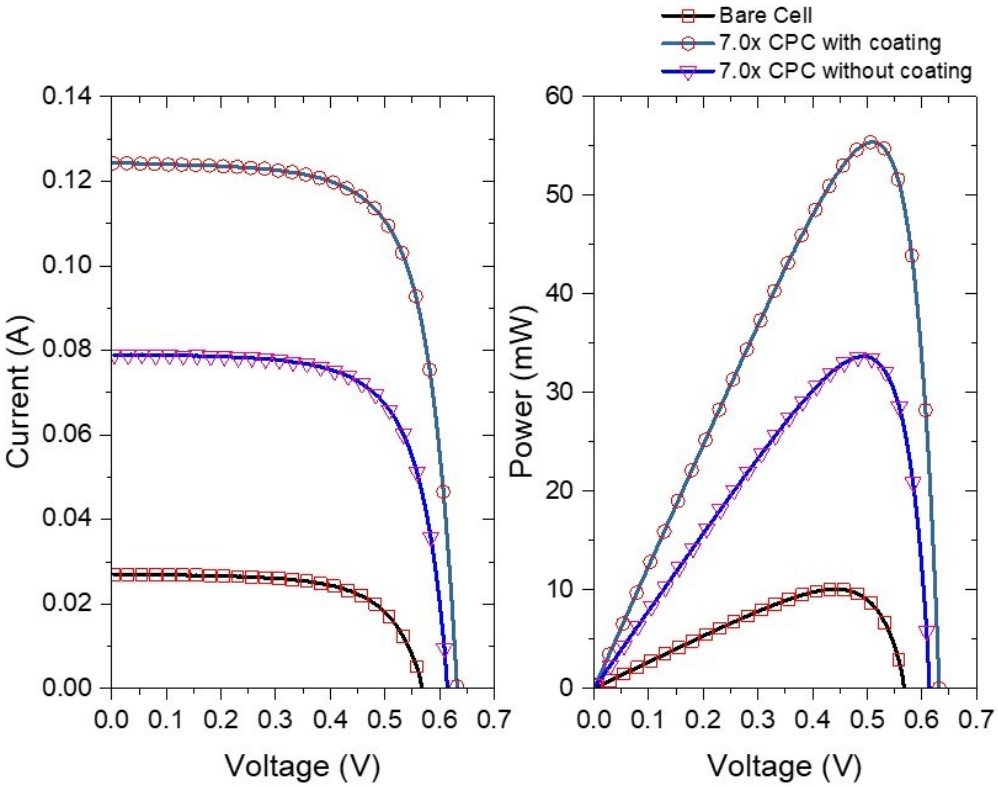

B5: I-V and Power curve for the five CCPCs concentrators at normal incidence angle (0°)

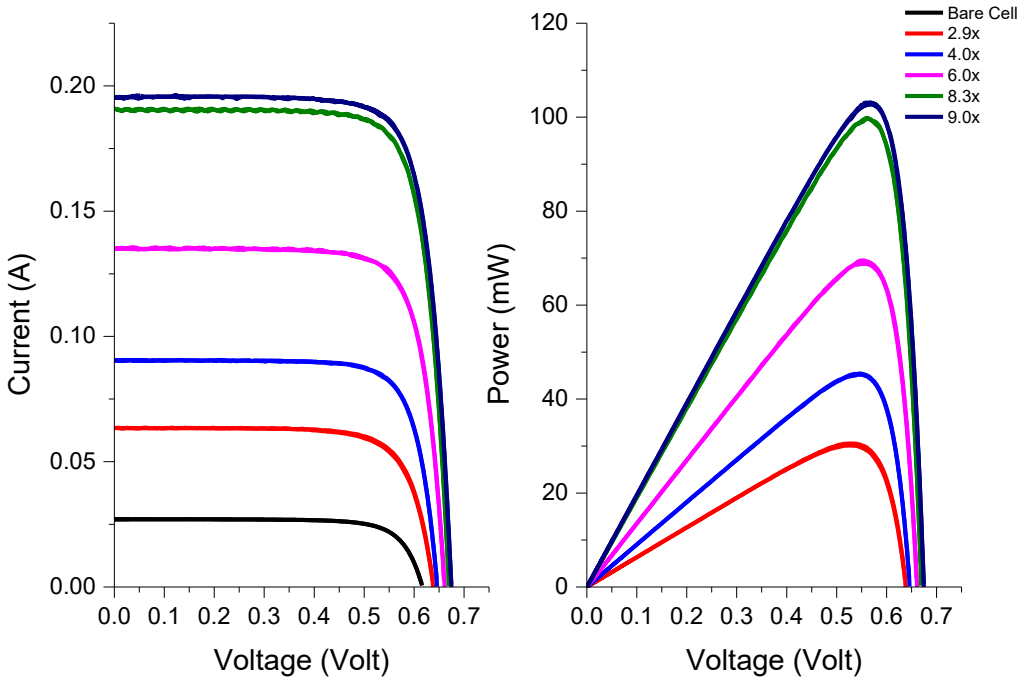

D1: SIMULINK simulation for real solar radiation

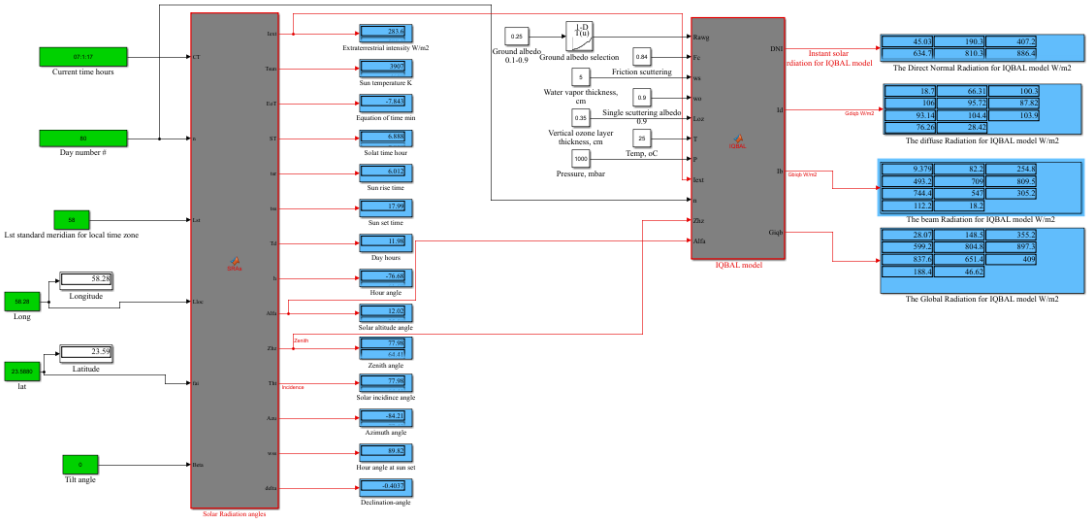

D2: real solar radiation on four concentrators

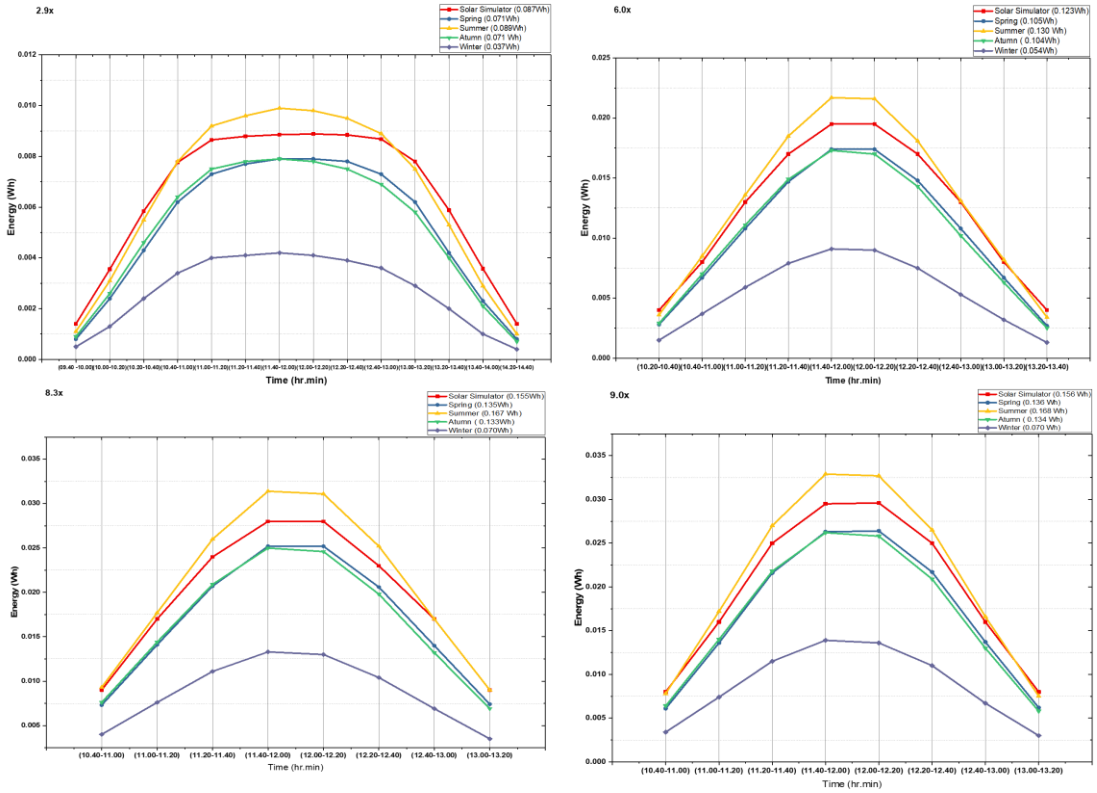

D3: Scaled up 9.0x CCPC dimensions

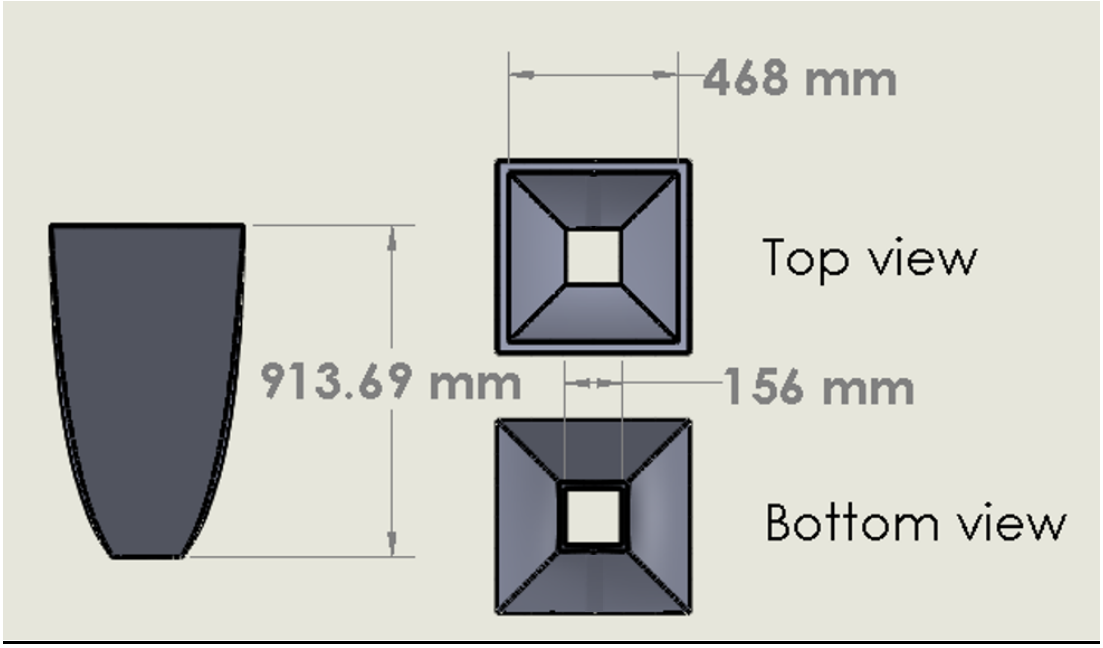

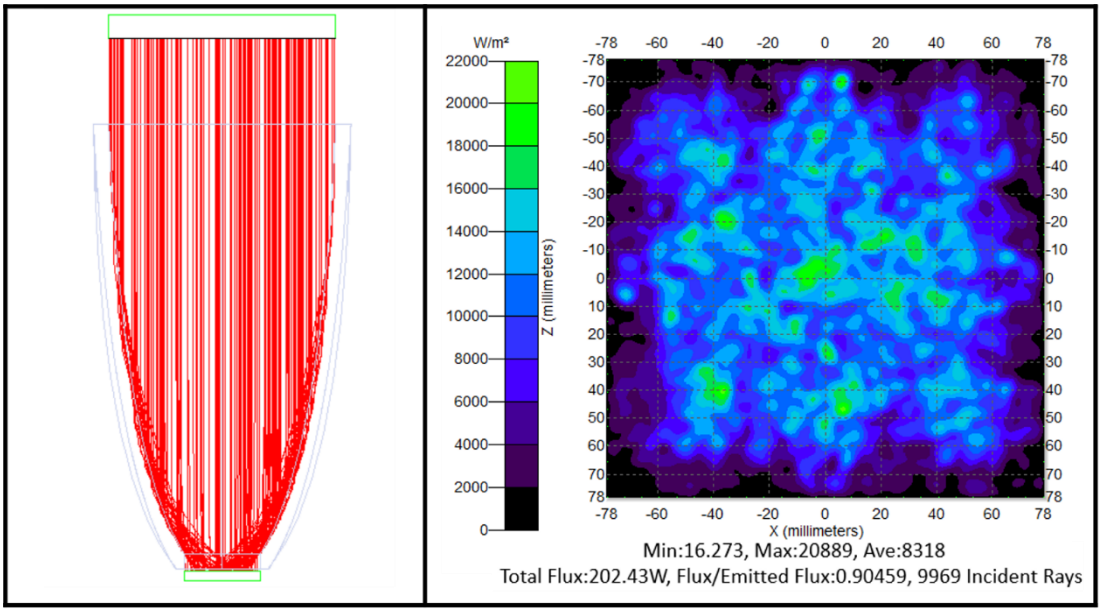

Angular optical efficiency for the five concentrators